

LAL 00-57

# New Insights into the Proton Structure with $ep$ Collider HERA

ZHIQING ZHANG

*Laboratoire de l'Accélérateur Linéaire  
IN2P3 - CNRS et Université de Paris-Sud  
Bât. 200, BP 34  
F-91898, Orsay Cedex  
France  
E-mail: zhangzq@lal.in2p3.fr*

## Abstract

Since its commissioning in 1991, the  $ep$  collider HERA has been running successfully for almost a decade without stopping improving its performance. In this report, the inclusive cross section and structure function measurements for the deep inelastic scattering of neutral and charged current processes in the full HERA kinematic domain are reviewed. The results are compared with the Standard Model expectations for the deep inelastic scattering processes. The new insights into the proton structure and on the underlying strong and electroweak interactions are discussed.

*Habilitation defended on Dec. 1, 2000*

# Contents

<b>1</b>	<b>Introduction</b>	<b>1</b>
<b>2</b>	<b>Experimental setups and techniques</b>	<b>3</b>
2.1	Kinematics of deep inelastic scattering . . . . .	3
2.2	The fixed-target experiments . . . . .	5
2.3	The HERA accelerator . . . . .	8
2.4	The H1 detector . . . . .	12
2.4.1	The tracking detectors . . . . .	13
2.4.2	Calorimetry . . . . .	14
2.4.3	Muon detectors . . . . .	16
2.4.4	Very forward detectors . . . . .	17
2.4.5	Luminosity detector and electron taggers . . . . .	17
2.4.6	Trigger and event reconstruction . . . . .	18
2.5	Monte Carlo technique and detector simulation . . . . .	20
2.6	Kinematics reconstruction and coverage . . . . .	21
2.6.1	Reconstruction of kinematic variables . . . . .	21
2.6.2	Coverage of the kinematic phase space . . . . .	22
<b>3</b>	<b>Theoretical framework</b>	<b>25</b>
3.1	Deep inelastic scattering and the quark parton model . . . . .	25
3.1.1	Cross sections and structure functions . . . . .	25
3.1.2	Structure functions in the quark parton model . . . . .	27
3.2	Quantum Chromodynamics and parton density evolution equations	31
3.2.1	Structure functions in QCD . . . . .	32
3.2.2	Evolution of structure functions . . . . .	33

3.2.3	Higher twist . . . . .	35
3.3	Parameterizations of parton distribution functions . . . . .	36
3.3.1	Global analysis of parton distribution functions . . . . .	36
3.3.2	Dynamical parton distributions . . . . .	40
3.3.3	Other model parameterizations . . . . .	41
3.4	Radiative corrections and hard radiative processes . . . . .	42
3.4.1	Radiative corrections for neutral and charged current DIS processes at HERA . . . . .	42
3.4.2	Hard radiative processes . . . . .	45
<b>4</b>	<b>Measurement of structure functions and their interpretation</b>	<b>46</b>
4.1	Pre-HERA results and expectations . . . . .	46
4.2	First measurements at low $x$ from HERA . . . . .	48
4.3	First $F_2(x, Q^2)$ measurement at values of $Q^2$ beyond those covered by fixed-target experiments . . . . .	49
4.3.1	Event selection and background filters . . . . .	50
4.3.2	Monte Carlo simulation . . . . .	52
4.3.3	Kinematic reconstruction . . . . .	53
4.3.4	Measurement procedure of the structure function $F_2(x, Q^2)$ . . . . .	56
4.3.5	Results . . . . .	58
4.4	The structure function $F_2$ at low $Q^2$ from radiative events . . . . .	62
4.4.1	Extended kinematic domain using radiative events . . . . .	62
4.4.2	Event selection and background studies . . . . .	64
4.4.3	Monte Carlo simulation . . . . .	68
4.4.4	Kinematic reconstruction . . . . .	68
4.4.5	Measurement of the structure function $F_2(x, Q^2)$ . . . . .	71
4.4.6	Higher order QED correction . . . . .	77
4.4.7	$F_2$ results . . . . .	78
4.5	Precision measurement at HERA . . . . .	81
4.6	Current knowledge of the gluon density . . . . .	85
4.6.1	Impact of the HERA $F_2$ data on the determination of the gluon density at low $x$ . . . . .	85
4.6.2	Uncertainty and future improvements . . . . .	88

4.7	Longitudinal structure function $F_L(x, Q^2)$ . . . . .	92
4.7.1	Current knowledge of $F_L(x, Q^2)$ . . . . .	92
4.7.2	Feasibility study and a new method for a direct measurement of $F_L$ at HERA . . . . .	93
4.8	The strong coupling constant $\alpha_s$ . . . . .	103
<b>5</b>	<b>Neutral and charged current interactions at high <math>Q^2</math></b>	<b>108</b>
5.1	Technical aspects . . . . .	109
5.1.1	Event selections and background studies . . . . .	109
5.1.2	Alignment and electron angle measurement . . . . .	114
5.1.3	Electron energy measurement . . . . .	119
5.1.4	Hadronic energy measurement . . . . .	121
5.1.5	Calorimetric noise suppression . . . . .	125
5.1.6	Trigger efficiency for charged current events . . . . .	127
5.2	Measurement of inclusive cross sections at high $Q^2$ . . . . .	129
5.2.1	Systematic sources and resulting uncertainties on the cross section measurements . . . . .	130
5.2.2	Measurement and comparison of NC and CC reduced cross sections in $e^+p$ collisions at two center-of-mass energies . .	132
5.2.3	Measurement and comparison of NC and CC reduced cross sections in $e^+p$ and $e^-p$ collisions . . . . .	136
5.2.4	Measurement of the structure function $x\tilde{F}_3$ at high $Q^2$ . .	136
5.2.5	Helicity structure of the CC cross sections . . . . .	139
5.2.6	Measurement and comparison of the $Q^2$ dependence of NC and CC cross sections in $e^+p$ and $e^-p$ collisions . . . . .	139
5.2.7	Measurement and comparison of the $x$ dependence of NC and CC cross sections in $e^+p$ and $e^-p$ collisions . . . . .	145
5.3	Valence quark distribution at high $Q^2$ and high $x$ . . . . .	149
5.3.1	Local extraction of valence quark densities . . . . .	150
5.3.2	Valence quark densities from a new NLO QCD Fit . . . .	151
5.4	Electroweak tests at HERA . . . . .	155
5.5	Searches for new physics beyond the Standard Model . . . . .	158
5.5.1	Search for leptoquarks at HERA . . . . .	158
5.5.2	Search for supersymmetry at HERA . . . . .	160

5.5.3	Search for contact interactions . . . . .	166
<b>6</b>	<b>Summary and outlook</b>	<b>170</b>
	<b>Bibliography</b>	<b>174</b>

# Chapter 1

## Introduction

Scattering experiments have proven to be a very effective technique for probing the structure of matter. The large angle scattering of  $\alpha$  particles (a few MeV) off a gold foil led Rutherford to conjecture around 1910 that the bulk of the mass of the atom must be contained in a very small, positively charged nucleus of the atom. The energy available in such a collision is related to a certain wavelength. The higher the energy, the shorter the wavelength and thus the smaller the distances which can be resolved. To investigate atomic nuclei with higher accuracy it is therefore necessary to bombard them with particles of higher energy. In the 1950s and 1960s, starting with electron scattering experiments at Stanford [1], experiments were performed at Darmstadt, Orsay, Yale, CEA and DESY. At the energies available, the experiments were however restricted to elastic scattering or excitation of the low-lying resonances. As higher energy electron beams (up to 16 GeV) became available at SLAC in the late 1960s, inelastic scattering experiments could be performed. These experiments [2, 3] together with those at DESY [4] showed that at large four-momentum transfers, the inelastic nucleon structure functions were independent of any dimensional quantity, a phenomenon known as scaling. This result was interpreted as evidence for the existence of point-like constituents in the nucleons. These constituents are now known as quarks. Subsequent fixed-target lepton-nucleon scattering experiments<sup>1</sup> at still higher energies have established the existence of violations of the scaling behavior [5, 6] which has been one of the most dramatic successes of perturbative Quantum Chromodynamics (QCD).

Apart from the important roles deep inelastic scattering (DIS) has played in understanding nucleon structure, it also contributed to our understanding in other ways (see e.g. [7]). Neutral-current phenomena, which provided the first

---

<sup>1</sup>The use of high energy leptons (electrons, muons and neutrinos, along with their antiparticles) as probes of nucleon structure is unique because the leptons do not interact strongly, so that they are able to penetrate the nuclear surface; their short wavelength implies that the leptons collide with individual charged or weakly interacting constituents [7].

demonstration of the  $SU(2) \times U(1)$  unification of weak and electromagnetic interactions, were discovered [8] and corroborated [9] in neutrino-nucleon experiments; interference between neutral weak and electromagnetic propagators was demonstrated first in an electron-nucleon inelastic scattering experiment [10]. The most precise measurement of the weak mixing angle  $\theta_W$ , parametrizing the weak neutral current coupling, used to be measured from neutrino-nucleon data. Today, the most precise DIS data are being widely used to determine the momentum distributions of partons in hadrons allowing to predict cross sections in high energy hadron collisions.

The fixed-target experiments, though precise, are limited in their kinematic range. The “Hadron Elektron Ring Anlage” (HERA), the first electron proton collider ever built (Sec.2.3), running at a center-of-mass energy of up to  $\sqrt{s} \simeq 320$  GeV, equivalent to a fixed-target experiment with a lepton beam of 50 TeV, has significantly extended the kinematic domain explored so far. The proton structure are being probed at 10 times smaller distances (down to  $\sim 10^{-16}$  cm, which is one per mill of the proton radius) than previously accessible. Partons can be studied down to very small fractional proton momenta, Bjorken  $x \sim 10^{-6}$ . Two general purpose experiments, H1 and ZEUS, are dedicated to the study of this physics.

Already the first  $0.02 \text{ pb}^{-1}$  of luminosity delivered by HERA in 1992 has brought striking results which have opened new interest in QCD. Since then the luminosity has been increased by three orders of magnitude and the latest results achieved are comparable in precision with fixed-target experiments but in a different kinematic regime. At high momentum transfers, based on an early data sample of 1994-1996, an excess of events with respect to the expectation of the standard DIS has been reported by both H1 [11] and ZEUS [12]. This has again initiated a considerable amount of theoretical interest in possible explanations within both the Standard Model(SM) and models beyond the SM [13]. Results obtained using full data taken from 1994 to 2000 will be reviewed in this report. The emphasis will however be put on the experimental understanding of the detector performance by showing in some detail how some of the measurements have been carried out.

The report is organized as follows. In Chapter 2, the experimental aspects concerning the HERA machine, the H1 detector and the kinematic reconstruction are described. In Chapter 3, the theoretical framework is briefly reviewed. In Chapter 4, the structure function results at low momentum transfers and the interpretation within QCD are given. In Chapter 5, events at high momentum transfers are studied. Also discussed are their impact both within the SM for valence quark distributions and electroweak tests and beyond the SM for new physics search. A summary and an outlook are presented in Chapter 6.

# Chapter 2

## Experimental setups and techniques

Deep inelastic scattering (DIS) experiments can roughly be regrouped into three generations. The first generation of fixed-target experiments between 1968 and the mid-1970s has played an essential role in establishing the point-like sub-structure of the nucleons and in discovering the underlying weak neutral current interactions. The second generation of fixed-target experiments of higher energies and precision has helped in establishing and testing the quantum chromodynamics (QCD) and in providing data for extracting a first set of parton distribution functions. A list of selected DIS experiments is briefly presented in Sec.2.2 after having introduced the kinematics in Sec.2.1. The third generation experiments at HERA  $ep$  collider are described in more detail in the later sections.

### 2.1 Kinematics of deep inelastic scattering

The kinematics of the inclusive DIS processes for neutral current (NC) interaction  $lp \rightarrow lX$  and charged current (CC) interaction  $ep \rightarrow \nu X$  or  $\nu p \rightarrow lX$  (Fig.2.1) at the given center-of-mass energy squared,  $s = (k + P)^2$ , is determined by two independent Lorentz invariant variables, which could be any of following variables:

$$Q^2 = -q^2 = (k - k')^2, \quad Q^2 \in [0, s], \quad (2.1)$$

$$x = \frac{Q^2}{2P \cdot q}, \quad x \in [0, 1], \quad (2.2)$$

$$y = \frac{q \cdot P}{k \cdot P}, \quad y \in [0, 1], \quad (2.3)$$

$$W^2 = (q + P)^2, \quad W^2 \in [M_p^2, s]. \quad (2.4)$$

The square of the four momentum transfer (the invariant mass of the exchanged vector boson),  $q^2 < 0$ , is space-like and determines the hardness of the interaction,

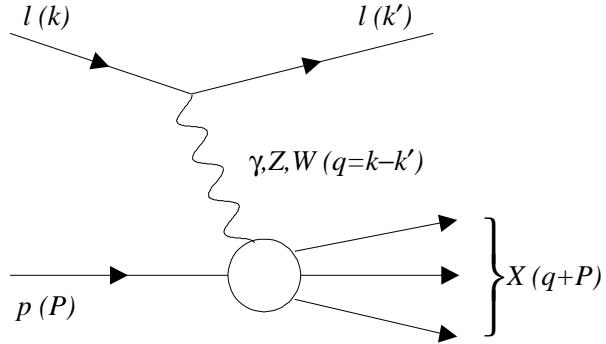


Figure 2.1: Schematic diagrams of lepton ( $l$ ) and proton ( $p$ ) scattering via photon and  $Z$  exchange for NC and  $W$  exchange for CC. The four momentum vectors of the particles or particle systems are given in parentheses.

or in other words, the resolving power of the interaction. The Bjorken variable  $x$  is interpreted as the fraction of the proton momentum carried by the struck parton in the quark parton model (QPM). The variable  $y$  measures the inelasticity of the interaction and its distribution reflects the spin structure of the interaction in the rest frame of the target.

The variable  $\nu$

$$\nu = \frac{q \cdot P}{M} \quad (2.5)$$

is often used in fixed-target experiments where  $\nu = E - E'$  and  $M$  is the target mass.

## 2.2 The fixed-target experiments

Fixed-target DIS experiments may be divided into two classes depending on the nature of the probe used, which in turn determines the force involved. In electroproduction, electrons or muons are scattered off the target nucleon and the force involved is electromagnetic. The leading process of the scattering is that of single-photon ( $\gamma$ ) exchange. The second class of processes is called neutrino production and, in this, neutrinos are scattered off the target nucleons by the weak force. The leading process is that of single- $W$ -boson exchange for charged current interactions and of single- $Z^0$ -boson exchange for neutral current interactions.

The earlier electroproduction experiments used electrons as probe. However due to their large synchrotron radiation, the largest electron energy used for scattering experiments was limited to about 12 GeV (Cornell) and 26 GeV (SLAC). The kinematic range was extended by muon-nucleon scattering to higher energies ( $20 < E < 500$  GeV).

The neutrino production experiments complement the charged lepton scattering experiments and comparisons between neutrino and charged lepton deep inelastic experiments provide tests of universality of the parton density functions. In addition, the neutrino production experiments are unique as they are able to distinguish quark flavors within target nucleons (Sec.3.1.2). On the other hand, these experiments were in practice difficult to realize as the electrically neutral, weakly interacting neutrinos cannot be directed by electric and magnetic fields, as can electrons; and building a usable neutrino beam is a complicated process. First, a primary beam of protons is accelerated to high energy and is made to collide with a stationary target such as a piece of iron. From these collisions, a host of secondary particles, mainly mesons, will emerge in the general direction of the incident proton beam, although with somewhat smaller energies. These secondary mesons can then decay into neutrinos or antineutrinos and various other particles by decays such as  $\pi^\pm \rightarrow \mu^\pm + \nu_\mu(\bar{\nu}_\mu)$ . Because the muon-decay mode of the mesons is generally the most common, it is mainly muon-type neutrinos which make up the beam. Finally, the neutrinos are isolated by guiding the secondary beam through a barrier of steel and rock equivalent of, perhaps, 0.5 km of earth. Only the weakly interacting neutrinos can pass through this amount of matter and so the beam emerging from the far side of the barrier is a pure neutrino beam with a typical intensity of about  $10^9$  particles per second. Two types of high energy beams are commonly used: narrow band beams with a momentum and charge selection of the secondary beam, and wide band beams without such selection. The narrow band beams provide a measurement of the incident neutrino energy and flux. Furthermore, the beams are either almost purely neutrino or almost purely antineutrino, with little cross contamination. Wide band beams provide an order of magnitude more neutrinos; however, there is no direct check on the event neutrino energy and no direct measure of the flux.

Table 2.1: A list of selected fixed-target DIS experiments. Only the main targets used are indicated with  $p$ ,  $d$ , and Fe standing respectively for proton, deuterium, and iron targets (the use of heavy nuclear targets have the advantage of high rate).

Experiment	Year	Reaction	Beam Energy (GeV)	Reference
SLAC-MIT	1968	$ep, ed$	4.5-20	[2, 3, 14, 15]
DESY	1969	$ep$	6	[4, 16]
Gargamelle*	1971-1976	$\nu_\mu(\bar{\nu}_\mu)p(d)$	< 10	[8]
SLAC	1974-1975	$\mu$ Fe	56.3, 150	[5]
BEBC*	1975-1983	$\nu_\mu(\bar{\nu}_\mu)p(d)$	< 200	[18]
Fermilab	1977-1978	$\mu p$	47, 96, 219	[6]
CDHS	1979-1990	$\nu_\mu(\bar{\nu}_\mu)$ Fe	< 200	[19]
CCFR	1979-1988	$\nu_\mu(\bar{\nu}_\mu)$ Fe	$\leq 600$	[20]
BCDMS	1981-1985	$\mu p, \mu d$	100, 120, 200, 280	[17]
NMC	1986-1989	$\mu p, \mu d$	90, 120, 200, 280	[22]
E665	1987-1992	$\mu p, \mu d$	470	[23]

\* The Gargamelle and BEBC (Big European Bubble Chamber) experiments used bubble chambers while other cited experiments used electronic detectors. The bubble chambers have opted for wide-band beams that maximize neutrino flux.

A few selected fixed-target DIS experiments are listed in Table 2.1. The early fixed-target experiments between 1968 and the mid-1970s have discovered a wealth of information on the structure of the proton, to name a few:

- **Point-like constituents:** The approximate independence of the measured structure functions of  $Q^2$  [2, 3, 4, 15] indicated scattering off point-like constituents analogous to the classic Rutherford experiment on atomic structure.
- **Quark spin:** The near vanishing of  $F_L$  in electron-nucleon scattering [14, 16] supported the assignment of half-integer spin for the quarks.
- **Fractional charge:** The comparison of structure functions in electron and neutrino scattering reactions supported the assignment of fractional charges to the quarks.
- **Scaling violations and QCD:** The muon scattering experiments at high energies provided first evidences for scaling violations [5, 6]. The scaling violations of the DIS data have helped in establishing the theory of QCD (Sec.3.2).

- **Gluon:** The momentum sum rules in both electron- and neutrino-proton scattering [24] suggested that quarks carry only about half of the total proton momentum. The other half was thought to be carried by neutral gluons, the quanta of the interquark field force.

The neutrino scattering experiments have played other particular roles:

- **Discovery of neutral currents:** The first observations of neutral currents were reported by the Gargamelle Collaboration [8]. This was the first experimental success of the electroweak theory of the Standard Model.
- **Precise measurement of  $\sin \theta_W$ :** Before the advent of LEP and SLC, the electroweak mixing parameter  $\sin \theta_W$  was best measured by the neutrino scattering experiments with a first result ( $\sin \theta_W = 0.28 \pm 0.05$ ) [25] already in 1976 leading to a  $W$  mass value of 70 GeV [26] well before the direct observation of the  $W$  boson in early 1980s.
- **First experimental hint of charm:** Neutrino productions of opposite-sign dimuon ( $\mu^- \mu^+$ ) in subprocesses  $\nu_\mu + (d, s) \rightarrow \mu^- + c + X$  and  $\bar{\nu}_\mu + (\bar{d}, \bar{s}) \rightarrow \mu^+ + \bar{c} + X$  (the second muon arises from the semileptonic decay of the charmed hadrons emerged from the charged quark  $c$ ) provided a first experimental hint of charm [27].
- **Strange quark sea and evidence for an  $SU(3)$  asymmetric flavor sea:** The subprocess  $\bar{\nu}_\mu + \bar{s} \rightarrow \mu^+ + \bar{c} + X$  offered a unique probe to measure the strange component of the nuclear sea. The subprocess  $\nu_\mu + (d, s) \rightarrow \mu^- + c + X$  provided a measure of the momentum fraction carried by the strange sea quarks relative to that carried by the non-strange sea  $s/(\bar{u} + \bar{d})$  revealing an asymmetric strange sea.
- **Unique direct measurement of  $|V_{cd}|$ :** The Cabibbo suppressed subprocess  $\nu_\mu + d \rightarrow \mu^- + c + X$  has been the only direct measurement of the Kobayashi-Maskawa matrix element  $|V_{cd}|$  [19].

During the last decade, several precise data have been published and a few old data have been reanalyzed. A number of previously observed discrepancies between different experiments have been resolved. For a recent review, see Ref.[28].

## 2.3 The HERA accelerator

The HERA project was authorized in April 1984 and the construction was completed late 1990 in accordance with the original time schedule. The layout of the HERA accelerator and its preaccelerator facilities is shown schematically in Fig.2.2. The electrons and protons are injected into HERA from PETRA (a previous  $e^+e^-$  collider) with 14 GeV and 40 GeV respectively. HERA is a double ring collider. The electron ring is made of superconducting cavities and normal

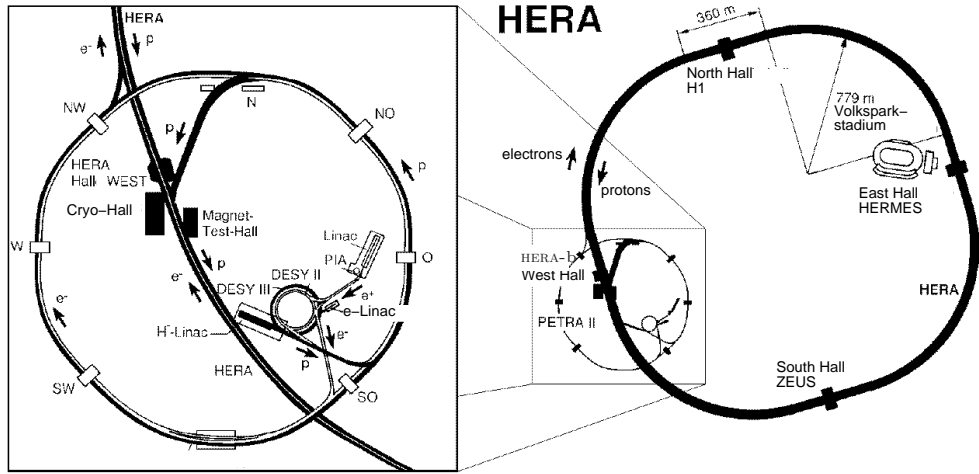


Figure 2.2: *The layout of the HERA accelerator and its preaccelerator facilities.*

conducting magnets for accelerating the electrons of 14 GeV up to the nominal electron energy of 30 GeV. The electron ring provides either electron or positron beam<sup>1</sup>. The year-dependent lepton-beam charges and energies are shown in Table 2.2. The actual maximum electron beam energy of 27.5 GeV is limited by the maximum available radio frequency (RF) voltage. The proton ring consists of conventional RF cavities and superconducting magnets of 4.68 Tesla magnetic field for accelerating the protons from 40 GeV to 820 GeV, maintaining them at this energy and keeping them on orbit. The quality of the magnets is such that it is possible to rise the strength of the magnetic field up to 5.8 Tesla, which would correspond to 1 TeV proton beam.

HERA has four straight sections (interaction points) spaced evenly around its 6.3 km circumference. The electron and proton beams collide head-on in two of these points occupied by two general purpose detectors H1 [29] (Sec.2.4) and ZEUS [30]. Two fixed-target experiments HERMES [31] and HERA-B [32] are located at the other two interaction regions. At HERMES spin rotator provide the longitudinally polarized electron beam in collision with a polarized gas target

<sup>1</sup>In the following, the generic name electron is used for electrons as well as for positrons unless stated otherwise.

Table 2.2: The year-dependent lepton-beam charges and energies and the corresponding center-of-mass energy  $\sqrt{s}$  of the HERA collider.

Year	$e^\pm$ beam	$E_e$ (GeV)	$E_p$ (GeV)	$\sqrt{s}$ (GeV)
1992-93	$e^-$	26.7	820	296
1994	$e^-$	27.5	820	300
	$e^+$			
1995-97	$e^+$	27.5	820	300
1998	$e^-$	27.5	920	320
1999	$e^-$	27.5	920	320
	$e^+$			
2000	$e^+$	27.5	920	320

Table 2.3: The main HERA parameters achieved so far compared with the design values.

Parameter	Design	Achieved
$I_e$ (mA)	58	51.8
$I_p$ (mA)	160	109
# bunches	210	189
$\sigma_x^p$ at IP ( $\mu\text{m}$ )	280	179
$\sigma_y^p$ at IP ( $\mu\text{m}$ )	50	48
$\sigma_z^p$ at IP (cm)	11	11
$\mathcal{L}_{\text{inst}}$ ( $10^{31} \text{ cm}^{-2}\text{s}^{-1}$ )	1.5	1.8

for studying spin dependent structure functions, while HERA-B uses the halo of the proton beam with wire targets in an attempt to detect CP violation in the  $B$  system.

HERA has made steady progress since 1992. This can be seen from Fig.2.3 in which the time evolution of the following information is shown: (1) the peak luminosity, (2) the integrated luminosity collected by H1, (3) the mean as well as maximum lepton and proton beam currents, and (4) the number of colliding bunches. A comparison of the best achieved and design values of the main HERA parameters is shown in Table 2.3. The improvement of the luminosity as a function of time can be understood from the formula:

$$\mathcal{L} \propto \frac{I_e I_p}{\sigma_x \sigma_y}. \quad (2.6)$$

The improvement in 1993 with respect to 1992 was mainly due to the increases in the beam currents; from 0.94 to 10.8 mA for protons and from 1.33 to 7.7 mA

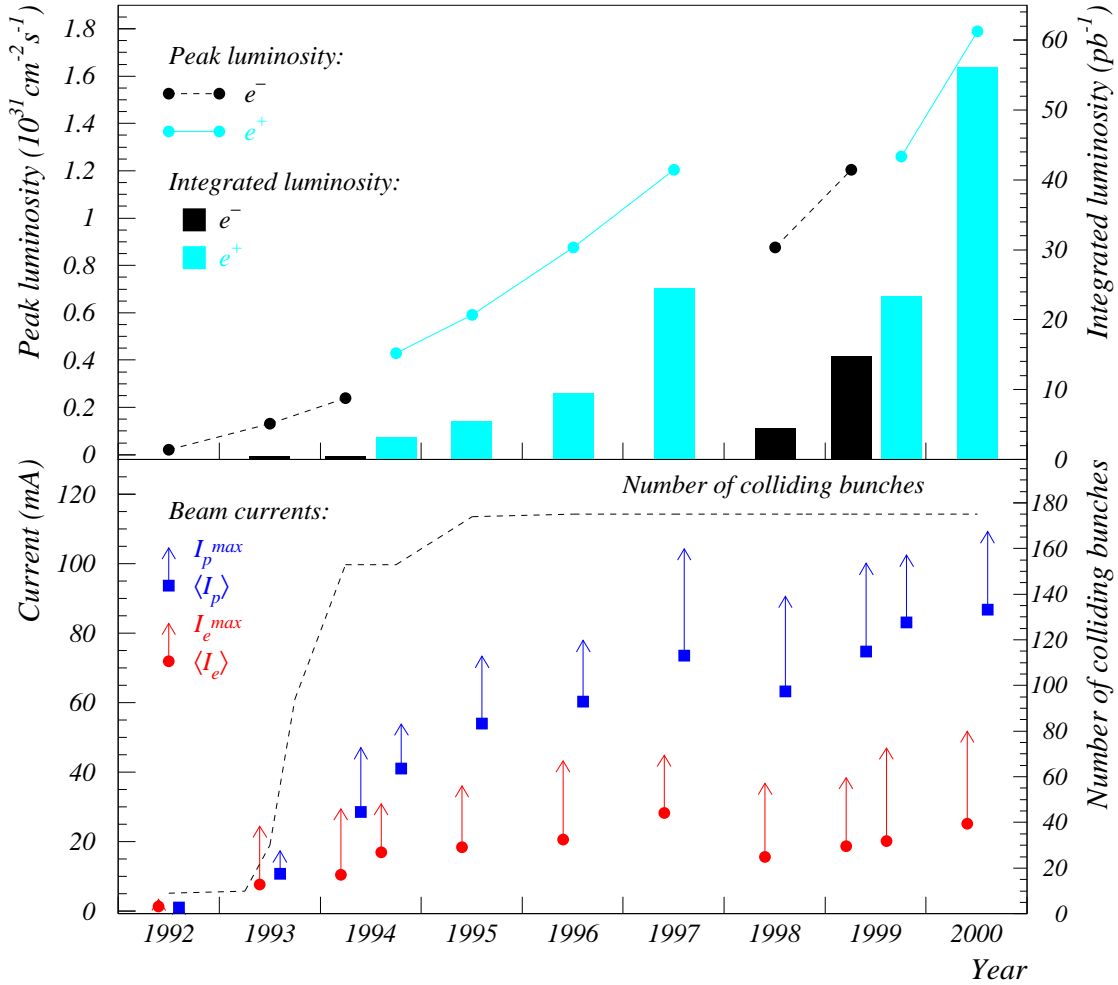


Figure 2.3: The time evolution of the following information: (1) the peak luminosity, (2) the integrated luminosity collected by  $H1$ , (3) the mean as well as maximum lepton and proton beam currents, and (4) the number of colliding bunches.

for electrons. This was achieved mainly by increasing the number of colliding bunches from 9 in 1992 up to 84 in 1993. During the summer of 1994, the electron beam was replaced by a positron beam which has considerably improved the beam lifetime<sup>2</sup> at high currents. The number of colliding bunches have increased subsequently to 153 in 1994 and then to about 175 since 1995 with a maximum number of 189. In addition to these colliding bunches, some bunches are left unpaired (so-called pilot bunches, i.e. the corresponding bunch in the other beam

<sup>2</sup>The electron lifetime was severely limited due to presumably its interaction with positively ionized impurities in the beam pipe. To cure the problem, the original ion getter pumps of the electron ring have been replaced in the 1997/1998 shutdown by passive non-evaporating getter pumps (adsorption pumps without high voltage that do not accelerate dust particles into the beam vacuum).

is empty). These pilot bunches are used for evaluating the beam related backgrounds both for the luminosity determination and for physics analyses. Two successive bunches are separated in time by 96 ns. This is to be compared with the collision frequency of  $22\ \mu\text{s}$  and 25 ns respectively at LEP<sup>3</sup> and LHC.

Other improvements include

- the full exploitation in the aperture margin of the machine in order to squeeze the beam cross sections at the collision point down to  $179\ \mu\text{m} \times 48\ \mu\text{m}$ , which are two times smaller than the design value,
- significant progress in the proton beam intensity by improving controls and beam handling in the injector chain. The maximum proton beam current achieved in  $ep$  collisions is now 109 mA (or  $\sim 8 \times 10^{10}$  protons per bunch).

The maximum electron current obtained is 51.8 mA. The beam current is limited by the available RF power. Therefore, although the beam currents still fall short of expectations, the maximum peak luminosity achieved  $1.8 \times 10^{31}\ \text{cm}^{-2}\text{s}^{-1}$  exceeds the design goal of  $1.5 \times 10^{31}\ \text{cm}^{-2}\text{s}^{-1}$  by focusing very tightly the beams at the interaction points.

An important ungrading program has been prepared and has started since September 2000. After the upgrade, an increase in the luminosity of more than a factor of 5 is expected [33].

---

<sup>3</sup>The number corresponds to four bunches per  $e^\pm$  beam during the early (late) run of 1989-1992 (1996-2000), the collision frequency was reduced by a factor of two or more by increasing the number of bunches for the years between 1992 and 1995.

## 2.4 The H1 detector

The H1 detector [29] (Fig.2.4) is nearly hermetic multi-purpose apparatus built to investigate  $ep$  interactions at HERA. The main components are the tracking

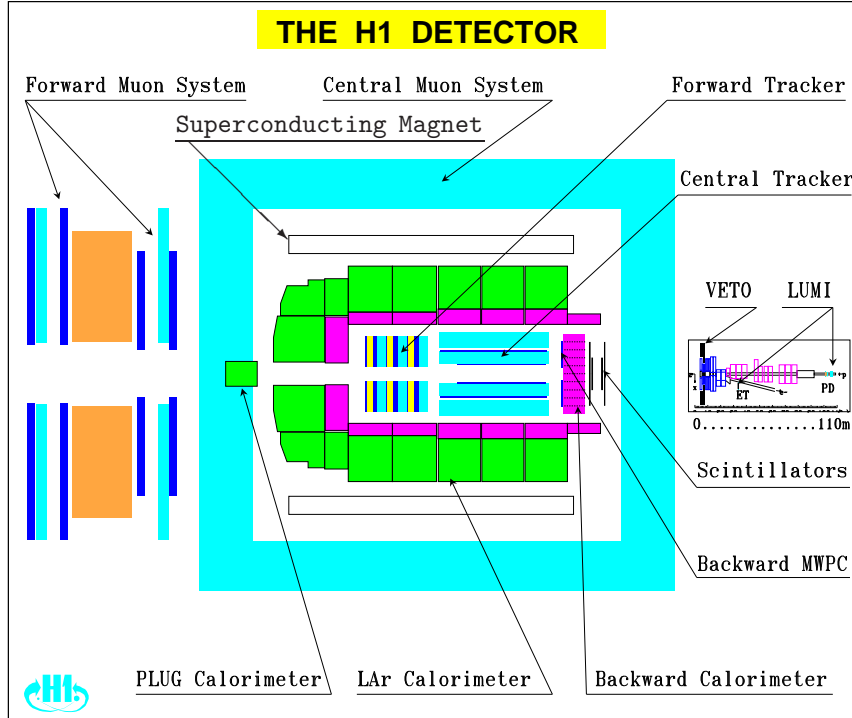


Figure 2.4: An overview of the H1 detector.

detectors (Sec.2.4.1), the calorimetry (Sec.2.4.2), the superconducting magnet, the muon detectors (Sec.2.4.3), the very forward detectors (Sec.2.4.4) and the luminosity detectors and various electron taggers (Sec.2.4.5). In many aspects, the H1 detector<sup>4</sup> does not differ strongly from the detectors at  $e^+e^-$  or  $p\bar{p}$  colliders. Specific at HERA is however the imbalance in the energy of the two colliding beams, which requires an asymmetric detector.

<sup>4</sup>The ZEUS detector [30] is rather similar to the H1 detector in many aspects. The main difference lies in the main calorimeter; as described in Sec.2.4.2, the liquid-argon calorimeter of H1 has a fine granularity and a good resolution for electromagnetic objects whereas the uranium-scintillator calorimeter of ZEUS is compensating, giving equal response to hadrons and electrons, and has a good resolution for hadrons ( $\sigma(E)/E \simeq 35\%/\sqrt{E} \oplus 2\%$ ). The ZEUS calorimeter has in addition a good time resolution, which is better than 1 ns for energy deposits greater than 4.5 GeV thus providing a fast time information for triggers and background rejections. The location of the superconducting coil providing magnetic field for trackers is different as well; the coil of H1 is placed outside of the calorimeter thus minimizing the amount of dead material in front of the calorimeter, while ZEUS had placed it between the calorimeter and the tracker.

The coordinate system convention for the experiment defines  $x$  pointing to the center of the HERA ring,  $y$  the upward direction, and the forward, positive  $z$  direction as being that of the proton beam. The polar angle  $\theta$  is defined relative to this axis such that pseudo-rapidity,  $\eta = -\ln \tan \theta/2$ , is positive in the forward region.

### 2.4.1 The tracking detectors

The tracking detectors consist of central jet chambers (CJC1, CJC2), central trackers for measuring the  $z$  coordinate (CIZ, COZ), central multiwire proportional chambers for fast triggering (CIP, COP), forward tracking detector (FTD), backward tracking detector (BPC, BDC), and central and backward silicon microvertex detectors (CST, BST).

The CJC1 and CJC2, covering a polar angular range from  $15^\circ$  to  $165^\circ$ , are two large, concentric drift chambers. The inner chamber, CJC1, has 24 layers of sense wires arranged in 30 phi cells, while CJC2 has 32 layers of sense wires in 60 phi cells. The cells are at a  $30^\circ$  angle to the radial direction. The point resolution is  $170\,\mu\text{m}$  in the  $r - \phi$  direction. The  $z$  coordinate is measured by charge division and has an accuracy of 22 mm. A superconducting solenoid, which surrounds both the tracking system and the liquid argon (LAr) calorimeter, provides a uniform magnetic field of 1.15 Tesla. The momentum of charged particles may be determined from their track curvature in the magnetic field with a transverse momentum resolution of  $\sigma_{p_T}/p_T < 0.01p_T$  GeV. The  $dE/dx$  resolution for a well measured track is better than 7%.

Two thin cylindrical drift chambers CIZ and COZ have sense wires perpendicular to the beam axis, and therefore complement the accurate  $r - \phi$  measurement provided by the CJC with precise  $z$  coordinates. The CIZ is located at 18 cm inside the CJC1, while COZ is located at 47 cm between CJC1 and CJC2. These two chambers deliver track elements with typically  $300\,\mu\text{m}$  resolution in  $z$ . To each of the  $z$  chambers a proportional chambers (CIP/COP) is attached for triggering.

The FTD, covering an angular range from  $7^\circ$  to  $25^\circ$ , are integrated assemblies of three supermodules, each including, in order of increasing  $z$ , three different orientations of planar wire drift chambers (each rotated by  $60^\circ$  to each other in azimuth), a multiwire proportional chamber (FPC), a transition radiation detector and a radial wire drift chamber.

The backward proportional chamber BPC, located just in front on the backward calorimeter, is made of four planes of wires with vertical, horizontal and  $\pm 45^\circ$  orientations. The wires are strung every 2.5 mm, and signals from two wires are fed to one preamplifier. Three out of four planes are required in coincidence in order to reconstruct a space point with a spatial resolution of about

1.5 mm in the transverse plane. The BPC provided an angular measurement of the electron in the range from  $155^\circ$  to  $174^\circ$ , together with the vertex given by the main tracking detectors with a precision better than 1 mrad. This detector has been replaced in the 1994/95 shutdown by an eight layer drift chamber BDC with an extended acceptance between  $155.1^\circ$  and  $177.5^\circ$ .

### 2.4.2 Calorimetry

The calorimetry system consists of the LAr calorimeter, the backward electromagnetic calorimeter (BEMC/SPACAL), the forward calorimeter (PLUG) and the outer calorimeter, the so-called tail-catcher.

The emphasis is put on the electron recognition and energy measurement. This led to placing the LAr inside the magnetic coil in order to minimize the passive material. LAr was chosen because of its good stability, ease of calibration, possibility of fine granularity and homogeneity of response. The LAr calorimeter covers the polar angle range between  $3^\circ$  and  $155^\circ$ . The calorimeter along the beam axis is segmented into 8 “wheels”, with each wheel being further segmented into octants in  $\phi$  (Fig.2.5). The structure of the electromagnetic section (EMC) consists of a pile of G10-Pb-G10 sandwiches separated by spacers defining the LAr gaps. The hadronic section (HAC) is made of stainless steel absorber plates with independent readout cells inserted between the plates. The orientation of the plates varies with  $z$  such that particles always impact with angles greater than  $45^\circ$ . The granularity ranges from  $10 \rightarrow 100 \text{ cm}^2$  in the EMC section and to  $50 \rightarrow 2000 \text{ cm}^2$  in the HAC section. Longitudinal segmentation is 3-4 layers in the EMC over 20-30 radiation lengths ( $X_0$ ) and 4-6 layers in the HAC. The total depth of both sections varies between 4.5 and 8 interaction lengths ( $\lambda$ ). The most backward part of the LAr calorimeter is a smaller electromagnetic calorimeter (BBE) which covers the polar angle ranging from  $146^\circ$  to  $155^\circ$ . The LAr calorimeter has a total of 45 000 readout cells. The noise per cell ranges from 10 to 30 MeV. The resolution measured in the test beam is  $0.12/\sqrt{E(\text{GeV})} \oplus 0.01$  for an electromagnetic shower and  $0.5/\sqrt{E(\text{GeV})} \oplus 0.02$  for a hadronic shower (the symbol  $\oplus$  denotes addition in quadrature). The electromagnetic and hadronic energy scale uncertainty is respectively 1-3% and 2-4%. The calorimeter is non-compensating, with the response to hadrons about 30% lower than the response to electron of the same energy. An offline weighting technique is used to equalize the response and provide the optimal energy resolution [34, 35].

In the backward region, the LAr was complemented in the angular range from  $151^\circ$  to  $176^\circ$  by the BEMC, a conventional lead-scintillator sandwich calorimeter. The BEMC was replaced in the 1994/95 shutdown by a lead/scintillating fiber calorimeter (SPACAL). The calorimeter BEMC is made of 88 stacks with a size of  $16 \times 16 \text{ cm}^2$  and has a depth of  $21.7 X_0$ , or approximately  $1 \lambda$ , which on average contains 45% of the energy of a hadronic shower. The four inner stacks around the

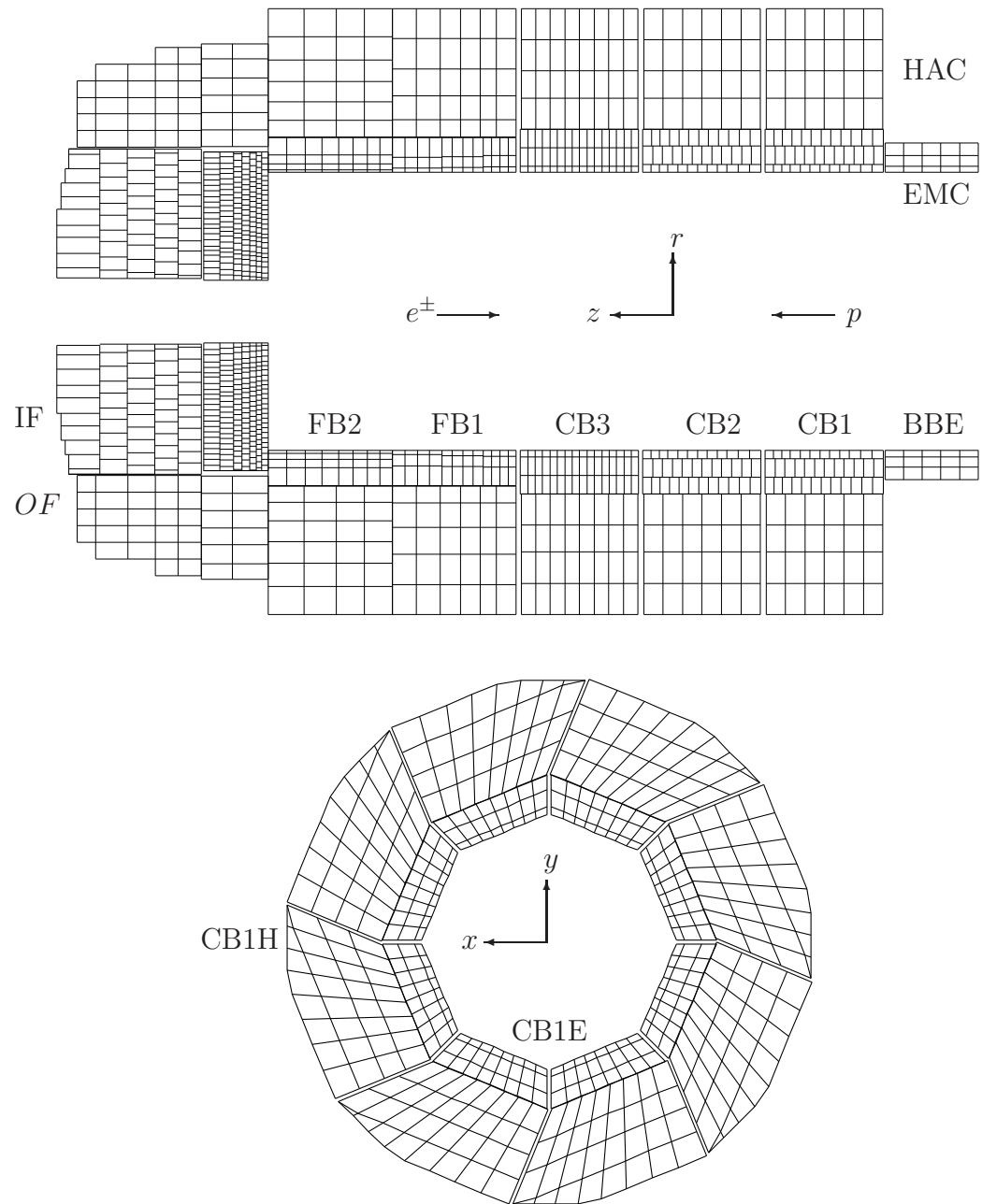


Figure 2.5: A schematic  $r - \phi$  view of the pad structure in different wheels (top) and a transverse view of the pad structure in 8 octants in CB1.

beam pipe are of triangle shape. A 1.5 cm spatial resolution of the lateral shower position is achieved using four photodiodes which detect the wavelength shifted light from each of the scintillator stacks. The electromagnetic energy resolution is  $\sigma/E = 10\%/\sqrt{E(\text{GeV})} \oplus 1.7\%$ . A scintillator hodoscope (TOF) situated behind the BEMC is used to veto proton induced background events based on their early time of arrival compared with nominal  $ep$  collision. The new calorimeter SPACAL has both electromagnetic and hadronic sections. The electromagnetic energy resolution is  $7.5\%/\sqrt{E(\text{GeV})} \oplus 2.5\%$ , and the hadronic section has  $2\lambda$  and an integrated timing function to veto proton beam induced background interactions (the old TOF system could thus be removed). The angular region covered is extended (from  $153^\circ$  to  $177.5^\circ$ ) compared to the BEMC, and the calorimeter has a very high granularity (1192 cells) yielding a spatial resolution of about 2 mm.

The LAr and BEMC/SPACAL calorimeters are surrounded by the iron return yoke, which is instrumented with 16 layers of limited streamer tubes (LST). Eleven of the 16 layers are equipped with readout electrodes (pads). From ionization energies of particles passing through the chambers the energy of tails of hadronic showers leaking out of the LAr are measured in the analog readout system. Therefore the system is also called tail-catcher (TC). The energy resolution is  $\sigma/E \approx 100\%/\sqrt{E(\text{GeV})}$ .

In the forward direction around the beam pipe, the angular range from  $0.3^\circ$  to  $3.3^\circ$  is covered by the PLUG, a sampling calorimeter consisting of nine copper absorber plates interleaved with eight sensitive layers of large area silicon detectors.

### 2.4.3 Muon detectors

Recognition of muons is very important in the study of heavy quarks, heavy vector mesons,  $W$ -production and in the search for exotic physics.

Muons in the central region are identified by looking for particles penetrating the calorimeter and coil and leaving signals in the TC. Three of the 16 instrumented LST layers are located before the first iron plate, and three after the last iron plate. There is a double layer after four iron plates, and eight single layers in the remaining gaps between the iron sheets. A minimum muon energy of 1.2 GeV is needed to reach the first LST, while 2 GeV muons just penetrate the iron.

In the very forward direction, a spectrometer composed of drift chambers surrounding a toroidal magnet with a field of 1.6 Tesla is used to measure muons. This spectrometer measures muons in the momentum range between 5 to 200 GeV. The lower limit is determined by the amount of material traversed, while beyond the upper limit the muon charge can no longer be measured unambiguously.

#### 2.4.4 Very forward detectors

H1 has spectrometers downstream of the main detectors in the proton beam direction to measure high energy protons, as well as calorimeters at zero degrees to measure high energy neutrons. These are used in the study of diffractive scattering as well as in the study of leading-particle production.

A forward proton spectrometer (FPS) has been installed since 1995 at 81 and 90 m away from the interaction point, which detects leading protons in the momentum range from 580 to 740 GeV and scattering angles below 1 mrad. The FPS has been extended with stations at 80 and 63 m since 1997. In all stations the protons are detected with scintillating fiber hodoscopes. The detector elements are mounted inside plunger vessels, so called Roman Pots, which are retracted during injection and are brought close to the beam after stable luminosity conditions are reached.

The forward neutron calorimeter (FNC) is located at 107 m downstream of the interaction point. The calorimeter consists of interleaved layers of lead and scintillating fibers. The calorimeter has a total depth of  $9.5 \lambda$  and has an acceptance  $> 90\%$  for neutrons with a production angle below 1 mrad.

#### 2.4.5 Luminosity detector and electron taggers

At HERA, the luminosity is determined from the rate of the bremsstrahlung (Bethe-Heitler) process  $ep \rightarrow ep\gamma$  (Sec.3.4.2) using a small luminosity system (the example from H1 is indicated schematically in Fig.2.4 and shown in a larger view in Fig.2.6). The process has a large and precisely known cross section. In

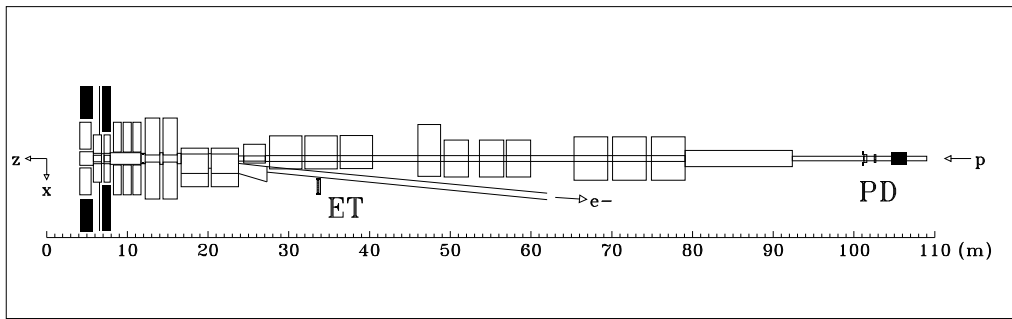


Figure 2.6: The layout of the H1 luminosity system consisting of an electron tagger (ET=etag) and a photon detector (PD). Note that the  $z$  axis coincides with the proton beam direction.

the H1 area, the final state electron, deflected by a set of low-beta quadrupoles and a bending magnet located in the region  $-23.8 \text{ m} < z < -5.8 \text{ m}$ , passes an exit window at  $z = -27.3 \text{ m}$  and hits the electron tagger (etag) at  $z = -33.4 \text{ m}$ . The

etag is located beside the electron beam pipe and is made of 49 crystals covering a total area of  $154 \times 154 \text{ mm}^2$ . The photon leaves the proton beam pipe through an exit window at  $z = -92.3 \text{ m}$  where the proton beam pipe bends upwards. The photon detector (PD), situated at  $z = -102.9 \text{ m}$  on the  $z$  axis, is built out of 25 crystals with a total surface of  $100 \times 100 \text{ mm}^2$  and a depth of 22 radiation lengths ( $X_0$ ). A  $2X_0$  Pb filter followed by a  $1X_0$  water Čerenkov veto counter (VC) in front of the PD protects the detector from the high synchrotron radiation flux. The VC eliminates events with photons interacting in the filter. The whole system provides a fast relative luminosity measurement with a statistical precision of about 2% at nominal beam conditions.

The luminosity system serves in addition several other purposes. It provides

- electron beam monitoring for the HERA machine,
- absolute luminosity measurement in the interaction region with an accuracy of better than 5%,
- tagging of photoproduction events,
- energy measurement for electrons scattered under small angles and
- energy measurement for photons from initial state radiation (Sec.3.4).

The etag at 33 m measures electrons in the energy range  $0.25E_e < E'_e < 0.75E_e$  with an average acceptance of 48%. The acceptance to higher energy ( $0.76E_e < E'_e < 0.96E_e$ ) is covered by a new tagger at 44 m installed since 1995. The lower energy is covered by yet another tagger at 4 m.

#### 2.4.6 Trigger and event reconstruction

The purpose of the trigger system is a fast separation of the interesting physics events from background events. The main background sources, common as those presented to other accelerator experiments, are synchrotron radiation from the electron beam, proton gas interaction in the beam pipe vacuum of about  $10^{-9} \text{ hPa}$  and stray protons, which produce particle showers by hitting the beam tube and other materials around the accelerator (beam-gas and beam-wall). Beam halo muons and muons from cosmic radiation also contribute. The rate of the background is up to  $10^4$  times higher than the rate of a variety of physics processes under study in  $ep$  collisions (Table 2.4). The rate of physics processes extends from photoproduction, where the visible  $ep$  cross section of several  $\mu\text{b}$  implies an event rate of 20-30 Hz at design luminosity (see Table 2.3), towards  $W$  production expected to occur a few times per week.

The trigger system is based on 4 levels in order to filter the interesting physics events, followed by the offline reconstruction of the kept events.

Table 2.4: A comparison of cross sections and/or rates between the main background sources and various physics processes at design luminosity.

Source/process	Cross section	Rate
Beam-gas(wall) interaction		50 kHz
Cosmic $\mu$ in barrel		700 Hz
Tagged $\gamma p$	$1.6 \mu\text{b}$	25 Hz
$c\bar{c}$ total	$1 \mu\text{b}$	15 Hz
DIS low $Q^2$	150 nb	2.2 Hz
DIS high $Q^2$ (e in LAr)	1.5 nb	$1.4 \text{ min}^{-1}$
Charged current DIS ( $p_T > 25 \text{ GeV}$ )	50 pb	$3 \text{ h}^{-1}$
$W$ production	0.4 pb	$0.5 \text{ d}^{-1}$

The trigger level 1 (L1) system makes a decision within  $2 \mu\text{s}$  on whether to accept or to reject an event using information provided by different subdetectors (“trigger elements (TE)”). The central trigger logic (CTL) combines these trigger elements into 128 “subtrigger (ST)”. Not all subdetectors can provide this information fast enough to make a decision after each bunch crossing (BC) immediately. Therefore the information is sent into pipelines where it is kept until all relevant subdetectors have provided their trigger elements. The delay of  $2 \mu\text{s}$  (24 BC) is necessary as some subdetectors are relatively slow: the CJC takes 11 BC due to the longest drift time of  $1 \mu\text{s}$  and the LAr takes 13 BC due to long integration time of the preamplifiers<sup>5</sup>. If any of the ST conditions is fulfilled by the event, the pipeline is stopped immediately and the signal is passed to the next trigger level<sup>6</sup>

The level 2 (L2) and level 3 (L3)<sup>7</sup> triggers operate during the primary dead time of the readout of about 1.5 ms. They work on the same data as the L1, and reach a decision within  $20 \mu\text{s}$  and  $800 \mu\text{s}$ , respectively. While at the L1, only minimum correlation between different subdetectors (e.g. between the MWPC and LAr) is used, the L2 and L3 make full use of the detailed, high granularity trigger data of most subsystems. The L2 system includes a complex topological correlation and a neural network approach.

The level 4 (L4) trigger is based on full event reconstruction in MIPS R3000 based processor boards. Algorithms similar to the ones used for the offline analysis are used to select valid events. The events accepted by L4 are written to tapes

<sup>5</sup>The typical drift time of an ionized electron in the LAr gap is about 200 ns/mm, a gap of 2.35 mm between two absorber plates results already in about 500 ns, i.e. about 5 BC.

<sup>6</sup>Some subtriggers are prescaled such that not every event fulfilling the subtrigger conditions is kept.

<sup>7</sup>This trigger has not yet been used in H1.

with a rate of about 15 Hz.

The accepted raw data or those simulated Monte Carlo data are then fully reconstructed and assigned into different physics event classes. The data information is written in a compressed format to Data Summary Tapes (DST) which are the basis for physics analyses.

## 2.5 Monte Carlo technique and detector simulation

Monte Carlo (MC) technique has proven to be indispensable for the extraction of physical quantities from the measurements. For the cross section measurement, MC programs can be used to determine corrections for acceptance, efficiencies, background contamination, and resolution effects of the detector system. Some of these corrections can be obtained directly from the data though often with a limited statistical precision. The MC, which provides in principle unlimited event samples, allows therefore to model the data with a better precision. The simulated MC events are also very useful in defining variables and tuning cuts for selecting signal events from various background contributions.

More information concerning Monte Carlo generators used in different analyses will be given later together with the analyses. Once an event (either a signal or a background event) is generated, the H1 detector response to the particles generated in the event is simulated in detail using the H1 simulation package, H1SIM, which makes use of the GEANT program [36]. The parameters used by this program were determined in test beam measurements and optimized during  $ep$  data taking. For the simulation of the energy response of the calorimeter a fast parametrization is used for the development of electromagnetic and hadronic showers to save computing time. These simulated events are then subject to the same reconstruction program (Sec.2.4.6) as the data and the same analysis chain.

## 2.6 Kinematics reconstruction and coverage

### 2.6.1 Reconstruction of kinematic variables

For NC events, the kinematics is over-constrained as the HERA experiments measure both the scattered electron and the hadronic final state. Here are a few commonly used methods:

**Electron method** uses the energy,  $E'_e$ , and the polar angle,  $\theta_e$ , of the scattered electron measured relative to the proton beam direction:

$$Q_e^2 = 4E_e E'_e \cos^2 \left( \frac{\theta_e}{2} \right) \quad (2.7)$$

$$y_e = 1 - \frac{E'_e}{E_e} \sin^2 \left( \frac{\theta_e}{2} \right) \quad (2.8)$$

$$x_e = \frac{Q_e^2}{s y_e}. \quad (2.9)$$

Since the incident beam energy  $E_e$  appears both in  $Q_e^2$  and in  $y_e$ , this method is thus sensitive to the initial state radiation (the effective beam energy after radiation is smaller than  $E_e$ , see Sec.3.4, and Eq.(4.14) in Sec.4.4).

**Double angle (DA) method** [37] uses the electron polar angle,  $\theta_e$ , and the inclusive hadronic polar angle,  $\theta_h$ , which is the polar angle of the scattered quark in the QPM (Sec.3.1.2) with massless quarks

$$Q_{\text{DA}}^2 = \frac{E_e}{E_p} \frac{s}{\alpha_e(\alpha_e + \alpha_h)}, \quad (2.10)$$

$$y_{\text{DA}} = \frac{\alpha_h}{\alpha_e + \alpha_h}, \quad (2.11)$$

$$x_{\text{DA}} = \frac{Q_{\text{DA}}^2}{s y_{\text{DA}}}, \quad (2.12)$$

with

$$\alpha_e \equiv \tan \left( \frac{\theta_e}{2} \right) = \frac{\Sigma_e}{p_{T,e}}, \quad \alpha_h \equiv \tan \left( \frac{\theta_h}{2} \right) = \frac{\Sigma_h}{p_{T,h}} \quad (2.13)$$

$$\Sigma_e \equiv E'_e - p_{z,e}, \quad p_{T,e} \equiv E'_e \sin \theta_e \quad (2.14)$$

$$\Sigma_h \equiv \sum_i E_i - p_{z,i}, \quad p_{T,h} \equiv \sqrt{\left( \sum_i p_{x,i} \right)^2 + \left( \sum_i p_{y,i} \right)^2} \quad (2.15)$$

where the summations are over all particles of the hadronic final state. The DA method is also sensitive to photon emission of the primary electron.

On the other hand, it is, to a good approximation, insensitive to the energy scale uncertainties. It has thus been widely used in various analyses to check and improve the energy scales of the scattered electron and of the hadronic system.

**Sigma ( $\Sigma$ ) method** [38] is constructed such that no electron beam energy  $E_e$  is used directly in  $Q^2$  and  $y$ :

$$Q_\Sigma^2 = \frac{E_e'^2 \sin^2 \theta_e}{1 - y_\Sigma}, \quad (2.16)$$

$$y_\Sigma = \frac{\Sigma_h}{\Sigma_e + \Sigma_h}, \quad (2.17)$$

$$x_\Sigma = \frac{Q_\Sigma^2}{s y_\Sigma}. \quad (2.18)$$

This method is thus less sensitive to the radiative effects.

The fact that different methods can be used to reconstruct the event kinematics has two consequences:

- The kinematic domain is fully explored; for example the electron method is good at high  $y$  while the  $\Sigma$  method can be used at sufficiently low  $y$ .
- Important cross-checks of systematic effects are possible between different methods.

For a CC event, however, the kinematics can only be reconstructed from the hadronic final state:

$$Q_h^2 = \frac{E_{T,h}^2}{1 - y_h}, \quad (2.19)$$

$$y_h = \frac{\Sigma_h}{2E_e}, \quad (2.20)$$

$$x_h = \frac{Q_h^2}{s y_h}. \quad (2.21)$$

The understanding of the hadronic energy scale and its scale uncertainty is thus crucial for all CC measurements.

## 2.6.2 Coverage of the kinematic phase space

The HERA measurements in DIS cover a vast kinematic range as shown in Fig.2.7. The HERA measurements extend those of fixed-target experiments by more than 2 orders of magnitudes in both  $x$  and  $Q^2$ . At the highest values of  $Q^2$ ,

the measurements are still statistically limited (Chapter 5). The measurements for  $Q^2 \lesssim 4 \text{ GeV}^2$  have been made possible by using different techniques and by upgrading experimental apparatus:

- Using data in which the interaction point is shifted from its nominal position to the forward direction by  $\sim 70 \text{ cm}$  (so-called shifted vertex events). For the same backward calorimeter, the angular acceptance is increased when the interaction vertex is moved away from the nominal interaction point.
- Using data with hard initial state radiation. A large fraction ( $\sim 30\%$ ) of the photons from events with hard initial state radiation are measured in the photon calorimeters of the luminosity system (Sec.2.4.5). The resultant  $ep$  collisions therefore occur at lower center-of-mass energies, and lower  $Q^2$  and higher  $x$  values can be attained. As an example, the H1 analysis is shown in some detail in Sec.4.4 to illustrate how the measurement is realized in an extended kinematic region.
- Upgraded apparatus. The angular acceptance of the scattered electron has been significantly extended in the shutdown period 1994-95 by replacing the old backward calorimeter and proportional chamber, BEMC and BPC, with the new calorimeter and drift chamber, SPACAL and BDC (Sec.2.4). The ZEUS experiment has added a small angle electron calorimeter, the beam pipe calorimeter, in the same shutdown period.

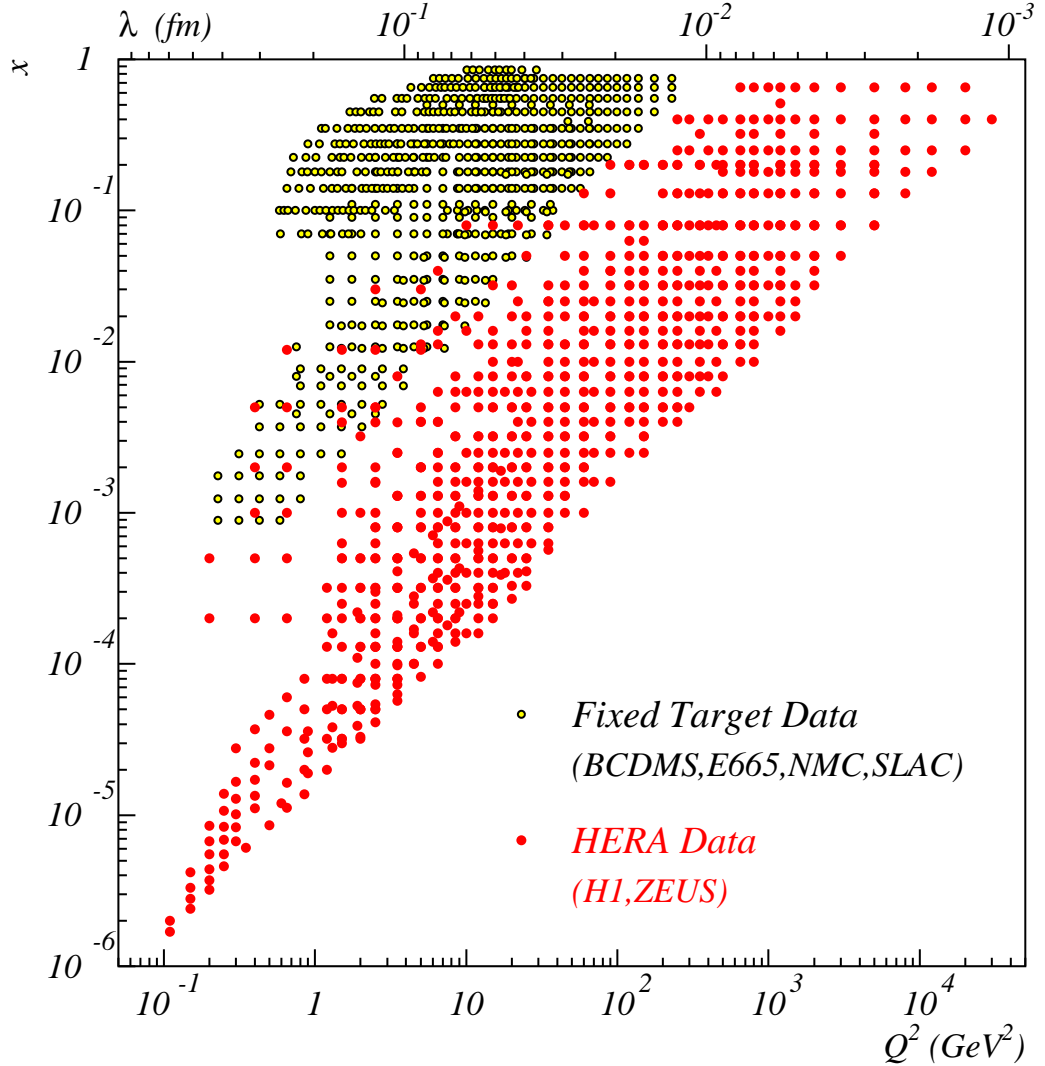


Figure 2.7: Coverage in the kinematic plane  $x - Q^2$  of the HERA experiments, H1 and ZEUS, compared with that of the fixed-target experiments from BCDMS [21], NMC [22], E665 [23], and SLAC [39]. The corresponding scale ( $\lambda$ ) probed by a virtual boson is also indicated. The points indicate the location where cross sections or structure functions have been measured.

# Chapter 3

## Theoretical framework

### 3.1 Deep inelastic scattering and the quark parton model

#### 3.1.1 Cross sections and structure functions

The neutral current cross section for charged leptons scattering off nucleons  $l^\pm N \rightarrow l^\pm X$  studied in all fixed-target experiments and in the low  $Q^2$  part of the HERA kinematic domain arises to a good approximation from the photon exchange only. Taking the proton as an example, the cross section is directly proportional to the amplitude squared [40]

$$\frac{d^2\sigma^{l^\pm p}}{dxdy} \propto |\mathcal{A}|^2 = \frac{1}{q^4} L_{\mu\nu} W^{\mu\nu} \quad (3.1)$$

with

$$\mathcal{A} = \frac{1}{q^2} j_\mu J^\mu \quad (3.2)$$

where the term  $1/q^2$  corresponds to the propagator of the exchanged photon,  $j_\mu$  and  $J^\mu$  are respectively the lepton and proton currents. In Eq.(3.1),  $L_{\mu\nu}$  and  $W^{\mu\nu}$  are respectively the leptonic and hadronic tensors. The leptonic part is completely determined by QED, whereas the hadronic one contains all the information about the interaction of the electromagnetic current  $j_\mu$  with the proton target. By writing down the most-general possible combinations of all the momenta appearing in the reaction in  $L_{\mu\nu}$  and  $W^{\mu\nu}$  and then simplifying the result using general theoretical assumptions such as parity and time-reversal invariance, the cross section can finally be expressed as

$$\frac{d^2\sigma^{l^\pm p}}{dxdy} = \frac{4\pi\alpha^2(s - M^2)}{Q^4} \left[ \left( 1 - y - \frac{M^2 xy}{s - M^2} \right) F_2 + \frac{y^2}{2} 2x F_1 \right], \quad (3.3)$$

where  $\alpha$  is the fine structure constant,  $M$  is the proton target mass, and  $F_2(x, Q^2)$  and  $2xF_1(x, Q^2)$  are so-called structure functions, to be determined by the deep inelastic experiments (Chapter 4). There are two structure functions because there are two essential degrees of freedom. The exchanged virtual photon can be transversely or longitudinally polarized. If one defines  $\sigma_{\text{tot}}^{\gamma^* p}$  as the total  $\gamma^* p$  cross section, then it can be decomposed into the longitudinal part  $\sigma_L$  and the transverse one  $\sigma_T$  as

$$\sigma_{\text{tot}}^{\gamma^* p} = \sigma_L + \sigma_T, \quad (3.4)$$

with

$$\sigma_T = \frac{2\pi^2\alpha}{xMK} 2xF_1, \quad (3.5)$$

$$\sigma_L = \frac{2\pi^2\alpha}{xMK} F_L. \quad (3.6)$$

For virtual photon, the flux factor  $K$  cannot be unambiguously defined. The longitudinal structure function  $F_L$  is a combination of  $F_2$  and  $2xF_1$ :

$$F_L = \left(1 + \frac{4M^2x^2}{Q^2}\right) F_2 - 2xF_1. \quad (3.7)$$

The measurement is carried out either directly on  $F_L$  or on  $R$ , the cross-section ratio of the longitudinally polarized over transversely polarized virtual photon:

$$R = \frac{\sigma_L}{\sigma_T} = \left(1 + \frac{4M^2x^2}{Q^2}\right) \frac{F_2}{2xF_1} - 1, \quad (3.8)$$

so that the arbitrary flux factor  $K$  does not enter.

At HERA, high  $Q^2$  regime ( $Q^2 \gtrsim M_Z^2$ ) is reached, where the contribution from pure  $Z^0$  exchange and its interference with  $\gamma$  exchange becomes increasingly important. As the weak neutral current does not conserve parity, an additional term ( $x\tilde{F}_3(x, Q^2)$ ) has to be taken into account in Eq.(3.3):

$$\begin{aligned} \frac{d^2\sigma^{l^\pm p}}{dxdQ^2} &= \frac{4\pi\alpha^2}{xQ^4} \left[ (1-y)\tilde{F}_2 + \frac{y^2}{2} 2x\tilde{F}_1 \mp \left(y - \frac{y^2}{2}\right) x\tilde{F}_3 \right] \\ &= \frac{2\pi\alpha^2}{xQ^4} \left[ Y_+\tilde{F}_2 - y^2\tilde{F}_L \mp Y_-x\tilde{F}_3 \right], \end{aligned} \quad (3.9)$$

where  $Y_\pm = 1 \pm (1-y)^2$  are helicity functions and the term proportional to  $M^2$  has been neglected. Note that the structure functions  $F_2(x, Q^2)$ ,  $2xF_1(x, Q^2)$ , and  $F_L(x, Q^2)$  have been replaced respectively by  $\tilde{F}_2(x, Q^2)$ ,  $2x\tilde{F}_1(x, Q^2)$ , and  $\tilde{F}_L(x, Q^2)$  to account for the contributions from the  $\gamma Z^0$  interference and  $Z^0$  exchange terms (Eqs.(3.13),(3.22)).

The cross section for charged current processes,

$$\begin{aligned} \nu_\mu N &\rightarrow \mu^- X \\ \bar{\nu}_\mu N &\rightarrow \mu^+ X \end{aligned} \quad (\text{Fixed-target experiments}) \quad (3.10)$$

$$\begin{aligned} e^- p &\rightarrow \nu_e X \\ e^+ p &\rightarrow \bar{\nu}_e X \end{aligned} \quad (\text{HERA experiments}) \quad (3.11)$$

can be derived in a similar way and reads

$$\begin{aligned} \frac{d^2\sigma^{\text{CC}}}{dxdQ^2} = & \frac{G_F^2 M_W^4 (s - M^2)}{2\pi xs} \left( \frac{1}{Q^2 + M_W^2} \right)^2 \times \\ & \left[ \left( 1 - y - \frac{M^2 xy}{s - M^2} \right) F_2^{\text{CC}} + \frac{y^2}{2} 2x F_1^{\text{CC}} \pm \left( y - \frac{y^2}{2} \right) x F_3^{\text{CC}} \right], \end{aligned} \quad (3.12)$$

where  $M_W$  is the mass of the exchanged  $W$  boson. Again since the weak force does not respect parity invariance, a similar but different weak structure function  $x F_3^{\text{CC}}(x, Q^2)$  has to be introduced (compare Eqs.(3.14) and (3.27),(3.29)).

### 3.1.2 Structure functions in the quark parton model

Two ideas, both put forward in 1969, have played an important role in the development of the experiments and in our understanding of them. The two ideas are those of the parton model by Feynman [41] and of scaling by Bjorken [42].

The parton model is simply a formal statement of the notion that the nucleon is made up of smaller constituents, the partons. No initial assumptions about the partons are necessary as it is the purpose of the experiments to determine their nature.

The scaling prediction states that when the momentum carried by the probe becomes very large, the dependence of the cross section on parameters such as the energy  $\nu = E - E'$  and momentum squared  $q^2$ , transferred by the photon, becomes simple. In the parton model, the onset of this simple scattering behavior has a straightforward interpretation. The complicated scattering of the probe off a nucleon of finite spatial extent has been replaced by the scattering of the probe off a point-like parton. The photon ceases to scatter off the nucleon as a coherent object and, instead, scatter off the individual point-like partons incoherently.

When it became clear that the hypothesized point-like constituents, partons had properties characteristic of quarks, the parton model came to be called the Quark Parton Model (QPM).

While the cross sections shown in Eqs.(3.3),(3.9), (3.12) make no assumptions about the underlying structure of the hadron involved in the interaction, in the QPM, the structure functions  $\tilde{F}_2^{l\pm p}, x\tilde{F}_3^{l\pm p}$  can be expressed in terms of parton

distribution functions:

$$\tilde{F}_2^{l\pm p}(x, Q^2) = \sum_i A_i(\lambda, Q^2) x [q_i(x) + \bar{q}_i(x)], \quad (3.13)$$

$$x\tilde{F}_3^{l\pm p}(x, Q^2) = \sum_i B_i(\lambda, Q^2) x [q_i(x) - \bar{q}_i(x)], \quad (3.14)$$

$$\tilde{F}_L = \tilde{F}_2 - 2x\tilde{F}_1 = 0, \quad (3.15)$$

where the sum runs over all quark flavors with  $xq(x)$  specifying the probability of finding a parton  $q$  carrying a momentum fraction  $x$  of the proton's momentum in a frame where the proton's momentum is large. The last relation is so called Callan-Gross relation [43] and is a direct consequence of quark spin 1/2 due to the fact that a spin-1/2 quark cannot absorb a longitudinally polarized vector boson. The couplings of the fermions to the currents depend on the lepton-beam polarization  $\lambda$ :

$$A_i(\lambda, Q^2) = \frac{1-\lambda}{2} A_i^L(Q^2) + \frac{1+\lambda}{2} A_i^R(Q^2), \quad (3.16)$$

$$B_i(\lambda, Q^2) = \frac{1-\lambda}{2} B_i^L(Q^2) + \frac{1+\lambda}{2} B_i^R(Q^2), \quad (3.17)$$

with

$$A_i^{L,R}(Q^2) = e_i^2 - 2e_i(v_l \pm a_l)v_i P_Z + (v_l \pm a_l)^2(v_i^2 + a_i^2)P_Z^2, \quad (3.18)$$

$$B_i^{L,R}(Q^2) = \mp 2e_i(v_l \pm a_l)a_i P_Z \pm 2(v_l \pm a_l)^2 v_i a_i P_Z^2, \quad (3.19)$$

for  $l^-p$  scattering, the corresponding structure functions for  $l^+p$  scattering are obtained by swapping  $L \rightarrow R$ ,  $R \rightarrow L$  in Eqs.(3.18),(3.19). The vector and axial-vector couplings of the fermions are given by

$$v_f = T_{3f} - 2e_f \sin^2 \theta_W, \quad a_f = T_{3f}, \quad (3.20)$$

where the definition holds for both charged leptons and quarks,  $T_{3f}$  is the third component of weak isospin, and  $\theta_W$  is the Weinberg angle. The  $Z^0$  propagator appears in the quantity  $P_Z$  as:

$$P_Z = \frac{Q^2}{Q^2 + M_Z^2} \frac{1}{\sin(2\theta_W)}. \quad (3.21)$$

For unpolarized lepton beams, Eqs.(3.13) and (3.14) can be expressed<sup>1</sup> as

$$\tilde{F}_2 = F_2 - v_l P_Z F_2^{\gamma Z} + (v_l^2 + a_l^2) P_Z^2 F_2^Z \approx F_2 + a_l^2 P_Z^2 F_2^Z \quad (3.22)$$

$$x\tilde{F}_3 = -a_l P_Z x F_3^{\gamma Z} + 2a_l v_l P_Z^2 x F_3^Z \approx -a_l P_Z x F_3^{\gamma Z} \quad (3.23)$$

---

<sup>1</sup>Here we have taken the convention that  $v_{e+} \equiv v_{e-} = -1/2 + 2 \sin^2 \theta_W$  and  $a_{e+} \equiv a_{e-} = -1/2$ .

with  $F_2$ ,  $F_2^{\gamma Z}$  and  $F_2^Z$

$$\left[ F_2, F_2^{\gamma Z}, F_2^Z \right] = \sum_i \left[ e_i^2, 2e_i v_i, v_i^2 + a_i^2 \right] x (q_i + \bar{q}_i) \quad (3.24)$$

standing for contributions respectively from pure photon exchange,  $\gamma Z^0$  interference and pure  $Z^0$  exchange. The terms  $xF_3^{\gamma Z}$  and  $xF_3^Z$

$$\left[ xF_3^{\gamma Z}, xF_3^Z \right] = \sum_i \left[ 2e_i a_i, 2v_i a_i \right] x (q_i - \bar{q}_i) \quad (3.25)$$

have similar meanings. The dominant correction to  $F_2$  arises from the  $Z^0$  exchange term (the  $F_2^Z$  term in Eq.(3.22)) since  $v_l$  is small with respect to  $a_l$ . For the same reason, the dominant contribution to  $x\tilde{F}_3$  is from the  $\gamma Z^0$  term (the  $xF_3^{\gamma Z}$  term in Eq.(3.23)). As shown in Fig.3.1, the generalized structure function  $\tilde{F}_2$  is always larger than the electromagnetic structure function  $F_2$  and does not depend on the charge of the incident lepton beam, whereas the structure function  $x\tilde{F}_3$  has a negative (positive) interference for a positron (electron) beam and its contribution is large than that from the  $F_2^Z$  term. As a result, the full cross section is expected to be smaller (larger) than that from pure photon exchange in the HERA kinematic range.

The structure functions for charged current processes  $\bar{\nu}_\mu p \rightarrow \mu^+ X$ ,  $e^- p \rightarrow \nu_e X$  with left handed polarization are defined as

$$F_2^{\text{CC}}(x) = 2xF_1^{\text{CC}}(x) = 2x \left[ u(x) + c(x) + \bar{d}(x) + \bar{s}(x) \right], \quad (3.26)$$

$$xF_3^{\text{CC}}(x) = 2x \left[ u(x) + c(x) - \bar{d}(x) - \bar{s}(x) \right], \quad (3.27)$$

and  $F_2^{\text{CC}} = 2xF_1^{\text{CC}} = F_3^{\text{CC}} = 0$  for  $e^- p \rightarrow \nu_e X$  with right handed polarization. The corresponding structure functions for processes  $\nu_\mu p \rightarrow \mu^- X$ ,  $e^+ p \rightarrow \bar{\nu}_e X$  with right handed polarization are given by

$$F_2^{\text{CC}}(x) = 2xF_1^{\text{CC}}(x) = 2x \left[ d(x) + s(x) + \bar{u}(x) + \bar{c}(x) \right], \quad (3.28)$$

$$xF_3^{\text{CC}}(x) = 2x \left[ d(x) + s(x) - \bar{u}(x) - \bar{c}(x) \right], \quad (3.29)$$

and  $F_2^{\text{CC}} = 2xF_1^{\text{CC}} = F_3^{\text{CC}} = 0$  for  $e^+ p \rightarrow \bar{\nu}_e X$  with left handed polarization.

Comparing Eqs.(3.26),(3.28) with Eq.(3.13), one notices an important feature of the charged current interactions: they are able to distinguish between the partons and the antipartons of the target nucleon. This is because the space-time structure of the weak interaction ensures that target partons of differing helicities are affected differently. In the relativistic limit, in which the rest mass of a particle is regarded as being negligible, the parton and antiparton helicities are opposite, so they will interact with the  $W$ -boson probe differently. Also, because the  $W$ -boson probe is electrically charged, the target parton must be able to absorb the charge. This rules out the participation of some types of parton, making the weak interaction a more selective probe of the nucleon's structure than the photon probe.

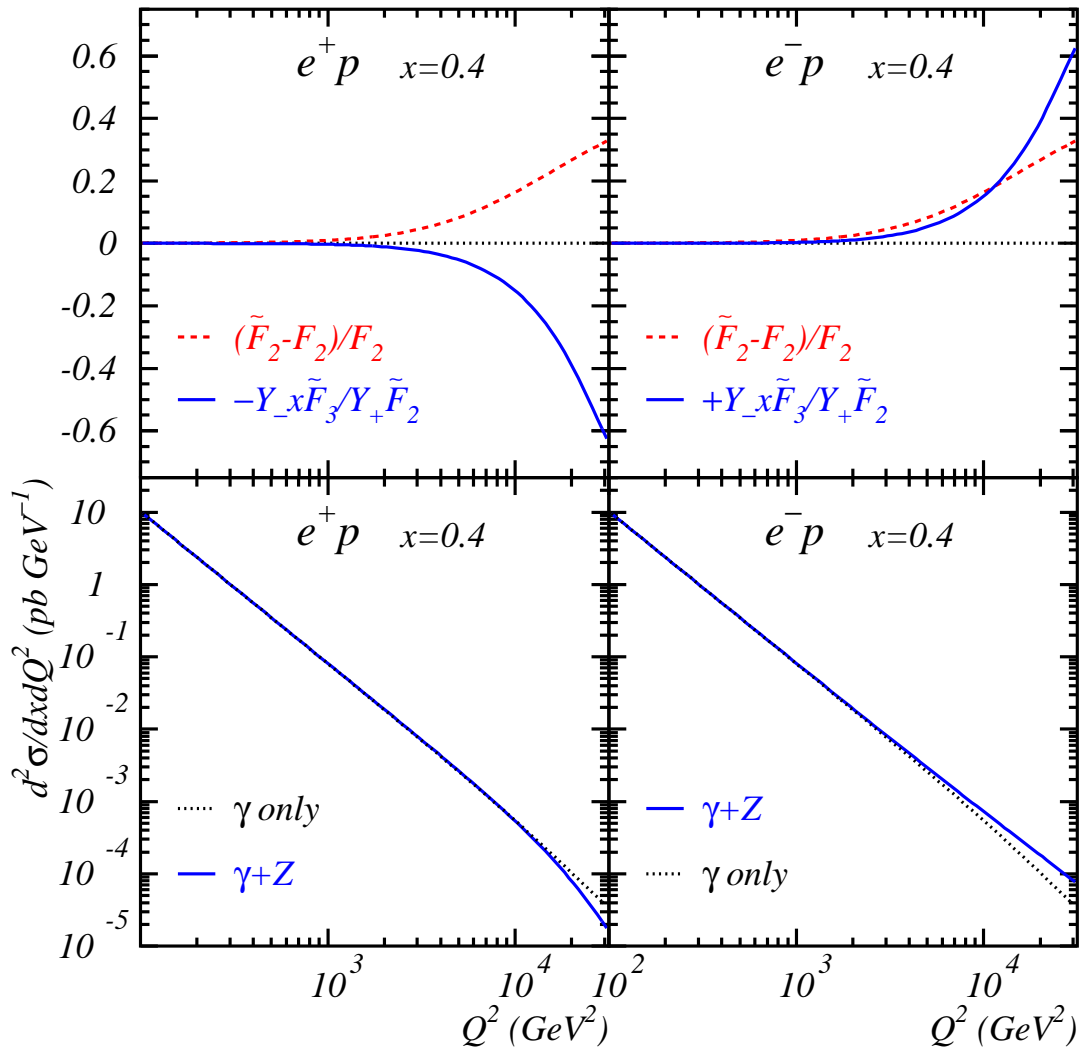


Figure 3.1: Comparisons of the generalized structure function  $\tilde{F}_2$  with the electromagnetic structure function  $F_2$  and of the structure function  $x\tilde{F}_3$  with  $\tilde{F}_2$  for  $e^+p$  and  $e^-p$  collisions, and of the full cross sections with that from pure photon exchange.

## 3.2 Quantum Chromodynamics and parton density evolution equations

The QPM has been successful in describing the early DIS data, a few serious problems need, however, to be solved. The first is the absence of free quark, which may be ascribed to some confinement mechanism which requires very strong binding forces between the quarks, to prevent them getting out. The second has to do with the seemingly violated Pauli principle for having two identical  $u$  valence quarks existing in a same proton. Finally, the successful description of lepton scattering by nucleons in terms of elastic scattering by quasi-free quarks equally requires very weak binding forces between them, apparently inconsistent with the first problem. These problems are naturally understood in the framework of the non-Abelian gauge theory of the strong interactions of colored quarks and gluons, the Quantum Chromodynamics (QCD), one of the components of the  $SU(3) \times SU(2) \times U(1)$  Standard Model, with the  $SU(2) \times U(1)$  for the electroweak sector of the gauge theory.

The gauge bosons, gluons, are massless like the photons in the electromagnetic interaction but in contrast to the photons, they interact among themselves. This results in a strong scale dependence of the coupling strength  $\alpha_s$ , one fundamental constant of QCD that must be determined from experiment (Sec.4.8). At small distance (large energy scale) the coupling between the quarks and gluons is small, this is known as “asymptotic freedom”. At large distance the coupling increases which leads to confinement. Taking  $Q^2$  as the energy scale, the coupling strength in leading order (LO) and next-to-leading order (NLO) is given respectively by

$$\alpha_s^{\text{LO}}(Q^2) = \frac{1}{\beta_0 \ln(Q^2/\Lambda^2)}, \quad (3.30)$$

$$\alpha_s^{\text{NLO}}(Q^2) = \frac{1}{\beta_0 \ln(Q^2/\Lambda^2)} \left[ 1 - \frac{\beta_1}{\beta_0} \frac{\ln \ln(Q^2/\Lambda^2)}{\ln(Q^2/\Lambda^2)} \right], \quad (3.31)$$

where  $n_f$  is the number of quarks with mass less than the energy scale  $Q^2$ ,  $\Lambda$  represents the scale at which the coupling would diverge [40], and  $\beta_i$  are functions which control the renormalization scale dependence of the coupling:

$$\mu \frac{\partial \alpha_s}{\partial \mu} = -\frac{\beta_0}{2\pi} \alpha_s^2 - \frac{\beta_1}{4\pi^2} \alpha_s^2 - \frac{\beta_3}{64\pi^3} \alpha_s^3 - \mathcal{O}(\alpha_s^4) \quad (3.32)$$

with

$$\beta_0 = 11 - \frac{2}{3} n_f \quad (3.33)$$

$$\beta_1 = 51 - \frac{19}{3} n_f \quad (3.34)$$

$$\beta_2 = 2857 - \frac{5033}{9} n_f + \frac{325}{27} n_f^2 \quad (3.35)$$

where contrary to  $\beta_0$  and  $\beta_1$ ,  $\beta_2$  is scheme dependent (see below).

### 3.2.1 Structure functions in QCD

In QCD, the structure function definitions of the QPM are modified to accommodate strong interactions between the partons and to include mass effects. Using the factorization theorem, the structure function can be expressed as

$$\tilde{F}_2(x, Q^2) = \sum_i \hat{\sigma}_i \left( \frac{x}{z}, \frac{Q^2}{\mu^2}, \frac{\mu_F^2}{\mu^2}, \alpha_s(\mu^2) \right) \otimes xq_i(z, \mu_F, \mu^2), \quad (3.36)$$

where, as illustrated in Fig.3.2(a),  $i$  is the parton label and  $f \otimes g$  denotes a convolution integral

$$f \otimes g = \int_x^1 \frac{dy}{y} f(y) g\left(\frac{x}{y}\right), \quad (3.37)$$

of the hard vector-boson-parton cross section  $\hat{\sigma}$  and the parton distribution function  $xq$ . The hard cross section  $\hat{\sigma}$  can be calculated in perturbative QCD:

$$\hat{\sigma}\left(\frac{x}{z}, \frac{Q^2}{\mu^2}, \frac{\mu_F^2}{\mu^2}, \alpha_s(\mu^2)\right) = \hat{\sigma}_0 \delta\left(1 - \frac{x}{z}\right) + \alpha_s(\mu^2) \hat{\sigma}_1 \left(\frac{x}{z}, \frac{Q^2}{\mu^2}, \frac{\mu_F^2}{\mu^2}\right) + \mathcal{O}(\alpha_s^2), \quad (3.38)$$

where  $\hat{\sigma}_0$  is the contribution in the QPM (Fig.3.2(b)). In performing calculations

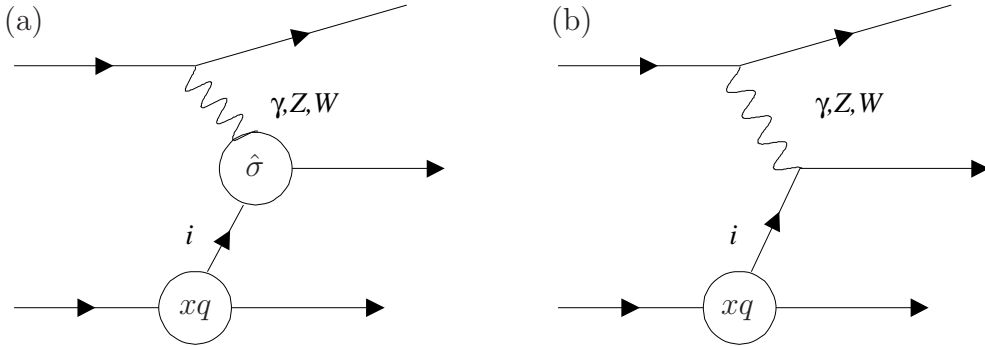


Figure 3.2: (a) Schematic diagram showing QCD corrections and factorization theorem in DIS, (b) diagram in the QPM.

beyond leading order, various divergences arise and the renormalization scale  $\mu$  is introduced to regulate these divergences. The factorization scale  $\mu_F$  serves to define the separation of short-distance from long-distance scale. Roughly speaking, any propagator that is off-shell by  $\mu_F$  or more will contribute to  $\hat{\sigma}$  while it is grouped into  $xq$  below this scale. Since the physical structure function  $\tilde{F}_2(x, Q^2)$  is independent<sup>2</sup> of the scheme and scale dependence, these dependences of  $\hat{\sigma}$  must

<sup>2</sup>This is true only when the result is summed to all orders. Truncating the perturbative series at a given order spoils the perfect compensation and introduces an artificial dependence on the choice of the scale.

be compensated by corresponding dependences of the parton distribution functions  $xq$ . In the inclusive DIS analysis, these scales are usually chosen to be  $Q^2$ , the characteristic large momentum scale of the process, to avoid logarithms of large ratios  $\ln(Q^2/\mu^2)$  and  $\ln(\mu_F^2/\mu^2)$ .

The two most commonly used schemes are the modified minimal subtraction  $\overline{\text{MS}}$  [44] and DIS. The  $\overline{\text{MS}}$  scheme is appealing for its theoretical elegance and calculational simplicity. The DIS scheme [45], on the other hand, is appealing for its close correspondence to experiment. In this scheme, one demands that, order-by-order in perturbation theory, all corrections to the structure functions  $\tilde{F}_2$  be absorbed into the distributions of the quarks and antiquarks, such that the higher order formula for  $\tilde{F}_2$  is the same as the leading-order formula. On the other hand, both  $\tilde{F}_L$  and  $x\tilde{F}_3$  acquire nontrivial order  $\alpha_s$  corrections. For example the structure function  $\tilde{F}_L(x, Q^2)$  reads

$$\tilde{F}_L(x, Q^2) = \frac{\alpha_s(Q^2)}{\pi} \int_x^1 \frac{dz}{z} \left(\frac{x}{z}\right)^2 \left[ \frac{4}{3} \tilde{F}_2(z, Q^2) + 2c \left(1 - \frac{x}{z}\right) zg(z, Q^2) \right], \quad (3.39)$$

where  $c = N_f$  for neutrino scattering and  $c = \sum_i e_i^2$  for charged lepton scattering. Higher order corrections and possibly non-perturbative contributions are sizable [46]. At small  $x$  ( $x \lesssim 10^{-3}$ ) the second terms dominates. In fact for  $z \simeq 2.5x$ , a measurement of  $\tilde{F}_L$  is almost a direct measure of the gluon distribution [47].

### 3.2.2 Evolution of structure functions

The most powerful quantitative prediction of perturbative QCD is the breaking of Bjorken scaling in DIS. Although the parton distribution functions in the hadron cannot be calculated from first principle, their  $Q^2$  dependence can be calculated within perturbative QCD. The scale dependence of the parton distribution functions in QCD has its origin in the interactions of the quarks and gluons via such elementary processes (Fig.3.3) as gluon emission from quarks,  $q \rightarrow qg$ , the creation of quark-antiquark pairs by gluons,  $g \rightarrow q\bar{q}$ , and gluon emission by gluons,  $g \rightarrow gg$ . In describing the way in which scaling is broken in QCD, it is convenient to define nonsinglet and singlet quark distributions:

$$q^{NS} = q_i - q_j, \quad (3.40)$$

$$q^S = \sum_i (q_i + \bar{q}_i). \quad (3.41)$$

It is understood that the parton distribution functions  $q^{NS}$  and  $q^S$  are functions of  $x$  and  $Q^2$ . The nonsinglet structure functions have nonzero values of flavor quantum numbers such as isospin or baryon number. The variation with  $Q^2$  of these and the gluon distribution function  $g(x, Q^2)$  is described by the so-called

DGLAP (Dokshitzer-Gribov-Lipatov-Altarelli-Parisi) equations [48], valid to all orders in  $\alpha_s$ :

$$\frac{\partial q^{NS}}{\partial \ln Q^2} = \frac{\alpha_s(Q^2)}{2\pi} P_{qq} \otimes q^{NS}, \quad (3.42)$$

$$\frac{\partial}{\partial \ln Q^2} \begin{pmatrix} q^S \\ g \end{pmatrix} = \frac{\alpha_s(Q^2)}{2\pi} \begin{pmatrix} P_{qq} & P_{qg} \\ P_{gq} & P_{gg} \end{pmatrix} \otimes \begin{pmatrix} q^S \\ g \end{pmatrix}. \quad (3.43)$$

The splitting functions  $P_{ij}(x)$ , representing the probability of a parton  $j$  emitting a parton  $i$  with a fraction  $x$  of the parent's momentum, is calculable in perturbative QCD:

$$\frac{\alpha_s(Q^2)}{2\pi} P_{ij}(x, Q^2) = \frac{\alpha_s(Q^2)}{2\pi} P_{ij}^1(x) + \left( \frac{\alpha_s(Q^2)}{2\pi} \right)^2 P_{ij}^2(x) + \dots \quad (3.44)$$

The splitting functions in leading order  $P_{ij}^1$  [49] correspond to contributions shown in Fig.3.3. The truncation after the first two terms in Eq.(3.44) defines the NLO

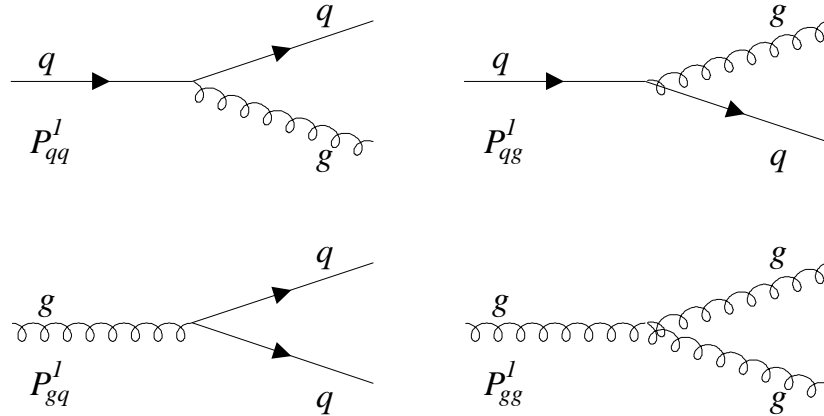


Figure 3.3: *Leading-order diagrams contributing to the splitting function  $P_{ij}^1$ .*

evolution. The splitting functions at NLO have been calculated since long. The splitting functions at next-to-NLO are however only known partially [50].

As we will see in later chapters, the conventional DGLAP evolution equations have been working very successful in describing the HERA structure function data. However, due to the approximation in which only terms involving  $(\alpha_s \ln Q^2)^n$  are summed to all orders in  $n$  in LO and  $\alpha_s (\alpha_s \ln Q^2)^n$  in NLO, it is believed that it may not be applicable at very low  $x$  when  $\alpha_s \ln(1/x) \sim 1$ . Indeed, in BFKL (Balitsky-Fadin-Kuraev-Lipatov) equation [51] terms involving  $(\alpha_s \ln(1/x))^n$  are summed instead. The solution of the equation gives a functional form for the gluon distribution as

$$xg \sim x^{-\omega} \quad (3.45)$$

with  $\omega = 12 \ln 2\alpha_s/\pi \simeq 0.5$  for  $\alpha_s = 0.19$ . Recently, the next-to-leading logarithmic (NLL) corrections have been obtained [52] giving  $\omega = 2.65\alpha_s - 16.3\alpha_s^2 \simeq -0.12$  for the same  $\alpha_s$  value. Unfortunately, neither LL nor NLL value is compatible with the data. For the latest development, see [53, 54] and references therein.

When  $Q^2$  is large and  $x$  is small, namely  $\alpha_s \ln Q^2 \ln(1/x) \sim 1$  but  $\alpha_s \ln Q^2$  and  $\alpha_s \ln(1/x)$  are both small, terms involving  $(\alpha_s \ln Q^2 \ln(1/x))^n$  have to be summed to all orders in  $n$  to give the so-called double leading logarithmic (DLLA) approximation. Theoretical research has been trying to find a more general approximation scheme resulting in an equation that is applicable in these different regions. For example, the CCFM equation [55] gives BFKL at small- $x$  and DGLAP at large  $x$ .

Understanding the dynamics of the small  $x$  region is one of the fundamental problems of QCD. For a relatively low transverse scale of  $p_T$  in a process at a future high energy hadron machine with a center-of-mass energy  $\sqrt{s}$ , the value of  $x = p_T/\sqrt{s}$  can be low. When  $x$  is small enough, the density of partons becomes very large so that partons start to interact and overlap, the perturbative QCD will eventually fail not because the strong coupling  $\alpha_s$  is large but because the parton density is high.

### 3.2.3 Higher twist

The predictions of QCD discussed so far is at leading twist (twist two). In QCD, the structure functions have higher-twist power corrections:

$$F_2(x, Q^2) = F_2^{(2)}(x, Q^2)(1 + h(x)/Q^2 + \dots) \quad (3.46)$$

where  $h(x)$  has a form  $(1 - x)^{-1}$  according to a phenomenological analysis of the structure function data of BCDMS and SLAC [56]. The higher twist contribution is therefore expected to be important at high  $x$  and low  $Q^2$ .

The higher twist contribution involves presumably reinteraction of the struck quark with the proton remnant and thus a full calculation may have to await a solution to the problem of confinement.

### 3.3 Parameterizations of parton distribution functions

One of the main strands of interest in experiments on DIS is to determine the parton distribution functions. This is related to the fact that the parton distribution functions have a key feature, universality, i.e. they are independent of the structure functions in which they appear, and of the physical processes to which they are applied. Therefore, the parton distribution functions can be extracted from a quantitative comparison of experimental data from a wide range of physical processes with QCD master equations, Eqs.(3.36),(3.42),(3.43). These can then be used in other applications to make predictions as well as to provide stringent tests of the self-consistency of the perturbative QCD framework itself or the Standard Model in general. Since any compelling indications of inconsistency of the Standard Model are signs of new physics, and since even direct search for new physics must rely heavily on understanding of the background from conventional physics, the systematic analysis of parton distributions is intimately tied to all these ventures.

#### 3.3.1 Global analysis of parton distribution functions

The analysis of structure function data in extracting parton density functions has a long history, the earlier parameterizations dated around the late 1970's. These together with many new generation parameterizations are available in the package PDFLIB [57]. There are many subtle differences among analyses by different groups or even a same group at different times, but the technique used can be broadly summarized as follows.

- **Initial scale  $Q_0^2$ :** The initial scale is arbitrary, but should be large enough to ensure that  $\alpha_s(Q_0^2)$  is small enough for perturbative calculations to be applicable.
- **Functional forms:** Functional forms for parton distributions (valence, sea and gluon, or non-singlet, singlet and gluon) are assumed to be valid at  $Q_0^2$ :

$$xu_v(x) = A_u x^{B_u} (1-x)^{C_u} P_u(x), \quad (3.47)$$

$$xd_v(x) = A_d x^{B_d} (1-x)^{C_d} P_d(x), \quad (3.48)$$

$$xS(x) = A_S x^{B_S} (1-x)^{C_S} P_S(x), \quad (3.49)$$

$$xg(x) = A_g x^{B_g} (1-x)^{C_g} P_g(x), \quad (3.50)$$

where  $P_i(x)$  takes the function form  $1 + \epsilon_i \sqrt{x} + \gamma_i x$  for the MRS (Martin, Roberts, Stirling) group [58] and  $1 + \gamma_i x^{\epsilon_i}$  for CTEQ (the Coordinated Theoretical-Experimental project on QCD) group [59]. In some (earlier)

analyses, the gluon distribution takes a simplified form  $1 + \gamma_g x$ . While the difference in a given parton density using these two functional forms does usually not exceed  $\mathcal{O}(1)\%$  level over a large  $x$  range when same precise data are used, large differences are possible at the kinematic boundaries [60].

- **Evolution:** With a particular value of  $\Lambda$ ,<sup>3</sup> the DGLAP equations (3.42) and (3.43) are then used to evolve the parton distributions up to a different  $Q^2$  value, where they are convoluted with coefficient functions, appropriate to the chosen renormalization scheme, in order to make predictions for various processes corresponding to the chosen measurements.
- **Data sets and comparison between data and parameterizations through minimization:** Data sets from various measurements are selected and compared with the corresponding predictions. The free parameters are obtained by a minimizing procedure (e.g. with the MINUIT package [62]) and by taking into account the experimental errors. Some of the parameters are constrained by the flavor counting rules and the momentum sum rule.

A typical set of parton distributions at  $Q^2 = 20 \text{ GeV}^2$  obtained by the MRS group [58] is shown in Fig.3.4. The core constraint for these parton density functions comes from the DIS structure function data at low  $x$  by the HERA experiments, as will see in Chapter 4, and at high  $x$  from fixed-target data. As an example, four combinations  $u + \bar{u}$ ,  $d + \bar{d}$ ,  $\bar{u} + \bar{d}$ , and  $s$  can be derived from the following structure functions<sup>4</sup> in the leading-order form:

$$F_2^{lp} - F_2^{ln} = \frac{1}{3}x(u + \bar{u} - d - \bar{d}), \quad (3.51)$$

$$\frac{1}{2}(F_2^{lp} + F_2^{ln}) = \frac{5}{18}x(u + \bar{u} + d + \bar{d} + \frac{4}{5}s), \quad (3.52)$$

$$F_2^{\nu N} = F_2^{\bar{\nu} N} = x(u + \bar{u} + d + \bar{d} + 2s), \quad (3.53)$$

$$\frac{1}{2}x(F_3^{\nu N} + F_3^{\bar{\nu} N}) = x(u - \bar{u} + d - \bar{d}), \quad (3.54)$$

where  $p$ ,  $n$ ,  $N$  stands respectively for proton, neutron, and isoscalar targets.

The fact that  $u$  valence shape is different from that of  $d$  valence has been known since the earliest days of neutrino scattering when neutrino and antineutrino scattering data on protons and deuterium were compared [63, 64]. The recent data which fix these valence shapes have come from taking the difference and the ratios of  $F_2^{\mu p}$  and  $F_2^{\mu n}$  from NMC [22]. At large  $x$ , when only valence

<sup>3</sup>Depending on the analyses, the variable  $\Lambda$  was either treated as a free parameter or fixed using the precise value from other independent measurements [61].

<sup>4</sup>When deriving Eqs.(3.51)-(3.54), we have neglected the charm contribution and assumed  $s = \bar{s}$ .

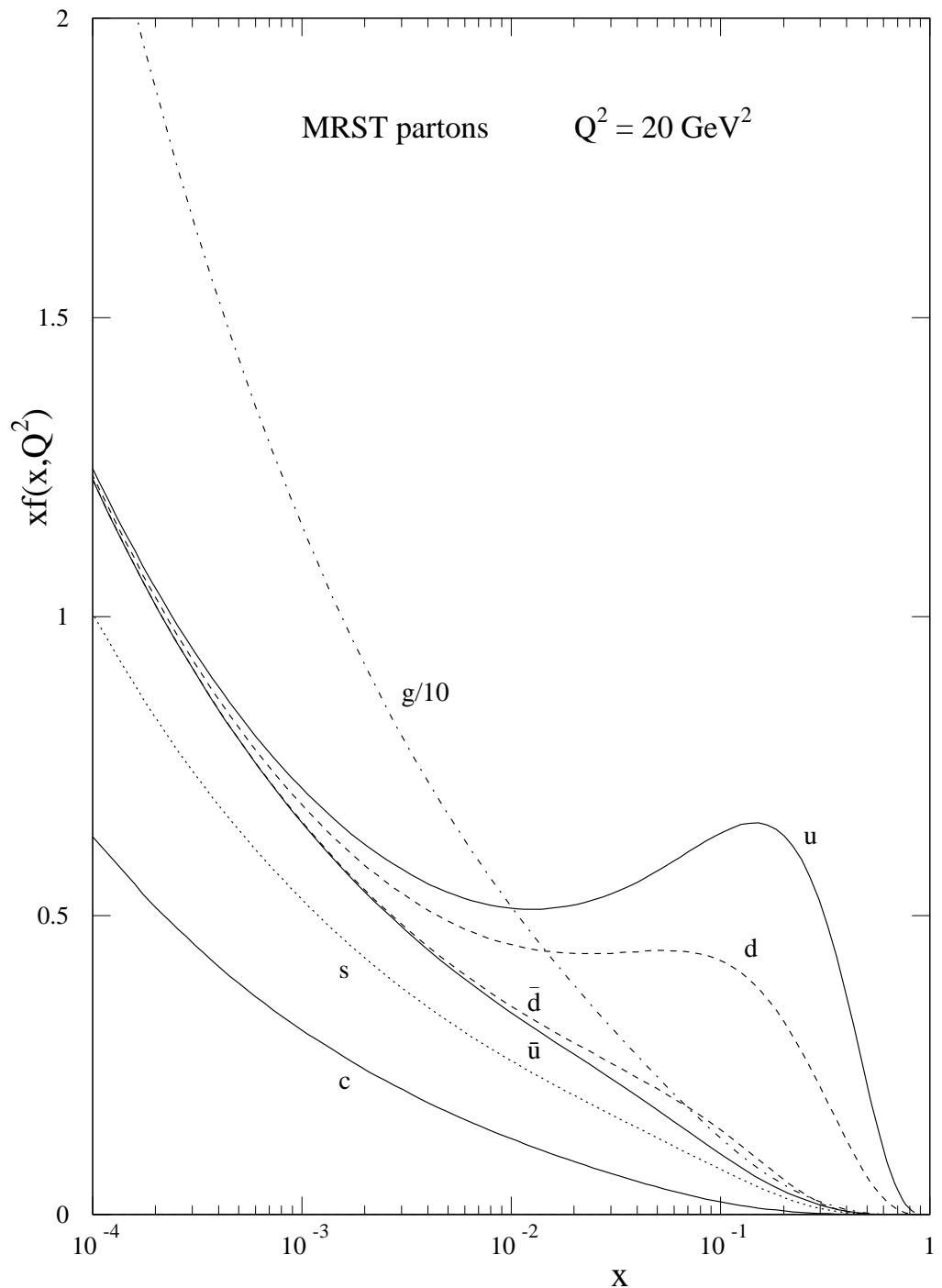


Figure 3.4: Parton distributions at  $Q^2 = 20 \text{ GeV}^2$  from the MRST parameterizations [58]. The gluon density is scaled down by a factor of 10.

distributions are significant, one has in leading order

$$\frac{F_2^{\mu p}}{F_2^{\mu n}} = \frac{1 + 4d_v/u_v}{4 + d_v/u_v}. \quad (3.55)$$

The  $W^\pm$  charge asymmetry at the Tevatron  $p\bar{p}$  collider provides additional information in the region of  $x \sim 0.1$  and  $Q^2 \sim M_W^2$ . Because the  $u$  quarks in the proton carry more momentum on average than the  $d$  quarks, the  $W^+$  bosons tend to follow the direction of the incoming proton and the  $W^-$  bosons that of the antiproton. When  $x \rightarrow 1$ , the behavior of the ratio  $d_v/u_v$  is, however, largely unsettled with model predictions varying between 0 [65] and 0.2 [66] (Sec.5.3).

In the global analysis of the parton distribution functions, the sea quark is assumed to be the same as the anti-quark sea, i.e.  $q_i = \bar{q}_i$ . In the earlier analyses, the flavor symmetry  $\bar{u} = \bar{d}$  is also assumed. In 1992 the NMC data [67] together with the Gottfried sum rule [68]

$$\int_0^1 \frac{dx}{x} (F_2^p - F_2^n) = \frac{1}{3} \int_0^1 dx (u_v - d_v) + \frac{2}{3} \int_0^1 dx (\bar{u} - \bar{d}) \quad (3.56)$$

gave the first evidence that  $\bar{d} > \bar{u}$ . The recent global analyses [58, 69] also use the asymmetry of Drell-Yan production in  $pp$  and  $pn$  collisions first from NA51 [70] for  $x = 0.18$  and then from E886 [71] for an extended  $x$  range ( $0.04 < x < 0.3$ ) to determine directly  $\bar{u} - \bar{d}$ . The semi-inclusive DIS data from HERMES are expected to give confirmation or independent information on the  $\bar{u}$  and  $\bar{d}$  flavor asymmetry.

In Fig.3.4, the strange quark sea  $s$  is shown to be different from the quark seas  $\bar{u}$  and  $\bar{d}$ . In fact in the recent global analysis of e.g. MRST,  $s$  is assumed to have the same  $x$  dependence as  $\bar{u} + \bar{d}$  but suppressed by 50%. This is supported by the CCFR dimuon data [72]. The suppression is presumably due to the mass difference between  $s$  and  $u$  and  $d$  though they all have been treated as massless quarks in the global analysis.

The charm sea  $c$  is further suppressed with respect to other light quark seas. Until recently different groups have used different procedures. One such procedure is to treat the charm quark (similarly for the bottom quark) as infinitely massive below a threshold  $Q^2 = m_c^2$ , and as massless above the threshold thus evolving according to the normal massless evolution equations. Up to NLO in  $\alpha_s$  this prescription guarantees that the correct results are obtained asymptotically, but it is unsatisfactory near the threshold. An alternative procedure considers the charm as being produced from the hard scattering between the electroweak boson and a gluon, i.e. the boson gluon fusion process (Fig.3.5). The latter treatment incorporates the correct threshold behavior automatically but is unsuitable for  $Q^2 \gg m_c^2$  due to the unsummed potentially large logarithm in  $Q^2/m_c^2$ . The recent measurements of charm production at HERA [73, 74] have emphasized the

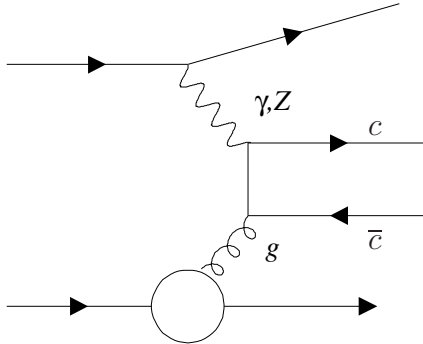


Figure 3.5: *Diagram of the boson-gluon fusion in deep-inelastic lepton-proton scattering.*

importance of having a consistent theoretical framework for heavy flavor production in DIS. This has been achieved and applied in the recent global analyses of parton distribution functions [58, 69]. As a consequence, contrary to light quarks, the charm quark density is determined by the other parton distributions and no extra parameters are introduced apart from the charm quark mass.

At values of  $Q^2$  far above that shown in Fig.3.4, the bottom quark sea becomes increasingly important and eventually all sea quark distributions evolve to a common form, concentrated at small values of  $x$ , since they are driven by  $g \rightarrow q\bar{q}$  transitions.

### 3.3.2 Dynamical parton distributions

Whereas the parameterizations of the global analyses depend crucially on the non-perturbative input parameterizations at  $Q_0^2$ , the ones of the GRV group [75, 76, 77] are constructed to be less dependent on their inputs.

The original idea behind these parameterizations is that at some very low scale  $Q^2 = \mu^2$  with  $\mu \simeq 3\Lambda$ , the nucleon is assumed to consist only of constituent valence quarks. As  $Q^2$  increases, one generates the gluon and sea quarks in the nucleon dynamically from the valence quarks, through the conventional DGLAP equations for the processes  $q \rightarrow qg$ ,  $g \rightarrow q\bar{q}$ . The resulting predictions turned out, however, to be too steep in the small  $x$  region and subsequently the parameterizations for the sea quarks and gluons were modified to be valence like instead of being null. This modification was made based on the argument that partonic quark distributions should rather be identified with the current quark content of hadrons instead of the constituent quarks.

In an earlier version in 1992 [75], only fixed-target DIS data at high  $x$  ( $x > 0.01$ ) were used in fixing the valence-like input parameters at  $\mu^2$ . The resulting prediction at low  $x$  was in qualitative agreement with first structure function mea-

surements at HERA (see Sec.4.2). Quantitatively, however, it could still deviate systematically from the later more precise data from HERA. The parameterizations were thus updated first in 1994 [76] and then in 1998 [77] by including the HERA structure function data together with other DIS and non-DIS data. Therefore, as far as the used data sets are concerned, the GRV parameterizations do not differ from the other global analyses. The only important remaining difference lies in the chosen initial scale which is much smaller than in the other analyses. It is from this low scale that the gluon and sea quarks acquire the sufficient large radiative evolution length  $\ln(\alpha_s(\mu^2)/\alpha_s(Q^2))$  to change dynamically its behavior from valence-like ( $B_i > 0, i = g, S$ , see Eqs.(3.49) and (3.50)) to sea-like ( $B_i < 0$ ) found in the other global analyses choosing  $Q_0^2 \sim \mathcal{O}(4) \text{ GeV}^2$ .

### 3.3.3 Other model parameterizations

In addition to the parameterizations described in the previous subsections, there are a number of other models or parameterizations [78]. One example is the model based on the Regge theory [79]. The Regge theory has been very successful in describing the energy dependence of the soft hadron interactions:

$$\sigma \sim s^{\alpha_P - 1} \quad (3.57)$$

where  $\alpha_P = 1.08$  is the intercept of the soft pomeron (the so-called Regge trajectory corresponding to the exchange of families of particles with different spin). The connection between the small  $x$  and the energy is made by  $W^2$ , the invariant mass of hadronic system defined in Eq.(2.4):

$$W^2 = Q^2(1/x - 1) \simeq Q^2/x. \quad (3.58)$$

In this approach, the gluon distribution is expected to behave therefore as [80]

$$xg \sim x^{1-\alpha_P}. \quad (3.59)$$

When this description is applied to the HERA structure function data, it is found unsuccessful as soon as  $Q^2$  reaches  $\mathcal{O}(1) \text{ GeV}^2$  (see Sec.4.4). The model has been extended recently to include a hard pomeron in addition to the soft one to describe the HERA data [81]. One interesting finding of the new model is that while the hard pomeron is needed to describe the strong rise of the  $F_2$  as  $x$  decreases (Sec.4.2), the contribution of the soft pomeron at  $Q^2 = 5 \text{ GeV}^2$  dominates at high  $x$  and can be still important for  $x$  down to  $\sim 0.0002$ , a behavior of the higher-twist contribution (Sec.3.2.3).

## 3.4 Radiative corrections and hard radiative processes

We have given explicitly in Sec.3.1.1 the Born cross sections corresponding to the contributions from the lowest order lepton-nucleon scattering processes shown in Fig.3.2(b). Experimentally, the inclusive cross sections that are measured include higher order electroweak corrections. These corrections, in particular the conventional electromagnetic (QED) bremsstrahlung corrections, can be very large ( $> 100\%$ ) depending on the kinematic phase space and the kinematic reconstruction method used [82, 83, 84]. These QED contributions do not contain additional information about the strong and weak interaction part of the complete theory, and are generally removed from the measured cross sections.

### 3.4.1 Radiative corrections for neutral and charged current DIS processes at HERA

For the neutral current (NC) process, higher order electroweak contributions can be separated into the QED and weak corrections as shown respectively in Figs.3.6 and 3.7.

The QED contributions can be further subdivided into

- the leptonic corrections described by diagrams containing an additional photon attached to the electron line, i.e. the photon emission from the electron line, Figs.3.6(a) and 3.6(b), and the photonic lepton vertex correction combined with the self energies of the external fermion lines, Fig.3.6(e);
- the quarkonic corrections represented by diagrams with an additional photon at the quark line, Figs.3.6(c), 3.6(d) and 3.6(f);
- the interference of bremsstrahlung from the electron and the quark line, Figs.3.6(a)-(d), and the box diagrams, Figs.3.6(g) and 3.6(h), which connect the electron and the quark line by an extra virtual photon.

The leptonic corrections constitute the bulk of all radiative corrections and represent the practically most important contribution. There are two reasons why these corrections can be large. First, large logarithmic term of the form  $\alpha/\pi \ln(Q^2/m_e^2)$  are present due to the radiation of photon collinear with the emitted lepton. Secondly, the emission of a very energetic photon shifts the momentum in the propagator of the exchanged photon to a value which is essentially smaller than determined from the energy and momentum of the final electron. The second effect is primarily of kinematical nature; it can be reduced in magnitude by applying suitable cuts (Sec.4.3.1) and depends on the method used to

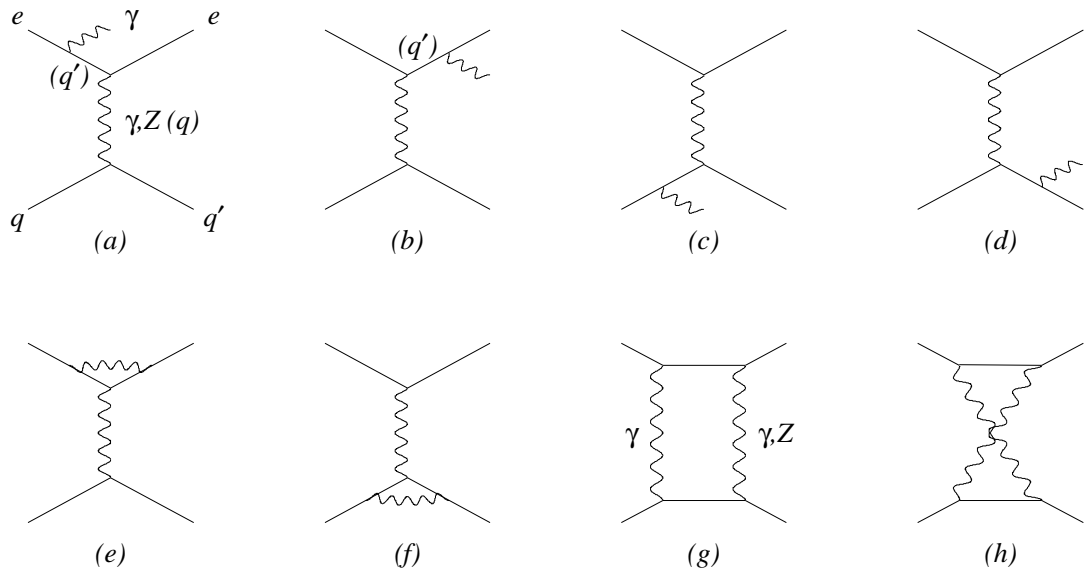


Figure 3.6: *Diagrams of QED corrections to the NC DIS process.*

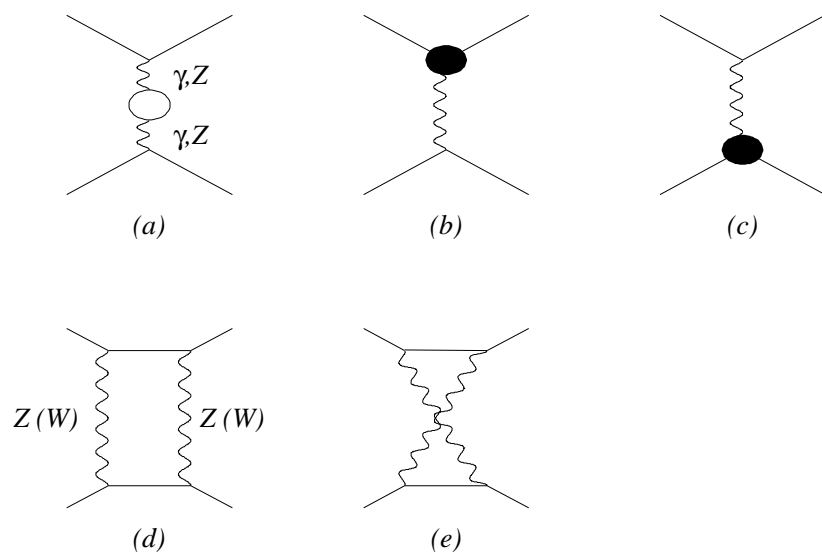


Figure 3.7: *Diagrams of weak corrections to the NC DIS process.*

reconstruct the event kinematics (Sec.2.6.1). The process in which the emission of an energetic photon occurs in the incident electron line (Fig.3.6) can be further used to measure the structure function  $F_2$  in an extended kinematic region (Sec.4.4) and the longitudinal structure function  $F_L$  (Sec.4.7.2).

The quarkonic corrections exhibit a different behavior: they are essentially smaller in magnitude, typically a few percent, and are flat functions of  $Q^2$ . The main reason for this difference is the absence of the kinematical effect in the photon propagator, which dominates the radiation from the lepton. The occurrence of quark mass singularities of the type  $\alpha/\pi e_q^2 \ln(Q^2/m_q^2)$  can be absorbed into the quark distribution functions.

The interference corrections are not affected by either lepton or quark masses and therefore free of the mass singularities.

The weak corrections (Fig.3.7) are infrared finite and numerically small (of the order of 1%).

Diagrams of electroweak corrections for the charged current (CC) process is shown in Fig.3.8. In contrast to the NC process the subsets of the real

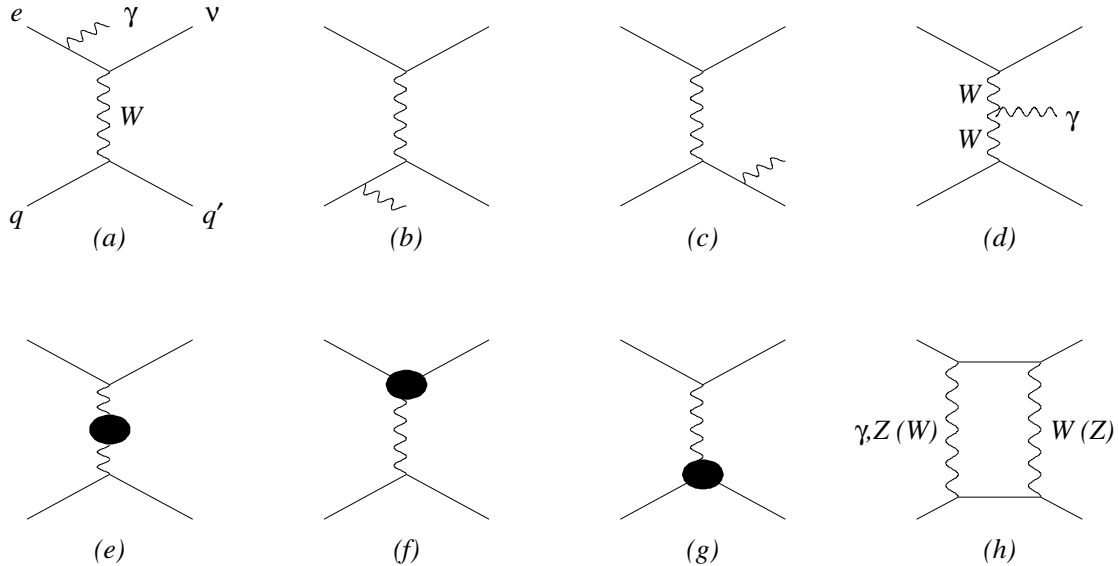


Figure 3.8: *Diagrams of electroweak corrections to the CC DIS process. In addition to (h), the corresponding crossed diagram also contributes.*

bremsstrahlung diagrams for the CC process are not gauge invariant. Moreover the appearance of the non-abelian  $\gamma WW$  vertex in the real (Fig.3.8(d)) and virtual (Figs.3.8(f) and 3.8(g)) corrections, not present within the conventional QED but typical for a non-abelian gauge theory, indicates that the classification convenient for NC processes is less sensible in the CC case. The radiative corrections for CC are flat functions of  $Q^2$ , in contrast to the QED corrections in the

NC case. This is a consequence of the absence of the photon exchange diagram; the kinematical effect of the lowering the exchanged  $Q^2$  is less important in the  $W$  propagator due to the presence of the large  $W$  mass.

### 3.4.2 Hard radiative processes

In the process,  $ep \rightarrow e\gamma X$ , where a real photon is emitted (Fig.3.6(a) and 3.6(b)), the virtuality of the intermediate electron  $Q'^2$  can be defined

$$Q'^2 = -q'^2 = \begin{cases} -(k - K)^2 & \text{(Fig.3.6(a))} \\ -(k' + K)^2 & \text{(Fig.3.6(b))} \end{cases} \quad (3.60)$$

in analogy to that of the exchanged virtual boson,  $Q^2$ , defined in Eq.(2.1), where  $k, k'$  and  $K$  are respectively the four momentum of the incident electron, the scattered electron, and the radiative photon.

The presence of the real photon introduces in the cross section formula an additional propagator due to the intermediate virtual electron. One has therefore

$$\frac{d^2\sigma}{dQ^2 dQ'^2} \sim \frac{1}{Q^4} \frac{1}{(Q'^2 - m_e^2)^2}. \quad (3.61)$$

Depending on the relative values of  $Q^2$  and  $Q'^2$ , one refers to the following processes:

- **Bethe-Heitler and radiative photoproduction processes** correspond respectively to the elastic and inelastic channel when  $Q^2 \rightarrow 0$  and  $Q'^2 \rightarrow 0$ . The Bethe-Heitler process has the largest cross section and has been used by both H1 and ZEUS collaborations to provide the luminosity measurement (Sec.2.4.5).
- **QED Compton process** corresponds to the case when  $Q^2 \rightarrow 0$  but  $Q'^2 > 0$ . Since the radiative photon and the scattered electron can both be measured in the main detector, these events have been used to check and calibrate the energy scale of the electromagnetic calorimeters (Secs.4.4.4 and 5.1.3).
- **Radiative DIS process** corresponds to the case when  $Q^2 > 0$  and  $Q'^2 \rightarrow 0$ . These events are of particular interest, see Secs.4.4 and 4.7.2.

# Chapter 4

## Measurement of structure functions and their interpretation

### 4.1 Pre-HERA results and expectations

Before the advent of the HERA experiments, various structure functions have been precisely measured by several fixed-target experiments for  $x \lesssim 0.01$  and values of  $Q^2$  ranging from  $\mathcal{O}(10) \text{ GeV}^2$  to about  $100 \text{ GeV}^2$  (Fig.2.7). As an example, the proton structure function  $F_2$  measured by NMC [67] and BCDMS [21] is presented in Fig.4.1. These data have been used by various groups to extract parton density functions. A few parameterizations of the proton structure functions are also shown in Fig.4.1. These parameterizations, which all described the then existing low energy data, differ at  $x \simeq 10^{-4}$  by more than a factor of four. The large uncertainty at small  $x$  arises for two reasons

1. theoretically, there were concerns that within the perturbative QCD framework, the occurrence of powers of  $\ln(1/x)$  can spoil the conventional (twist-2) formalism,
2. phenomenologically, even within the standard approach, the initial parton distributions, which are needed in solving the evolution equations, were largely unknown at  $x \lesssim 10^{-2}$ , because the existing data did not extend into this region, and the only constraint, the momentum sum rule, does not fix the shape of the distributions.

All phenomenological analyses of parton distributions based on the usual QCD formalism used certain assumed parameterizations of the initial distribution functions that implicitly determined the extrapolated small- $x$  behavior. For the MRS D [85] parameterizations the small  $x$  evolution of the gluon density (at  $Q_0^2 = 4 \text{ GeV}^2$ ) was singular ( $B_g = -0.5$ , see Eq.(3.50)) for MRS D $-'$  and constant ( $B_g = 0$ ) for MRS D $0'$ . Similarly, for the CTEQ 1MS [86] parameterization

the gluon density was singular, but the sea quark density was not strongly coupled to the gluon density, leading to a slower rise of  $F_2$  with decreasing  $x$ . For the GRV [75] parameterization small  $x$  partons were dynamically generated according to the DGLAP equations, starting from “valence like” quark and gluon density functions at  $Q_0^2 = 0.3 \text{ GeV}^2$ .

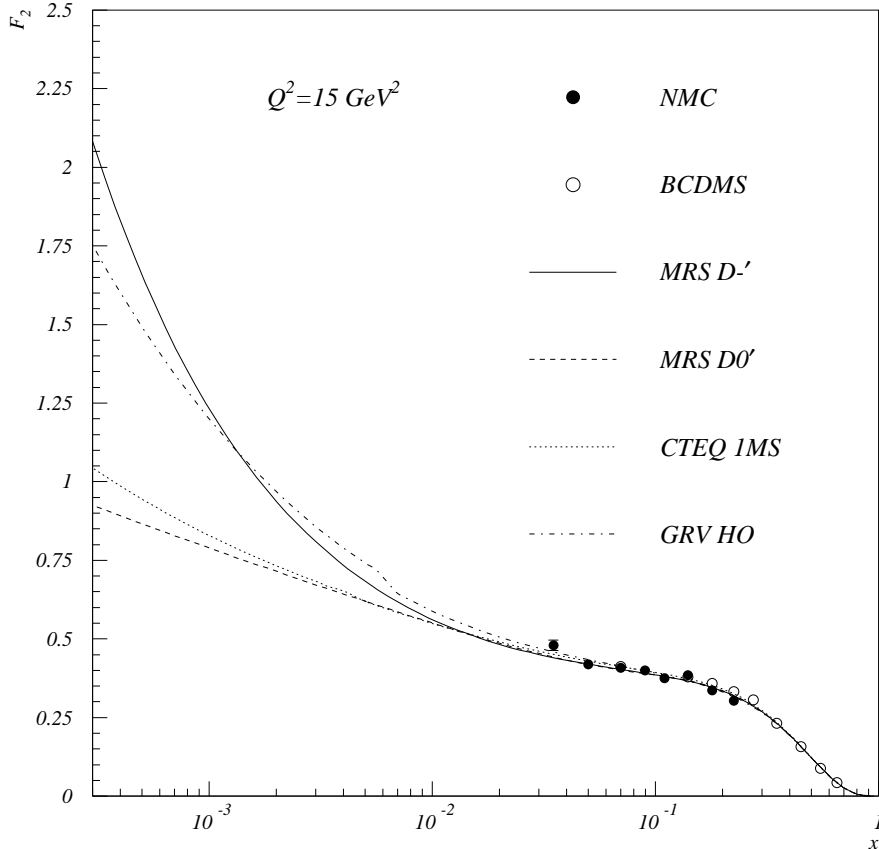


Figure 4.1: The proton structure function  $F_2$  measured by the fixed-target experiments NMC [67] and BCDMS [21] and compared with various parameterizations: MRS  $D-'$ , MRS  $D0'$  [85], CTEQ 1MS [86], GRV [75].

## 4.2 First measurements at low $x$ from HERA

With about  $25 \text{ nb}^{-1}$  of data collected in 1992, the first year of the HERA running, both H1 and ZEUS have made a first measurement [87, 88] at small  $x$  down to  $0.5 \times 10^{-4}$  at values of  $Q^2$  comparable with the low energy fixed-target data [67, 21]. The  $x$  dependence of the measured  $F_2$  for three selected  $Q^2$  values is shown in Fig.4.2.

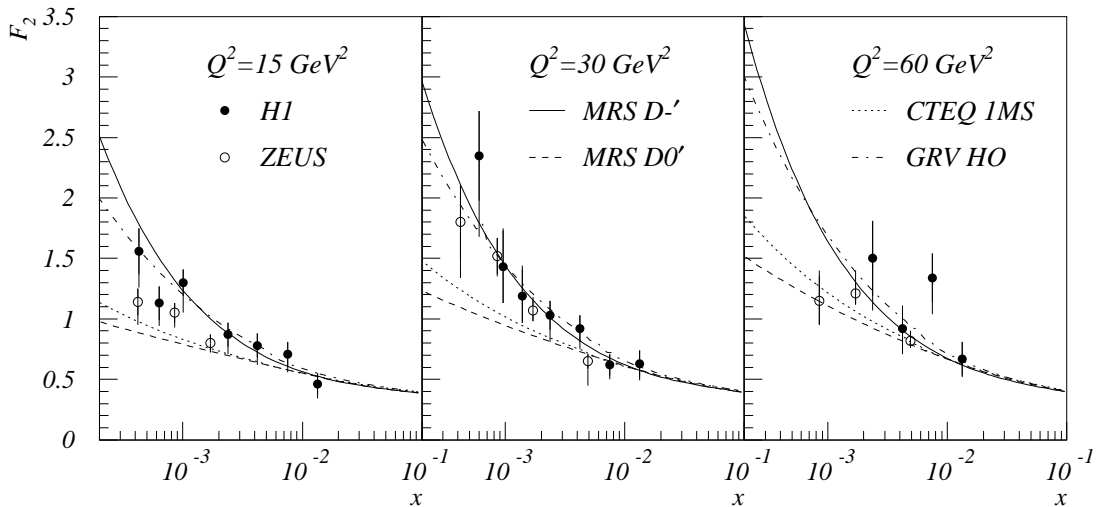


Figure 4.2: The first proton structure function  $F_2$  measured at HERA by H1 [87] and ZEUS [88] compared with 4 parameterizations: MRS  $D^-$ , MRS  $D0'$  [85], CTEQ 1MS [86], GRV [75].

The data showed a significant rise in  $F_2$  towards lower values of  $x$ . This is a striking feature compared to all previous structure function data obtained at fixed target experiments. These latter data can be successfully described [89] by a single nonperturbative pomeron with intercept close to 1.08 (Sec.3.3.3). This is no longer possible for the new data. These new data, though limited in precision, have been used by several QCD analysis groups to constrain the parton density functions at low  $x$  resulting in better parameterizations of MRS H [90] and CTEQ 2 [59]. The behavior of the strong  $x$  dependence has been subsequently confirmed with much improved precision already with 1993 data. The same data have allowed a first measurement be made at values of  $Q^2$  beyond those covered by fixed-target experiments. This analysis is presented in the next section to illustrate as an example how these measurements were performed.

### 4.3 First $F_2(x, Q^2)$ measurement at values of $Q^2$ beyond those covered by fixed-target experiments

In 1993, both H1 and ZEUS have collected a factor of 10 more data than in 1992. The integrated luminosity collected by H1 was  $0.271 \text{ pb}^{-1}$ . The kinematic region covered by the 1993 data is shown in Fig.4.3. The open region on the left

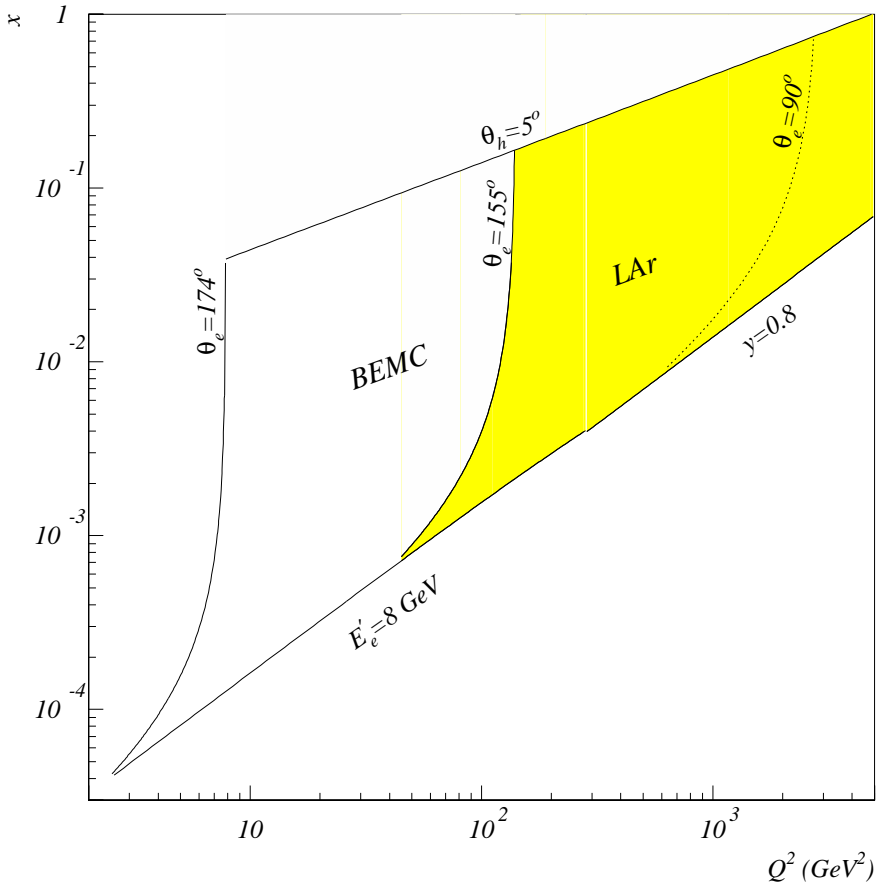


Figure 4.3: The kinematic region covered by 1993 data. It is limited on the top by the angular acceptance of the hadronic final state ( $\theta_h > 5^\circ$ ), on the left by the angular acceptance of the scattered electron, and from the bottom by the cuts on  $E'_e > 8 \text{ GeV}$  and  $y < 0.8$ . The shaded region, analyzed in the following, corresponds to the acceptance of the liquid argon (LAr) calorimeter, while the open area corresponds to the acceptance of the backward calorimeter (BEMC).

corresponds to the acceptance of the backward calorimeter (BEMC) in which the scattered electron is detected. The first measurement of  $F_2(x, Q^2)$  based on 1992 data was made in this region. The increase of the luminosity has significantly

extended the kinematic coverage to the higher  $Q^2$  region (shaded area in Fig.4.3) in which the scattered electron is measured in the liquid argon calorimeter (LAr). This kinematic region is covered in the following analysis.

### 4.3.1 Event selection and background filters

The selection of DIS events at high  $Q^2$  was based on an identified scattered electron in the LAr calorimeter and additional requirements for background rejection. One of the highest  $Q^2$  neutral current events measured by the H1 detector is shown in Fig.4.4.

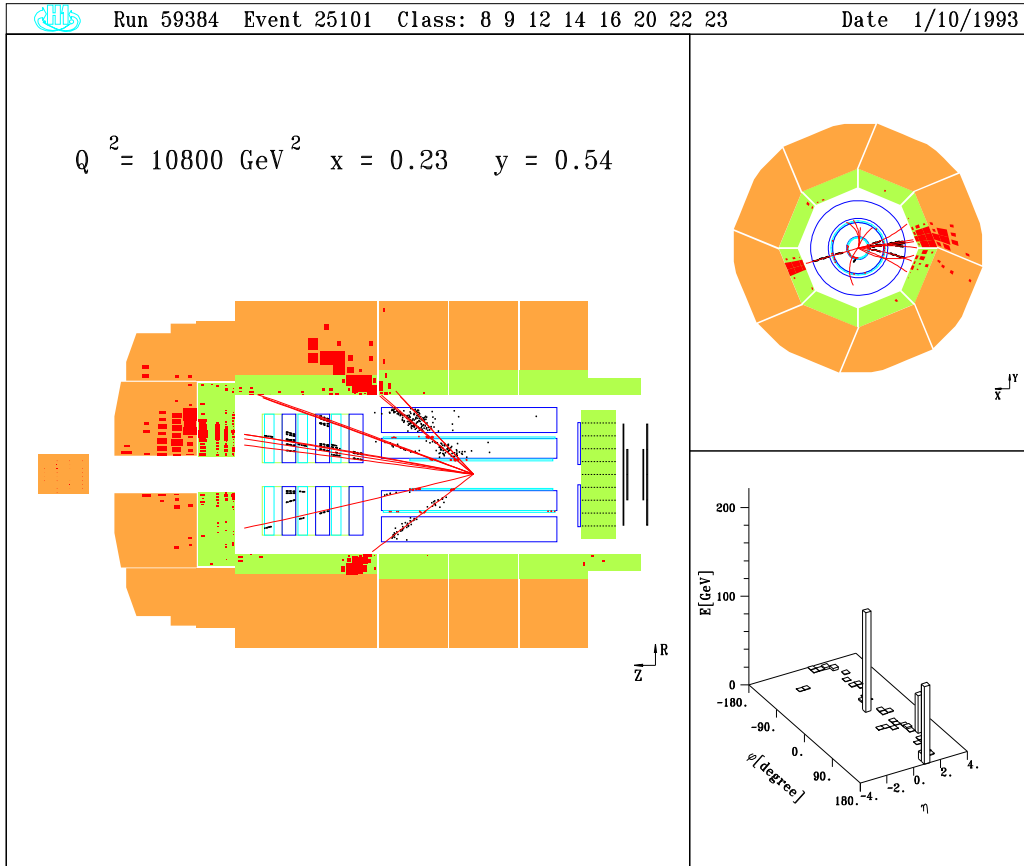


Figure 4.4: A neutral current event at high  $Q^2$  measured by the H1 detector in 1993. The event kinematics is also shown.

The electron identification algorithm developed for this analysis used the salient feature of the LAr calorimeter, namely the fine granularity in both lateral and longitudinal direction. Requiring the longitudinal profile of an isolated energy deposit (cluster) to be consistent with an electromagnetic object, the cluster

having the most compact lateral size was assigned as the scattered electron resulting in a very good efficiency and low misidentification probability [91]. As far as the inclusive cross section and structure function measurement is concerned, the misidentification is more critical since it results in a wrong kinematic reconstruction for a DIS event and brings in additional background contribution from other events. The misidentification probability was found to be  $1.2 \pm 0.5\%$  in data which was in good agreement with the simulation  $1.5 \pm 0.3\%$ . These values corresponded to an identification using purely calorimetric information<sup>1</sup>. A study based on the Monte Carlo events showed that if the track-cluster link were used, the misidentification probability would have been reduced by a factor of two.

The main non- $ep$  background in this high  $Q^2$  analysis was due to muons traveling off axis parallel to the proton beam. These muons are produced by proton beam halo interactions and occasionally generate an electromagnetic shower in the LAr calorimeter. Other important background sources included the cosmic ray events and beam gas/wall interactions. Most of these backgrounds were rejected by requiring

- a reconstructed event vertex around the nominal interaction point<sup>2</sup>:  
 $|z_{\text{vtx}} - z_0| < 30 \text{ cm}$  with  $z_0 = -5 \text{ cm}$  and
- at least one reconstructed charged track having less than 2 cm of the distance of closest approach between the track and the  $z$  axis.

The remaining background events were rejected by a few topological background filters developed for this analysis [91]. For example, the halo events were eliminated by searching for energy distributions in the LAr calorimeter which are very localized in the  $r - \phi$  plane while having large spread in the  $z$  direction. These background filters have been corroborated and complemented later with other filters [92, 93] and are being widely used in the current physics analyses [94].

The dominant  $ep$  background was from photoproduction in which the scattered electron escaped the detector along the beam pipe and an energy cluster from the hadronic final state faked a scattered electron. A sizable fraction of the background, concentrated at low energies and high  $y$ , was suppressed by the following cuts:

$$y_e < 0.8 \quad (4.1)$$

$$E'_e > 8 \text{ GeV} \quad (4.2)$$

$$\Sigma_e + \Sigma_h > 30 \text{ GeV} . \quad (4.3)$$

---

<sup>1</sup>The significant part of the inner central tracker was not operating in the whole 1993 data taking period due to the presence of broken wires, thus the track-cluster link could not be used in the electron identification.

<sup>2</sup>The cut corresponds to about three times of the proton-bunch length ( $\sigma_z^p = 11 \text{ cm}$ , see Table 2.3).

For  $Q^2$  below 284 GeV $^2$ , the minimum energy requirement is more restrictive than the  $y_e$  cut, the latter becomes effective at higher  $Q^2$  (Fig.4.3). The quantities  $\Sigma_e$  and  $\Sigma_h$  are defined respectively in Eqs.(2.14) and (2.15). Note that the sum  $\Sigma_e + \Sigma_h$  is rather insensitive to energy loss in the forward beam hole as the energy and the  $z$  component of the momentum essentially cancel, while it is very sensitive to energy loss (e.g. the scattered electron of a photoproduction event or the initial state radiative photon of a DIS event) in the backward beam hole. While the sum for a DIS event should be around  $2E_e$ ,<sup>3</sup> a smaller value is expected for the photoproduction events as the contribution from the scattered electron was not included in the sum. The same cut also rejects DIS events with an energetic photon radiated along the electron beam direction, thus reducing the radiative corrections to the measurement.

The final selected sample consisted of 1038 events. The residual non- $ep$  background was estimated to be smaller than 1.2% with dominant contribution from the cosmic ray event candidates and negligible other non- $ep$  background events by analyzing the pilot bunch data and a visual scan. The overall photoproduction contribution was less than 1.5% and the largest contribution at high  $y$  did not exceed 10%.

### 4.3.2 Monte Carlo simulation

For the high  $Q^2$  analysis, three Monte Carlo samples have been generated for the neutral current DIS interaction using the event generator DJANGO [95] and parton density distribution parameterizations MRS D $-\prime$ , MRS D0 $\prime$ , and MRS H. The DJANGO program is based on HERACLES [96] for the electroweak interaction and on LEPTON [97] to simulate the hadronic final state. HERACLES includes first order radiative corrections, the simulation of real bremsstrahlung photons and the longitudinal structure functions. The acceptance corrections were performed using the MRS H parameterization, which is constrained to the HERA  $F_2$  results of 1992. To describe higher order QCD radiative processes LEPTO uses the color dipole model [98] as implemented in ARIADNE [99] which is in good agreement with data on the energy flow and other characteristics of the final state as measured by H1 [100] and ZEUS [101]. The program JETSET [102] is then used for the fragmentation of the resulting partons into hadrons, and for their decay. JETSET is based on the Lund string model of fragmentation [103].

The “soft” vector meson contribution of the photoproduction interaction was simulated using the RAYVDM [104] program, and the “hard” scattering part using the PYTHIA [105] program. The relative contributions of both were adjusted to agree with the total photoproduction cross section analysis [106].

---

<sup>3</sup>The relation  $\Sigma_e + \Sigma_h = 2E_e$  is derived from the energy and momentum conservation:  $\Sigma_e + \Sigma_h = E_e - P_{e,z} + E_p - P_{p,z} \simeq 2E_e$  by neglecting the electron and proton mass.

### 4.3.3 Kinematic reconstruction

As mentioned in Sec.2.6.1, the kinematics for a neutral current DIS event can be redundantly reconstructed. Three methods have been studied and compared for this analysis: the electron method, the double angle method and the mixed method (Mixed). The first two methods have been defined already in Sec.2.6.1. In the third method, the  $Q^2$  is that of the electron method, i.e.  $Q_{\text{Mixed}}^2 = Q_e^2$ , while the  $y$  is determined from the hadronic system, i.e.  $y_{\text{Mixed}} = y_h$ .

For the electron method, the energy and the polar angle of the scattered electron were used. For values of  $Q^2 \gtrsim 120 \text{ GeV}^2$ , the scattered electron is detected in the LAr calorimeter. The polar angle  $\theta_e$  was defined with the cluster center in LAr with the vertex position. With the 1993 data, a 5 mrad accuracy and a 7 mrad resolution were obtained by using the Monte Carlo simulation and comparing data and the simulation with the central tracking chambers [91, 107].

Using the redundancy in the reconstruction of the kinematic variables by requiring  $Q_e^2 = Q_{\text{DA}}^2$  with  $Q_e^2$  and  $Q_{\text{DA}}^2$  being defined respectively in Eqs.(2.7) and (2.10), the energy of the scattered electron can be predicted

$$E_{e,\text{DA}} = E_e \frac{\alpha_e + \alpha_e^{-1}}{\alpha_e + \alpha_h} \quad (4.4)$$

where  $\alpha_e$  and  $\alpha_h$ , defined in Eq.(2.13), are related to the angles of the scattered electron and of the hadronic final state. The energy scale determined by test beam measurements [108] was thus refined using this method. The resulting systematic uncertainties in  $E'_e$  were smaller than 3% for the barrel part of the calorimeter and 5% in the BBE region and the cracks [91, 107].

The mixed method needs the hadronic final state for reconstructing  $y$ . The hadronic final state is measured in the LAr calorimeter<sup>4</sup>. The hadronic energy scale was known to 6% as determined from studies of the transverse momentum balance of DIS events. The test-beam data of pions between 3.7 GeV and 205 GeV showed agreement on 3% level with the Monte Carlo description [109].

The hadronic angle  $\theta_h$  was reconstructed according to Eq.(2.13) from the energy deposits in the calorimeter cells. The Monte Carlo simulation showed that the angle was well measured except for the small and large angles; at small angles it is sensitive to the calorimeter noise effect (see Sec.5.1.5 for more explanation), while at large angles, hadrons were not well contained in the BEMC.

The four quantities,  $E'_e$ ,  $\theta_e$ ,  $y_h$  and  $\theta_h$ , are compared in Fig.4.5 between data and the Monte Carlo simulation. Given the precision, the agreement was reasonably good.

---

<sup>4</sup>In fact, this is only true for medium and low  $y$ . For very high  $y$  hadrons are mainly reconstructed in the BEMC, but these events were suppressed due to the cuts on  $E'_e$  and  $y$ , see Eqs.(4.1) and (4.2).

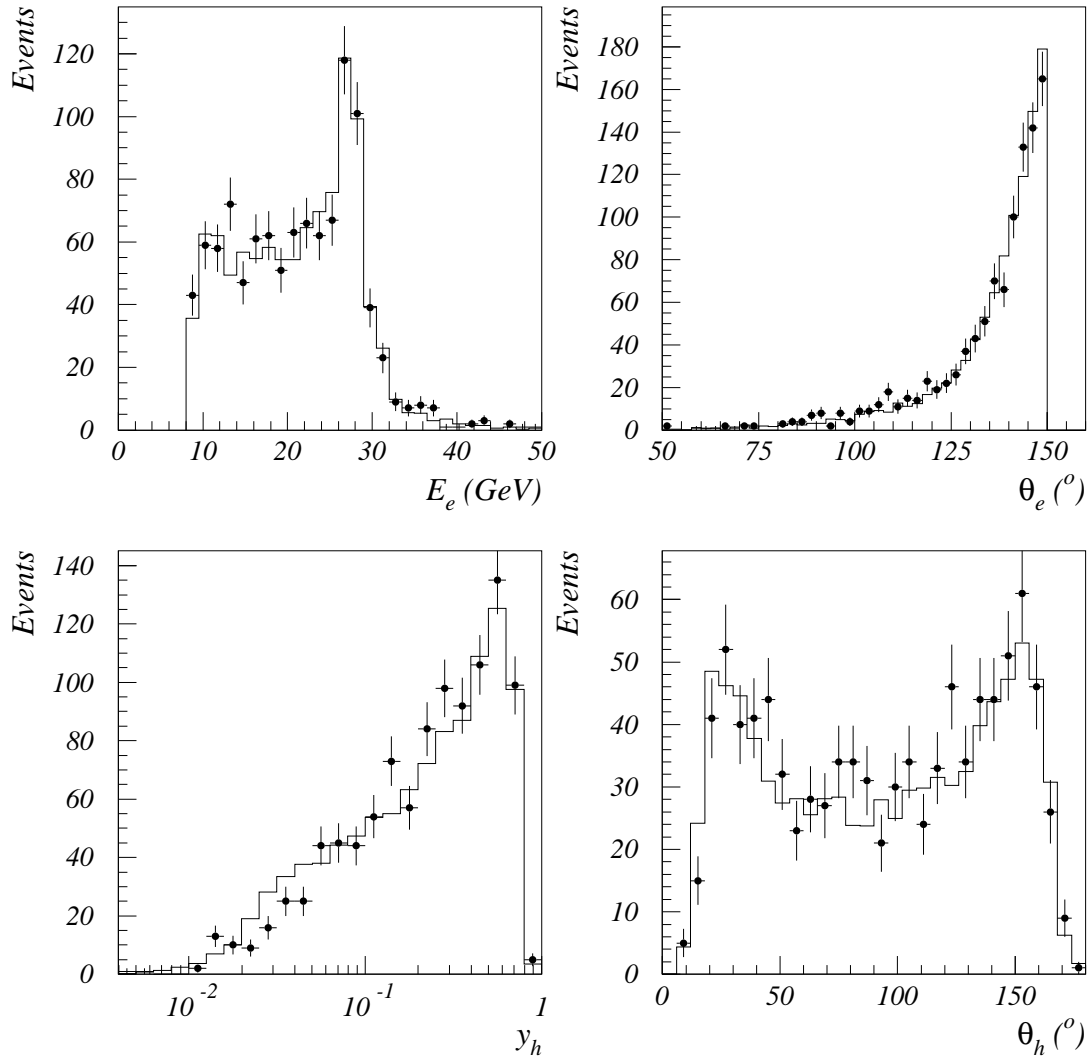


Figure 4.5: A comparison between data (points) and Monte Carlo (histograms) of quantities relevant for the kinematics reconstruction:  $E'_e$ ,  $\theta_e$ ,  $y_h$  and  $\theta_h$ .

Since different quantities were used in the reconstruction of the kinematic variables, the resulting precision could differ. This is illustrated in Fig.4.6. While  $Q_e^2$

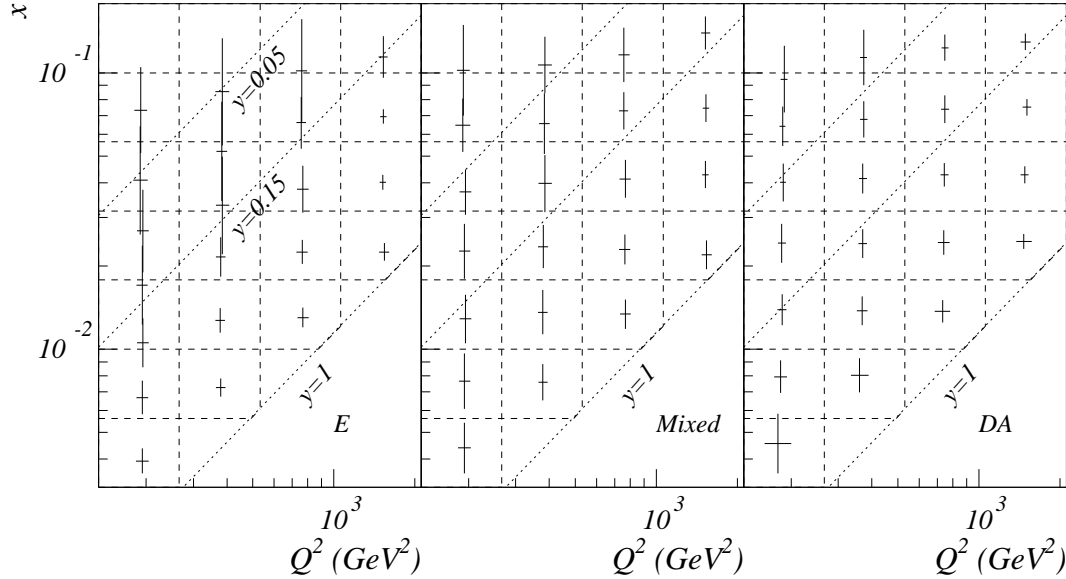


Figure 4.6: A comparison of the  $x$  and  $Q^2$  resolutions of the electron method (E), the mixed method (Mixed) and the double angle method (DA). The dashed lines indicate the bin boundary. Three  $y$  values are shown with the dotted lines. The averaged true kinematics is around the center of each bin. The location of the crosses with respect to the corresponding bin center indicates the magnitude of the migration of a method and the size of the crosses shows the resolution of the reconstructed kinematics.

resolution is the best over all the kinematic region studied, the  $x_e$  resolution deteriorates as  $y$  decreases, this can be easily understood by making the derivatives of  $Q_e^2$  and  $y_e$  defined respectively in Eqs.(2.7) and (2.8):

$$\frac{\delta Q_e^2}{Q_e^2} = \frac{\delta E'_e}{E'_e} \oplus \tan\left(\frac{\theta_e}{2}\right) \delta\theta_e \quad (4.5)$$

$$\frac{\delta y_e}{y_e} = \frac{1 - y_e}{y_e} \left[ \frac{\delta E'_e}{E'_e} \oplus \tan^{-1}\left(\frac{\theta_e}{2}\right) \delta\theta_e \right]. \quad (4.6)$$

The  $x_h$  resolution is better at lower  $y$  than that of  $x_e$  but is still worse than that of  $x_{DA}$ . Overall the double angle method alone gives maximum coverage of the available kinematic range with reasonable precision.

#### 4.3.4 Measurement procedure of the structure function $F_2(x, Q^2)$

In this section, the method used to measure the inclusive cross section and to extract the proton structure function  $F_2$  is first introduced. Various efficiencies and their systematic uncertainties relevant for the measurement are then very briefly mentioned only as their precisions have been superseded by high statistics data samples to be discussed in Chapter 5.

##### Method

What is measured experimentally is in fact the inclusive cross section. The measurement of the inclusive cross section and the extraction of the structure function  $F_2(x, Q^2)$  are performed in the following steps:

- **Bin definition:** In commensurating with the available statistics and the size of migration of the reconstructed kinematic variables due to the finite detector resolution, a finite bin size  $\Delta x \Delta Q^2$  in  $(x, Q^2)$  plane is defined.
- **Averaged cross section in a bin:** From the number of observed events in data  $N_{\text{data}}$  and the number of estimated background events  $N_{\text{bg}}$  normalized to the integrated luminosity  $\mathcal{L}$ , an integrated cross section over a defined bin  $\Delta x \Delta Q^2$  is measured

$$\sigma|_{\Delta x \Delta Q^2} = \frac{1}{\epsilon} \frac{N_{\text{data}} - N_{\text{bg}}}{\mathcal{L} \mathcal{A}} \quad (4.7)$$

where  $\epsilon$  is an extra correction factor for those efficiencies which are not simulated properly in Monte Carlo (see below). The variable  $\mathcal{A}$  includes the efficiency (acceptance) and unfolding corrections, which in the simplest bin-by-bin unfolding method is

$$\mathcal{A} = \frac{N_{\text{MC}}}{N_{\text{gen}}} = \frac{N_{\text{MC}}}{\mathcal{L}_{\text{gen}} \sigma_{\text{gen}}|_{\Delta x \Delta Q^2}}, \quad (4.8)$$

where  $N_{\text{MC}}$  and  $N_{\text{gen}}$  are respectively the number reconstructed and generated events within the bin, and  $\mathcal{L}_{\text{gen}}$  is the integrated luminosity of the generated Monte Carlo (MC). Other sophisticated methods have been proposed [110] to unfold the acceptance correction and the migration effects associated with the finite detector resolution, the (strong) variation in the DIS cross section, and the QED radiative corrections (Sec.3.4.1). However, in practice, since the Monte Carlo from which the unfolding matrix is generated describes the data reasonably well (after e.g. the extra correction mentioned above and the iteration on the input structure function, see below) the different methods give similar results for the unfolded data [111].

To some extent, the migration effects depend on the shape of the structure function, it is therefore important that the structure function parameterization used in generating the input Monte Carlo cross section  $\sigma_{\text{gen}}$  is not substantially different from the measured one. Otherwise (this is the case for the earlier analyses), an iteration is often necessary by reweighting<sup>5</sup> the Monte Carlo events by the measured cross section:

$$N_{\text{new}} = N_{\text{MC}} \frac{\sigma_{\text{new}}|_{\Delta x \Delta Q^2}}{\sigma_{\text{gen}}|_{\Delta x \Delta Q^2}}. \quad (4.9)$$

- **Differential cross section:** A differential cross section at a quoted kinematic point  $(x, Q^2)$  within a bin is obtained by applying a bin center correction

$$\frac{d^2\sigma(x, Q^2)}{dxdQ^2} \Big|_{\text{meas}} = \frac{\sigma|_{\Delta x \Delta Q^2}}{\sigma_{(\text{new})\text{gen}}|_{\Delta x \Delta Q^2}} \frac{d^2\sigma_{(\text{new})\text{gen}}(x, Q^2)}{dxdQ^2} \quad (4.10)$$

$$= \frac{1}{\epsilon} \frac{N_{\text{data}} - N_{\text{bg}}}{\mathcal{L}} \frac{\mathcal{L}_{\text{gen}}}{N_{(\text{new})\text{MC}}} \frac{d^2\sigma_{(\text{new})\text{gen}}(x, Q^2)}{dxdQ^2}. \quad (4.11)$$

- **Extraction of the structure function  $F_2(x, Q^2)$ :** Once the inclusive cross section is measured, to extract the structure function  $F_2(x, Q^2)$  from the cross section formula (Eq.(3.9)):

$$\frac{d^2\sigma}{dxdQ^2} = \frac{2\pi\alpha^2}{xQ^4} \left[ Y_+ \tilde{F}_2 - y^2 \tilde{F}_L + Y_- x \tilde{F}_3 \right] (1 + \delta_{\text{rc}}) \quad (4.12)$$

$$= \frac{2\pi\alpha^2}{xQ^4} \left\{ \left[ 2(1-y) + \frac{y^2}{1+\tilde{R}} \right] \tilde{F}_2 + Y_- x \tilde{F}_3 \right\} (1 + \delta_{\text{rc}}) \quad (4.13)$$

one needs to know the contribution of the  $\gamma Z^0$  interference and  $Z^0$  exchange to  $\tilde{F}_2$  (Eq.(3.22)), and the structure functions  $\tilde{R}(x, Q^2)$ <sup>6</sup> and  $x\tilde{F}_3(x, Q^2)$ , neither of which has been measured so far in the kinematic region covered by HERA. However, according to the QCD prediction,  $\tilde{R}$  is small. Due to the additional suppression factor  $y^2$ , its contribution was found to be well below 1% for most of the kinematic region considered and reached up to 4.5% at the high  $y$  region [91]. The related issue will be discussed later in Sec.4.7. At values of  $Q^2 < 1000 \text{ GeV}^2$ , the contribution from the  $Z^0$  exchange and  $\gamma Z^0$  interference is expected to be less than 1% (see Fig.3.1). At higher  $Q^2$ , the structure function  $x\tilde{F}_3$  becomes increasingly larger and the structure function  $\tilde{F}_2$  also deviates from  $F_2$  for the one-photon exchange. The largest

---

<sup>5</sup>The reweighting is in practice performed on an event-by-event basis using the true kinematics  $x$  and  $Q^2$ .

<sup>6</sup>The structure function  $\tilde{R}$  is generalized from the  $R$  defined in Eq.(3.8) when the  $\gamma Z^0$  interference and  $Z^0$  exchange contribution is taken into account.

correction was estimated to be 4.3% [91] for the highest  $Q^2 = 1600 \text{ GeV}^2$  studied in this analysis. The experimental evidence of the  $x\tilde{F}_3$  contribution at HERA will be discussed in Chapter 5. In addition, a radiative correction  $\delta_{rc}$  should be applied in order to extract the structure function from the measured cross section. First-order QED radiative effects were included in the Monte Carlo simulation. The dominant contribution, partially suppressed by the selection cut (Eq.(4.3)), is originating from the initial state radiation (Sec.3.4.1). The corrections are highly correlated with the method used in reconstructing the kinematics. Because of small separation angles between the final state radiative photon and the scattered electron, the photon is mostly not resolved from the scattered electron by the calorimeter despite of its fine granularity. This considerably reduces the kinematical migration effects caused by the final state radiation and therefore the radiative effects of the final state radiation are less important than those of the initial state radiation.

### Efficiencies and uncertainties

In Eq.(4.11), an efficiency correction  $\epsilon$  is explicitly shown to be applied. In principle, all efficiency corrections could be taken into account in the Monte Carlo simulation and if it is properly done, no additional correction is needed. In practice, this has to be verified and any systematic uncertainty has to be propagated into the measurement of the cross section or the structure function. In two cases, an additional correction will be needed:

1. when there should be a discrepancy between data and the Monte Carlo, e.g. the correction of the vertex efficiency in Sec.4.4,
2. when a correction is determined after the Monte Carlo has been made, e.g. the correction of the trigger efficiency in Secs.4.4 and 5.1.6.

All efficiencies were determined in this analysis from the data and compared with the Monte Carlo simulation. Agreement between the experimental and the simulated values for the individual efficiencies (trigger, vertex) was found to be better than 2%. An overall error of 4% was assigned due to the imperfect description of the various efficiencies.

#### 4.3.5 Results

The proton structure function  $F_2$  measured with the 1993 H1 data by this analysis is compared in Fig.4.7 with other analyses [112] using the electron method at low  $x$  and the sigma method at high  $x$ . Good agreement is observed with few exceptions.

For this comparison, only statistical errors are shown because the measurements were highly statistically correlated although there were differences in the electron identification and selection cuts, which can result in a systematic difference in the  $F_2$  measurements. Additional systematic differences can also arise because the analyses use different quantities in the kinematic reconstruction and do not have the same radiative corrections. Systematic uncertainties have been studied in detail [91, 112, 107]. Instead of giving the long list of considered systematic sources here, it is worth simply noting that most of the uncertainties were limited either directly or indirectly by the low statistics data sample available then. The cross section measurement and its precision have been much improved with the increased integrated luminosity, as we will see in Chapter 5. Nevertheless, these measurements together with others at low  $Q^2$  [107], shown in Fig.4.8, provided the basis for a QCD analysis [113] in which a first determination of gluon density was performed (Sec.4.6.1). Also shown in Fig.4.8 are the results from the ZEUS experiment [114], which are in good agreement with that of H1.

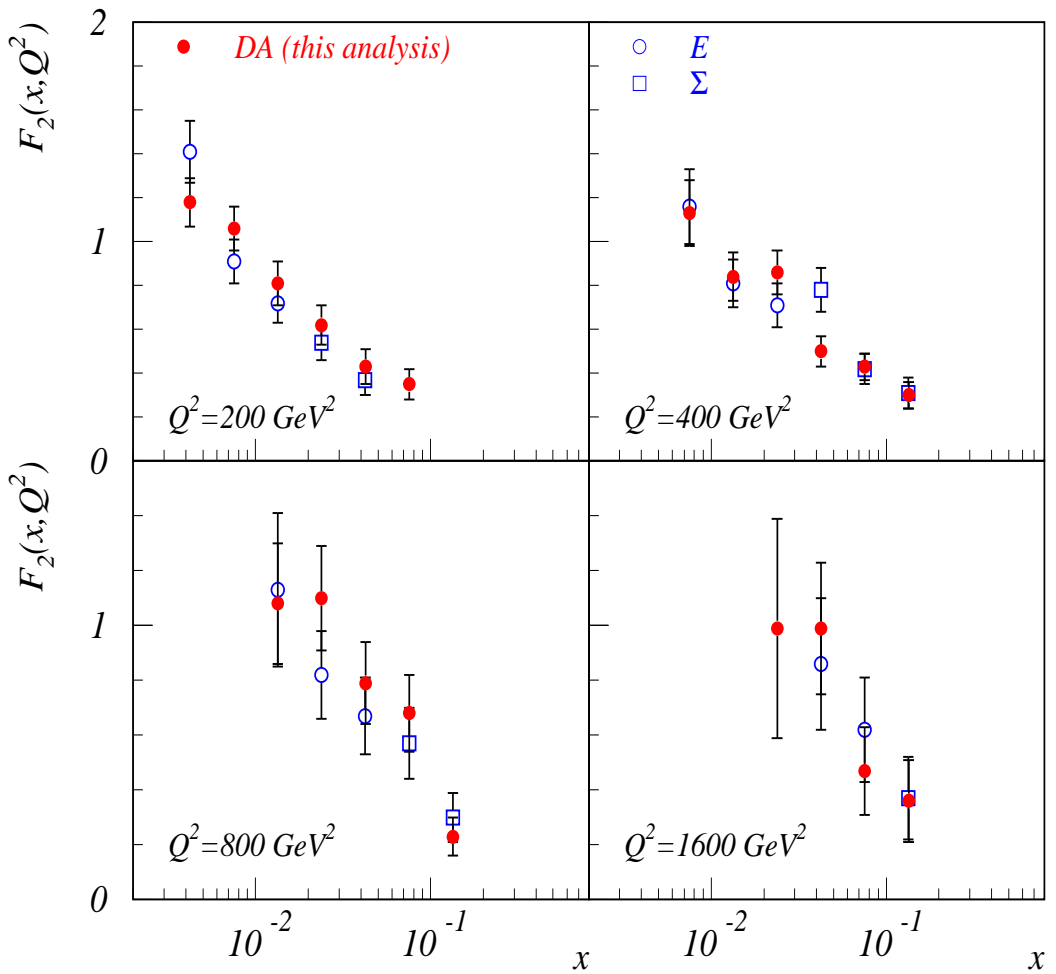


Figure 4.7: A comparison of the measured  $F_2(x, Q^2)$  from this analysis using the double angle (DA) method with other analyses [112] based on the electron (E) and sigma ( $\Sigma$ ) methods. The error bars show the statistical errors only.

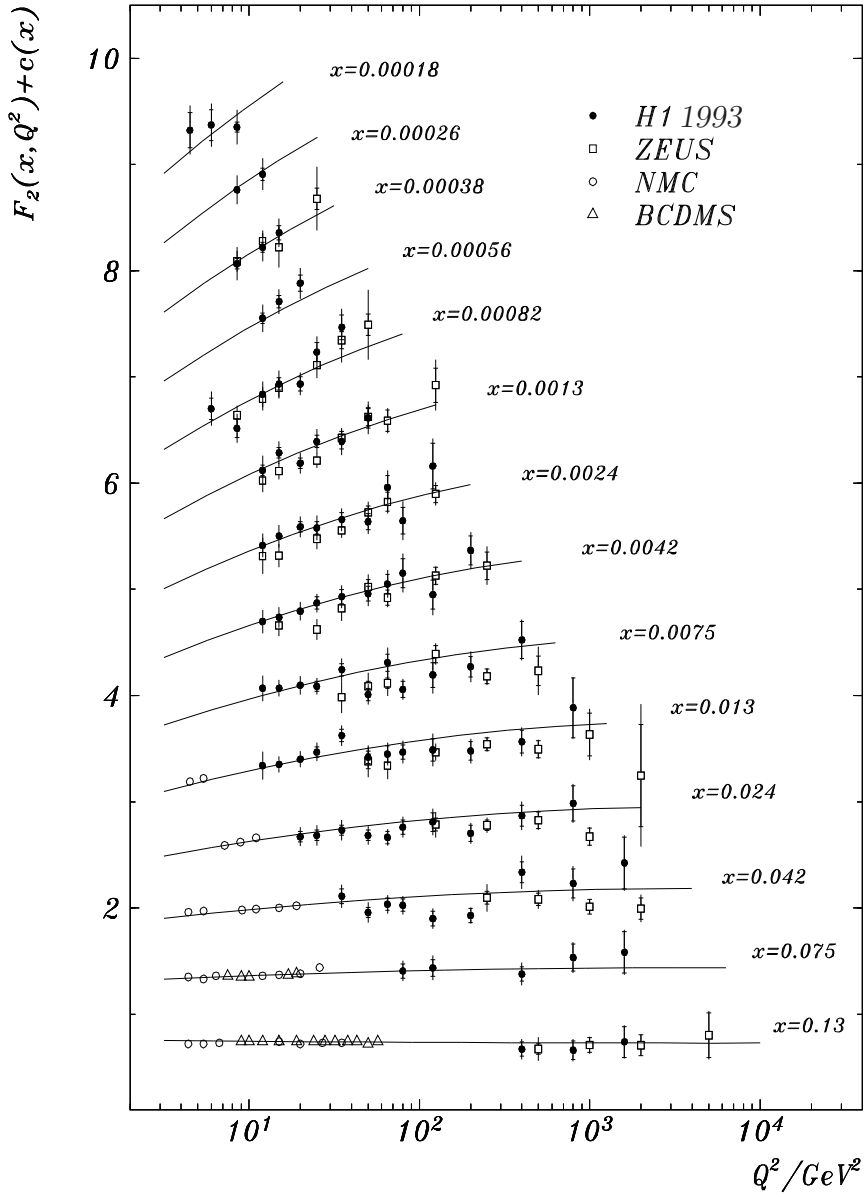


Figure 4.8: Measurement of the proton structure function  $F_2(x, Q^2)$  based on the 1993  $e^-p$  data from H1. The results of the ZEUS collaboration are also shown with open squares (the ZEUS  $F_2$  data were shifted to the H1  $x$  values by using the parameterization in [114]). The curves represent a phenomenological fit to the H1, NMC and BCDMS data (see Ref.[107]). The  $F_2$  values are plotted with all but normalization errors in a linear scale adding a term  $c(x) = 0.6(i_x - 0.4)$  to  $F_2$  where  $i_x$  is the bin number starting at  $i_x = 1$  for  $x = 0.13$ .

## 4.4 The structure function $F_2$ at low $Q^2$ from radiative events

### 4.4.1 Extended kinematic domain using radiative events

When extracting the structure functions from a measured inclusive cross section of DIS processes, one of the corrections that one has to make is the radiative correction. The effect is dominated for the electron scattering by the emission of the real energetic photons from the incident electrons. At HERA, a significant fraction ( $\sim 30\%$ ) of these initial state radiative (ISR) photons are detected in the photon detector of the luminosity system. The photon detector, situated at about 100 m from the interaction point, has an angular acceptance of about 0.45 mrad. These radiative photons can thus be considered as being emitted collinearly with respect to the incident electrons. The energy of the electron after the radiation

$$E_e^{\text{eff}} = E_e - E_\gamma \quad (4.14)$$

available for the subsequent deep inelastic interaction has effectively been reduced and so does the center-of-mass energy

$$s^{\text{eff}} = 4(E_e - E_\gamma)E_p = \frac{E_e^{\text{eff}}}{E_e} s, \quad (4.15)$$

where  $E_p$  and  $s$  are respectively the proton beam energy and the nominal center-of-mass energy squared.

When replacing  $E_e$  and  $s$  respectively by  $E_e^{\text{eff}}$  and  $s^{\text{eff}}$  in Eqs.(2.7)-(2.9), the resulting kinematic values can be very different from those of a non-radiative event depending on  $E_\gamma$ . This is illustrated in Fig.4.9 with a dotted curve originating from  $x = 0.00015$  and  $Q^2 = 6 \text{ GeV}$  and continuing upward to the left as the photon energy increases. As a consequence the limited kinematic region for the non-radiative events due to mainly the angular acceptance ( $\theta_e < 174^\circ$ ) of the scattered electron in the backward calorimeter BEMC is significantly extended to lower  $Q^2$  and high  $x$ .

A measurement of the structure functions in the extended kinematic region is of basic interest:

- The uncertainty in the size of the radiative correction originates from *a priori* unknown shape of the structure functions in the unmeasured kinematical region rather than from the technical aspects of the matrix element integration. The measurement of the cross section in the extended kinematical region allows thus a direct control of this uncertainty.
- The extended kinematical region covers an intermediate  $Q^2$  region between the photoproduction processes (at  $Q^2 \simeq 0$ ) and the DIS regime ( $Q^2 >$  a few

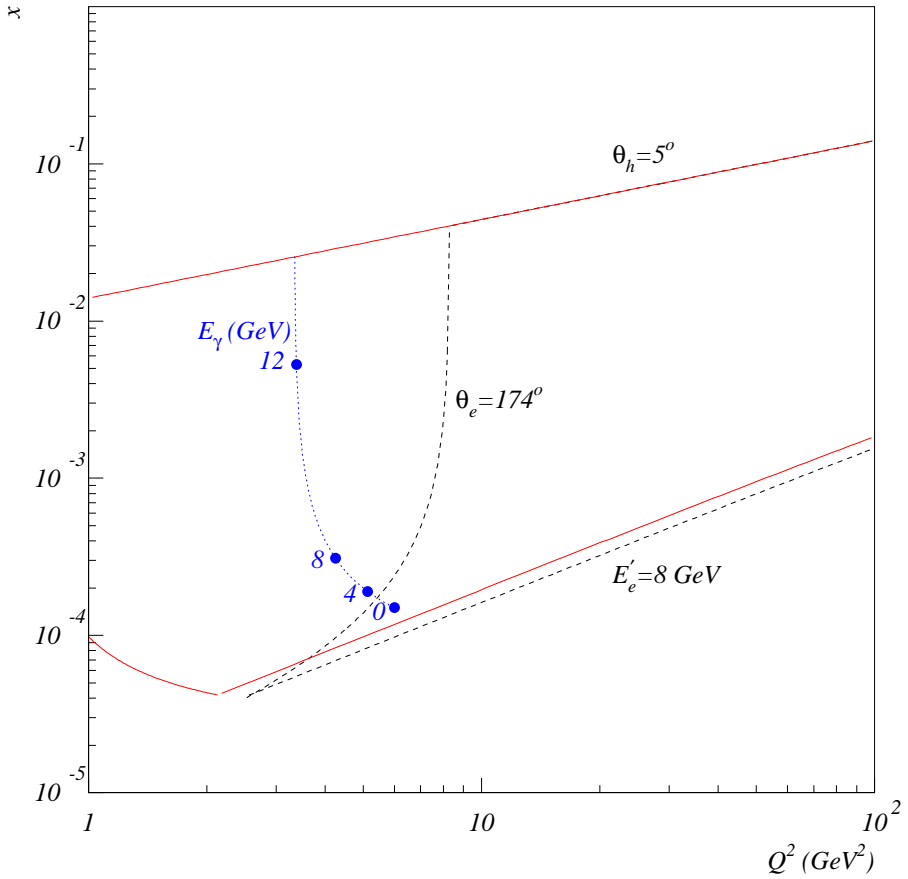


Figure 4.9: The extended kinematic domain from radiative events (the region enclosed by the full lines from the top by the inclusive hadronic angle  $\theta_h > 5^\circ$  and from the bottom by the energy threshold of the scattered electron  $E'_e > 8 \text{ GeV}$  for  $E_\gamma = 4 \text{ GeV}$  (Eq.(4.16))) compared with the corresponding one from non-radiative events (the region enclosed by the dashed lines, in addition to the limits on  $\theta_h$  and  $E'_e$ , the main limit is on the angular acceptance of  $\theta_e < 174^\circ$ ). The dotted curve and large dots illustrate how the kinematics is modified for different photon energies  $E_\gamma$ .

$\text{GeV}^2$ ). The measurement in this region may shed light on the underlying dynamics of the transition.

#### 4.4.2 Event selection and background studies

The analysis shown here is based on the data taken in 1994 by the H1 detector. The data correspond to an integrated luminosity of  $2.7 \text{ pb}^{-1}$ , which is about a tenfold increase with respect to the earlier data collected in 1992 and 1993, upon which first experimental studies of the radiative process were performed [115].

##### Event selection

The selection of DIS events with hard photon emission collinear to the incident electron is based on an identification of the scattered electron in the backward calorimeter BEMC, a measured radiative photon in the photon detector and additional requirements for background rejection. The non-*ep* background events, dominated by interactions of beam protons with residual gas and beam line elements upstream of the H1 detectors, are efficiently rejected at the trigger level using a time of flight system consisting of two scintillator planes installed behind the BEMC.

The scattered electron, which is defined to be the most energetic cluster in the BEMC, has to satisfy the following criteria:

- The energy of the cluster measured with the BEMC is larger than  $8 \text{ GeV}$ .
- The lateral size of the cluster is required to be smaller than  $5 \text{ cm}$ , as expected for the signature of an electron.
- The cluster in the BEMC is required to be associated with at least one reconstructed space point in the BPC by less than  $4 \text{ cm}$ .

An energetic photon detected in the photon detector (PD) is required to have:

$$E_\gamma = E_{\text{PD}} + E_{\text{VC}} > 4 \text{ GeV} \quad (4.16)$$

where  $E_{\text{PD}}$  and  $E_{\text{VC}}$  are the energies deposited in the photon detector and in the water Čerenkov veto counter (VC). This condition suppresses beam related background events and cosmic rays which produce energetic showers in the BEMC.

The remaining non-*ep* background events are further rejected by requiring an event vertex, reconstructed from tracks in the central and forward tracking

chambers, within  $\pm 35$  cm from the nominal interaction point. The vertex position together with the impact point of the scattered electron measured in the BPC/BEMC<sup>7</sup> also defines the polar angle  $\theta_e$  of the scattered electron.

The main source of  $ep$  background is pile-up events due to accidental coincidence of DIS and  $\gamma p$  events with a Bethe-Heitler [116] (BH) Bremsstrahlung event ( $ep \rightarrow e\gamma p$ , Sec.3.4.2) in a time window of  $\pm 5$  ns. These pile-up events are efficiently rejected with the following cuts:

$$\begin{aligned} E_{\text{etag}} &< 2 \text{ GeV} \\ \Delta &= \frac{E_\gamma - E_{\text{miss}}}{E_\gamma} < 0.5 \end{aligned} \quad (4.17)$$

where  $E_{\text{etag}}$  is the energy deposited in the electron tagger. The quantity  $\Delta$  compares the measured photon energy in the photon detector  $E_\gamma$  with the measured missing energy  $E_{\text{miss}}$  based on the main detector without including the photon detector:

$$E_{\text{miss}} = E_e(y_e - y_h) \quad (4.18)$$

with  $y_e$  and  $y_h$  being defined respectively in Eqs.(2.8) and (2.20). One expects for radiative DIS events  $\Delta = 0$  ( $E_\gamma = E_{\text{miss}}$ ) while for pile-up DIS+BH events  $\Delta = 1$  ( $E_{\text{miss}} = 0$ ). More details concerning these cuts and the remaining background events are discussed in the following paragraphs.

To ensure a high trigger efficiency, two fiducial cuts

$$\sqrt{x_{\text{BPC}}^2 + y_{\text{BPC}}^2} > 15 \text{ cm} \quad (4.19)$$

$$|x_{\text{BPC}}| + |y_{\text{BPC}}| > 18 \text{ cm} \quad (4.20)$$

are applied to remove the region around the beam pipe where the efficiency degrades (Fig.4.12).

## Background studies

After having applied the selection cuts described above, a sample of 8229 events is selected. It consists mainly of the following types of events<sup>8</sup>:

1. Radiative DIS events alone or in random coincidence with BH events (with the probability to be discussed below) where the radiated photon is detected in the PD,

---

<sup>7</sup>It is the position measured by the BPC that has been used as it has a better spatial resolution than the BEMC because of the coarse granularity of the latter.

<sup>8</sup>Note that the angular acceptance for photons from radiative DIS events is about 30% while for BH events it is about 98% due to the different angular distributions of photon emission.

2. Pile-up events due to radiative DIS with BH events where the radiated photon from the DIS event is not detected,
3. Pile-up events due to non-radiative DIS with BH events,
4. Pile-up events due to  $\gamma p$  with BH events or inelastic BH events alone.

Events of type 1 constitute the signal since the radiated photons are collinear with respect to the direction of the incident electron. All other events are background. The events of type 4 contribute because of the  $\pi^0 \rightarrow \gamma\gamma$  decay in the hadronic final state, and of the electromagnetic nature of the BEMC making an unambiguous separation between electrons and hadrons at low energies difficult.

The probability for random coincidence depends on the minimum photon energy ( $E_\gamma^{\min}$ ) of BH events. According to an analysis of BH events [117], this probability is 5.6% for  $E_\gamma^{\min} = 0.13 \text{ GeV}$ , which is consistent with the value determined using the  $\Delta$  distribution described below.

As mentioned above the variable  $\Delta$  can be used to reject pile-up events. The distribution of  $\Delta$  is shown in Fig. 4.10 for six different event samples. The plots on the left show those events which have activity in the electron tagger ( $E_{\text{etag}} > 2 \text{ GeV}$ , tagged sample) while the plots on the right correspond to the non-tagged sample. The dependence on  $E'_e$  is shown in three different energy ranges indicated with the axis on the right side. As expected, the peaks around one in the two upper plots are due to DIS+BH events. The normalization of this background is fixed<sup>9</sup> by the upper left plot and confirmed with the upper right one for events at high  $\Delta$  values ( $\Delta > 0.8$ ) where the expected signal (peaking around  $\Delta = 0$ ) does not contribute. The difference (4%) is taken as the uncertainty in the background subtraction of pile-up events of types 2 and 3.

The normalization for the events of type 4 is fixed by the lower left plot after the DIS+BH events have been subtracted. In this way, any possible background contribution from inelastic BH events (with photons being detected in the PD) is also taken into account. In fact, among the estimated background events of type 4, only about one third is expected from  $\gamma p$  events in random coincidence with BH events using the probability given above. A 30% uncertainty is assigned for this normalization due to the missing inelastic BH process in the MC and to the dependence on the low energy spectrum of the structure function.

The relative contribution of these background events after all selection cuts is smaller than 10% in most of the kinematic region to be measured and the largest contribution at high  $y$  does not exceed 30%.

---

<sup>9</sup>With this method we found a probability for random coincidence of 6.4% for  $E_\gamma^{\min} = 0.1 \text{ GeV}$ , which corresponds to 6.0% for  $E_\gamma^{\min} = 0.13 \text{ GeV}$ , and is consistent with the value mentioned above. The large value of this method may be understood since second order overlaps are included.

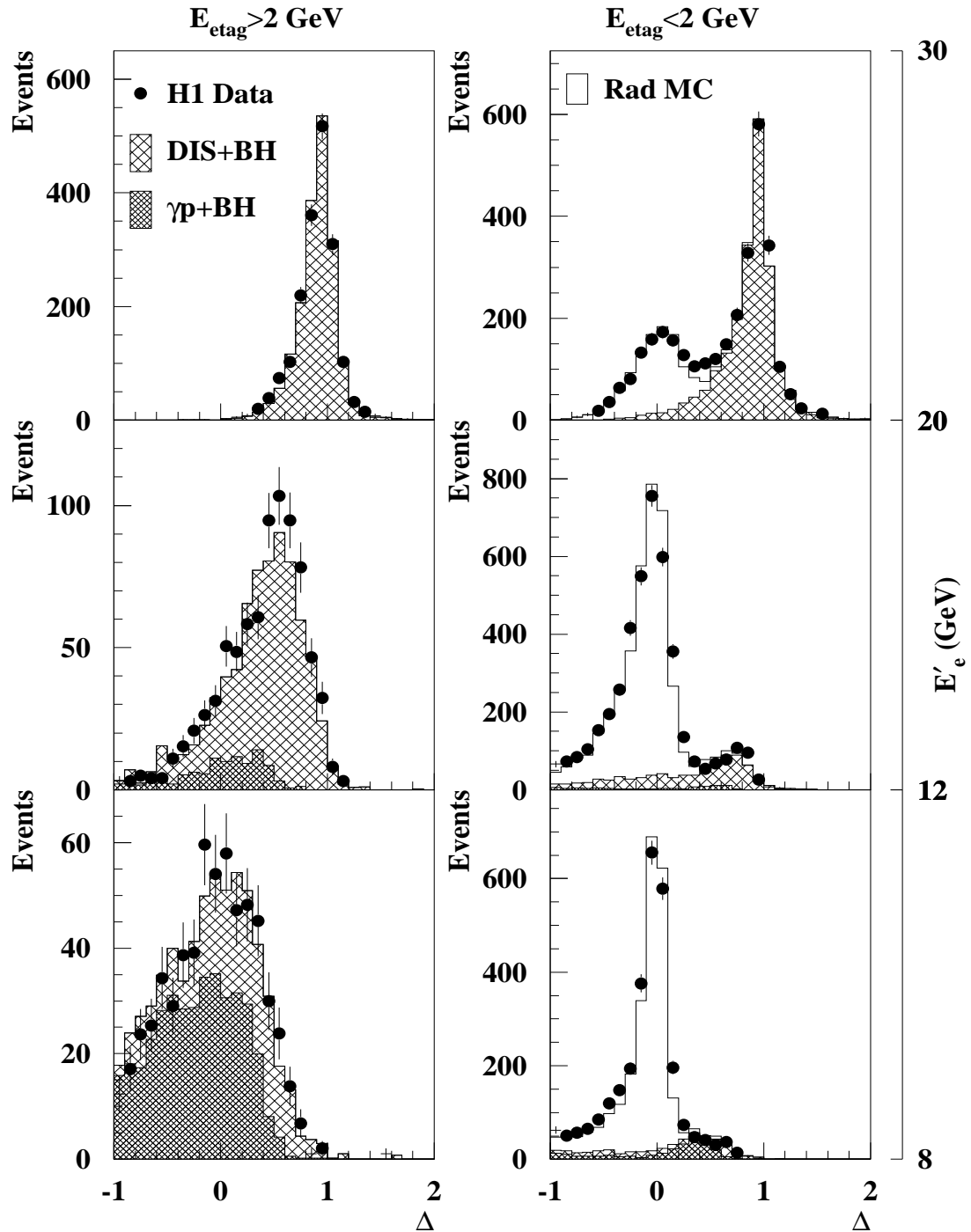


Figure 4.10: Distribution of  $\Delta$  (see Eq.(4.17) for definition) for tagged events (left plots) and for non-tagged events (right ones) in three different electron energy ranges as shown with the axis on the right side. The normalization for the simulated  $DIS+BH$  events is fixed by the upper left plot and the normalization for the  $\gamma p + BH$  events is fixed by the lower left plot.

### 4.4.3 Monte Carlo simulation

For this analysis, neutral current DIS events (both radiative events and non-radiative events) were generated using DJANGO [95]. The GRV [75] parton density parameterization was used for the generation of events because this parameterization provided a reasonable description of previous H1 and ZEUS measurements [87, 88] and was one of few parameterizations that provided structure function parameterization at both low and high  $Q^2$  needed for this analysis.

The  $\gamma p$  events were simulated using the PHOJET generator [118], which generates the total  $\gamma p$  cross section by taking into account both soft and hard processes.

The BH events were generated according to the Bethe-Heitler approximation [116] in which the proton recoil energy is neglected, i.e.  $E'_e + E_\gamma \simeq E_e$ . The acceptance of the electron tagger was determined directly from the H1 data.

### 4.4.4 Kinematic reconstruction

A precise reconstruction of the kinematic variables relies crucially on the measurement of the angle  $\theta_e$  and the energy  $E'_e$  of the scattered electron, of the energy  $E_\gamma$  of the radiative photon, and of the hadronic final state. Most of the measurement is better studied with the high statistics sample of non-radiative events [119]. This is the case for  $\theta_e$ ,  $E'_e$ , and the measurement of the hadronic system. The key points and the methods used for the measurement of these quantities are briefly discussed here. The calibration of  $E_\gamma$ , a quantity which is most relevant for this analysis, is then described.

The angle of the scattered electron is defined as the straight line between the reconstructed vertex and the impact point in the BPC. Several effects contribute to the precision of the  $\theta_e$  measurement:

1. the relative alignment of the BPC with respect to the central trackers,
2. the precision of the vertex reconstruction,
3. the amount of dead material the scattered electron encounters on its way to the BPC affecting the multiplicity of the BPC hits and thus the resolution of the impact point.

With the 1994 data, a systematic precision of up to 1 mrad is achieved.

The energy calibration and the resolution of the BEMC is originally determined with test beams [120]. Both the energy scale and the resolution are checked and improved based on the  $ep$  data using the following three methods.

- **The kinematic peak method** uses events in the pronounced peak of quasi-elastically scattered electrons in the region close to the beam energy.

The absolute energy scale of the individual stacks is calibrated. For the energy scale of the electron cluster, the effects of the presence of dead material in front of the BEMC (up to  $2X_0$ ) and of cracks between the BEMC stacks are taken into account by a Monte Carlo simulation.

- **The double angle method** uses the predicted electron energy  $E_{e,DA}$  as defined in Eq.(4.4) to an independent cross check of the energy scale of the cluster and of its uniformity over the whole BEMC and allows to perform additional corrections in the crack region, which is difficult to calibrate with sufficient precision.
- **The QED Compton method** uses events from the physical process corresponding to the Compton scattering of a quasi-real photon on an incident electron (Sec.3.4.2), with the dominant contribution due to the elastic channel ( $ep \rightarrow e p \gamma$ ). The energy and the angle of the scattered electron and of the photon are constrained by the QED theory, making this process well suited for calibration of the BEMC [121].

The three methods are complementary and allow the energy linearity be studied. After the recalibration, the systematic uncertainty on the energy scale is reduced from 1.7% obtained from 1993 data to 1%. The dead material description is also improved resulting in a comparable energy resolution between data and the Monte Carlo.

For a precise measurement of the energy of the radiated photon it is important to know the energy calibration [117] of the photon detector with high precision. The off-line calibration of the photon detector (and also of the electron tagger) has been determined with a sample of BH events. These events were selected using the following requirements:

$$\begin{aligned} E_{\text{etag}} &\geq 4 \text{ GeV} \\ E_\gamma &\geq 4 \text{ GeV} \\ 24 \text{ GeV} &\leq E_{\text{etag}} + E_\gamma \leq 31 \text{ GeV} \\ |x_{\text{etag}}| &\leq 65 \text{ mm} \quad \text{and} \quad |y_{\text{etag}}| \leq 65 \text{ mm} \end{aligned} \tag{4.21}$$

The last condition, where  $x_{\text{etag}}$  and  $y_{\text{etag}}$  are the coordinates of the impact point with respect to the center of the electron tagger, was used to reject events in which a large amount of energy leaks over the transverse detector boundaries. The crystal calorimeters were calibrated with events having  $E_{\text{VC}} \leq 0.2 \text{ GeV}$  making use of the kinematic constraint  $E_{\text{etag}} + E_\gamma = E_e$ , while the water Čerenkov veto counter was calibrated with those events having  $E_{\text{VC}} \geq 0.2 \text{ GeV}$ . In Fig. 4.11a) the correlation of  $E_\gamma$  and  $E_{\text{etag}}$  is shown for those Bremsstrahlung events with  $E_{\text{VC}} \leq 0.2 \text{ GeV}$ . The stability of the calibration was checked by dividing the selected event sample into 7 subsamples. For each subsample a gaussian function

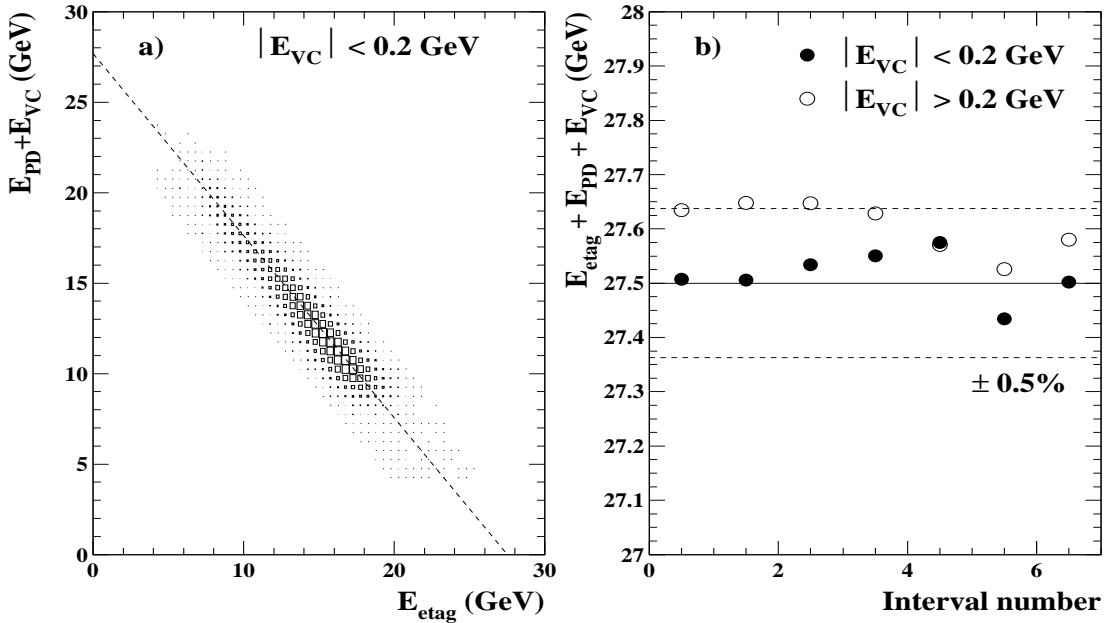


Figure 4.11: Correlation of the photon and electron energies for Bremsstrahlung events in a). The energy sum is expected to be 27.5 GeV. In b) the mean values of the energy sum is plotted for 7 different run intervals. The calibration is stable within  $\pm 0.5\%$ .

was iteratively fitted within  $\pm 2\sigma$  to the energy sum  $E_{\text{etag}} + E_\gamma$ . The resulting mean values of the fits are given in Fig. 4.11b), separately for the two event samples with and without energy deposit in the water Čerenkov counter. For both samples the calibration could be verified within 0.5%. The relative calibration of  $E_\gamma$  and  $E_{\text{etag}}$  is determined with a precision of 1.3% from studies of the  $E_\gamma$  and  $E_{\text{VC}}$  dependence of the mean  $E_\gamma + E_{\text{etag}}$ . Taking into account a maximum nonlinearity of 1.3% in the response of the photon arm the global energy scale is known with a precision of 1.5% for  $E_\gamma > 4$  GeV.

The precision of the kinematic variables reconstructed with the electron method is similar to that shown in Eqs.(4.5) and (4.6) except that, here, one has to take into account of an additional term  $\delta E_\gamma/E_\gamma$  and  $(1 - y_e)/y_e \delta E_\gamma/(E_e - E_\gamma)$  respectively for  $\delta Q_e^2/Q_e^2$  and  $\delta y_e/y_e$  arising from the energy resolution of the radiative photon. Therefore, as for non-radiative events,  $y_e$  degrades as  $y_e$  decreases. For this reason, the electron method is used only for  $y > 0.15$  and for lower  $y$ , the  $\Sigma$  method (Eqs.(2.16)-(2.18)) is used instead, which needs  $\Sigma_h$  in addition to  $\Sigma_e$  and  $P_{T,e}$ .

At lower  $y$ , the hadronic final state is measured by the LAr calorimeter. Its energy scale is controlled by checking the transverse momentum balance between  $P_{T,h}$  and  $P_{T,e}$ . A systematic uncertainty of 4% is obtained.

#### 4.4.5 Measurement of the structure function $F_2(x, Q^2)$

The analysis follows essentially the same method as used in the previous section. The only difference is that here, we measure the inclusive radiative cross section which is part of the QED radiative corrections to the usual DIS cross section. In the  $Q^2$  range of the present analysis, the effect of  $Z^0$  exchange is negligible and the double differential cross section for single virtual photon exchange in DIS, integrated over the solid angle within the acceptance of the photon detector  $\theta_\gamma < \theta_a \simeq 0.45$  mrad and from 0 to  $z_1 = 0.85$  corresponding to  $E_\gamma > 4$  GeV, is given by [122]

$$\frac{d^2\sigma}{dxdQ^2} = \int_0^{z_1} dz \frac{d^3\sigma}{dxdQ^2dz} \quad (4.22)$$

$$= \frac{\alpha^3}{xQ^4} \left[ 2(1-y) + \frac{y^2}{1+R} \right] F_2(x, Q^2)(1 + \delta_{ho}) \int_0^{z_1} dz P(z) \quad (4.23)$$

with

$$z = \frac{E_e^{\text{eff}}}{E_e} = \frac{E_e - E_\gamma}{E_e} \quad (4.24)$$

$$P(z) = \frac{1+z^2}{1-z} \ln \left( \frac{E_e^2 \theta_a^2}{m_e^2} \right) - \frac{2z}{1-z}$$

where  $R$ , defined in Eq.(3.8), is related to the longitudinal structure function,  $F_L$ . The higher order (ho) correction to the first order radiative contribution is given by  $\delta_{ho}$  (see Sec.4.4.6). In comparison with the usual DIS cross section, the radiative cross section to be measured here is thus suppressed by a factor of  $\frac{\alpha}{2\pi} \int_0^{z_1} dz P(z)$ .

#### Efficiencies and their uncertainties

The electron identification and most of the selection cuts described in Sec.4.4.2 are similar to the analysis on the sample dominated by non-radiative events. Their efficiencies have been studied with this high statistics sample and found to be well described by the Monte Carlo simulation [123, 119]. What are particular for this analysis are the trigger and vertex efficiencies. The trigger efficiency differs from the other analysis since a different cut on the minimum electron energy is applied (8 GeV versus 11 GeV). The hard radiation studied in this analysis also corresponds to a different event topology, on which the vertex efficiency strongly depends: a scattered electron at large polar angle beyond the acceptance of the central tracker in the backward direction is unlikely to contribute to the vertex reconstruction and similarly the efficiency also drops when the hadronic system goes very forward beyond the acceptance in the other direction<sup>10</sup>.

---

<sup>10</sup>The forward tracker can be and has been used for the vertex reconstruction, its efficiency is however worse than that of the central tracker due to the fact that the passive material in front

The events studied in this analysis are triggered by requiring a local energy deposit, or cluster of more than 4 GeV in the BEMC. The efficiency of this trigger was determined as function of the electron energy and the impact position with an independent data sample (dominated by non-radiative events) which were triggered with an independent tracker-related trigger.

During the 1994 data taking period the four inner triangle stacks in the BEMC did not contribute to the trigger for most of the time (“closed triangle” period). During the last weeks of data taking these modules were included in the trigger (“open triangle” period). It turned out that for the open triangle period the trigger efficiency did not depend on the impact position but on the electron energy only. For electrons with an energy of 8 GeV an efficiency of  $\simeq 80\%$  was found and from 11 GeV on it was found to be  $\simeq 100\%$ .

For the closed triangle period the trigger efficiency strongly depends on the impact position, as can be seen in Fig. 4.12. To ensure the trigger efficiency to be acceptably high an additional cut,  $\max\{|x_{\text{BPC}}|, |y_{\text{BPC}}|\} > 13.5 \text{ cm}$ , was applied for this period, as it is indicated in Fig. 4.12. In the region  $\max\{|x_{\text{BPC}}|, |y_{\text{BPC}}|\} > 17 \text{ cm}$  the trigger efficiency depended on the electron energy only, while in the region  $13.5 \text{ cm} < \max\{|x_{\text{BPC}}|, |y_{\text{BPC}}|\} < 17 \text{ cm}$  it was determined as function of the electron energy  $E'_e$  and  $\max\{|x_{\text{BPC}}|, |y_{\text{BPC}}|\}$ . More details on the trigger efficiencies are given in Refs.[124, 125].

The vertex inefficiency has two contributions: either there is no reconstructed vertex or there is a vertex but outside the vertex cut ( $\pm 35 \text{ cm}$ ). These contributions may be determined for radiative MC events in the following way:

$$\epsilon_{\exists z_{\text{vtx}}} = \frac{N(\text{all cuts except } |z_{\text{vtx}} - z_o| < 35 \text{ cm})}{N(\text{all cuts except } \exists z_{\text{vtx}} \text{ and } |z_{\text{vtx}} - z_o| < 35 \text{ cm})} \quad (4.25)$$

and

$$\epsilon_{|z_{\text{vtx}} - z_o| < 35 \text{ cm}} = \frac{N(\text{all cuts})}{N(\text{all cuts except } |z_{\text{vtx}} - z_o| < 35 \text{ cm})} \quad (4.26)$$

giving an overall value of respectively  $82.6 \pm 0.3\%$  and  $94.4 \pm 0.2\%$  for the selected radiative sample. Unfortunately this simple method when applied to the real data may bias the efficiency due to the residual background events contained in the denominators.

Alternative method exists [126], which is schematically shown in Fig.4.13. The vertex  $z_{\text{CIP}}$  is defined in this method as the crossing point between the  $z$  axis and a straight line formed with the impact point in the BPC and two CIP hits in coincidence in the  $r - z$  plane. This method deffers from the standard method in that  $z_{\text{vtx}}$  is still defined by charged particles from the hadronic final state when the electron track is inefficient in a DIS event or when there is no

---

of it is relatively more important and that the track density is higher because of the Lorentz boost in the proton beam direction.

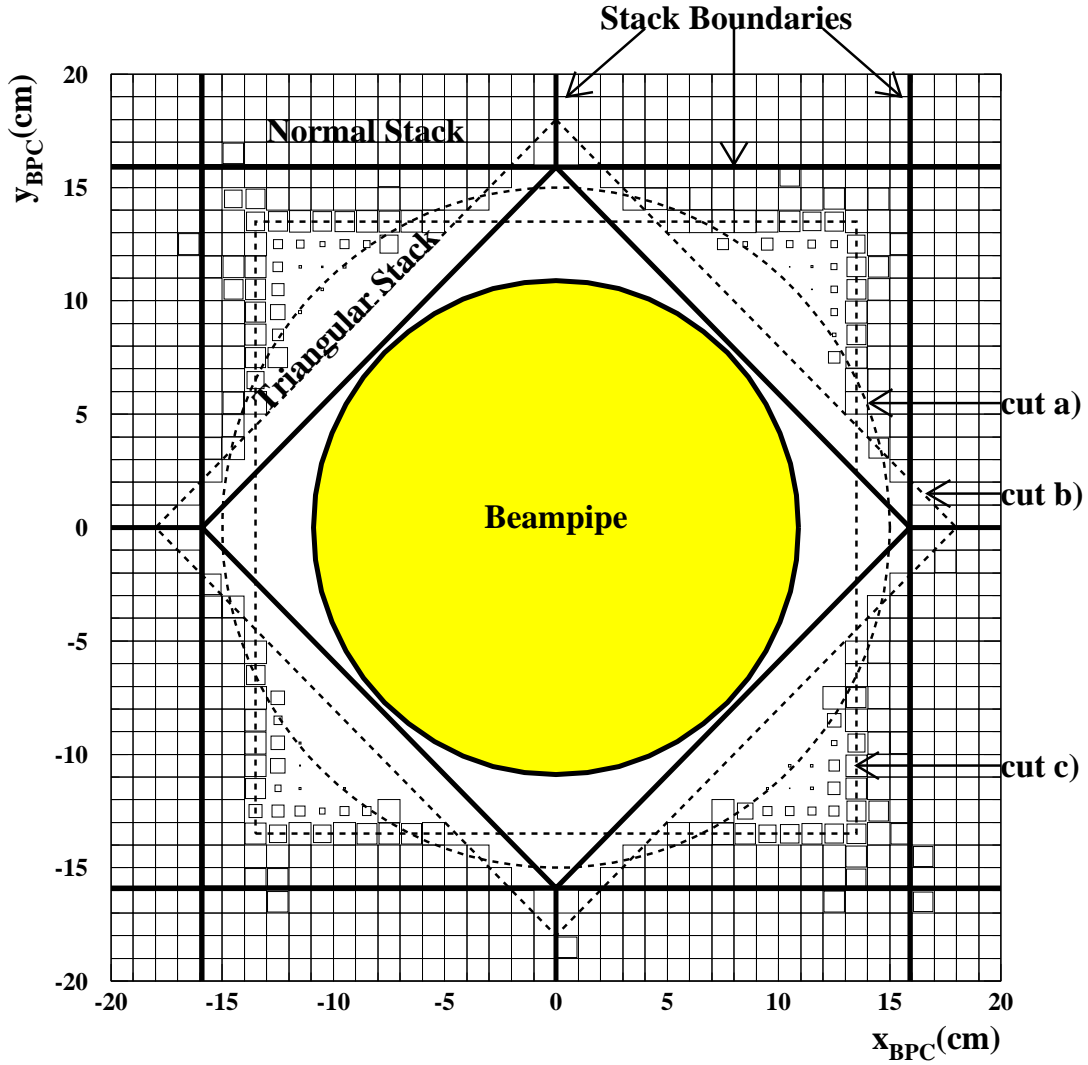


Figure 4.12: Trigger efficiency in the BEMC inner region as functions of the impact position  $(x_{\text{BPC}}, y_{\text{BPC}})$  for the closed triangle period. The efficiency is proportional to the box size with the full box size corresponding to 100%. The electron energy was required to be far above the trigger threshold to separate the spatial dependence of the trigger efficiency from the energy dependence. The cuts a) and b) are always applied, see Eqs.(4.19),(4.20). The cut c)  $\max\{|x_{\text{BPC}}|, |y_{\text{BPC}}|\} > 13.5 \text{ cm}$  was applied for the closed triangle period only to ensure a high trigger efficiency.

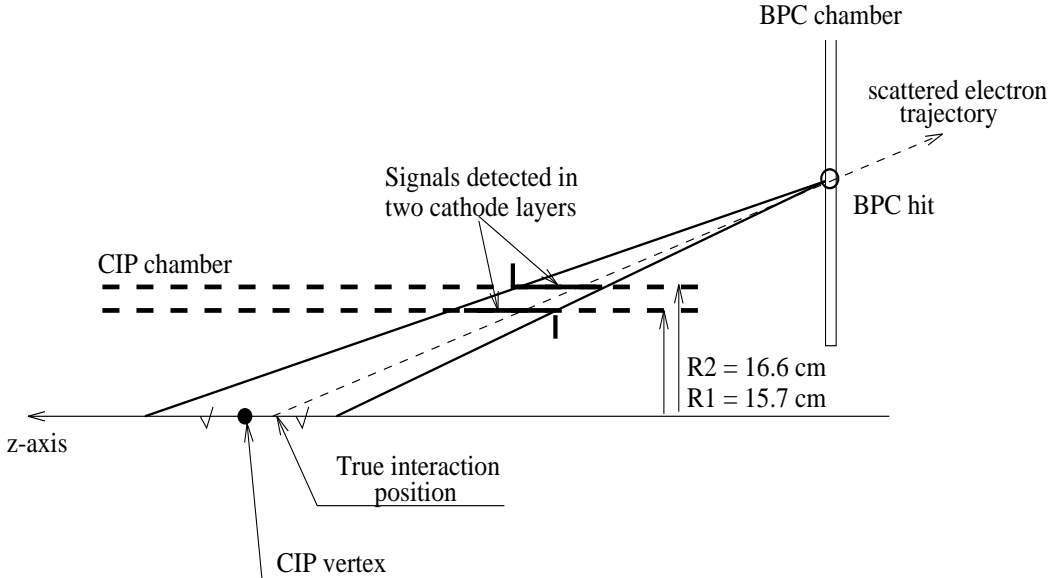


Figure 4.13: Schematic presentation of the CIP vertex definition, using the impact point in the BPC and two CIP hits in coincidence (figure taken from Ref.[119]).

such a track in a background event, while  $z_{\text{CIP}}$  can not be defined if there is no CIP hits associated the electron track. Therefore the CIP vertex is less sensitive to the photoproduction background. For DIS events it has been checked that a good correlation was obtained when both vertices were defined [124].

By applying the vertex cut using  $z_{\text{CIP}}$ , namely  $|z_{\text{CIP}} - z_o| < 35 \text{ cm}$  to both the numerators and the denominators in Eqs.(4.25) and (4.26), the vertex efficiencies are found to be consistent between the data and the MC. Globally, one has  $\epsilon_{\exists z_{\text{vtx}}} = 82.8 \pm 0.5\%$  and  $\epsilon_{|z_{\text{vtx}} - z_o| < 35 \text{ cm}} = 94.2 \pm 0.4\%$  in data to be compared with  $\epsilon_{\exists z_{\text{vtx}}} = 83.8 \pm 0.4\%$  and  $\epsilon_{|z_{\text{vtx}} - z_o| < 35 \text{ cm}} = 95.2 \pm 0.2\%$  in the MC. In principle, it is straightforward to compare the data and the MC more differentially, e.g. in terms of  $(x, Q^2)$  bins. However, due to the limited CIP geometrical acceptance, part of the sample in which the electrons scattered at large polar angles cannot be checked by this method. Here an improvement in the experimental apparatus is highly desirable. The installation of a backward silicon tracker certainly helps in this direction.

Selecting events only at the considered  $(x, Q^2)$  region, a difference shows up between the data and the MC when the efficiencies are plotted as a function of the hadronic invariant mass squared ( $W^2$ )<sup>11</sup> in Fig. 4.14. The difference is more

<sup>11</sup>We have chosen  $W^2$  on which the vertex efficiency depends in a similar way as it depends on the inclusive hadronic angle  $\theta_h$ . In fact, the smaller the  $W^2$  is, the more forward the hadronic

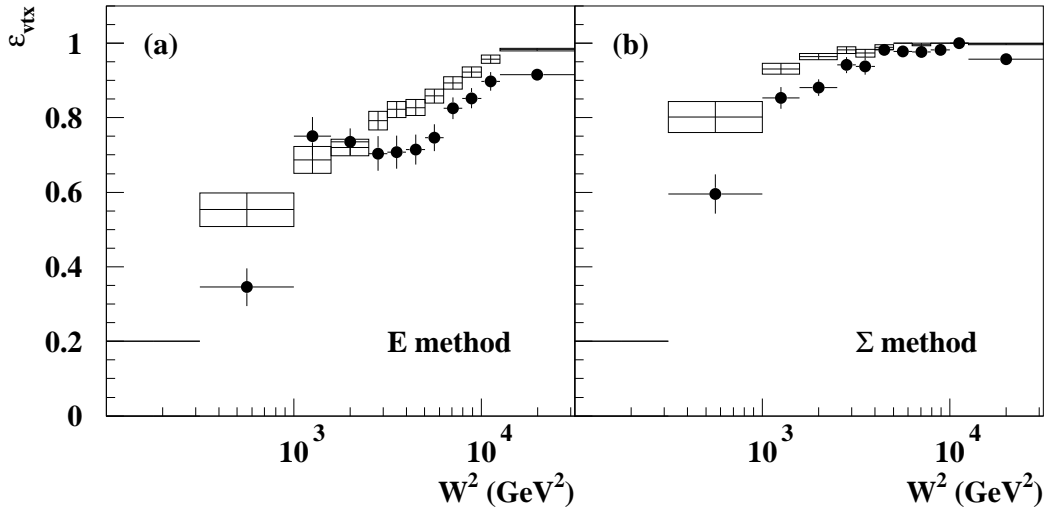


Figure 4.14: Vertex efficiency as a function of  $W^2$  for radiative DIS events within the considered  $(x, Q^2)$  bins in data(points) and in MC(open squares) for the  $E$ (a) and  $\Sigma$ (b) methods.

pronounced using the  $E$  method than using the  $\Sigma$  method. One explanation is that the former is more sensitive to higher order QED radiative contributions which are present in the data but are missing in the MC. If we assume that the difference between the data and the MC with the  $\Sigma$  method is entirely due to the vertex efficiency, then a correction of  $\sim 6\%$  is needed at low  $W^2$  values corresponding to low  $y$  values( $< 0.14$ )<sup>12</sup>. This correction has been applied for both  $E$  and  $\Sigma$  method in the low  $y$  region with a systematic error of 10% for the whole  $W^2$  region using the  $E$  method, and of 10% and 4% respectively for the low and high  $W^2$  values using the  $\Sigma$  method.

After having corrected for the trigger and vertex efficiency, data are compared in Fig. 4.15 with the MC for various relevant quantities used in the reconstruction of the kinematics. The MC events generated with the GRV parameterization have been reweighted according to Eq.(4.9) by a next-to-leading-order (NLO) fit<sup>13</sup> to the measured  $F_2$  for  $Q^2 > 5 \text{ GeV}^2$  based on the H1 non-radiative DIS events taken also in 1994 (see Sec.4.6.1). The data distributions are found to be fairly well described by the MC simulation.

---

system goes. The tracker covering the forward region has a smaller efficiency than the central tracker, see footnote 10.

<sup>12</sup>Using Eq.(3.58), the inelasticity  $y$  is related to  $W^2$  as  $y \simeq W^2/s^{\text{eff}}$ .

<sup>13</sup>More precisely, since the fit is done for  $Q^2 > 5 \text{ GeV}^2$ , so for lower  $Q^2$  values, it is in fact a backward extrapolation of the fit.

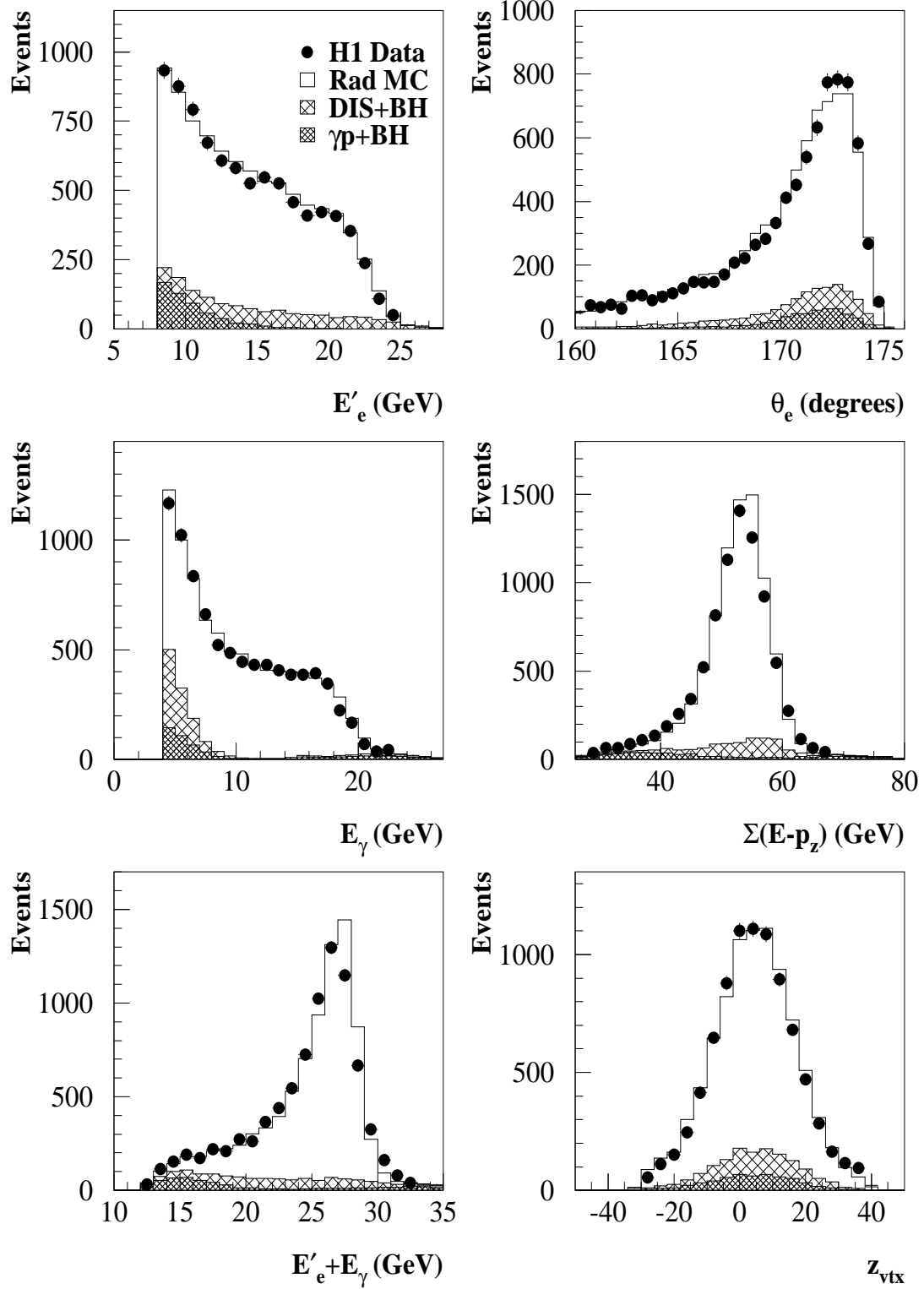


Figure 4.15: A comparison between data and MC for various quantities relevant for the kinematics reconstruction.

#### 4.4.6 Higher order QED correction

As shown in Eq.(4.23), we measure  $F_2(x, Q^2)$  using events with collinear hard photon radiation in first order. The measured inclusive cross section has thus to be corrected for higher order radiative contributions.

The effect of high order contributions, which is dominated by multiphoton emission collinear to the incident electron, is estimated with the event generator LESKO [127]:

$$1 + \delta_{ho} = \frac{\sigma^{YFS}}{\sigma^F} \quad (4.27)$$

where  $\sigma^F$  and  $\sigma^{YFS}$  are the two options of the LESKO program. The first option includes  $\mathcal{O}(\alpha)$  QED radiative corrections, and the second one describes multiphoton leptonic radiation in a framework of the Yennie-Frautschi-Suura exclusive exponentiation procedure [128]. The correction ( $\delta_{ho}$  in %) for the  $E$  method is shown with the upper number in each  $(x, Q^2)$  bin (separated with the dashed lines) in Fig. 4.16. The errors are statistical. The correction can be as large as

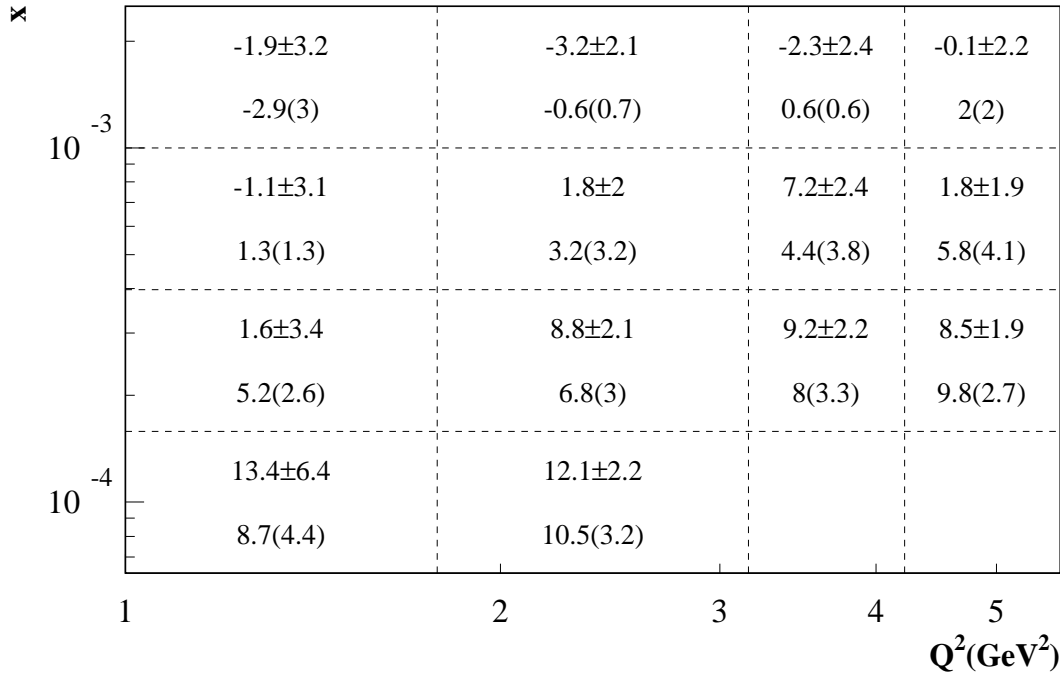


Figure 4.16: Higher order QED correction  $\delta_{ho}$  (in %) for the  $E$  method estimated with LESKO [127] (upper number, the error is statistical) and with an independent method based on HECTOR [129] (lower number). The numbers in brackets are the assigned systematics errors.

13% in the lowest  $x$  bins considered and becomes small for the high  $x$  (or low  $y$ ) region. The correction has been checked with an independent method [130]

in which the higher order effect was simulated using the HECTOR package [129] with the varying incident electron beam energy  $E_e^{\text{eff}} (= E_e - E_\gamma)$ ,  $E_\gamma$  being the energy spectrum of the radiated photon in first order). The results<sup>14</sup> are shown with the lower numbers in each bin in Fig. 4.16. Reasonable agreement is seen and occasional large differences are due either to an intrinsic cut on  $p_T > 1 \text{ GeV}$  in LESKO, which introduces some edge effect for the first  $Q^2$  bin at  $1.5 \text{ GeV}^2$ , or to a statistical fluctuation in LESKO, e.g. as a function of  $Q^2$  for the  $x$  bins in the second row from the top. Since both methods give comparable results and the latter one has less fluctuation, this latter correction was used with systematic uncertainties given with the numbers (in %) in brackets in Fig. 4.16. The correction for the  $\Sigma$  method is small ( $\lesssim 3\%$ ) and is rather uniform in the  $(x, Q^2)$  bins considered.

#### 4.4.7 $F_2$ results

The final proton structure function  $F_2$  combines the  $E$  method at high  $y$  ( $\gtrsim 0.15$ ) with the  $\Sigma$  method at the lower  $y$  region such that the measurable kinematic domain is significantly extended. The results of this analysis [131, 124] have been cross checked by an independent analysis [125]. The  $x$  dependence of  $F_2$  at four lowest  $Q^2$  values are shown in Fig. 4.17 and compared with the measured  $F_2$  from the other analyses using non-radiative events with the interaction point shifted in the proton beam direction by  $\sim 70 \text{ cm}$  (shifted vertex data), and the results of a similar analysis from the ZEUS collaboration [132]. The fixed-target experiment data from NMC [133] and a few parameterizations are also shown. Several observations can be made:

- This measurement has allowed to extend the HERA  $F_2$  measurement for  $Q^2$  down to  $1.5 \text{ GeV}^2$ . The rise of  $F_2$  with decreasing  $x$  observed in the previous HERA measurements for  $Q^2 \gtrsim 5 \text{ GeV}^2$  [87, 88, 107, 114] persists down to  $Q^2 = 1.5 \text{ GeV}^2$ . This extension to lower  $Q^2$  values is relative and remains true even after the angular acceptance of the BEMC is improved by the new backward calorimeter SPACAL. Indeed, when the same analysis technique was applied on the 1996 data collected with the SPACAL, the  $Q^2$  range has been further extended down to  $0.2 \text{ GeV}^2$  [134].
- This measurement has allowed to fill the gap between the HERA measurements at low  $x$  and that of fixed-target experiments at high  $x$ . In the common  $x$  region, the measurement is in good agreement with other measurements with a tendency to be slightly lower than e.g. those measured with a data sample ( $58 \text{ nb}^{-1}$ ) in which the interaction point was shifted to

---

<sup>14</sup>A cut on  $W^2 > 225 \text{ GeV}^2$  has been applied as higher order contributions at lower  $W^2$  values are unlikely to contribute according to Fig. 4.14 when a reconstructed vertex is required.

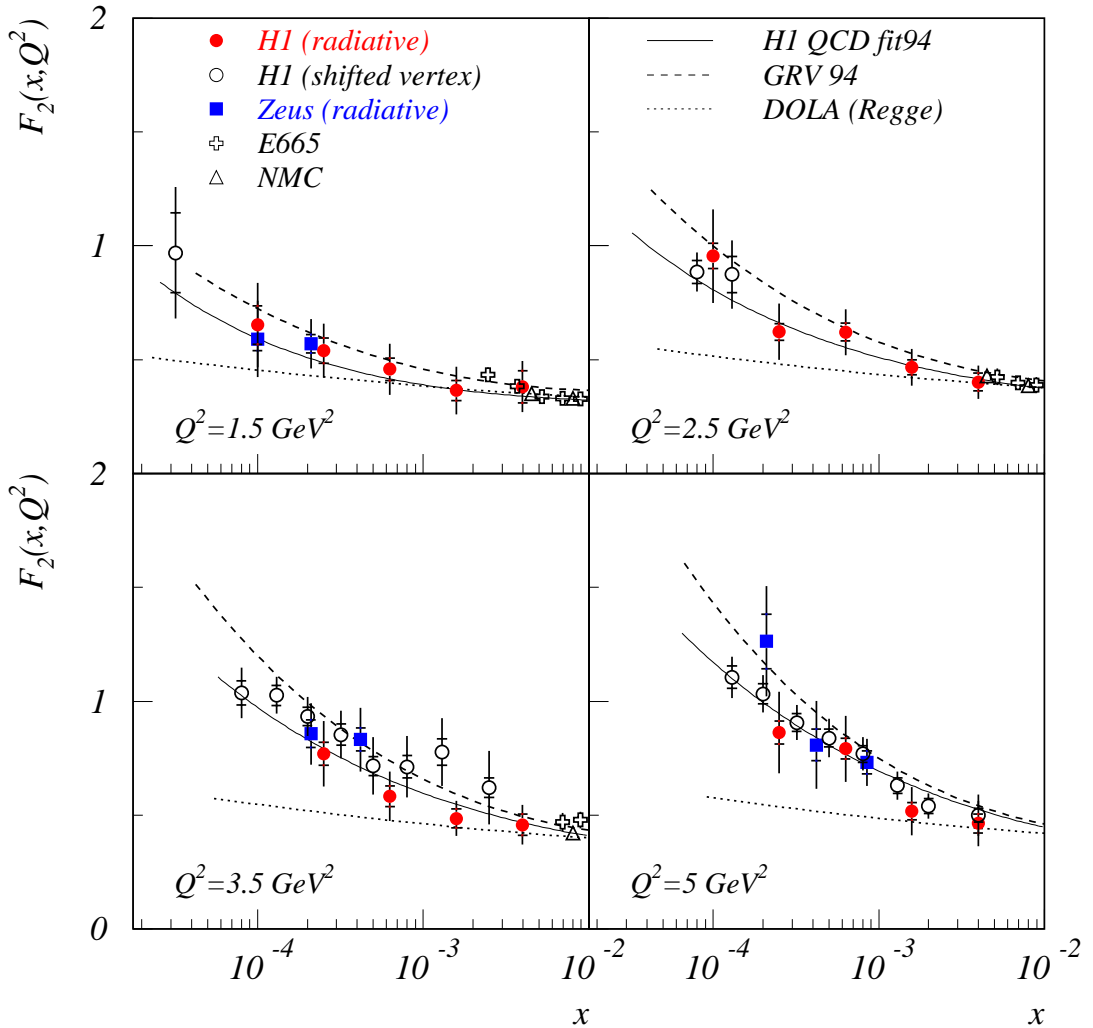


Figure 4.17: A comparison of the measured  $F_2(x, Q^2)$  from this analysis with other measurements from H1 (based on non-radiative DIS events with shifted vertex) [131], from ZEUS (based on radiative DIS events) [132], from E665 [23], and from NMC [22]; also shown is an extrapolation to low  $Q^2$  of the H1 QCD fit 94 [131] to the data at  $Q^2 \geq 5 \text{ GeV}^2$ , and two model predictions: GRV [76] and DOLA [80]. The inner error bars show the statistical errors only, while the outer ones represent statistical and systematic errors added in quadrature.

an averaged value of +67 cm with respect to the nominal interaction point in the proton beam direction (labeled “shifted vertex” in Fig.4.17). The shifted vertex data sample has a luminosity uncertainty of 3.5% which is independent of the uncertainty of 1.5% of this analysis.

- All measurements are compatible with the GRV [76] calculation except in the very low  $x$  region where the measurements seem to be (systematically) below the prediction.
- The parameterization DOLA [80], which is motivated by Regge theory and relates the structure function to Reggeon exchange phenomena, are seen to be ruled out by the measurement.
- The measurement agrees well with an extrapolation to low  $Q^2$  of a next-to-leading-order QCD fit [131], based on the H1 1994 data and fixed target data at  $Q^2 \geq 5 \text{ GeV}^2$ .

## 4.5 Precision measurement at HERA

With an increased data sample taken in 1996-1997, corresponding to an integrated luminosity of about  $20 \text{ pb}^{-1}$ , and the new backward apparatus, the H1 collaboration has recently published a precision measurement on the inclusive cross section and structure functions covering  $1.5 \leq Q^2 \leq 150 \text{ GeV}^2$  and  $3 \cdot 10^{-5} \leq x \leq 0.2$  [135]. The statistical accuracy of the measured cross section is better than 1% for a large part of the data. The systematic precision has reached 3% apart from the boundary of the covered region.

Contrary to the previous HERA measurements, the new measurements are presented in so-called reduced cross sections, which are related to the double differential cross sections defined in Eq.(3.9):<sup>15</sup>

$$\sigma_r = \tilde{\sigma} = \frac{Q^4 x}{2\pi\alpha^2 Y_+} \frac{d^2\sigma}{dxdQ^2} = F_2(x, Q^2) - \frac{y^2}{Y_+} F_L(x, Q^2) \quad (4.28)$$

with  $Y_+ = 1 + (1 - y)^2$  being the helicity function. Thus the dominant  $Q^2$  dependence in the double differential cross section due to the propagator of one photon exchange is explicitly suppressed in the reduced cross sections so that in most of the kinematic region the relation  $\sigma_r = F_2$  holds to good approximation. The only exception occurs at high  $y$ , where  $\sigma_r$  can be substantially different from  $F_2$  due to the sizable contribution from the longitudinal structure function  $F_L$ .

The reduced cross sections are shown in Fig.4.18 together with the  $\mu p$  data by the NMC [133] and BCDMS [21] experiments, and a new H1 NLO QCD fit to the new low  $Q^2$  data and the published  $e^+p$  high  $Q^2$  data taken in 1994-1997 [94] (Sec.5.2), for  $3.5 \leq Q^2 \leq 3000 \text{ GeV}^2$ . The cross section rises at low  $x$ . This rise is observed to be damped at the smallest values of  $x$  which is attributed to  $F_L$ , see Sec.4.7.

The data at  $Q^2 < 3.5 \text{ GeV}^2$  seem to overshoot the backward extrapolation of the QCD fit. A fit with  $Q_{\min}^2 = 1.5 \text{ GeV}^2$ , however, describes the low  $x$  data well. Theoretically one expects higher order logarithmic and power corrections to be larger for  $Q^2 \simeq 1 \text{ GeV}^2$  such that a NLO DGLAP treatment may be inadequate. Further exploration of this interesting effect requires low  $x$ , high precision data at low  $Q^2 \simeq 1 \text{ GeV}^2$ .

The proton structure function  $F_2(x, Q^2)$  can be extracted from the reduced cross sections by applying a (small) correction for the  $F_L$  contribution in Eq.(4.28). The resulting  $F_2$  is shown as a function of  $Q^2$  in Fig.4.19. Also shown are the structure functions obtained from H1 at high  $Q^2 (\geq 200 \text{ GeV}^2)$  and from the fixed-target data by SLAC [39], NMC [133], and BCDMS [21] at low  $Q^2$  and high  $x$ . To extract the  $F_2(x, Q^2)$  from the inclusive cross sections measured with

---

<sup>15</sup>In the considered kinematic region, the  $\gamma Z^0$  interference and  $Z^0$  exchange contributions can be safely neglected.

### H1 96-97

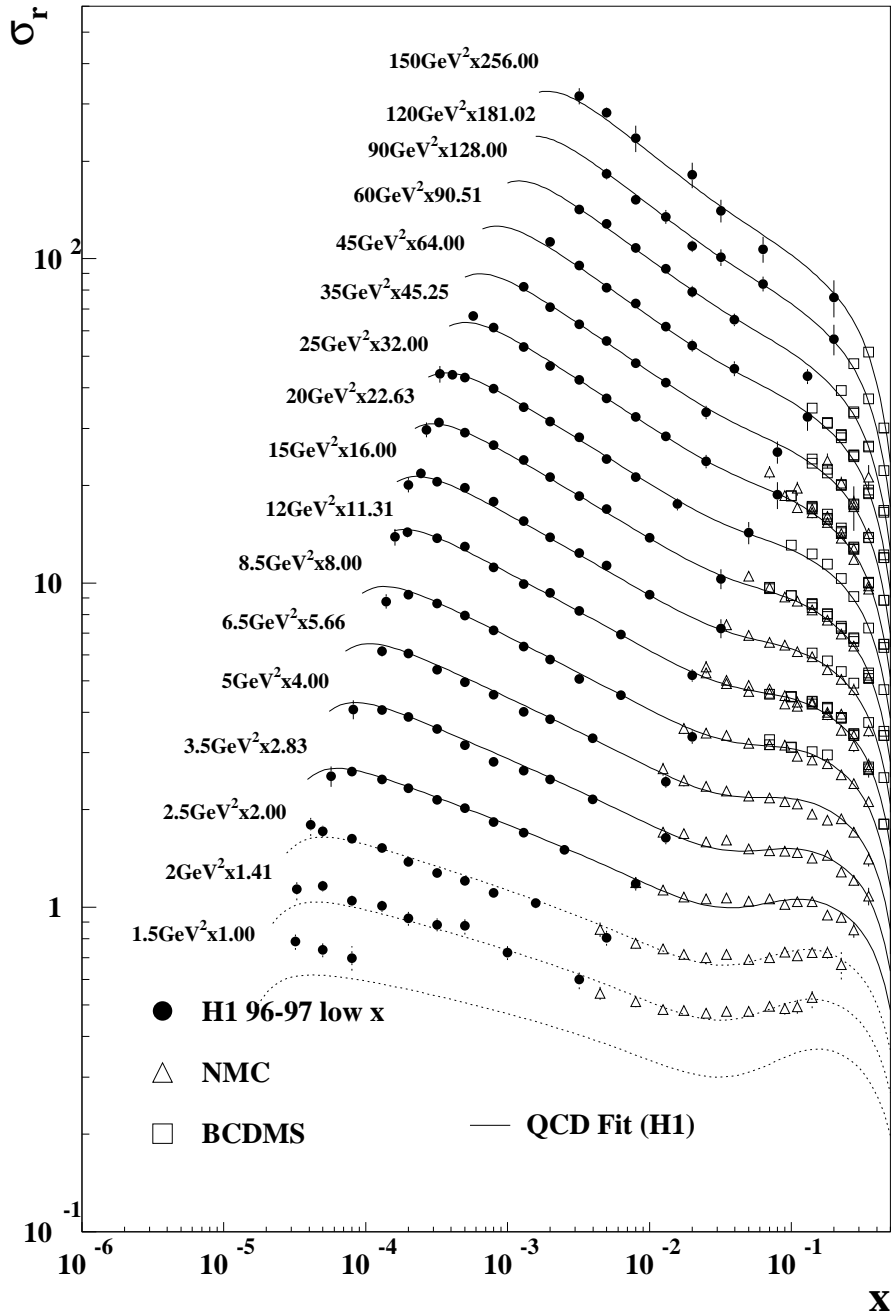


Figure 4.18: The precision measurement of the inclusive reduced cross sections from H1 [135] in comparison with the measurements from NMC [133] and BCDMS [21]. The full curves represent the corresponding theoretical expectation based on a NLO QCD fit to the H1 low  $Q^2$  data and the published high  $Q^2$  data taken in 1994-1997 [94] for  $3.5 \leq Q^2 \leq 3000 \text{ GeV}^2$ . The dashed curves show the extrapolation of the fit towards lower  $Q^2$ .

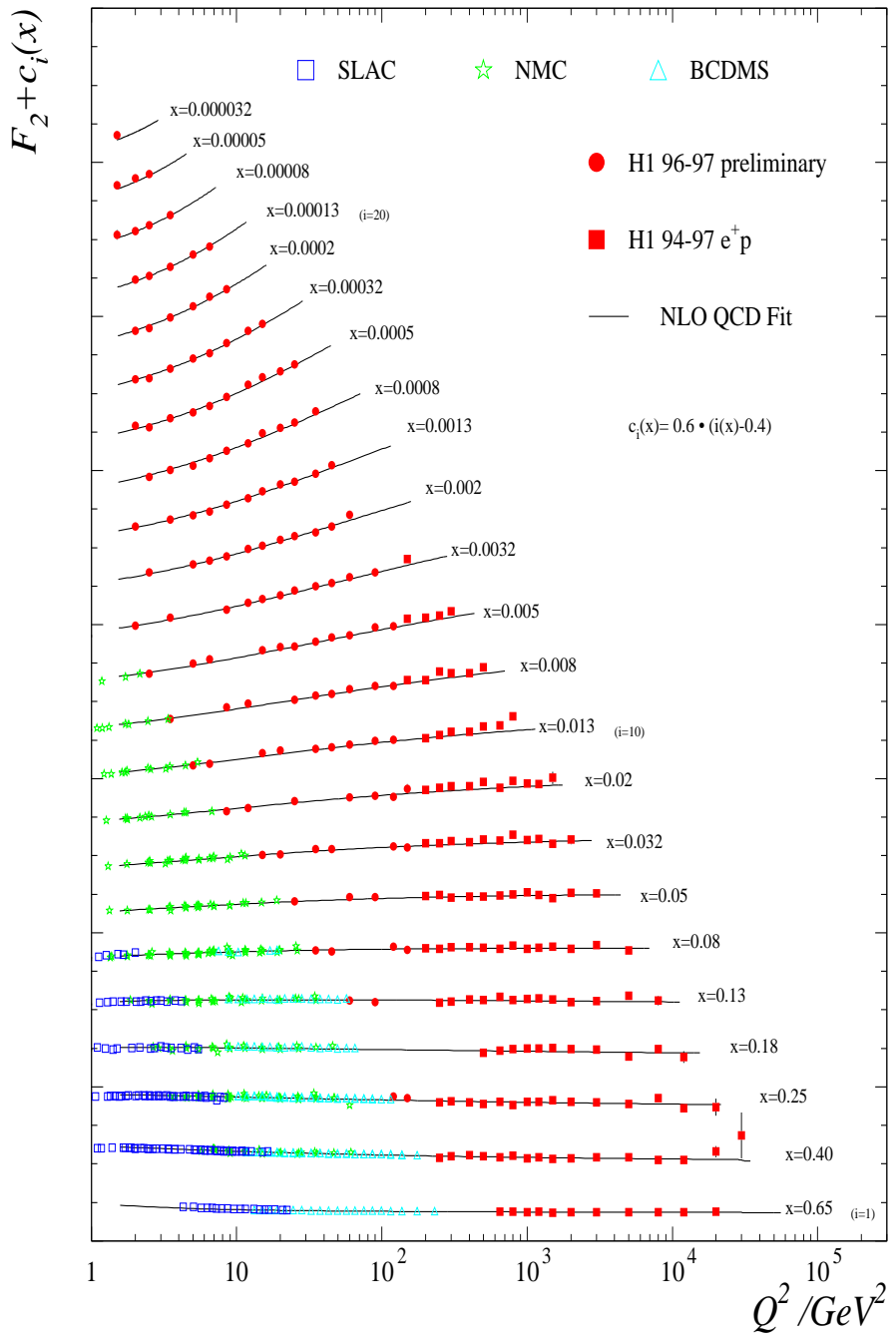


Figure 4.19: A compilation of the proton structure function  $F_2(x, Q^2)$  from the 1996-1997  $H1 e^+p$  data at low  $Q^2$  ( $\leq 150 \text{ GeV}^2$ ) and low  $x$  [135], from the 1994-1997  $H1 e^+p$  data at high  $Q^2$  ( $\geq 200 \text{ GeV}^2$ ) [94] (Sec.5.2), and from the fixed-target data by SLAC [39], NMC [133], and BCDMS [21]. The  $F_2$  values are plotted in linear scale adding a constant  $c(x) = 0.6(i - 0.4)$  where  $i$  is the  $x$  bin number starting at  $i = 1$  from  $x = 0.65$ . The full lines correspond to the NLO QCD fit [135].

the 1994-1997 H1  $e^+p$  data at high  $Q^2$  [94] (Sec.5.2), the increasingly important contributions from the  $\gamma Z^0$  interference and  $Z^0$  exchange have been subtracted.

The H1 NLO QCD fit, based on the H1 data alone, provides a good overall description to all data with a few exceptions at kinematic boundaries. The strong scaling violation is clearly displayed. It is this data feature and the precision of the data which allows the strong coupling constant  $\alpha_s$  and various parton density distributions in particular the gluon distribution to be determined within the QCD framework (Secs.4.6, and 4.8).

## 4.6 Current knowledge of the gluon density

### 4.6.1 Impact of the HERA $F_2$ data on the determination of the gluon density at low $x$

About half of the proton's momentum is carried by gluons. Despite this, the determination of the density of gluons  $g(x, Q^2)$  in the proton has turned out to be a difficult task. Before the advent of the HERA experiments, our knowledge on the gluon density distribution was very imprecise and limited to the region at  $x > 0.01$  [136, 137]. The principle difficulty in measuring the gluon density in deep inelastic scattering is that the gluons contribute only in high order processes through gluon bremsstrahlung from quarks and quark pair creation from gluons (Fig.3.3). At small  $x (< 10^{-2})$  the latter process dominates the scaling violation [47]. The HERA data on the proton structure function  $F_2(x, Q^2)$  at low values of  $x$  down to  $10^{-4}$  can thus be exploited to extract the gluon density in the kinematic range.

Indeed, already with the first  $F_2$  measurement in 1992, an extraction has been performed by H1 [138] and ZEUS [139] using the following approximation relation under the assumption that the quark contribution at low  $x$  is negligible [140]

$$xg(x, Q^2) \approx \frac{27\pi}{20\alpha_s(Q^2)} \frac{dF_2(x/2, Q^2)}{d \ln Q^2}. \quad (4.29)$$

It was derived that the gluon density rises strongly toward low  $x$ .

With the improved  $F_2$  measurement in 1993, both H1 and ZEUS have performed for the first time NLO QCD fits to  $F_2$  in a similar manner as in the global analyses by the MRS and CTEQ groups (Sec.3.3). The emphasis is however different. While in a global analysis, universal parton density functions are extracted, the analyses by the experimental collaborations emphasize the determination of the gluon density at low  $x$ . The result of the fit to  $F_2$  is also used to have a better parameterization of the cross section or the structure function than the initial one used in the Monte Carlo generation. For this reason, only a minimum number of data sets have been used in the analyses; in addition to the HERA  $F_2$  data at low  $x$ , a few data sets at high  $x$  from fixed-target experiments (e.g. BCDMS and NMC) were used. This is in contrast with the global analyses where in addition to the structure function data, other constraints from inclusive jet (and/or dijet) cross sections and the prompt photon data have also been used as illustrated in Fig.4.20.

The gluon density for  $Q^2 = 20 \text{ GeV}^2$  obtained by H1 [113] with the 1993 data is shown in Fig.4.21(a) in comparison with the result of ZEUS [141] and other determinations from the global analyses. The early parameterization MRS D0', which did not use HERA data, is clearly disfavored by the data as we have seen in

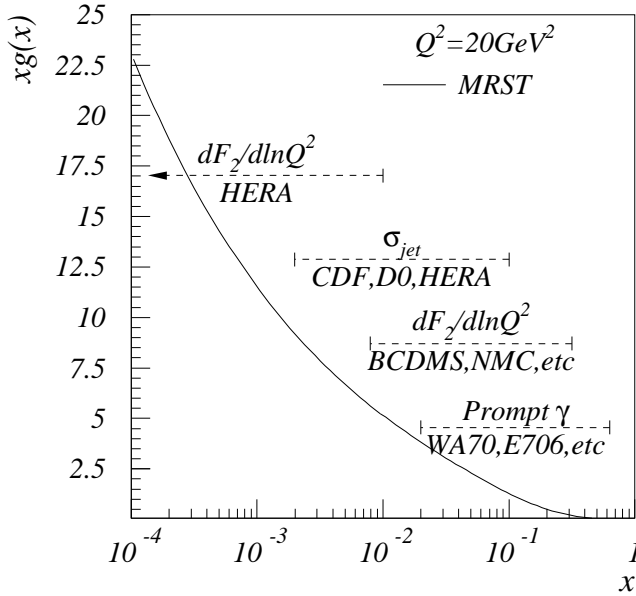


Figure 4.20: Various experimental measurements used by global QCD analyses to constrain the gluon density  $xg$  at different  $x$  range. The resulting  $xg$  from the MRST group [58] at  $Q^2 = 20 \text{ GeV}^2$  is shown with the curve. The ranges in  $x$  for the various measurements are only indicative since they are  $Q^2$  dependent. For instance, the HERA data reach to much large  $x$  values than indicated at higher  $Q^2$  though the statistical precision of the data there is still limited.

Fig.4.2. The other parameterizations which used the HERA  $F_2$  data are in good agreement with the results of H1 and ZEUS. The error band represents the experimental errors with the statistical and systematic errors added in quadrature. The experimental collaborations have the advantage of knowing the correlations between their systematic errors so that they could be properly treated [144]. As the integrated luminosity increases, the accuracy of the gluon density is further reduced by H1 (Fig.4.21(b)) using their 1994  $F_2$  data [131] and by ZEUS (Fig.4.21(c)) using both 1994 and 1995 data [143]. The most precise determination from H1 is shown in Fig.4.21(d). It is a result of a NLO DGLAP QCD fit to the recent H1  $ep$  cross section data (sec.4.5) and the BCDMS  $\mu p$  data. An experimental precision (the inner error band) of 3% at  $x \simeq 10^{-3}$  and  $Q^2 = 20 \text{ GeV}^2$  has been reached for the first time. The gluon distribution has been obtained together with the strong coupling constant  $\alpha_s$  (Sec.4.8). The effect of the uncertainty of the latter is shown with the middle error band. The outer error bands represent the uncertainties related to the QCD model and data range. For the first time, the gluon distribution has been determined with the H1 inclusive data only. Both determinations are in good agreement.

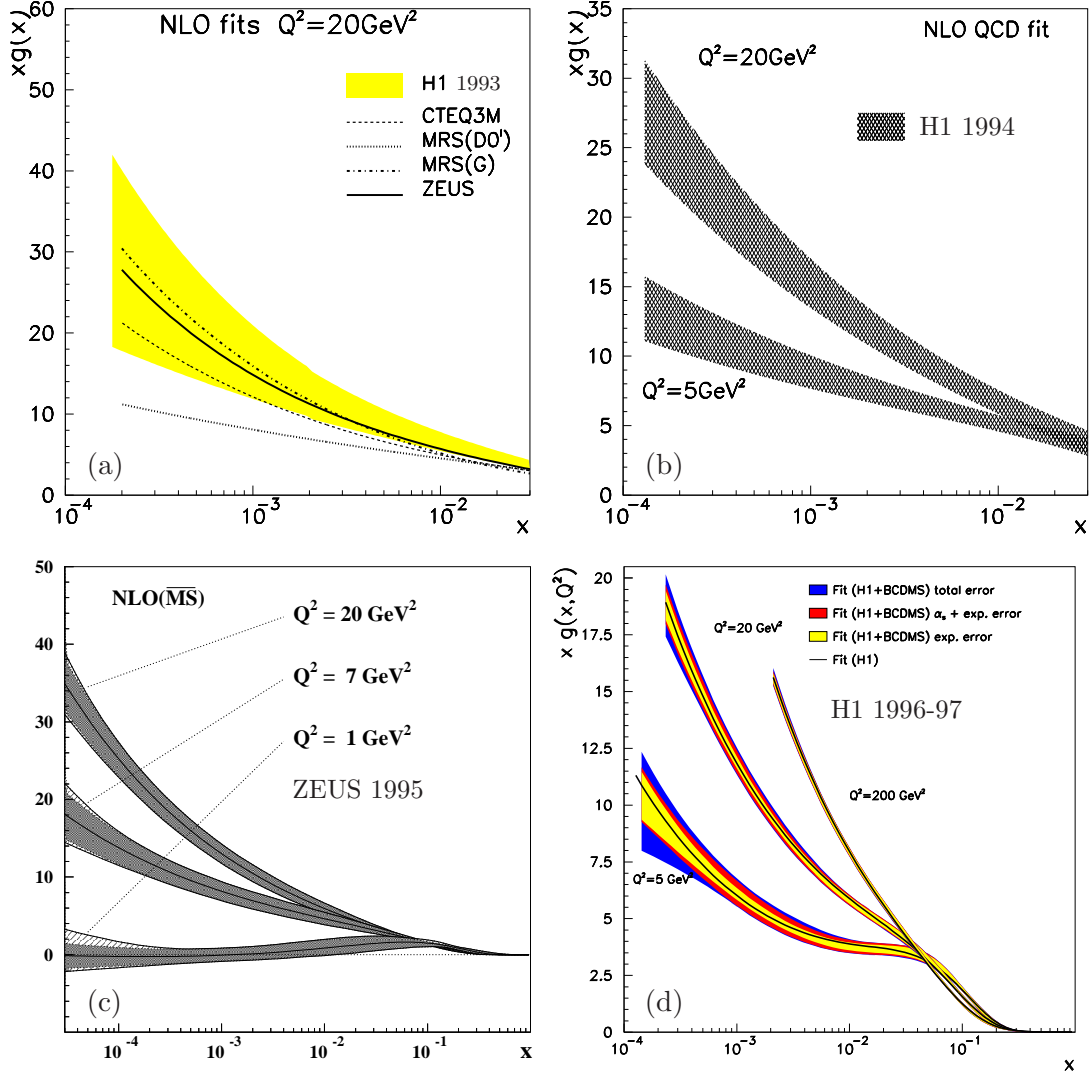


Figure 4.21: The time evolution of the determination of the gluon density  $xg(x)$  at HERA (a) the H1 result in 1993 [113] compared with the ZEUS result [141] and parameterizations CTEQ 3M [142], MRS( $D0'$ ) and MRS( $G$ ), (b) the H1 result in 1994 [131] and (c) the ZEUS result based on their 1994 and 1995 data [143], and (d) the most recent one from H1 using data taken in 1996-1997.

### 4.6.2 Uncertainty and future improvements

For a wide range of theoretical and experimental applications, it is important to know the range of uncertainties of the parton density functions. However the task of deriving a reliable uncertainty is extremely complex and difficult. The difficulty is related to many sources of uncertainty to be considered, to name a few:

- The choice of experimental measurements and data sets. As an example, the gluon density  $xg(x)$  at  $Q^2 = 25 \text{ GeV}^2$  from the most recent parameterizations MRST [58] and CTEQ5 [69] is compared in Fig.4.22. Both groups

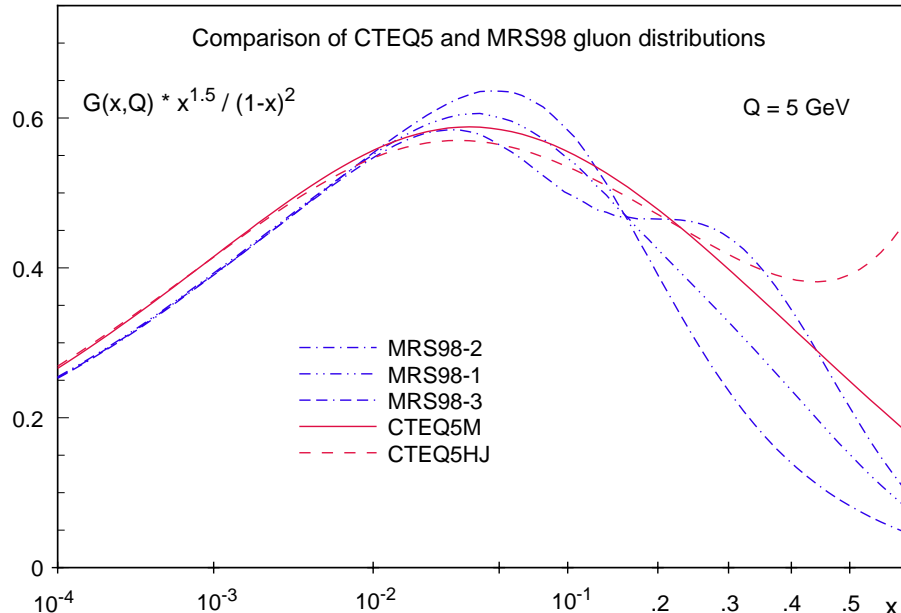


Figure 4.22: Comparison of the gluon density functions from MRST [58] (the parameterizations MRS98-1,2,3 correspond respectively to the standard, high-gluon and low-gluon options) with those from CTEQ5 [69] (the parameterizations CTEQ5M and CTEQ5HJ are respectively the standard and large-gluon options, the latter one being tailored to accommodate the Tevatron inclusive jet data, the high  $p_t$  tail of which was in excess with respect to the prediction based on previous parton density parameterizations). The figure is from Fig.19 of [69].

have used the HERA  $F_2$  measurements based on the data recorded in 1995 and before, which were the only available constraint at low  $x$  (see Fig.4.20). Consequently, there is little difference at low  $x$ . On the other hand, the difference is much larger at medium and large  $x$ ,<sup>16</sup> where in addition to

---

<sup>16</sup>The difficulty stems also from the fact that the gluon density becomes very small towards large  $x$  (Fig.4.21)

the DIS structure function data from fixed-target experiments, the prompt photon data from WA70 [145] and E706 [146] were used in the analysis of MRST, while the inclusive jet data from CDF [147] and D0 [148] were used instead in the analysis of CTEQ5.

- The experimental errors. The most precise structure function data are dominated by the systematic errors. The non-trivial part of these are the correlated systematic errors, which are not always available for the global analyses.
- The technical uncertainties due to the freedom in choosing the initial scale  $Q_0^2$  and the functional form at  $Q_0^2$  with varying number of free parameters, and the internal correlation among different parton density functions and between different  $x$  range.
- The theoretical uncertainties due to effects such as the higher-order corrections, scale- and scheme-dependence, soft-gluon resummation, higher-twist effects, and nuclear (deuteron) corrections.
- The evolution uncertainty related to the values of the strong coupling constant  $\alpha_s$  and the strategies applied. The determination of  $xg(x, Q^2)$  is strongly coupled with  $\alpha_s$ . One strategy is to determine  $\alpha_s$ , gluon and quark density functions together, an alternative is to take  $\alpha_s$  and its uncertainty from other independent measurements.

These uncertainties are often internally correlated. However one thing is clear, namely in order to reduce the uncertainties, both experimental and theoretical efforts are needed. On the experimental side, more precise data will directly reduce the experimental uncertainty. The precise data in an extended kinematical range also verify whether the chosen functional form is adequate within the conventional theoretical framework and test the validity of the latter. On the theoretical side, one of the most urgent tasks is to have a better understanding of the comparison between the measured prompt photon data (E706) with the QCD prediction so that the uncertainty of  $xg(x, Q^2)$  at large  $x$  can be reduced.

More independent (direct) measurements are highly desirable to either provide more constraints or check whether new physics phenomena have been artificially absorbed into the chosen functional form. As far as the gluon density is concerned, several measurements could be used either as testing ground or as a source of new constraints.

One such measurement is the open charm production at HERA. The production of the charm quark at HERA proceeds in perturbative QCD almost exclusively via photon-gluon fusion, where the exchanged photon interacts with a gluon in the proton by forming a quark-antiquark pair ( $\gamma g \rightarrow c\bar{c}$ , Fig.3.5). This holds both for DIS and for photoproduction where the exchanged photon is quasi

real. Based on the data collected from 1994 to 1996, the H1 measurement [149] is shown in Fig.4.23. The determination of the gluon density is in good agreement

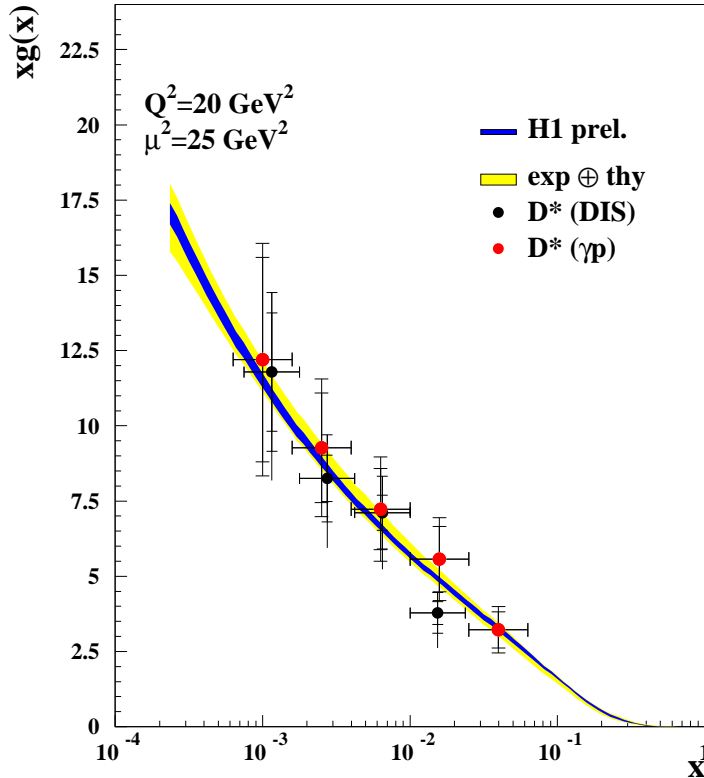


Figure 4.23: The gluon density at  $\mu^2 = 25 \text{ GeV}^2$  determined from the open charm data collected by H1 in 1994-1996 [149] compared with the preliminary gluon density at  $Q^2 = 20 \text{ GeV}^2$  based on the indirect scaling violation data 1996-1997.

with the other determinations described above. The errors were however still too large to be competitive with the other determinations. Both high luminosity at HERA and improved experimental setups (e.g. use of silicon vertex detectors) will allow considerable improvements in the future.

Inelastic  $J/\psi$  photoproduction at HERA has been suggested as a measurement which could allow one to measure the gluon density. However it appears that the perturbative calculation does not behave well in the limit  $p_T(J/\psi) \rightarrow 0$ , and if the small  $p_T$  region is excluded from the analysis the predictions are not very sensitive to the small  $x$  behavior of the gluon. Elastic (diffractive)  $J/\psi$  production in DIS and in photoproduction is more promising, since the cross section depends on  $(xg(x, \bar{Q}^2))^2$ , where the scale of the process is given by  $\bar{Q}^2 = (Q^2 + M_{J/\psi}^2)/4$  with  $Q^2$  and  $M_{J/\psi}$  being respectively the virtuality of the photon and the rest mass of the  $J/\psi$  [150]. These data could give information on the gluon distribution in the region  $10^{-4} < x < 10^{-2}$ . At the present time the theoretical

framework for extracting the gluon distribution from these measurements is still under development and the experimental precision of the data is still fairly low.

From Eq.(3.39), one sees that the longitudinal structure function  $F_L$  receives a direct contribution from the gluon, which dominates at low  $x$ . Under certain conditions, a measurement of  $F_L$  is almost a direct determination of the gluon. Therefore it is important to measure the longitudinal structure function at HERA. This will be the subject of the next section.

## 4.7 Longitudinal structure function $F_L(x, Q^2)$

The longitudinal structure function is an important quantity to measure. The earlier results on the smallness of  $R$  supported the assignment of half-integer spin for the quarks. A precise measurement allows an independent check of the gluon density derived from the indirect scaling violation of the structure functions. The knowledge of  $F_L$  is also needed to extract in a model independent way the structure function  $F_2$  from the measured cross section.

### 4.7.1 Current knowledge of $F_L(x, Q^2)$

Using Eqs.(3.4)-(3.8) and neglecting the target mass term, the differential cross section for one-photon exchange given in Eq.(3.3) can be rewritten in terms of  $R$  and  $\sigma_T$  as<sup>17</sup>

$$\frac{d^2\sigma(x, Q^2)}{dxdQ^2} = \frac{\alpha}{2\pi x Q^2} Y_+ [1 + \varepsilon R(x, Q^2)] \sigma_T(x, Q^2), \quad (4.30)$$

where  $Y_+ = 1 + (1 - y)^2$ ,  $R = \sigma_L/\sigma_R$ , and

$$\varepsilon = \frac{2(1 - y)}{Y_+}, \quad (4.31)$$

is the polarization of the virtual photon exchanged in the process. Therefore for measuring  $R$  at a given  $(x, Q^2)$  point, it is necessary to vary  $\varepsilon$ , i.e.  $y$  or the center-of-mass energy squared  $s$  because  $y$  is related to  $s$  as

$$y = \frac{Q^2}{xs}. \quad (4.32)$$

The difficulty in measuring  $R$  or the longitudinal structure function  $F_L$  is then directly related to a good control of the relative normalization and systematic errors at two different energies. This explains why measurements of  $F_L(x, Q^2)$  are so delicate, and why only a few fixed-target results have been published.

The most extensive results from early fixed-target experiments were obtained by BCDMS [21], and SLAC who has reanalyzed the data [152], covering respectively the kinematic range  $0.07 \leq x \leq 0.65$ ,  $15 \leq Q^2 \leq 50 \text{ GeV}^2$  by BCDMS and  $0.01 \leq x \leq 0.9$ ,  $0.6 \leq Q^2 \leq 20 \text{ GeV}^2$  by SLAC. The data lie in a region where non-perturbative effects are likely to be important. Most recently  $R$  has been measured by a new SLAC experiment E140X [153], by CCFR [154] and NMC [22], the latter reached a lowest  $x$  value at 0.002, which is still one or two orders of magnitude larger than the relevant kinematic region at HERA.

---

<sup>17</sup>In writing Eq.(4.30), we have used the Hard convention [151]  $K = \nu = Q^2/(2xM)$  for the flux of the virtual photon in analogy to the real photon.

At HERA, as the integrated luminosity increases, the latest cross section data become precise enough to see the sensitivity to  $F_L$  at the high  $y$  region (see Fig.4.18). Two methods have been used to extract  $F_L(x, Q^2)$  by H1. This first method [155], used for  $Q^2 > 10 \text{ GeV}^2$ , assumes that the dominant contribution to the cross section from  $F_2$  can be described by perturbative QCD by an evolution from lower  $Q^2$  at low  $y < 0.35$ , where the contribution of  $F_L$  to the cross section is small. The second method [135], applied for  $Q^2 < 10 \text{ GeV}^2$ , is derived from the cross section derivative

$$\frac{\partial \sigma_r}{\partial \ln y} = \frac{\partial F_2}{\partial \ln y} - F_L 2y^2 \frac{2-y}{Y_+^2} - \frac{\partial F_L}{\partial \ln y} \frac{y^2}{Y_+} \quad (4.33)$$

taken at fixed  $Q^2$  for  $y = Q^2/sx$ . At high  $y$  the second term dominates [135]. This is in contrast to the  $F_L$  influence on the reduced cross sections  $\sigma_r$ , where the contribution of  $F_2$  dominates for all  $y$ . A further important advantage of the derivative method is that it can be applied down to very low  $Q^2$  where the first method can no longer be applied as reliable assumptions on the QCD description of  $F_2$  are prohibited. The most recent extraction is shown in Fig.4.24 in comparison with the other direct measurements mentioned above. The extracted  $F_L$  is in good agreement with the expectation from the NLO QCD fit. It should be emphasized however that such an extraction does not represent a real measurement but a determination under specific assumptions.

#### 4.7.2 Feasibility study and a new method for a direct measurement of $F_L$ at HERA

A direct measurement can be achieved by running the collider with reduced beam energy [156], but this procedure has the obvious draw back that a significant running time is lost for high energy physics and that the collider is not operated in optimal conditions. For the  $F_L$  measurement itself, in addition to the relative normalization uncertainty mentioned above, a major experimental problem is the photoproduction background, when a hadron is wrongly taken as the electron candidate.

Another method proposed by Krasny et al. [157] makes use of the radiative events that we have discussed in Sec.4.4, namely those DIS events in which a real photon has been emitted in the direction of the incident electron beam, which corresponds to an effective decrease of the beam energy. The spectrum of measured photon energies induces, for given  $x$  and  $Q^2$  values, a continuous distribution of the  $y$ ,  $s$  and  $\varepsilon$  variables. The relations (4.31) and (4.32) stay the same, but the value of  $s$  changes from event to event, depending on the photon energy.

The advantages of this method are that it can be used in parallel with normal data taking, that it avoids luminosity normalization problems, and that the sta-

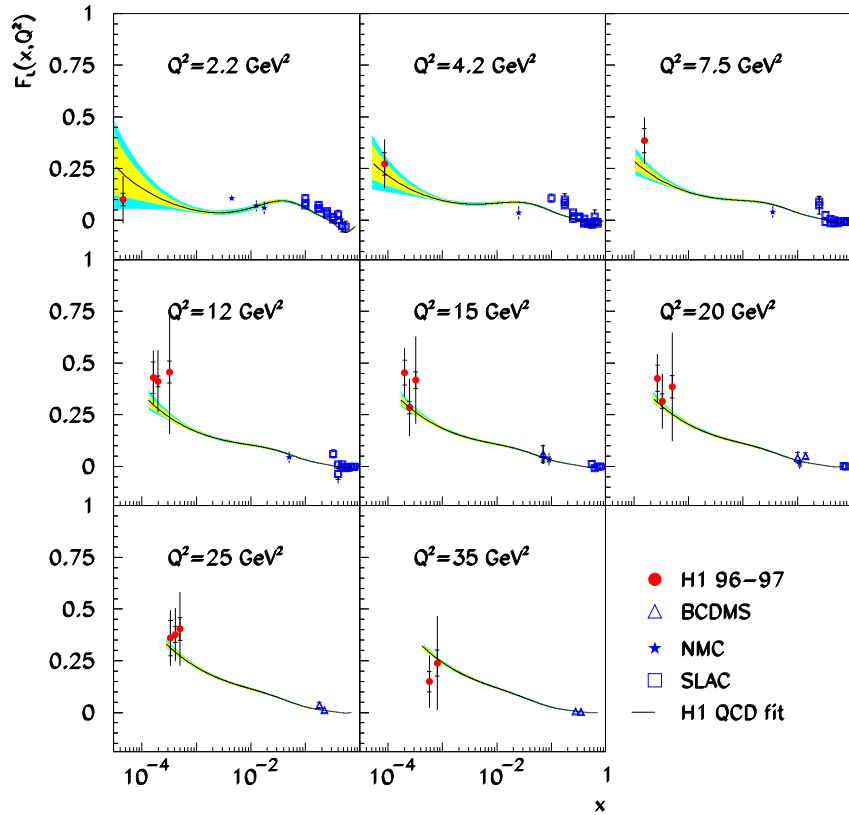


Figure 4.24: The extracted longitudinal structure function  $F_L(x, Q^2)$  by H1 [135] in comparison with the direct measurements by charged lepton-nucleon fixed-target experiments BCDMS [21], NMC [22], and SLAC [152]. The inner error bars denote the statistical error. The outer error bars represent the systematic and model errors. The curves and error bands show the NLO QCD fit to the recent H1 low  $Q^2$  data [135] and the high  $Q^2$  from 1994-1997 [94] for  $y < 0.35$  and  $Q^2 \geq 3.5 \text{ GeV}^2$ .

tical and systematic precisions increase continuously during data taking. As the basic principle of the  $R(x, Q^2)$  measurement is to perform a linear fit of cross section, Eq.(4.30), as a function of  $\varepsilon$ . The  $R(x, Q^2)$  is thus determined from the *slope* of the cross section. This procedure is independent of the knowledge of  $F_2$ , however, it requires a very large integrated luminosity (of the order of 200 pb $^{-1}$ ) to provide a significant measurement of  $R$  (with a statistical precision of 20% – 50%) [157].

In Ref.[158], a new method was proposed, in which we have considered to use the available measurements of  $F_2$  and to exploit the dependence on  $R$  of the *shape* of the  $\varepsilon$  distribution itself for radiative events. This is possible because the structure function  $F_2$  has been measured very precisely at HERA, and in view of the good understanding of DIS processes with initial state radiation as demonstrated by the H1 [131] (Sec.4.4) and ZEUS [132] analyses.

As an illustration, the  $\varepsilon$  distribution is presented in Fig.4.25 for  $R = 0$  (full line) and  $R = \infty$  (dashed line), for the full kinematic domain covered by the five bins in  $x$  and  $Q^2$  shown in Fig.4.26. Three bins are designed for value of  $Q^2$  around 2 GeV $^2$  (with  $x$  ranging from  $4 \cdot 10^{-5}$  to  $2 \cdot 10^{-4}$ ), and two bins for  $Q^2$  around 5 GeV $^2$  (with  $x$  ranging from  $10^{-4}$  to  $3 \cdot 10^{-4}$ ).

In Fig.4.27, the  $\varepsilon$  distributions are presented for each of these 5 bins. These distributions are obtained from a Monte Carlo simulation using the GRV [76] parameterization of the proton structure function  $F_2$ .

The simulated integrated luminosity corresponds to 10 pb $^{-1}$ , which is the luminosity expected from data at the time of the study. The electron and proton beam energy is respectively 27.5 GeV and 820 GeV. The following kinematical cuts are applied for the feasibility study:

$$\begin{aligned} E'_e &> 2 \text{ GeV}, \\ \theta_e &< 177^\circ, \\ E_\gamma &> 4 \text{ GeV}, \end{aligned} \quad (4.34)$$

where  $E'_e$  and  $\theta_e$  are the energy and the polar angle (defined with respect to the proton beam direction) of the scattered electron. As will be discussed later (see Fig.4.31), the sensitivity of the method depends significantly on the lowest energies  $E'_e$  which can be accepted. With the new H1 backward detectors, these are expected to be below 5 GeV and possibly as low as 2 GeV, the value thus chosen here.

The  $R$  dependence of the  $\varepsilon$  distribution can be studied using the variable  $\rho(R; \varepsilon_0)$ , defined as the ratio of the numbers of events with  $\varepsilon$  smaller or larger than a chosen value  $\varepsilon_0$ :

$$\rho(R; \varepsilon_0) = \frac{N(R; \varepsilon < \varepsilon_0)}{N(R; \varepsilon > \varepsilon_0)}. \quad (4.35)$$

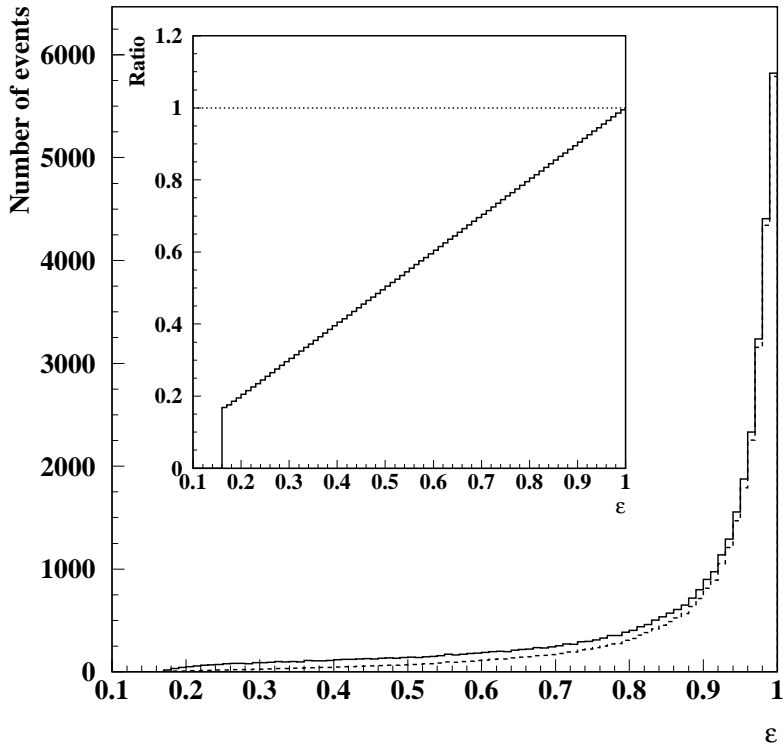


Figure 4.25: Distributions of the  $\varepsilon$  parameter of radiative events generated according to Eq.(4.34) using the GRV parameterization of the structure function  $F_2$  for  $R = 0$  (full line) and  $R = \infty$  (dashed line), and for the kinematic domain covered by the bins shown in Fig.4.26. The ratio of the two distributions is shown in the inset. The electron and proton beam energy is respectively 27.5 GeV and 820 GeV.

Fig.4.28 shows the  $\rho(R; \varepsilon_0)$  dependence on  $R$  in the selected  $(x, Q^2)$  bins, for the typical input value  $R = 0.5$  as obtained by H1 [155] in a first analysis using one of the methods mentioned in Sec.4.7.1. Since each bin covers a different  $\varepsilon$  range, the chosen optimal value  $\varepsilon_0$  is bin dependent. The dashed curves show the  $\rho(R)$  distribution for an input structure function  $F_2$  modified by  $\pm 10\%$  at  $x = 10^{-4}$ , the modification decreasing linearly to  $\pm 5\%$  at  $x = 10^{-2}$ . This corresponded to a conservative estimate of the uncertainty on  $F_2$  at the time of study. The uncertainty has been improved since. The grey bands correspond to the statistical precision of the  $\rho(R)$  measurement for an integrated luminosity of  $10 \text{ pb}^{-1}$ .

The measurement of  $R$  is deduced from the intersection of the grey bands with the spread of curves describing the  $\rho(R)$  dependence of the input structure function  $F_2$ . The inner error bars in Fig.4.29 show the statistical precision of the  $R$  measurement for the cuts (4.34), an integrated luminosity of  $10 \text{ pb}^{-1}$  and the quoted uncertainty on  $F_2$ .

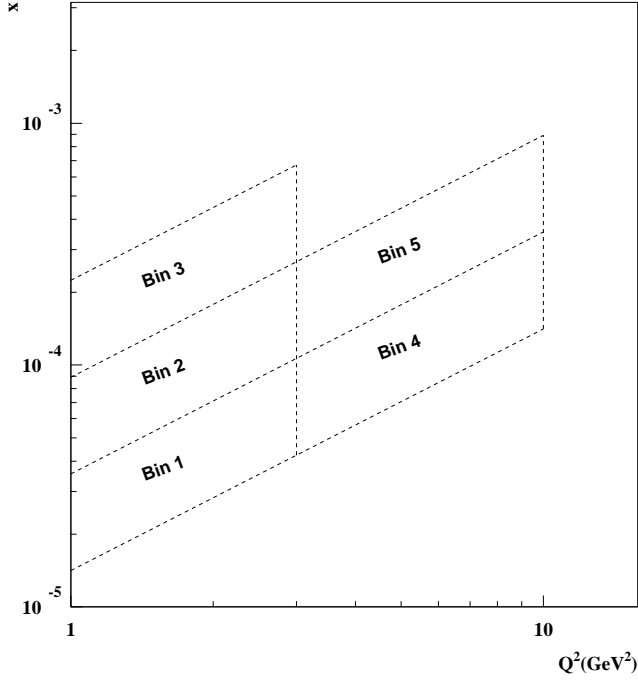


Figure 4.26: Selected  $(x, Q^2)$  bins.

To estimate the sensitivity of the proposed method to several experimental parameters, the variable  $\Sigma$  is defined as

$$\Sigma(\varepsilon_0, \mathcal{L}, F_2) = \frac{|\rho(R = 0; \varepsilon_0) - \rho(R = \infty; \varepsilon_0)|}{\sqrt{\sigma_{\rho, R=0}^2 + \sigma_{\rho, R=\infty}^2}} \quad (4.36)$$

for a given choice of  $\varepsilon_0$ , of the integrated luminosity  $\mathcal{L}$  and of the input structure function  $F_2$ ,  $\sigma_{\rho, R}$  being the statistical error on  $\rho(R)$ , estimated through the Monte Carlo simulation. This variable quantifies the possibility of distinguishing between the two extreme values of  $R$ :  $R = 0$  and  $R = \infty$ .

Fig.4.30 shows that the sensitivity  $\Sigma$  for each  $(x, Q^2)$  bin is only weakly dependent on the  $\varepsilon_0$  value over a rather large domain in  $\varepsilon_0$ . It is found that it also depends little on detector smearing effects.

On the other hand, as can be seen in Fig.4.31, the sensitivity  $\Sigma$  is strongly dependent on the detector acceptance conditions, in particular the electron energy threshold which is related to the  $y$  and  $\varepsilon$  ranges. For the same luminosity, the sensitivity is enhanced by a factor of 2.1 for  $E'_e$  decreasing from 6 to 2 GeV. A decrease on the photon energy threshold  $E_\gamma$  also improves significantly the sensitivity. The lowering of the electron energy threshold is a challenge for the HERA experiments because of the significant background from photoproduction interactions in which low energy hadrons are misidentified as the scattered elec-

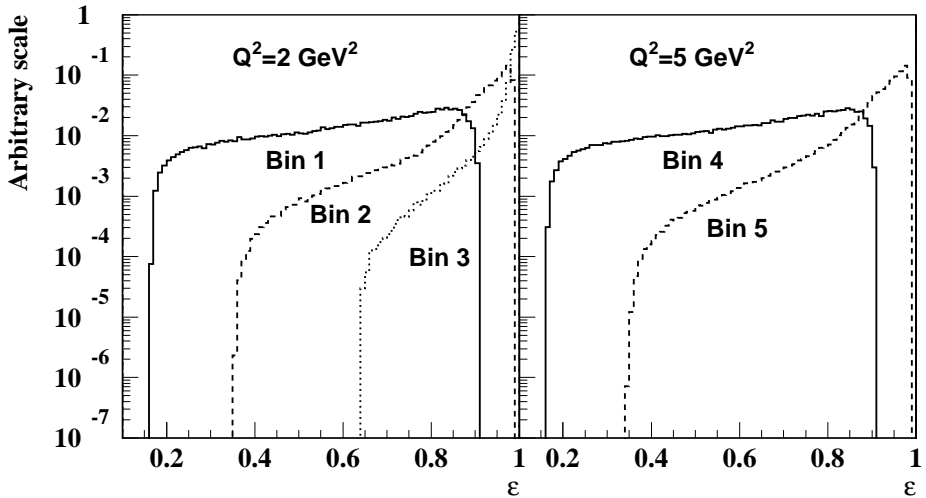


Figure 4.27: Distributions of the  $\varepsilon$  parameter in the selected bins, for the GRV parameterization of the structure function  $F_2$  and for  $R = 0.5$ .

tron.

Studies have been performed of the effects of experimental uncertainties, which are in general bin to bin dependent. The detector resolution was simulated using realistic smearing functions for the H1 experiment; in addition, systematic uncertainties were taken into account (1% on  $E'_e$ , 1 mrad on  $\theta_e$  and 1.5% on  $E_\gamma$ ). The effects of these uncertainties, combined in quadrature with the statistical errors and the effects of the uncertainty on the structure function  $F_2$ , are displayed as the outer error bars on the  $R$  measurements of Fig.4.29.

The subtraction of the remaining photoproduction background is another important source of systematic uncertainty, which affects mostly the lower x bins. There, it was found to induce systematic errors of the same order as the errors due to detector resolution. One more source of systematic error will be the overlap of non radiative deep inelastic events with bremsstrahlung events for which the photon is detected in the photon detector and the scattered electron is not detected. An electron tagger with a large energy acceptance is an important tool to reduce this background. Finally, as far as the uncertainty on the structure function  $F_2$  is concerned, it is observed in Fig.4.28 that it does not imply a large systematic uncertainty on  $R$ .

Taking all these effects into account, we concluded that for an integrated luminosity of  $10 \text{ pb}^{-1}$  a statistical precision of  $\geq 30\%$  can be achieved under the considered experimental conditions and the statistical errors dominate over the systematic errors in most of the chosen bins. With increased statistics, a significant improvement of the measurement precision is thus to be expected. Detailed optimization studies are also expected to improve the measurement precision.

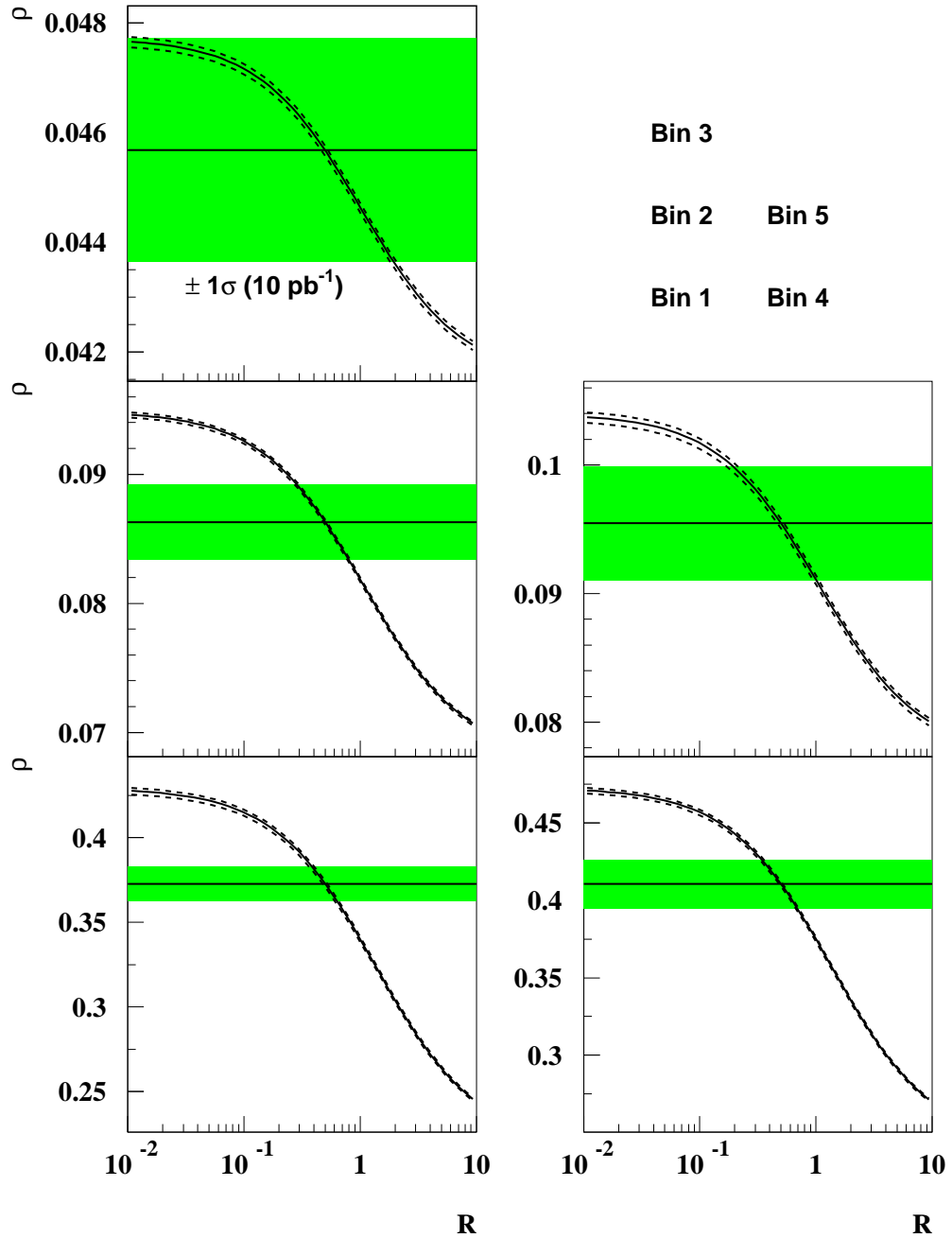


Figure 4.28: The dependence of  $\rho(R)$  on  $R$  for the GRV parameterization (full curves) and for the modified parameterizations described in the text (dashed curves), in the selected bins. The grey bands correspond to  $\pm 1\sigma$  statistical errors for an integrated luminosity of  $10 \text{ pb}^{-1}$  and for  $R = 0.5$ .

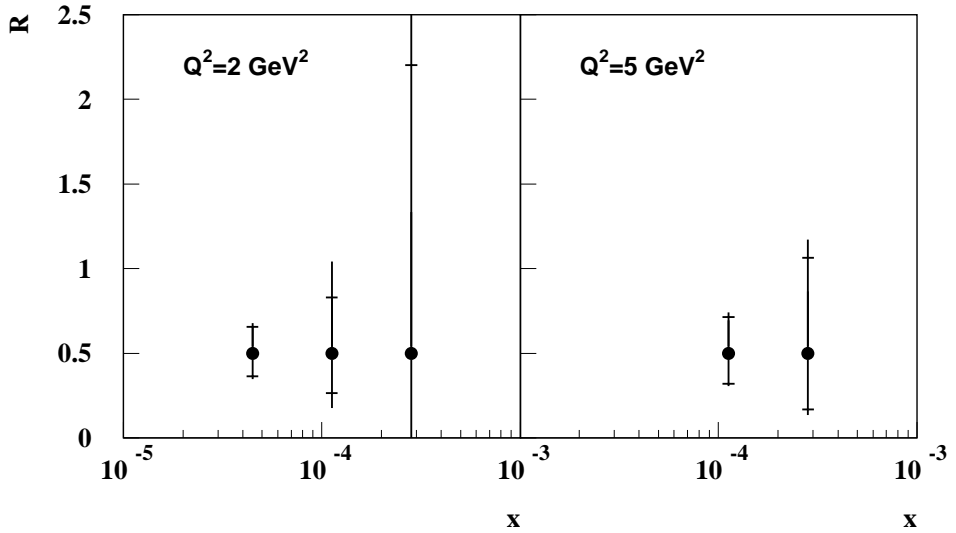


Figure 4.29: Typical precision of the  $R$  measurement in the selected bins, under the experimental conditions specified in Eq.(4.34). The inner error bars show the measurement precision for an integrated luminosity of  $10 \text{ pb}^{-1}$ , taking also into account the uncertainty on the structure function parameterization described in the text. The outer error bars include, added in quadrature, the effects of the uncertainties on  $E'_e$ ,  $\theta_e$  and  $E_\gamma$ .

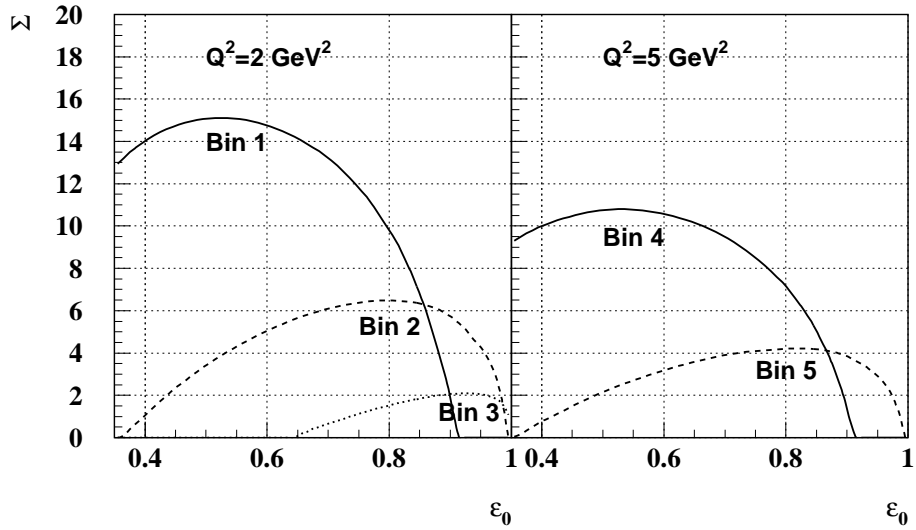


Figure 4.30: Dependence of the sensitivity  $\Sigma$  on the  $\varepsilon$  parameter in the selected bins, for the GRV structure function.

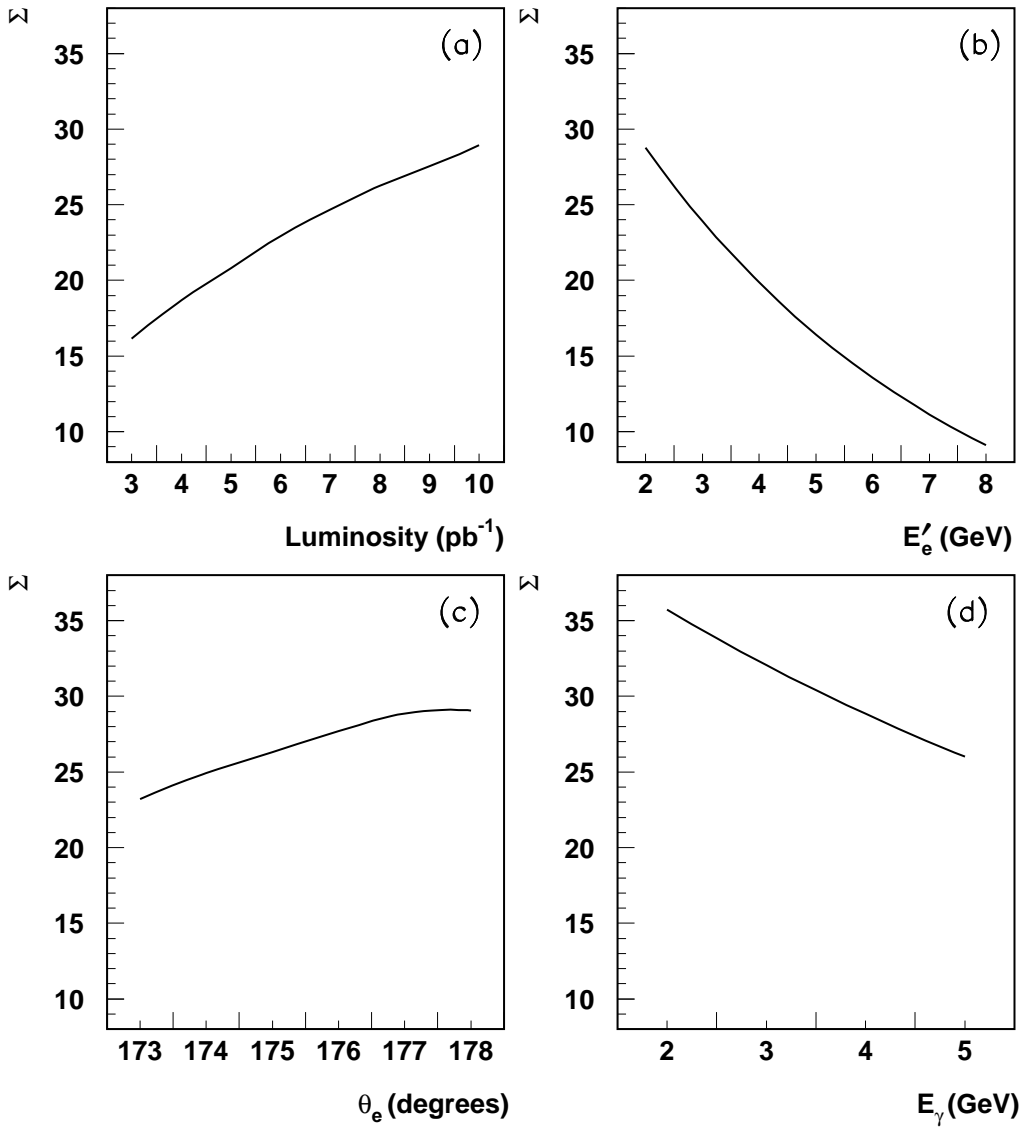


Figure 4.31: Sensitivity  $\Sigma$  as a function of a) the integrated luminosity; b) the electron energy threshold  $E'_e$ ; c) the electron angular acceptance  $\theta_e$ ; d) the photon energy threshold  $E_\gamma$ , for the GRV parameterization under the experimental conditions specified in Eq.(4.34) and in the total kinematical region covered by the selected bins.

By now, we have collected by each HERA experiment a factor of ten more luminosity than what has been used in the feasibility study, therefore statistically there should be more than enough luminosity to provide a first direct  $F_L$  measurement. The challenges are to achieve the best sensitivity with the lowest possible electron and photon energy thresholds and to keep the experimental systematic uncertainties under control. Currently the method is being used in an attempt to realize such a measurement.

## 4.8 The strong coupling constant $\alpha_s$

The strong coupling constant  $\alpha_s$ , the only fundamental parameter of the strong interaction sector of the Standard Model, has been measured in last decades by a great variety of processes [159, 160, 161]. Here we briefly mention a few recent measurements of  $\alpha_s(M_Z)$  based on DIS data, in particular those using the HERA data showing the impact of the precision measurement of the structure function data [135] (Sec.4.5).

One of the methods used on fixed-target data is the analysis of sum rules. One such measurement is derived by using the nonsinglet structure function data  $xF_3$  in the Gross-Llewellyn Smith sum rule [162] which is known to order  $\alpha_s^3$

$$\int_0^1 dx [F_3^{\bar{\nu}p}(x, Q^2) + F_3^{\nu p}(x, Q^2)] = 3 [1 - a_s (1 + 3.58a_s + 19.0a_s^2 - \Delta HT)] \quad (4.37)$$

where  $a_s = \alpha_s/\pi$ , and the higher-twist contribution  $\Delta HT$  is estimated to be  $(0.09 \pm 0.045)/Q^2$  in Refs.[163, 164] and to be somewhat smaller by Ref.[165]. The CCFR experiment [166], combines their data with that from other experiments [167] and gives  $\alpha_s(\sqrt{3} \text{ GeV}) = 0.28 \pm 0.035(\text{expt}) \pm 0.05(\text{syst})^{+0.035}_{-0.030}(\text{th})$ . The systematic uncertainty is dominated by the extrapolation of the integral to the regions  $x < 0.01$  where no measurements exist, and to  $x > 0.5$  which is substituted by  $F_2$  data since it is more precise and has little correlation to the poorly known gluon density at high  $x$ . The error from higher-twist terms dominates the theoretical uncertainty. If the higher-twist result of Ref.[165] is used, the central value increases to 0.31 and corresponds to [61]

$$\alpha_s(M_Z) = 0.118 \pm 0.011. \quad (\text{CCFR, } xF_3 \text{ sum rule}) \quad (4.38)$$

The original and still one of the most powerful quantitative tests of perturbative QCD is the breaking of Bjorken scaling in DIS. The earliest and many subsequent determinations of  $\alpha_s$  in DIS were obtained by analyzing the scaling violation of the structure function data. As an example, a combined analysis of SLAC and BCDMS  $F_2$  data in a  $Q^2$  range from 0.5 to 260 GeV $^2$  gives  $\alpha_s = 0.113 \pm 0.005$  [56]. For several years, this result together with the one,  $\alpha_s(M_Z) = 0.111 \pm 0.002(\text{stat}) \pm 0.003(\text{syst}) \pm 0.004(\text{th})$ , obtained by CCFR [168] based on  $xF_3$ <sup>18</sup> (and also  $F_2$  at high  $x$  for the same reason mentioned above thus resulting in a statistically more precise measurement of  $\alpha_s$ ) is the most significant from DIS data. However, these measurements are numerically smaller than typical values obtained from  $e^+e^-$  annihilation,  $\alpha_s(M_Z) \sim 0.120$ , thus raising speculations about possible explanations. These speculations came to a halt when

---

<sup>18</sup>The advantage of using the less precise structure function  $xF_3$  instead of  $F_2$  is that it has no correlation to the gluon density functions.

the CCFR collaboration corrected their previous result, due mainly to effects of a new calibration of the detector, to [20]

$$\alpha_s(M_Z) = 0.119 \pm 0.002(\text{expt}) \pm 0.004(\text{th}) . \quad (\text{CCFR, } xF_3) \quad (4.39)$$

Recent scaling violation analyses include also HERA structure function data extending thus significantly the lever arm in the  $Q^2$  evolution. In Ref.[169], a NLO QCD fit is performed using the early  $F_2$  data of H1 from 1993 [107] (Sec.4.3) giving

$$\alpha_s(M_Z) = 0.122 \pm 0.004(\text{expt}) \pm 0.009(\text{th}) . \quad (\text{BF, H1 } F_2 \text{ 93}) \quad (4.40)$$

The dominant part of the theoretical error is from the scale dependence; errors from terms that are suppressed by  $1/\ln(1/x)$  in the quark sector are included [170] while those from the gluon sector are not.

In another analysis [171], where the 1994  $F_2$  data by H1 [131] (Sec.4.4) and ZEUS [172] are used together with the fixed-target data from SLAC [39], BCDMS [21], and E665 [173] in a fit including all known NNLO terms, the resulting  $\alpha_s$  is

$$\alpha_s(M_Z) = 0.1172 \pm 0.0017(\text{expt}) \pm 0.0017(\text{th}) , \quad (\text{SY, HERA } F_2 \text{ 94}) \quad (4.41)$$

where the theoretical error includes the uncertainties in the quark masses, higher-twist and target-mass corrections, and errors from the gluon distributions. But the scale uncertainty is not explicitly taken into account, and therefore following Ref.[61] the total error is increased to 0.0045.

The H1 collaboration have used their recent precise  $F_2$  data together with the BCDMS data [21] to obtain a precise determination of  $\alpha_s$  as well as the gluon density [135] (Sec.4.6.1):

$$\alpha_s(M_Z) = 0.1150 \pm 0.0017(\text{expt})^{+0.0011}_{-0.0012}(\text{model}) , \quad (\text{H1, } F_2 \text{ 96-97}) \quad (4.42)$$

where the model error includes all uncertainties associated with the construction of the QCD model used for the fit. In addition, a rather large theoretical uncertainty resulting from the renormalization and factorization scale choices should be added. This uncertainty amounts to about  $\pm 0.005$  as is discussed in Refs.[174, 175].

At HERA, the strong coupling can also be determined in other ways. One such measurement is obtained by comparing the rates for  $(1+1)$  and  $(2+1)$  jet<sup>19</sup> processes. A final state of  $(1+1)$  jet is produced at lowest order in  $\alpha_s$  in the  $ep$  scattering process, while a  $(2+1)$  jet final state is produced at next order in  $\alpha_s$  due to photon-gluon fusion (Fig.3.5) and QCD-Compton processes (Fig.4.32). Unlike

---

<sup>19</sup>The notation “+1” refers to the proton remnant jet.

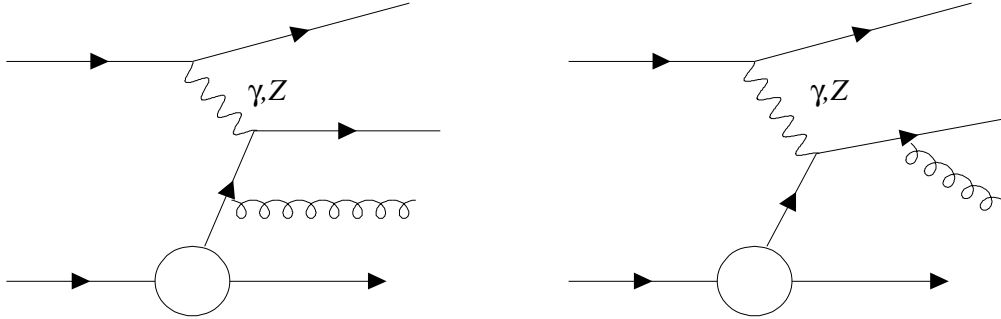


Figure 4.32: *Diagrams of the QCD-Compton process in deep-inelastic lepton-proton scattering.*

the similar measurements from the  $e^+e^-$  experiments, the ones in  $ep$  scattering are not at a fixed energy scale thus allowing the running of  $\alpha_s$  to be tested in a single experiment (see Fig.4.33 below). The first determination by H1 was based on the data from 1993 [176]. A similar determination by ZEUS was obtained from the 1994 data [177]. In the meantime, the NLO QCD calculation have been improved such that the prediction can be used to compare with experimental data in an extended kinematic phase space [178]. Using the new prediction, the H1 collaboration has had an update using the 1994-1995 data[179]. The latest result was determined from the measured inclusive jet cross section  $d^2\sigma_{\text{jet}}/dE_T dQ^2$  in the range  $49 < E_T^2 < 2500 \text{ GeV}^2$  and  $150 < Q^2 < 5000 \text{ GeV}^2$  using the 1995-1997  $e^+p$  data [180]. Jets were defined by the inclusive  $k_T$  cluster algorithm [181] in the Breit frame<sup>20</sup> in the pseudorapidity range  $-1 < \eta < 2.5$  in the laboratory frame. The values determined in different  $E_T$  range are shown in Fig.4.33 and are consistent with the scale dependence predicted by the renormalization group equation. The combined result choosing  $E_T$  as the renormalization scale yields

$$\alpha_s(M_Z) = 0.1186 \pm 0.0030(\text{exp}) \pm 0.0051(\text{th}) . \quad (\text{H1, jet 95-97}) \quad (4.43)$$

The most recent result from ZEUS was derived from the measured dijet rate in the range  $470 < Q^2 < 20\,000 \text{ GeV}^2$  using the 1996-1997 data [182]

$$\alpha_s(M_Z) = 0.1161^{+0.0039}_{-0.0047}(\text{exp})^{+0.0057}_{-0.0044}(\text{th}) . \quad (\text{ZEUS, dijet rate 96-97}) \quad (4.44)$$

The dominant experimental error in both experiments is from the hadronic energy scale uncertainty, which is expected to be significantly reduced according to recent studies (Sec.5.1.4). The theoretical error includes uncertainties arising from scale choice, parton density functions, and hadronization correction.

<sup>20</sup>In the Breit frame, the gauge boson exchanged in the  $t$  channel is purely space-like with four momentum  $q = \{0, 0, 0, -Q\}$  and collides head-on with a parton from the proton. In the leading process ( $1 + 1$  jet) the incoming quark is back-scattered and no transverse energy is produced. The high  $E_T$  inclusive jet cross section receives only higher order contribution and is therefore directly sensitive to the strong coupling constant  $\alpha_s$ .

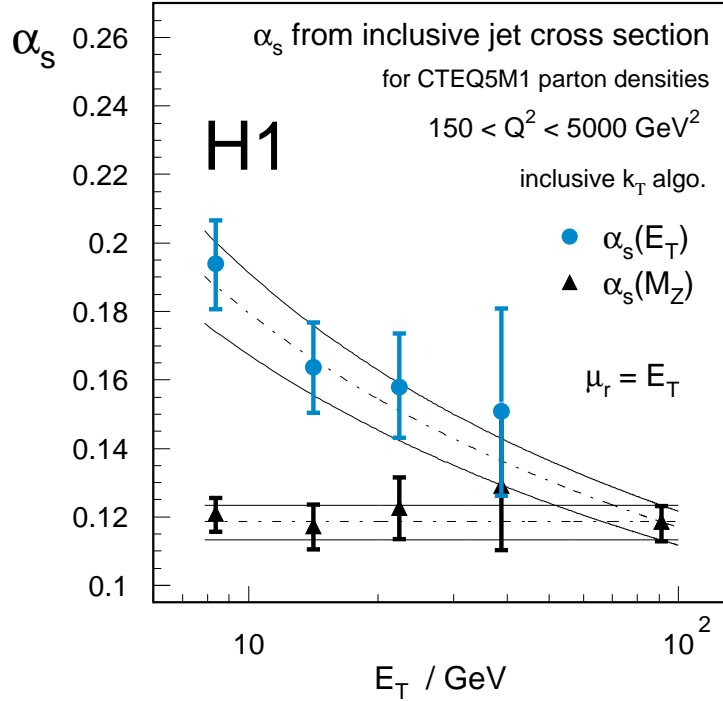


Figure 4.33: Values of  $\alpha_s$  determined from the inclusive jet cross section. The results are shown for each  $E_T$  value (circles). The single values are extrapolated to the  $Z^0$  mass (triangles). The upper curves show the expected scale dependence and the size of the error band indicates the precision of the combined result.

These results are shown in Fig.4.34 together with the new world average value  $\alpha_s = 0.118 \pm 0.002$  [61] and one of the most precise measurements from  $\tau$  lepton decays by ALEPH [183]. The comparison shows that the results from the DIS experiments are consistent among themselves and also with the other independent measurement. Furthermore, the DIS measurements are now becoming increasingly precise, in particular in terms of the experimental uncertainties. The future high statistics HERA data are expected to improve further the experimental precision. Similar improvement on the theoretical side is also expected when higher order QCD calculations for the structure functions and the jet rates will become fully available.

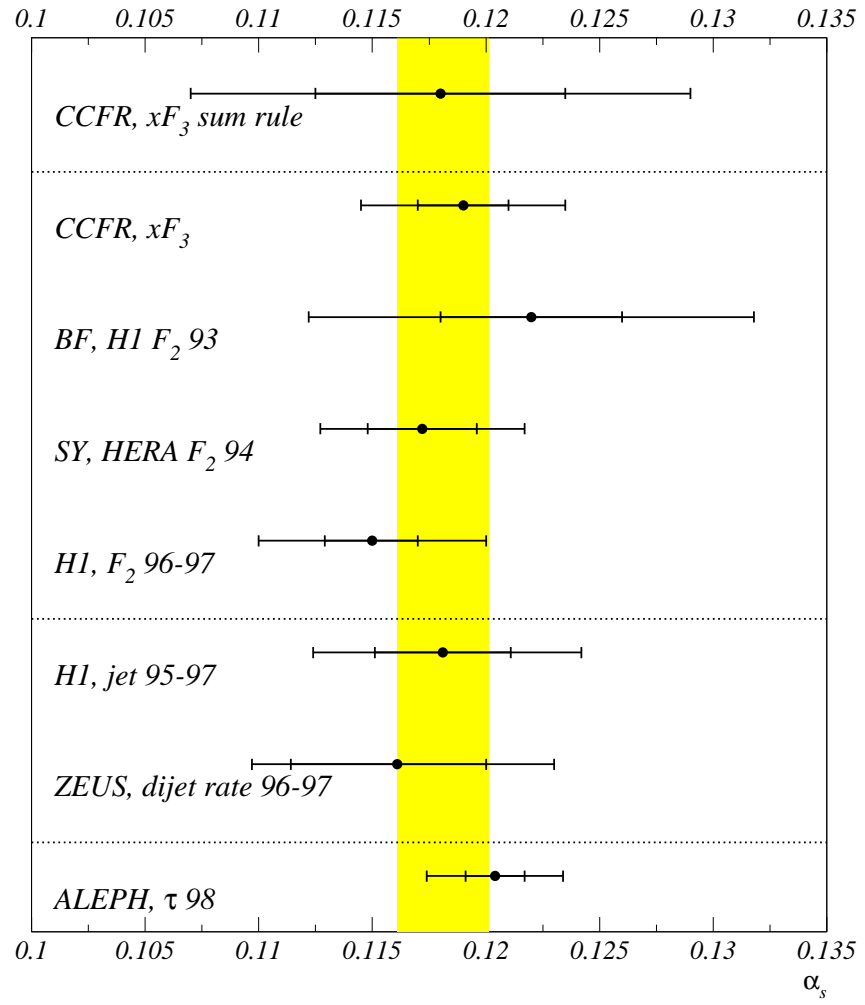


Figure 4.34: A comparison of a few selected  $\alpha_s$  measurements from the DIS data. Also shown are one of the most precise measurements from  $\tau$  lepton decays by ALEPH [183] and the new world average from [61] (the shaded band). The inner and full error bars represent respectively the experimental and total errors. See text for the label definitions and the references.

# Chapter 5

## Neutral and charged current interactions at high $Q^2$

In the previous chapter, the emphasis was put on the measurements of structure functions at relatively low  $Q^2$  and also low  $x$ , a new kinematic domain unexplored by fixed-target experiments, and their impact on the determination of parton (in particular gluon) density functions of the proton. As the integrated luminosity increases, the new kinematic domain at high  $Q^2$  up to a few  $10\,000\,\text{GeV}^2$  has seen sufficient data to be studied for the first time. Contrary to low  $x$  HERA data, these data at high  $Q^2$  cover a range of  $x$  values which have been precisely measured by fixed-target experiments. This allows the DGLAP evolution equations be tested over four orders of magnitude in  $Q^2$ . Deviations from the standard DIS expectations may be found as the largest  $Q^2$  value attainable at HERA is equivalent to a resolution power of one thousandth of the proton radius. In fact, already with the data from years in 1994 to 1996, H1 and ZEUS have reported a low statistics excess of events at high  $Q^2$  and large  $x$ . In this chapter, the analysis on three independent data samples taken since 1994 will be discussed in some detail. The first  $e^+p$  data sample, corresponding to an integrated luminosity of  $35.6\,\text{pb}^{-1}$  and a center-of-mass energy of  $300\,\text{GeV}$  (see Table 2.2), was taken from 1994 to 1997. Both the  $e^-p$  data of 1998-1999 and the  $e^+p$  data of 1999-2000 are taken at a center-of-mass energy of  $320\,\text{GeV}$  resulting from the increased proton energy of  $920\,\text{GeV}$ . The  $e^-p$  data have an integrated luminosity of  $16.4\,\text{pb}^{-1}$ . The recent higher energy  $e^+p$  data of  $45.9\,\text{pb}^{-1}$  correspond to the data taken until the beginning of June, 2000.<sup>1</sup> In Sec.5.1 a few relevant technical issues will be discussed first. The cross section results are given in Sec.5.2.

---

<sup>1</sup>The data taking continued till the beginning of September 2000 when a long upgrade shutdown has taken place.

## 5.1 Technical aspects

The inclusive neutral (NC) and charged current (CC) cross section analysis on the later  $e^-p$  data of 1998-1999 and  $e^+p$  data of 1999-2000 did not differ significantly from the one on the earlier  $e^+p$  data from 1994 to 1997 apart from a few technical improvements. Therefore in the following discussion, no separation is given unless stated otherwise.

### 5.1.1 Event selections and background studies

#### NC event selection

The selection of NC events is only briefly described here as it did not differ in essence from the one on the earlier data of 1993 described in Sec.4.3 and was based on the characteristic feature of the events; an identified scattered electron [184] in the liquid argon (LAr) calorimeter and the hadronic final state which is mainly measured in the LAr calorimeter as well. In fact the main selection cuts were only slightly modified with respect to the one used in the earlier analysis:

- A reconstructed event vertex  $|z_{\text{vtx}} - z_0| < 35 \text{ cm}$ . As mentioned already in the previous analyses (Secs.4.3 and 4.4), this requirement suppresses efficiently the non- $ep$  background contributions.
- An energy  $E'_e$  of the scattered electron measured in the LAr calorimeter greater than  $11 \text{ GeV}$ . Above this threshold the trigger was fully efficient and a small fraction of inefficient regions was excluded by applying fiducial cuts [185, 186].
- An inelasticity  $y_e$  lower than 0.9. This cut becomes more restrictive than the cut on  $E'_e$  for  $Q^2 \geq 907.5 \text{ GeV}^2$ .
- A longitudinal momentum conservation verifying  $\Sigma_e + \Sigma_h$  greater than  $35 \text{ GeV}$ . For an ideal detector without energy loss, the sum is expected to be  $2E_0$ .

The last three requirements minimize the size of radiative corrections and reduce the background from photoproduction.

The dominant remaining background contribution was from photoproduction events where a hadronic final state faked the scattered electron. For the analysis on the 1994-1997  $e^+p$  data, it was subtracted statistically according to the simulated photoproduction Monte Carlo events generated using the PYTHIA [187] generator. The size of the subtraction was controlled with a subsample in which the genuine scattered electron is tagged in the small angle electron tagger at

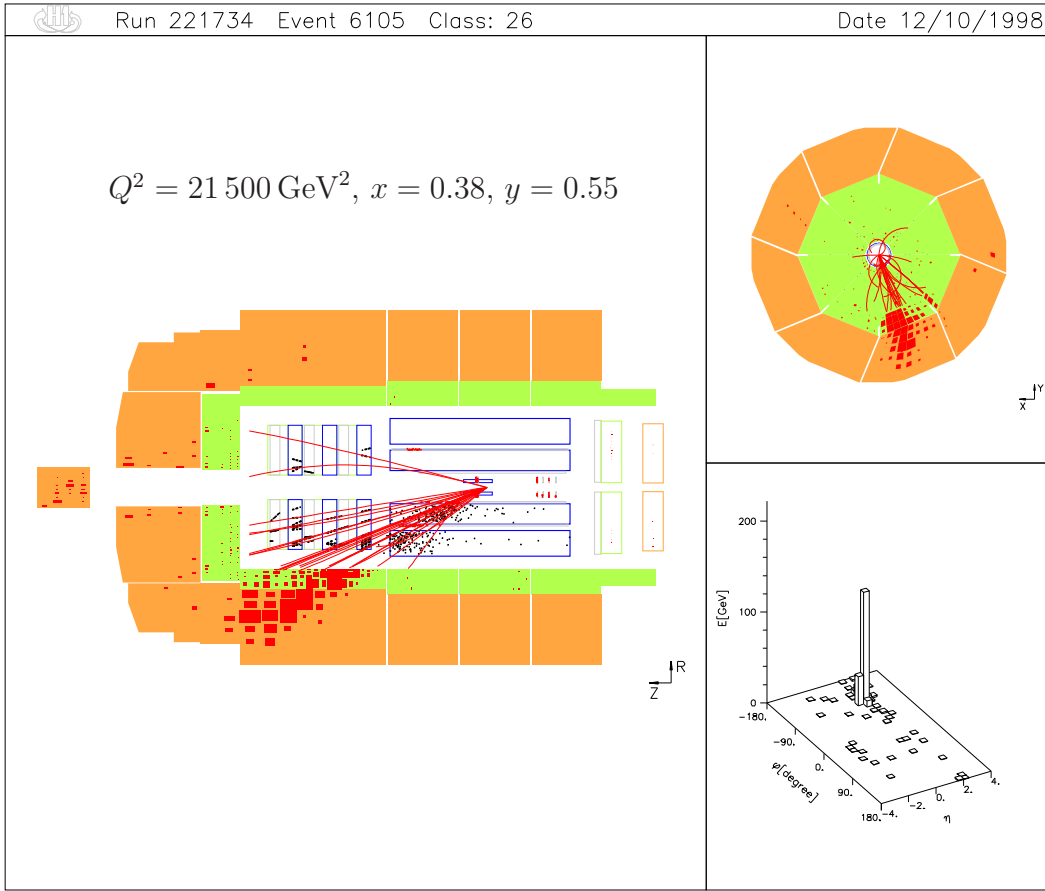


Figure 5.1: A typical charged current event measured by the H1 detector.

$z = -33$  m away from the interaction point. This method suffers however from a large uncertainty (30%) on the estimated background events to be subtracted. For the analysis on the new data recorded since 1998, a new method was applied relying on the fact that the track charge associated to the electron candidate in the photoproduction event could be either negative or positive instead of being negative as expected from the  $e^-p$  collisions. Therefore, the background can be subtracted with two times of positive charged tracks based on the data itself thereby reducing considerably the uncertainty in the subtraction.

### CC event selection

Contrary to the NC selection, the selection of CC events represents a major challenge. The CC events are characterized by a missing transverse momentum  $p_T^{\text{miss}} \equiv p_{T,h}$  due to the undetected neutrino in the final state (see Fig.5.1 for a typical CC event). The main selection cut was

$$p_{T,h} > 12 \text{ GeV}, \quad (5.1)$$

which was much lower than the cut  $p_{T,h} > 25 \text{ GeV}$  applied in the earlier studies [188, 189, 190] based on the 1993-1994 data. While the kinematic coverage has been significantly extended to the lower  $Q^2$  (Fig.5.2), the acceptance to the background events were opened up at the same time. In addition to the  $p_{T,h}$  cut

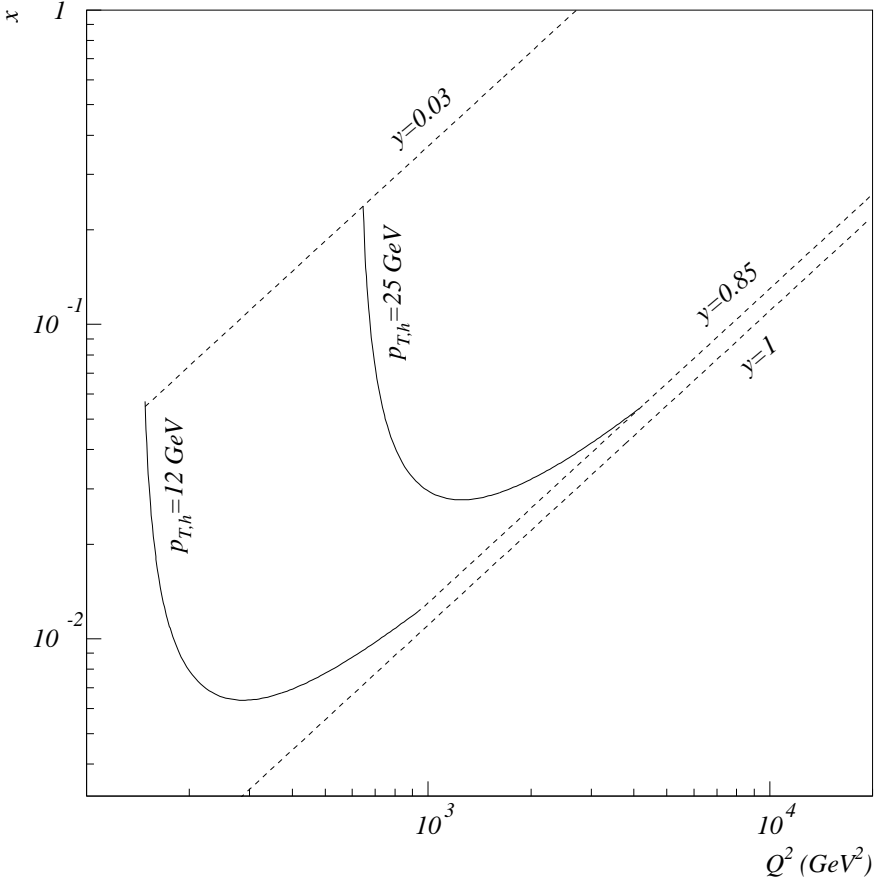


Figure 5.2: The extended kinematic region when the cut  $p_{T,h} > 25 \text{ GeV}$  is lowered to  $p_{T,h} > 12 \text{ GeV}$ . Also indicated are the HERA kinematic limit  $y = 1$  and the actually analyzed  $y$  range  $0.03 < y < 0.85$ .

and the same vertex requirement as for the NC analysis, the CC analysis was limited in the inelasticity range  $0.03 < y < 0.85$  as also indicated in Fig.5.2 in order that the kinematic quantities which can only be reconstructed from the hadronic final state are reasonably precise and that the trigger efficiency remains reasonably large (Sec.5.1.6).

Three background sources contribute in the remaining non- $ep$  background events. These sources are halo muons, cosmic rays and beam-gas and beam-wall interactions. Since the rate of these background events are a few orders of magnitude higher than the CC rate (Table 2.4), there is a high probability that these events pile up among themselves or with other  $ep$  events. An example of such pile-up events is shown in Fig.5.3.



Run 55920 Event 19103 Class: 8 9 13

Date 2/05/1994

Three events in one

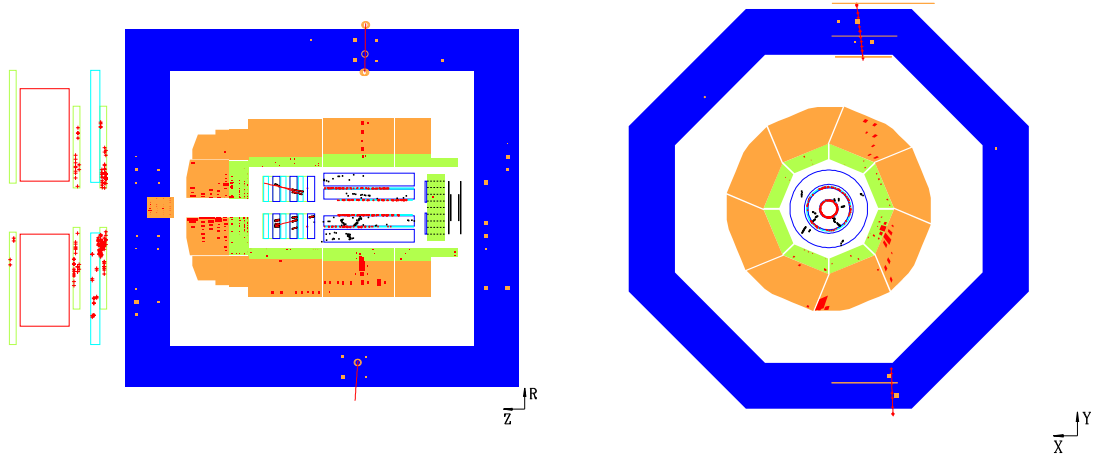


Figure 5.3: A pile-up event from three background sources: halo muon, cosmic ray, and beam-gas/wall interaction.

One efficient rejection was achieved by applying the timing informations provided by both the central jet chambers (CJC) and the LAr calorimeter. The CJC timing,  $t_{\text{CJC}}$ , was determined from tracks which cross the sense wire planes, and has a resolution around 2 ns. The LAr timing [191],  $t_{\text{LAr}}$ , was determined from energy deposits in the trigger readout, which consists of 512 big towers<sup>2</sup>, a coarser structure compared to the highly segmented cell granularity. The resolution of  $t_{\text{LAr}}$  is about 10% of a bunch crossing (96 ns).

The other powerful rejection used a set of topological filters QBGFMAR [93], which was based on the characteristic signature of cosmic and halo muon events. Part of the filters were developed for the earlier analysis described in Sec.4.3. The efficiency of the background filters was determined to be well above 95% based on the pseudo-CC sample (see Sec.5.1.6) and was in good agreement with the MC simulation.

The residual background events were further reduced by other track based criteria. Two examples are

---

<sup>2</sup>A small fraction of the big towers are formed from the backward calorimeter BEMC/SPACAL and the forward PLUG calorimeter.

- **Track-Cluster link:** For the pile-up events, the charged tracks contributing to the event vertex have in general no correlation with the energy deposit in the LAr calorimeter. These events were efficiently suppressed by requiring a minimum distance of 0.5 in the  $\phi$  and pseudo-rapidity  $\eta$  plane between the tracks and two largest energy deposits in transverse momentum.
- **Track multiplicity:** The track multiplicity of a beam-gas or beam-wall event can be large. An important fraction of these tracks do not originate from a common vertex. These events were rejected by requiring that there were 10 or more tracks originating far away from the event vertex by more than 35 cm along  $-z$  direction.

The final contamination of non- $ep$  background events in the CC sample was determined by visual scanning to be 3.7% for the 1994-1997  $e^+p$  analysis and was improved by a factor of two for the new data and subsequently removed from the CC sample. The visual scanning technique as part of the final selection procedure was important because it revealed not only often the need for further improvements in the background rejection but also occasionally interesting (exotic) events. In fact, the first events of observed isolated lepton events with large missing transverse momentum were found in this way.

The dominant  $ep$  background sources originated from NC events and photoproduction events due to the finite detector resolution and the limited geometrical acceptance (including the crack region in  $\phi$  and  $z$ ). Nevertheless, in the transverse plane the energy flow is expected to be more isotropic in the photoproduction and NC events than in CC events. This is quantified by the ratio  $V$  of two variables  $V_{ap}$  and  $V_p$  defined [192] as:

$$V_{ap} = - \sum_i \frac{\vec{P}_{T,i} \cdot \vec{P}_{T,h}}{P_{T,h}} \quad \text{for} \quad \vec{P}_{T,i} \cdot \vec{P}_{T,h} < 0 \quad (5.2)$$

$$V_p = \sum_i \frac{\vec{P}_{T,i} \cdot \vec{P}_{T,h}}{P_{T,h}} \quad \text{for} \quad \vec{P}_{T,i} \cdot \vec{P}_{T,h} > 0 \quad (5.3)$$

standing respectively for the transverse energy flow antiparallel and parallel to the direction of the transverse momentum of the event. The sum in (5.2) and (5.3) extends over all hadronic final state situated in the hemisphere which is opposite to or along  $\vec{P}_{T,h}$ . For the analysis on the 1994-1997  $e^+p$  data, the background was significantly suppressed by requiring

$$V = \frac{V_{ap}}{V_p} < 0.15. \quad (5.4)$$

For the analysis of the new data, the photoproduction rejection was improved by introducing a new variable  $\Delta\phi_{h,\text{PLUG}}$  [193]:

$$\Delta\phi_{h,\text{PLUG}} \equiv |\phi_h - \phi_{\text{PLUG}}|, \quad (5.5)$$

where  $\phi_h$  and  $\phi_{\text{PLUG}}$  are the  $\phi$  angles of the hadronic final state measured respectively in the LAr calorimeter and in the forward PLUG calorimeter. While the  $\Delta\phi_{h,\text{PLUG}}$  distribution is nearly flat for the  $CC$  events, the photoproduction events are mainly distributed at large angles as illustrated in Fig.5.4 for  $P_{T,h} < 25 \text{ GeV}$ . In order to optimize the efficiency and the background contribution, a  $P_{T,h}$  dependent cut for  $P_{T,h} < 25 \text{ GeV}$  is applied as

$$\Delta\phi_{h,\text{PLUG}} < 90 + \frac{180 - 90}{V(P_{T,h}) - 0.2} (V - 0.2), \quad (5.6)$$

with

$$V(P_{T,h}) \equiv 0.2 \left( \frac{P_{T,h} - 12}{25 - 12} \right)^2 \quad (5.7)$$

and  $\Delta\phi_{h,\text{PLUG}}$  in degrees and  $P_{T,h}$  in  $\text{GeV}$ . At the same time, the  $V$  cut is extended from 0.15 to 0.2. Consequently the photoproduction contamination has been further suppressed by a factor of two for an efficiency which is hardly affected at  $P_{T,h} < 25 \text{ GeV}$  and better at higher  $P_{T,h}$  values (Fig.5.5). The final photoproduction contribution, which was statistically subtracted from the data, was estimated to be 2.9% and 1.4% respectively for the 1994-1997  $e^+p$  and 1998-1999  $e^-p$  analysis. The largest contribution is located at low  $Q^2$  and high  $y$  and did not exceed 1% in most of the kinematic region studied.

Part of the NC DIS background contribution was suppressed by the  $V$  cut. The remaining contribution was further reduced by requiring that if an isolated lepton candidate was identified, neither the lepton in the LAr nor the associated track should satisfy  $|\phi - \phi_h| > 120^\circ$ , where  $\phi$  and  $\phi_h$  were respectively the  $\phi$  angle of the lepton (or of the track) and of the hadronic final state. The final NC background was estimated for both  $e^+p$  and  $e^-p$  analyses to be around 0.7% of the total selected samples. Again as for the photoproduction background the largest contribution was distributed at the low  $P_{T,h}$  region and was negligible for most of the kinematic region under consideration.

The final CC samples comprised about 700 events for 1994-1997  $e^+p$  as well as 1998-1999  $e^-p$  analyses<sup>3</sup>, and 1000 events for the 1999-2000  $e^+p$  analysis.

### 5.1.2 Alignment and electron angle measurement

For the NC analysis, one of the key quantities needed for the kinematic reconstruction is the polar angle of the scattered electrons. The polar angle is determined both by the trackers and the position measured in the high granularity calorimeter together with the event vertex. The two determinations are complementary:

---

<sup>3</sup>The integrated luminosity of the  $e^+p$  1994-1997 data was about a factor of three larger than that of the  $e^-p$  1998-1999 data. On the other hand, the cross sections are the other way around so that the total selected number of events were about the same for the two data samples.

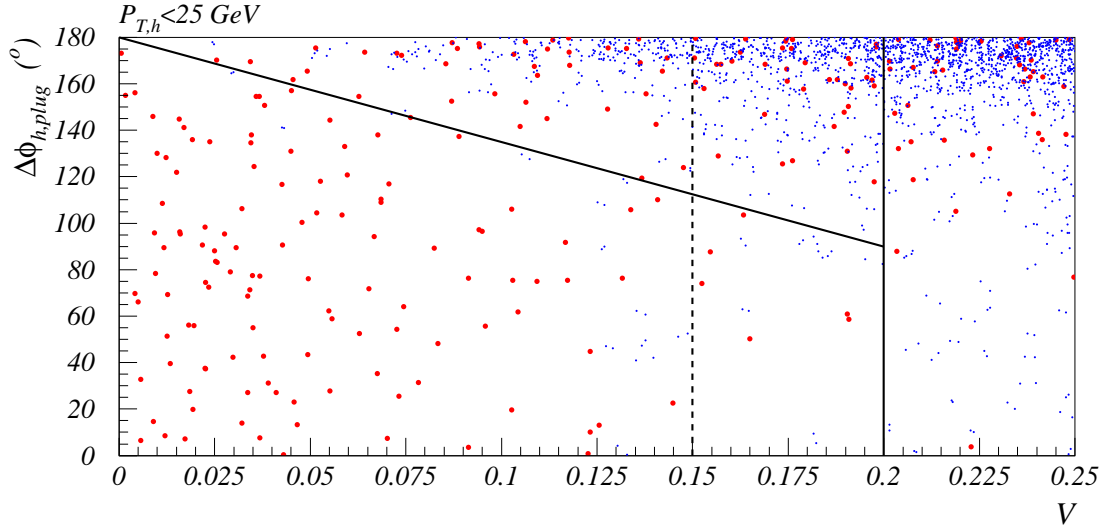


Figure 5.4: Distribution of  $\Delta\phi_{h,PLUG}$  versus  $V$  (see (5.5) and (5.4) for definitions) for CC candidates in the real data (large dots) and for the simulated photoproduction Monte Carlo events (small dots) which represent a factor of six larger integrated luminosity than in data. The full lines indicate the new cut applied for two example  $P_{T,h}$  values at 12 GeV and  $\geq 25$  GeV<sup>2</sup> in the  $e^-p$  analysis while the dashed line for the old cut applied in the  $e^+p$  analysis.

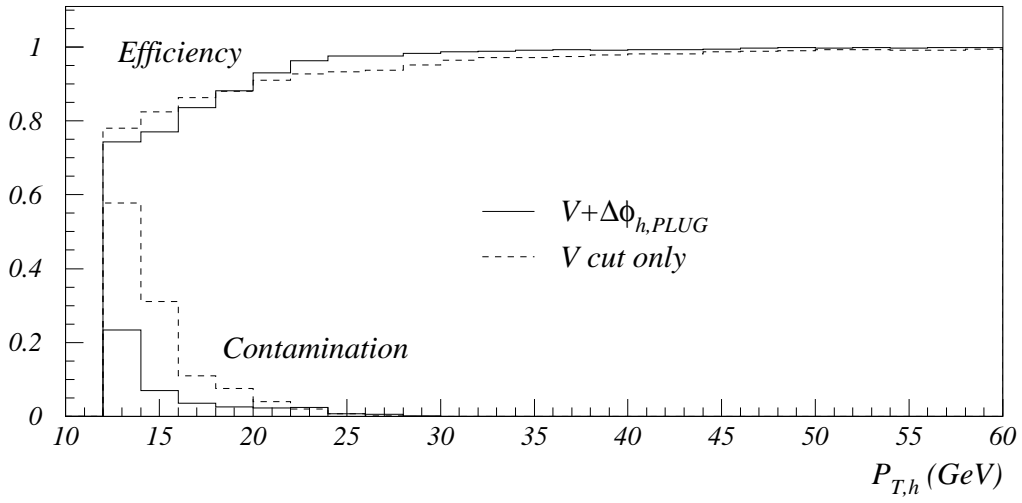


Figure 5.5: Improvement on the CC selection efficiency and the suppression of the photoproduction contamination as a function of  $P_{T,h}$  for the 1998-1999  $e^-p$  analysis with the  $V$  and  $\Delta\phi_{h,PLUG}$  cuts (full lines) compared with the  $V$  cut only (dashed lines) used in the 1994-1997  $e^+p$  analysis.

- When the trackers are fully operational, the former determination gives a better precision than the latter one. On the other hand, it suffers from occasional inefficiencies of part of the tracking system<sup>4</sup> and needs a delicate modeling of the fraction of inefficient regions and its time dependence in the Monte Carlo simulation.
- The latter determination though intrinsically less precise is more stable as a function of time. However, it is achieved when the calorimeter is well aligned to the tracking system.

The alignment was performed in this analysis based on a subsample where the track associated to the scattered electron was well measured by the central tracking device (i.e. both the CJC and the inner and outer  $z$  chambers were operational). Under such condition, the polar angle of the track  $\theta_{\text{trk}}$  gave a good reference for the angle of the scattered electron  $\theta_e$ . This is illustrated by Fig.5.6 where the angle  $\theta_{\text{trk}}$  is found in good agreement with  $\theta_{e,\text{gen}}$ , the generated angle of the scattered electron, independent of the impact position  $z_{\text{trk}}$  of the track on the front of the calorimeter. An octagon around the  $z$  axis with a minimum radius

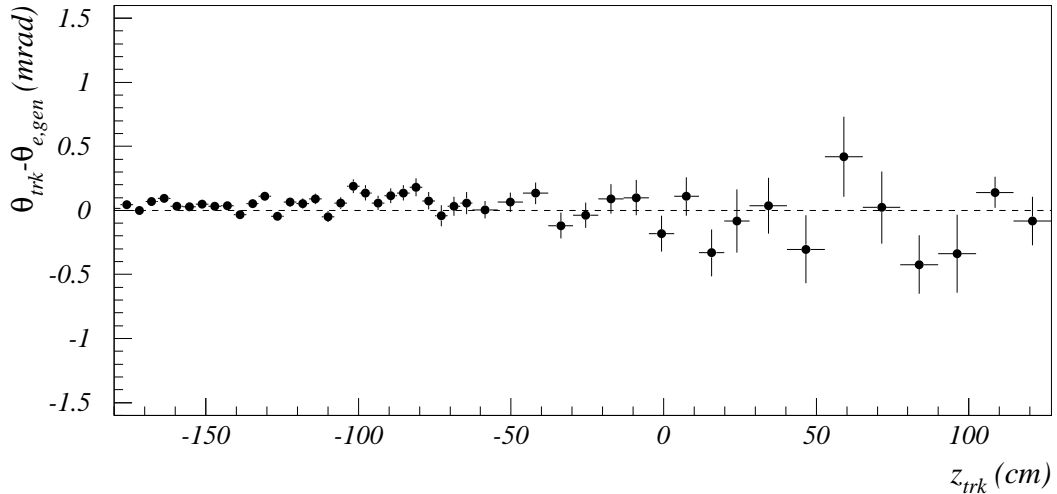


Figure 5.6: The polar angle difference between the generated scattered electron and the associated track as a function of the  $z$  impact of the track.

of 105 cm was taken to approximate the front plane of the calorimeter. The track impact point was defined on this octagon after having been extrapolated from the event vertex ( $x_{\text{vtx}}, y_{\text{vtx}}, z_{\text{vtx}}$ ) taking into account its curvature measured by the tracker within the magnetic field. The impact position of the corresponding cluster measured in the LAr calorimeter on the same octagon was obtained,

<sup>4</sup>In order to maximize the statistical precision of the cross section measurements, which is still limited at high  $Q^2$ , the data sample used includes data in which part of the trackers could be temporarily off.

Table 5.1: Parameters describing the relative alignment between the LAr calorimeter and the central tracking system for the 1997  $e^+p$ , 1998-1999  $e^-p$ , and 1999-2000  $e^+p$  data.

Year	$x_{\text{LAr}}$ (mm)	$y_{\text{LAr}}$ (mm)	$z_{\text{LAr}}$ (mm)	$\alpha$ (mrad)	$\beta$ (mrad)	$\gamma$ (mrad)
1997 $e^+p$	$-0.5 \pm 0.2$	$-1.5 \pm 0.2$	$-4.2 \pm 0.08$	$0.6 \pm 0.1$	$-1.7 \pm 0.1$	$0.7 \pm 0.06$
98-99 $e^-p$	$0.6 \pm 0.2$	$-0.5 \pm 0.2$	$-1.7 \pm 0.07$	$-0.5 \pm 0.1$	$-0.0 \pm 0.1$	$2.4 \pm 0.06$
99-00 $e^+p$	$0.9 \pm 0.1$	$0.4 \pm 0.1$	$-2.0 \pm 0.03$	$-0.6 \pm 0.05$	$-0.2 \pm 0.05$	$0.9 \pm 0.03$

however, with a straight line between the barycenter of the cluster and the event vertex.

Defining  $(x_{\text{LAr}}, y_{\text{LAr}}, z_{\text{LAr}})$  as the center of the LAr calorimeter in the coordinate system of CJC with additional parameters  $\alpha$ ,  $\beta$ , and  $\gamma$  being respectively for anti-clock-wise rotations around the  $x$ ,  $y$  and  $z$  axes, the cluster barycenter  $(x_e, y_e, z_e)$  of the scattered electron measured in the LAr calorimeter can be written in the CJC system as<sup>5</sup>

$$\begin{aligned} x'_e &= x_e - x_{\text{LAr}} + \beta z_e - \gamma y_e, \\ y'_e &= y_e - y_{\text{LAr}} - \alpha z_e + \gamma x_e, \\ z'_e &= z_e - z_{\text{LAr}} + \alpha y_e - \beta x_e. \end{aligned} \quad (5.8)$$

The parameters were determined by minimizing the sum of the difference  $a_{\text{trk}} - a'_e$  with  $a = x$ ,  $y$  and  $z$ . The resulting parameters are shown in Table 5.1 for the 1997  $e^+p$ , 1998-1999  $e^-p$ , and 1999-2000  $e^+p$  data. As an example, Fig.5.7 shows how the alignment on the 1997  $e^+p$  data improves the difference  $a_{\text{trk}} - a'_e$ . Before the alignment, there was a significant rotation around the  $y$  axis which resulted in a tilt in the  $x - z$  plane. Around the other axes, there were no important rotation, but the shifts in  $y$  and in particular in  $z$  were sizable. As far as the measurement of the scattering angle  $\theta_e$  is concerned, the quantity  $z_{\text{trk}} - z'_e$  is most relevant, which as shown in Fig.5.7 is in better agreement with the Monte Carlo simulation after the alignment. The overall shape, which stems partly from the pad structure and partly from the energy distribution on the pads from which the barycenter can be defined, cannot of course be improved by the alignment. But this effect can be and has been corrected for based on the Monte Carlo.

For the 1994-1997  $e^+p$  data analysis, the final angle of the scattered electron was determined from the track when it was well measured by the central tracking system ( $\theta_e > 35^\circ$ ) and in other cases from cluster measured in the calorimeter.

<sup>5</sup>Since the rotation angles are expected to be small, the following approximations  $\cos x \simeq 1$  and  $\sin x \simeq x$  can thus be made. The  $z$  component  $z_e$  in data should be replaced by  $z_e^{\text{cold}}$  which is related to  $z_e$  by  $z_e^{\text{cold}} = 23.67 + (z_e - 23.67)(1.0 - 0.0027)$ . This correction arises because during the final step of data processing the LAr geometrical parameters were mistakenly taken to correspond to a warm environment instead of the cold LAr in reality.

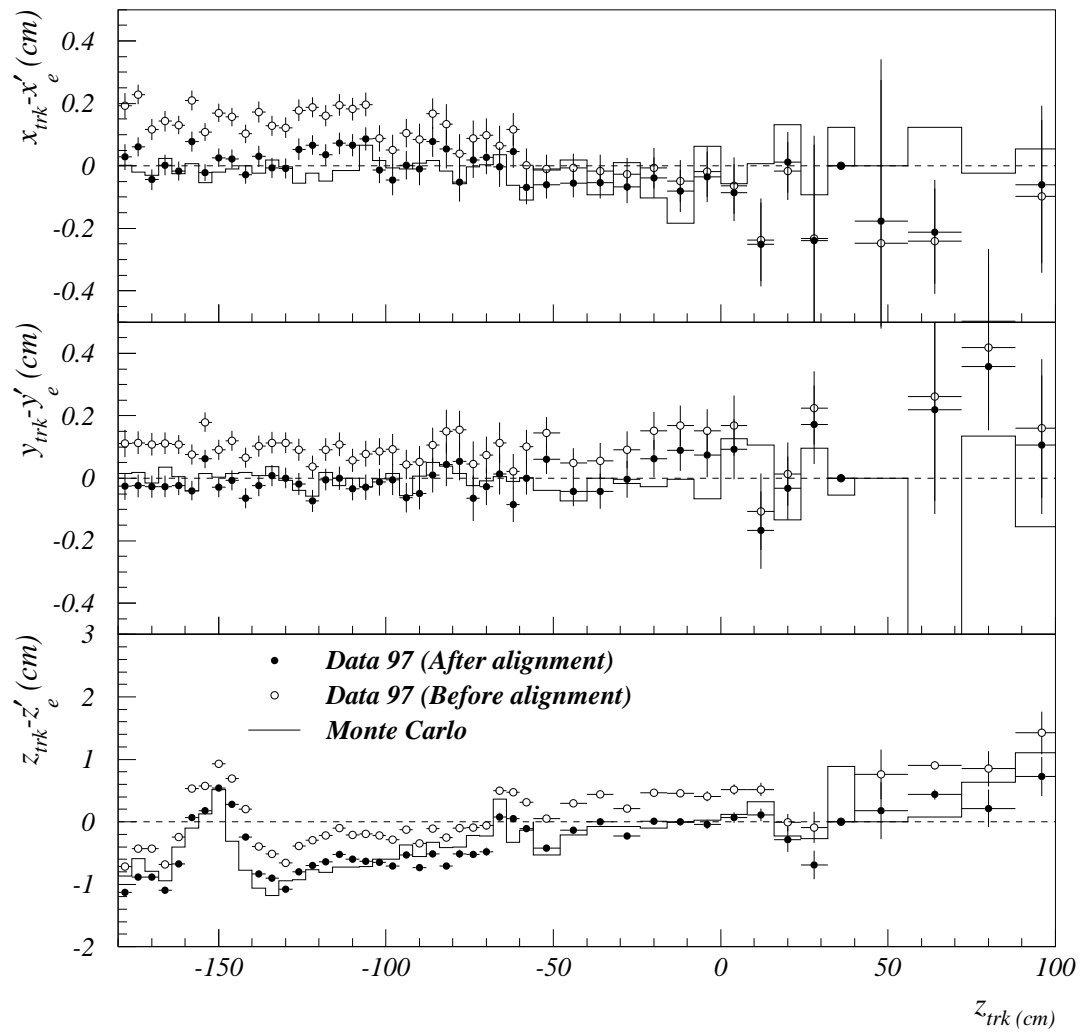


Figure 5.7: The difference of the impact point  $x$ ,  $y$  and  $z$  between track and cluster as a function of  $z$  impact of the track before and after the alignment.

The fraction of latter determination was about 40% and 100% respectively for  $\theta_e > 35^\circ$  and  $\theta_e < 35^\circ$ . The corresponding systematic uncertainty from the tracker and the calorimeter was respectively 1 mrad and 3 mrad. For the analyses of other data samples, the angle was determined from the cluster position in the calorimeter together with the event vertex due to a reduced efficiency of the central trackers.

### 5.1.3 Electron energy measurement

For the cross section measurements to be shown below, the energy measurement of the scattered electron has been improved by an *in situ* calibration by using the increased event sample and the overconstrained kinematic reconstruction.

Several complementary methods and event samples have been used:

- **The double angle method based on NC DIS events (DIS DA):** As shown in (4.4), the energy of the scattered electron can be predicted from the polar angles of the electron  $\theta_e$  and of the hadronic system  $\theta_h$ . The resolution of  $\theta_h$  is sufficiently good when one uses the subsample at  $y_\Sigma < 0.3$  ( $y_\Sigma < 0.5$ ) for  $80^\circ \lesssim \theta_e \lesssim 153^\circ$  ( $40^\circ \lesssim \theta_e \lesssim 80^\circ$ ). In this region, the event statistics is large enough to improve the energy measurement locally in finely segmented  $z$  and  $\phi$  grid defined by the impact position of the electron track on the LAr calorimeter.
- **The elastic QED Compton events and exclusive two photon  $e^+e^-$  pair production (QED Compton/ $e^+e^-$ ):** Due to the limited number of events from NC DIS process in the forward region ( $\theta_e < 40^\circ$ ), two additional event samples are used to check and obtain the calibration constant together with the DIS sample. These samples are the elastic QED Compton events and the exclusive two photon  $e^+e^-$  pair production. Contrary to the DIS events, these samples provide two leptonic final states for the calibration when both are measured in the LAr calorimeter. Furthermore since these events cover a large energy range, they allow the energy linearity be studied.
- **The  $\omega$  method based on NC DIS events ( $\omega$  DIS):** This is an approximate kinematic method [194] which assumes that the relative error in the measured  $\Sigma_h$  and  $P_{T,h}$  is the same (i.e.  $\delta\Sigma_h/\Sigma_h = \delta P_{T,h}/P_{T,h}$ ). This method was also based on the NC DIS sample and therefore it was not independent of the DA method. On the other hand, the  $\omega$  method is less sensitive to the effects of initial state QED radiation than the DA method.

The resulting electromagnetic energy scale as determined for the 1994-1997  $e^+p$  data analysis is shown in Fig.5.8 together with the quoted systematic uncertainty as indicated by the error band.

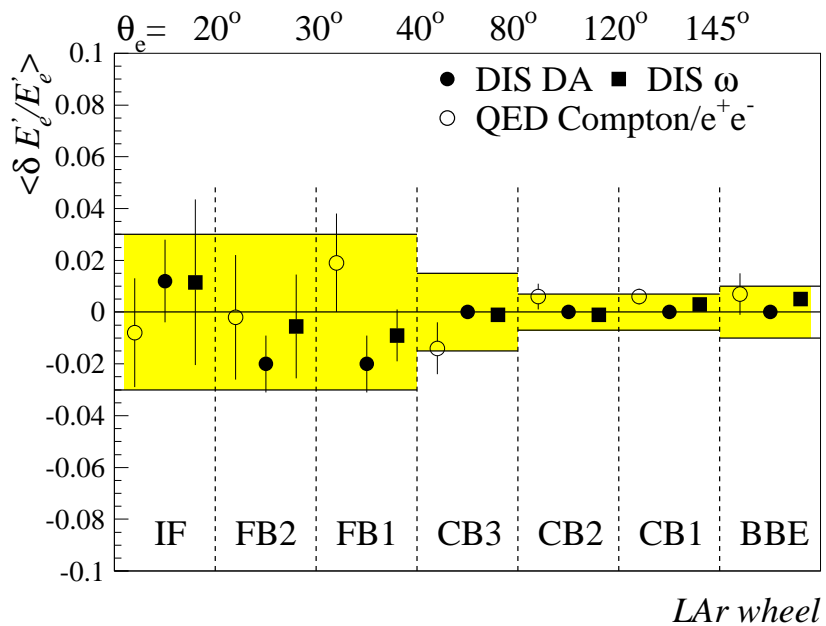


Figure 5.8: Comparison of the electromagnetic energy scale as determined by different methods and event samples. Shown is the mean fractional energy shift of the different method from the absolute energy scale,  $\langle \delta E'_e/E'_e \rangle$ . The shaded error band shows the systematic uncertainty on the energy scale quoted for the cross section measurement, which varies from 0.7% to 3%, depending on the location of the electron in the detector.

For the analyses on the new data, the energy scale was checked using the newly available event sample. Small variation within the quoted systematic uncertainty was found and taken into account in the new analysis.

### 5.1.4 Hadronic energy measurement

A precise hadronic energy measurement is crucial for all measurements relying on the hadronic final state for the kinematic reconstruction. In fact many of these measurements are now limited by the uncertainty of the hadronic energy scale, which was estimated to be about 4%. For instance, such an uncertainty dominates the experimental error of the  $\alpha_s(M_Z^2)$  measurement of  $\alpha_s(M_Z^2)$  based on the inclusive jet cross section [180] (Sec.4.8).

For the cross section measurements presented here, a detailed study was carried out [195] in order to improve the uncertainty. While the precision of the electron energy calibration was limited in the forward region due to the limited statistics, the hadron energy calibration does not have such a limitation as the hadronic final state covers rather uniformly all the calorimeter region. The calibration method is based on the transverse energy conservation, namely the transverse momentum of the hadronic final state  $P_{T,h}$  should be equal to that of the scattered electron  $P_{T,e}$ , the latter can be again predicted with the double angle method as  $P_{T,DA}$ .

A clean and unbiased calibration sample is defined as follows:

- An identified scattered electron having  $P_{T,e} > 10 \text{ GeV}$ ,
- The predicted  $P_{e,DA}$  is not strongly affected by the initial state QED radiative events by requiring<sup>6</sup>  $P_{T,e}/P_{T,DA} > 0.88$ ,
- One and only one reconstructed jet based on the cone algorithm [196] with a cone radius of 1 rad in the  $\phi$  and pseudorapidity  $\eta$  plane and a minimum transverse momentum of 4 GeV. In addition, in order that the calibration factor to be determined is relevant for the LAr calorimeter, the jet has to be well contained in the LAr calorimeter by requiring that there is no more than 1% energy or transverse energy deposit in either the backward calorimeter or the tail-catcher. The jet is also required to be well away from the beam pipe in the forward direction ( $\theta_{\text{jet}} > 7^\circ$ ) so that the calibration would not correct for the beam energy loss.

The calibration is then performed in two steps. In the first step, the relative difference in  $P_{T,h}/P_{T,DA}$  between data and the Monte Carlo simulation is

---

<sup>6</sup>As mentioned previously, a cut on  $\Sigma_e + \Sigma_h$  is also very efficient in suppressing the radiative effect. On the other hand, since the sum includes a contribution which is directly proportional to the energy scale of the hadronic final state, such a cut may bias the calibration.

determined in finely segmented  $\phi$  and  $\theta'_{\text{jet}}$ <sup>7</sup> grid to account for possible detector effects which may be year dependent. In the second step, an absolute hadronic energy scale is achieved both in data and simulation by imposing the transverse momentum balance between the scattered electron and the hadronic final state.

Fig.5.9 shows the performance of the calibration based on a large inclusive event sample which was selected with less restrictive cuts as was used for defining the calibration sample. Before the calibration, the hadronic scale was found to be significantly lower than expected and there was in addition a strong  $P_{T,h}$  dependence. The difference between data and the simulation was about 4%. After the calibration, a precision of 2% was achieved for the first time in H1 both on the hadronic scale and the systematic difference between data and simulation.

The performance of the calibration was further checked on a few other aspects:

- **Hadronization model dependence:** The check concerns whether there is any dependence of the calibration on the usage of two different hadronization models in the Monte Carlo event simulations. One model uses the color dipole model in its ARIADNE implementation and the other model uses the matrix element plus parton shower model (MEPS) as implemented in LEPTO. While some differences were found in each calibration step, the overall calibration procedure was found to be independent of the Monte Carlo models as expected because of the imposed balance in transverse momentum.
- **Independent event sample:** While the calibration correction factors were obtained using the clean one jet sample, the performance of the calibration was checked with an independent sample in which two or more jets are reconstructed.
- **Other jet reconstruction algorithms:** The calibration factors obtained from the cone algorithm were applied to jets which were reconstructed with two other jet algorithms to check the dependence on the jet reconstruction.

In all cases, the results obtained were within the quoted systematic uncertainty. In addition, the absolute energy calibration also improved the relative energy resolution  $\sigma(P_{T,h})/P_{T,h}$  by 5% at  $P_T \simeq 35 \text{ GeV}$  and 15% at  $P_T \sim 12 \text{ GeV}$  [195].

The reduced systematic uncertainty on the hadronic energy scale has an important impact on analyses relying on the hadronic final state. One example is the measurement of the charged current cross sections. This is illustrated in Fig.5.10(a). The magnitude and turn-over behavior at around  $2000 \text{ GeV}^2$  depend on the selected event distribution shown in Fig.5.10(b). At the intermediate  $Q^2$ ,

---

<sup>7</sup>The quantity  $\theta'_{\text{jet}}$  differs from  $\theta_{\text{jet}}$  in that the former is calculated always with a fixed vertex position at zero instead of with the measured event vertex as in the latter. In this way, the angle  $\theta'_{\text{jet}}$  is well defined independent of the vertex position.

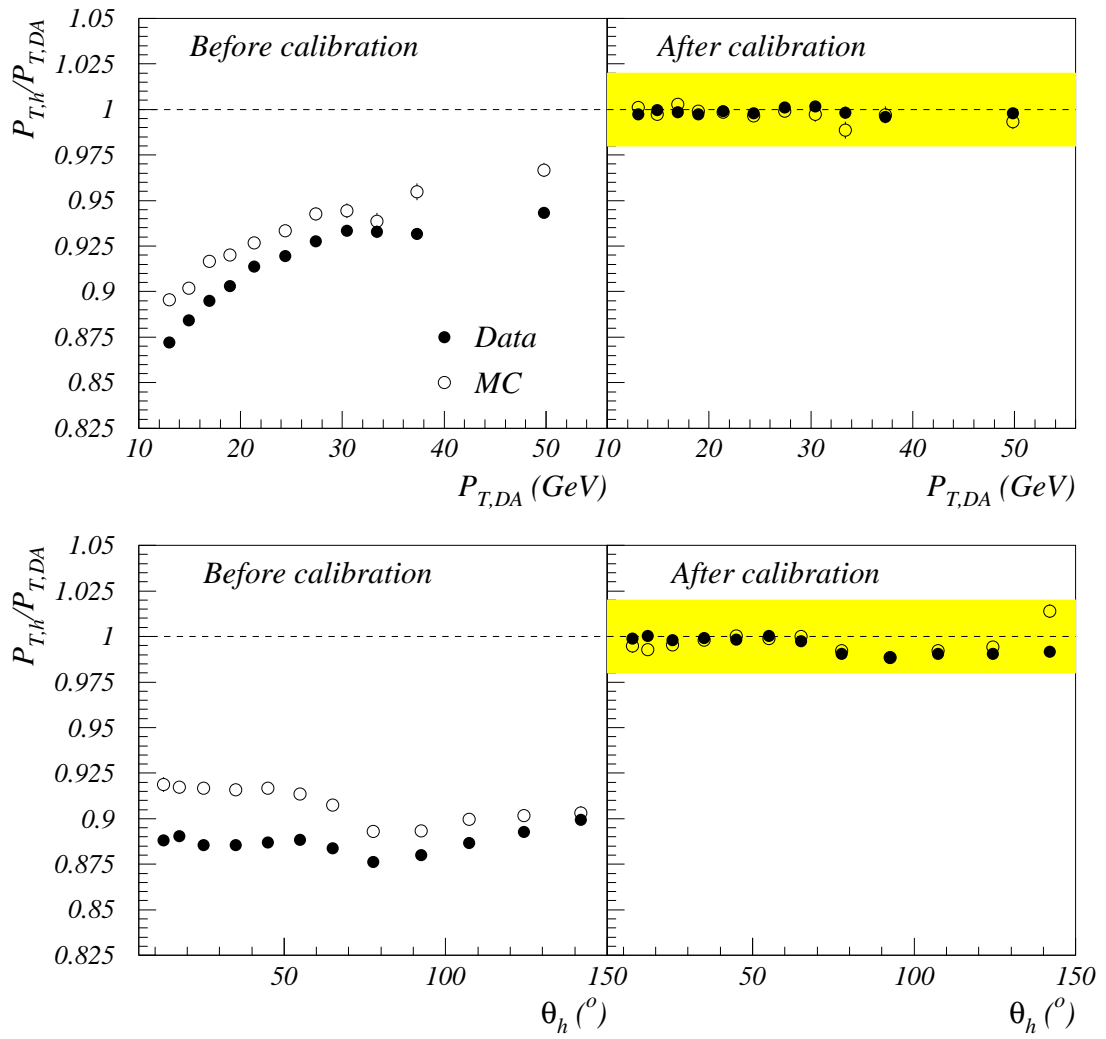


Figure 5.9: The transverse momentum of the hadronic final state,  $P_{T,h}$ , over that of the scattered electron,  $P_{T,DA}$ , as predicted with the double angle method, as function of  $P_{T,DA}$  and the inclusive angle of the hadronic final state  $\theta_e$  before and after the calibration.

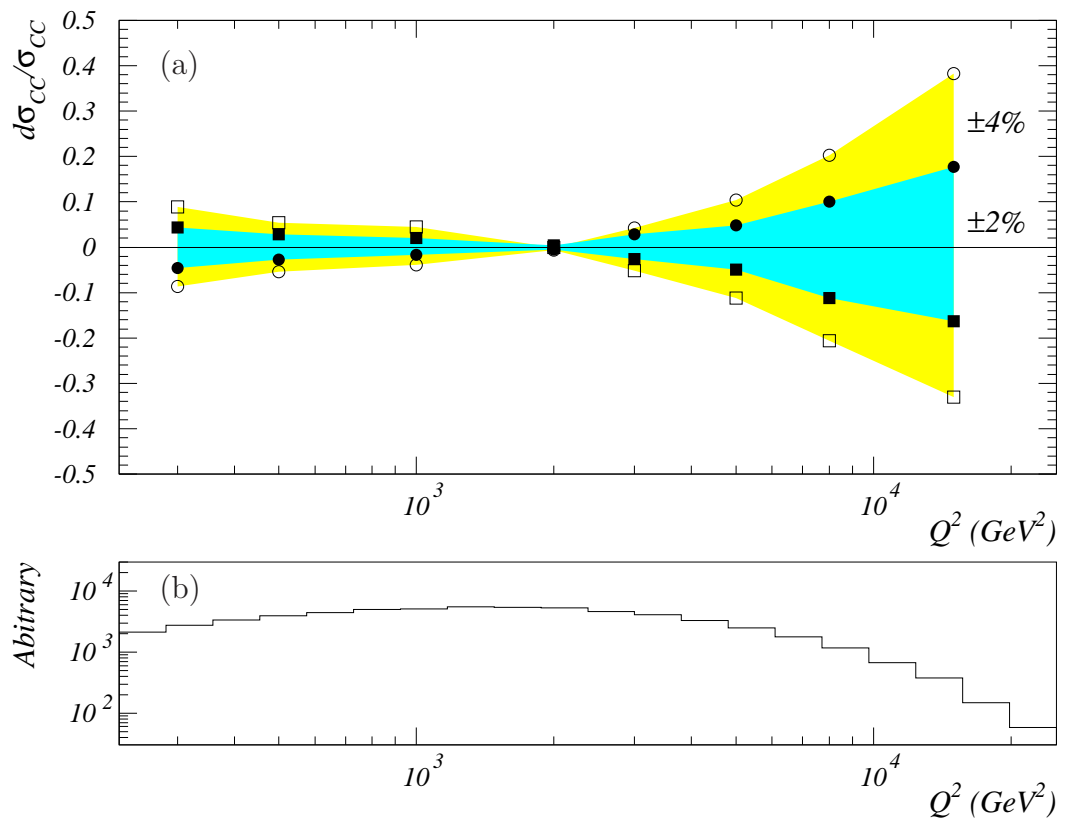


Figure 5.10: (a) The resulting uncertainties on the measurement of the  $e^+p$  CC cross section from the improved hadronic energy scale uncertainty of  $\pm 2\%$  (dark shaded area enclosed with full points) in comparison with an uncertainty of  $\pm 4\%$  (light shaded area enclosed with open points). (b) The selected event distribution as a function of  $Q^2$  upon which the form of the uncertainty depends.

the event distribution is rather flat and the energy scale uncertainty on the cross section is smallest, as the event migration from one side compensates the migration from the other side. At lower  $Q^2$  the drop in the event distribution is completely due to the the selection cuts, while at higher  $Q^2$  the selection efficiency is very high and therefore the shape of the event distribution is intrinsically due to the falling cross section as  $Q^2$  increases.

### 5.1.5 Calorimetric noise suppression

One of the problems in the analyses relying on the liquid argon calorimeter (LAr) is the distorted measurement of the kinematic variables at the low  $y$  region [195]. The problem is related to the fact that at low  $y \lesssim 0.05$ , hadrons are produced in the forward direction. The  $z$  component  $p_{z,h}$  is comparable with the energy  $E_h$  thereby resulting in a small value of  $\Sigma_h \equiv E_h - p_{z,h} (\lesssim 2.76 \text{ GeV})$ . Any background energy located in the barrel and backward calorimeter if taken as part of the hadronic final state will thus distort significantly the total  $\Sigma_h$  (the more backward a given energy  $E_h$  is deposited, the larger the resulting  $E_h - p_{z,h}$ ). Background energies arise primarily from the following sources:

- **Electronic noise:** the noise inherent in the electronics of the calorimeter readout,
- **Backscattering:** the contribution from the secondary scattering of final state particles,
- **Pile-up events:** the contribution from the accidental coincidence of a low  $y$  event with a background process, e.g. a beam halo or a cosmic ray event,<sup>8</sup>
- **Hadron/photon separation:** the large angle radiative photons measured in the LAr are misinterpreted as part of the hadronic final state if they are not explicitly identified,
- **Hadron/electron separation:** for neutral current events, a wrong separation between the scattered electron and the hadronic final state can result in a biased measurement for the  $E_h - p_{z,h}$  measurement. This could happen when the scattered electron is misidentified. The imperfect cluster algorithm can give rise to multiple clusters for the scattered electron in particular when it hits a  $\phi$  crack between two octants, or a  $z$  crack between two wheels, or the overlapping region between the BBE and the backward calorimeter SPACAL. In such a case, part of the electron energy may be wrongly attributed to hadrons. Since the electron is located predominantly

---

<sup>8</sup>The LAr time sensitivity of several microseconds allows energy deposits of these background events to pile up on real physics events.

at large polar angle in the backward region of the calorimeter, a fraction of its energy if assigned to hadrons may dominate over the small  $\Sigma_h$  in the forward region, thus bias the hadronic measurement.

The last source, which affects only neutral current events, can be eliminated by improving either the current electron identification programs or the clustering algorithm. The radiative contribution is more difficult to deal with for an inclusive analysis. In order to study the other noise contributions, these last two contributions are explicitly removed or suppressed from Monte Carlo samples used.

Part of the electronic noise has been suppressed during the online and the offline reconstruction [197]. The remaining background contribution was further suppressed in the past by various noise suppression algorithms. The basic idea of one of these algorithms, to be called “old suppression” [198] in the following, is to identify and subsequently suppress isolated low energy deposits (clusters) in the LAr calorimeter. After the suppression, a significant improvement is achieved in particular for  $y$  down to  $\sim 0.05$  (Fig.5.11(a)). For the region at smaller  $y$ , there is still an important bias to the measured  $y_h$ .

A closer look at the energy distribution as a function of  $\theta_h$  (Fig.5.11(b)) for  $y < 0.1$  shows that there is an energy surplus towards the large angles. A detailed study [199] revealed that two distinct types of background energies contribute: energetic deposits affect a small fraction of the sample and less energetic ones affect the majority of the events. The first type originates from the accidental coincidence of a DIS event with a halo or a cosmic muon event. These background muons can produce rather energetic showers resulting in very large distortions in the measurement of  $y_h$  (up to an order of magnitude with respect to  $y_{\text{true}}$ ). Two specific algorithms were thus developed to identify the background energy patterns and subsequently suppress them from the energy measurement. The second type is due to other contributions such as the residual electronic noise and the backscattering contribution. To suppress these background energies, a higher energy threshold was found necessary [199]. After the “new suppression”, the improvement is clearly demonstrated not only on the average value of the measured  $y_h$  (Fig.5.11(a)) but also in terms of the energy distribution over the detector (Fig.5.11(b)). It should be pointed out that the measured  $E_h$  and  $y_h$  do not have to coincide with the generated quantities as the absolute calibration discussed in the previous section is not applied for this comparison. At very low  $y$ , the energy loss in the beam pipe becomes increasingly important (see the energy distributions at small angles in Fig.5.11(b)), one expects  $y_h$  to be smaller than  $y_{\text{true}}$ .

It has been checked [199] based on the simulated MC samples that what has been suppressed were indeed the various noise contributions discussed above and there was no evidence that signal energies were affected. The suppressed noise

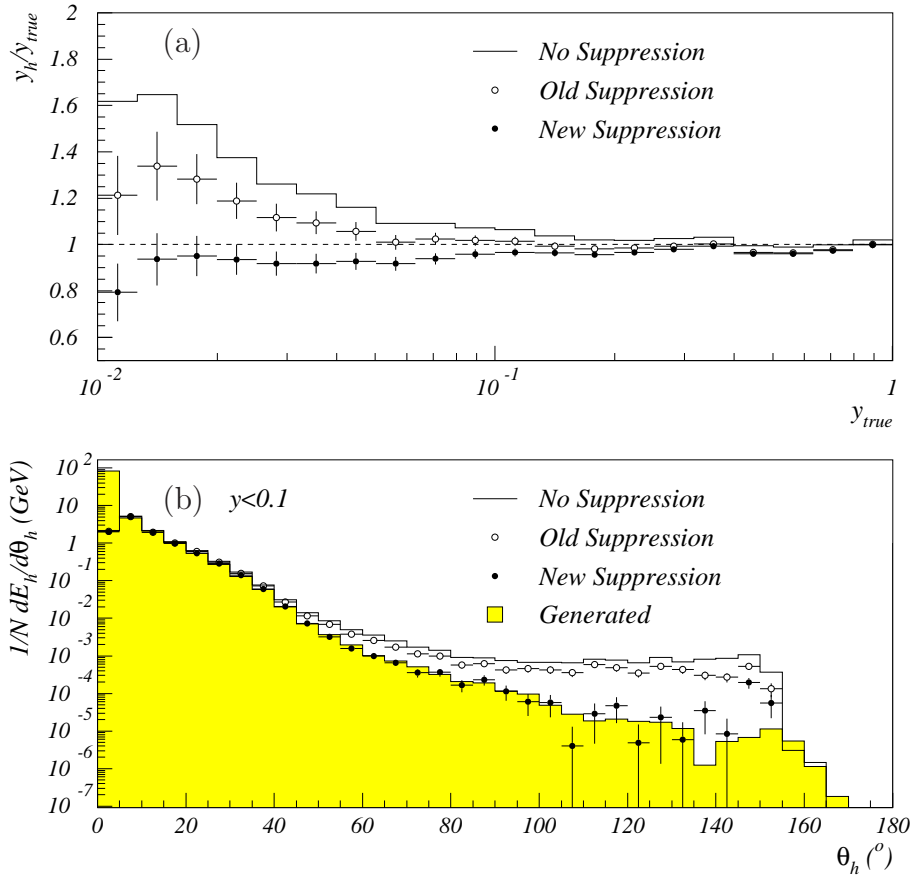


Figure 5.11: A comparison of the measured  $y_h$  as a function of  $y$  (a), and of the measured  $E_h$  as a function of  $\theta_h$  at low  $y < 0.1$  (b) based on the neutral current MC files.

in the data is finally compared with that in the simulation using the NC  $e^-p$  data taken in the years from 1998 to 1999 as an example. First in Fig.5.12(a), the event distribution as a function of  $\Sigma_{noise}/2E_e$  ( $\Sigma_{noise} = E_{noise} - p_{z,noise}$ ) is compared. In Fig.5.12(b), the relative contribution of the suppressed  $\Sigma_{noise}$  to the total measured  $\Sigma$  including  $\Sigma_{noise}$  is shown as a function of  $y_h$ , which does not include the contribution from the suppressed noise. The shaded bands show the quoted systematic uncertainty ( $\pm 25\%$ ) on the noise suppression. Within the uncertainty quoted, the data are well described by the simulation.

### 5.1.6 Trigger efficiency for charged current events

The trigger efficiency for CC events is one of the most critical parts among the various efficiencies needed for the cross section measurements as it was not automatically simulated in the Monte Carlo production.

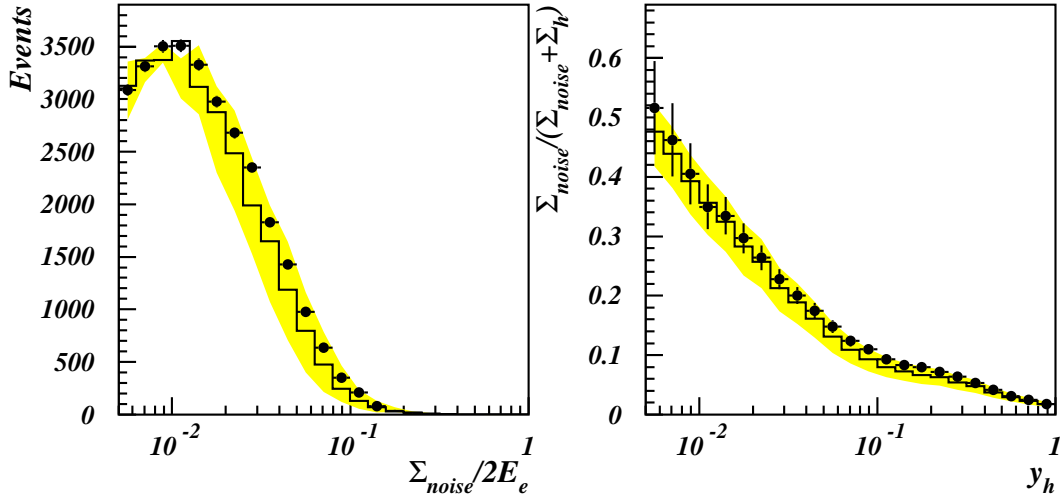


Figure 5.12: Comparison of (a) the event distribution as a function of  $\Sigma_{\text{noise}}/2E_e$ , (b) the relative contribution of the suppressed  $\Sigma_{\text{noise}}$  to the total measured  $\Sigma$  ( $= \Sigma_h + \Sigma_{\text{noise}}$ ) as a function of  $y_h$ . The data (points) are the NC events from the  $e^-p$  data taken in 1998-1999, while the histograms show the corresponding Monte Carlo simulation. The shaded error bands represent the quoted systematic uncertainty ( $\pm 25\%$ ) on the suppressed noise contribution.

The logics designed for triggering CC events are based mainly on the missing transverse energies provided by the LAr calorimeter and on the timing information from either the proportional chambers or the LAr calorimeter. From the detector point of view, the hadronic final state of a CC event is the same as that of a NC event. Therefore, the CC trigger efficiency as well as other CC efficiencies can be determined from high statistics NC events from real data when all information associated to the scattered electron is removed. This is the so called pseudo-CC sample<sup>9</sup> mentioned already in Sec.5.1.1.

The CC trigger efficiencies for three different run periods are compared in Fig.5.13 as functions of the missing transverse momentum  $P_{T,h}$  and the kinematic variable  $y_h$ . The lower cuts on these two quantities in the analysis are respectively 12 GeV and 0.03 (Sec.5.1.1). This ensures that the trigger efficiency is always above  $\sim 50\%$ . During the shutdown between 1997 and 1998, part of the preamplifiers with large capacity were upgraded by low-noise amplifiers. With this upgrade [200] and other hardware modifications [201], the trigger efficiency is expected to be improved as indeed seen at the low  $y$  region. Unfortunately, during the first part ( $\sim 64\%$ ) of the  $e^-p$  data taking period, the missing transverse energies provided from the LAr trigger towers were modified to correspond to an earlier bunch crossing instead of the nominal one thereby resulting in a

<sup>9</sup>These events were further reweighted to the CC cross section such that they behave kinematically just like real CC events.

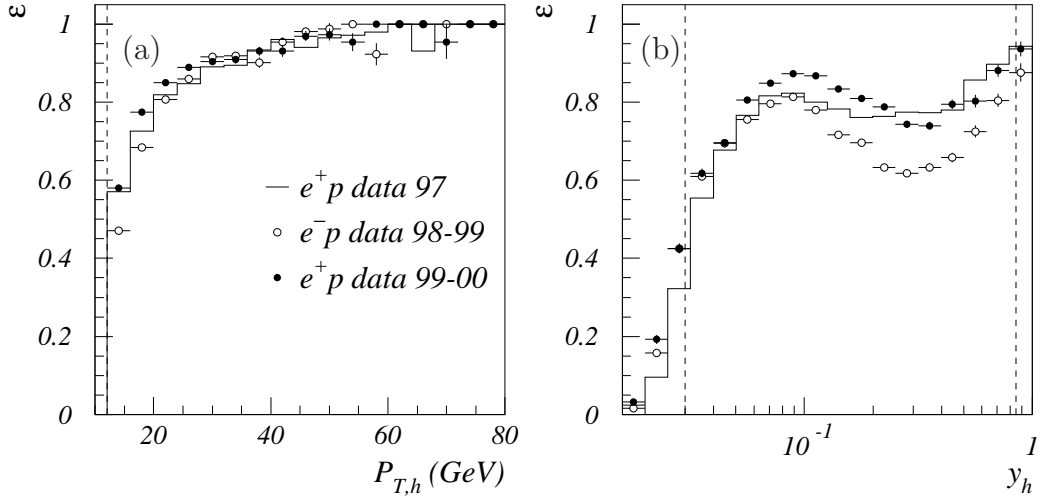


Figure 5.13: Comparisons of CC trigger efficiencies from three different run periods as a function of (a) the missing transverse momentum  $P_{T,h}$  and (b) the kinematical variable  $y_h$ . The selection cuts  $P_{T,h} > 12 \text{ GeV}$  and  $0.03 < y_h < 0.85$  are indicated with the dashed lines.

significant efficiency loss. The problem was fixed in the second part of the data taking. The efficiency shown in Fig.5.13 for the  $e^-p$  data is the averaged value of the two parts. The inefficiency at the low  $y$  region occurs because two big towers close to the forward beam pipe are not considered so far for the sum in the missing transverse energies. Currently there has been efforts investigating the possibility of reopening these trigger towers to improve the situation.

## 5.2 Measurement of inclusive cross sections at high $Q^2$

In this section, many cross section results will be given and compared with the standard DIS expectations. The cross sections are obtained following the measurement procedure shown in Sec.4.3.4. The results are presented in the form of reduced cross sections, which are related with the double differential cross sections (Eq.(3.9)) as:

$$\tilde{\sigma}^\pm = \frac{Q^4 x}{2\pi\alpha^2 Y_+} \frac{d^2\sigma^\pm}{dxdQ^2} = \tilde{F}_2(x, Q^2) - \frac{y^2}{Y_+} \tilde{F}_L(x, Q^2) \mp \frac{Y_-}{Y_+} x \tilde{F}_3(x, Q^2) \quad (5.9)$$

where  $\sigma^\pm$  stand for cross sections respectively for  $e^+p$  and  $e^-p$  collisions and  $Y_\pm = 1 \pm (1 - y)^2$  are the helicity functions.

Similarly the CC reduced cross sections are related with the double differential

cross sections (Eq.(3.12))<sup>10</sup>

$$\tilde{\sigma}_{\text{CC}}^{\pm} = \frac{2\pi x}{G_F^2} \left( \frac{Q^2 + M_W^2}{M_W^2} \right)^2 \frac{d^2\sigma_{\text{CC}}^{\pm}}{dxdQ^2} = \frac{1}{2} (Y_+ F_2^{\text{CC}} - y^2 F_L^{\text{CC}} \mp Y_- x F_3^{\text{CC}}) \quad (5.10)$$

and have the following simple quark flavor decomposition when the LO structure function formula in Eqs.(3.26)-(3.29) are used:

$$\tilde{\sigma}_{\text{CC}}^+ = x [(\bar{u} + \bar{c}) + (1 - y)^2 (d + s)] \quad (5.11)$$

$$\tilde{\sigma}_{\text{CC}}^- = x [(u + c) + (1 - y)^2 (\bar{d} + \bar{s})]. \quad (5.12)$$

Before presenting these results, various systematic sources and their effects on the cross sections will be discussed.

### 5.2.1 Systematic sources and resulting uncertainties on the cross section measurements

The uncertainties in the measurement lead to systematic errors on the cross sections which can be point to point correlated or uncorrelated. All the correlated systematic errors were checked to be symmetric to a good approximation and are assumed so in the following. The correlated systematic errors and main uncorrelated systematic errors of the NC and CC cross sections are given below:

- An uncertainty of the energy of the scattered electron is (see Fig.5.8) 1% if the  $z$  position<sup>11</sup> of its impact on the calorimeter is in the backward part ( $z < -145$  cm), 0.7% in the CB1 and CB2 wheels ( $-145 < z < 20$  cm), 1.5% for  $20 < z < 100$  cm and 3% in the forward part ( $z > 100$  cm). These uncertainties are obtained by the quadratic sum of an uncorrelated uncertainty and a point to point correlated uncertainty. This correlated uncertainty comes mainly from the potential bias of the calibration method and is estimated to be 0.5% in the whole LAr calorimeter. The resulting correlated (uncorrelated) systematic error on the NC cross sections is  $\lesssim 3$  (5)% except for the measurement at the two highest  $x$  values [94]. Due to the smaller luminosity for the 1998-1999  $e^-p$  data, the uncertainty in the CB1 and CB2 wheels was verified to 1% with the same uncertainty for the rest of the calorimeter region [204]. For the high statistics  $e^+p$  data of 1999-2000, the uncertainty of the electron energy scale is expected to be improved in particular in the forward region. For the preliminary cross section results which were based on about 2/3 of the full data sample, the uncertainty was conservatively quoted to be the same as the  $e^-p$  data [202].

---

<sup>10</sup>In the considered kinematic range ( $Q^2 \gtrsim 300 \text{ GeV}^2$ ), the proton mass term  $M^2$  can be neglected.

<sup>11</sup>The variation as a function of  $z$  is mainly a reflection of the statistical precision of the data samples with which the uncertainty could be checked.

- A correlated uncertainty of 1 mrad on the electron polar angle, and an uncorrelated uncertainty of 2.8 mrad when the angle is determined with the position measured in the calorimeter and the event vertex. The resulting correlated (uncorrelated) systematic error is small, typically  $\lesssim 1(2)\%$ .
- An uncertainty of 2% on the hadronic energy in the LAr calorimeter which is obtained from the quadratic sum of an uncorrelated systematic uncertainty of 1.7% and a correlated one of 1% originating from the calibration method and from the uncertainty of the reference scale of the scattered electron. The resulting correlated systematic error increases at low  $y$ , and is typically  $\lesssim 4\%$  except at high  $Q^2$  for the CC measurements (see Fig.5.10). For the preliminary results of the 1999-2000  $e^+p$  data, a conservative uncertainty of 3% was quoted. It should be noted that the same uncertainty on the hadronic energy measurement can result in different uncertainties on the cross section measurements. For CC cross sections at high  $Q^2$ , it is larger for the  $e^+p$  data at  $\sqrt{s} \simeq 300$  GeV and smaller for the  $e^-p$  data at  $\sqrt{s} \simeq 320$  GeV due to different  $Q^2$  dependences of the cross sections (see Sec.5.2.6).
- An uncertainty of 7(3)% on the energy of the hadronic final state measured in the SPACAL (tracking system<sup>12</sup>). Their influence on the cross sections is small compared to the uncorrelated uncertainty of the LAr calorimeter energy.
- A correlated uncertainty of 25% on the energy identified as noise in the LAr calorimeter (see Sec.5.1.5). The resulting systematic error is largest at low  $y$ , reaching 10 – 15% at  $x = 0.65$  and  $Q^2 \leq 2000$  GeV $^2$  in the NC measurements, while it remains below 5% for the CC measurements.
- A variation of the anti-photoproduction cuts (see Sec.5.1.1). The resulting correlated systematic error reaches a maximum of 12% at low  $x$  and  $Q^2$  in the CC analyses.
- An uncertainty of 30% on the subtracted photoproduction background. The resulting correlated error is always smaller than 5% in the NC and CC analyses and is further reduced in the analyses of the 1998-1999  $e^-p$  and 1999-2000  $e^+p$  data due to the improved subtraction method for NC and the additional anti-photoproduction cut for CC.

The other considered uncertainties giving rise to uncorrelated systematic errors on the cross sections are:

---

<sup>12</sup>An improvement in the energy resolution of about 10 – 20%, for events having a  $P_{T,h}$  between 10 to 25 GeV, is obtained by using a combination of the momentum of low transverse momentum particles ( $P_T < 2$  GeV) measured in the central tracking detector with the energy deposited by other particles of the hadronic final state measured in the calorimeter.

- An error of 2% (4% at  $y > 0.5$  and  $Q^2 < 500 \text{ GeV}^2$ ) from the electron identification efficiency in the NC analyses.
- an error of 1% from the efficiency of the track-cluster link requirement in the NC analyses.
- An error of 0.5 (3–8)% from the trigger efficiency in the NC (CC) analyses.
- An uncertainty of 1(3)% from the QED radiative corrections in the NC (CC) analyses [185].
- An error of 3% from the efficiency of the non- $ep$  background filters in the CC analyses.
- An error of 2% (5% for  $y < 0.1$ ) from the efficiency of the event vertex reconstruction in the CC analyses.

The typical total systematic error for the NC (CC) double differential cross section is about 4(8)%. In addition a normalization error of 1.5%, 1.8%, and 1.7% respectively for the 1994-1997  $e^+p$  data, the 1998-1999  $e^-p$  data and the 1999-2000  $e^+p$  data has to be taken into account, which is not included in the results shown in the following subsections.

### 5.2.2 Measurement and comparison of NC and CC reduced cross sections in $e^+p$ collisions at two center-of-mass energies

The NC reduced cross sections obtained from  $35.6 \text{ pb}^{-1}$  of the  $e^+p$  data taken from 1994 to 1997 at the center-of-mass energy of  $300 \text{ GeV}$  has recently been published by H1 [94]. The measurement covers a kinematic region for  $Q^2$  between  $150$  and  $30\,000 \text{ GeV}^2$ , for  $x$  between  $0.0032$  and  $0.65$ , and for  $y$  between  $0.007$  and  $0.88$ . This kinematic range has significantly extended the previous HERA measurements [131] both in  $Q^2$  (from  $5000$  to  $30\,000 \text{ GeV}^2$ ) and towards higher  $x$ , with measurements at  $x = 0.65$  for  $Q^2$  between  $650$  and  $20\,000 \text{ GeV}^2$ . At  $Q^2 \lesssim 500 \text{ GeV}^2$  the total error is dominated by the systematic uncertainties in the energy scale and identification efficiency of the scattered electron and by the uncertainty in the energy scale of the hadronic final state. In this region the systematic error is typically 4%. At higher  $Q^2$  the statistical error becomes increasingly dominant.

The new  $e^+p$  data of  $45.9 \text{ pb}^{-1}$  at a higher center-of-mass energy of  $320 \text{ GeV}$  has been analyzed and the preliminary results have been made available for the summer conferences [202]. The new data with slightly improved statistical precision cover the same kinematic range as the 1994-1997  $e^+p$  data. The two independent measurements are compared in Fig.5.14 and found in good agreement. The

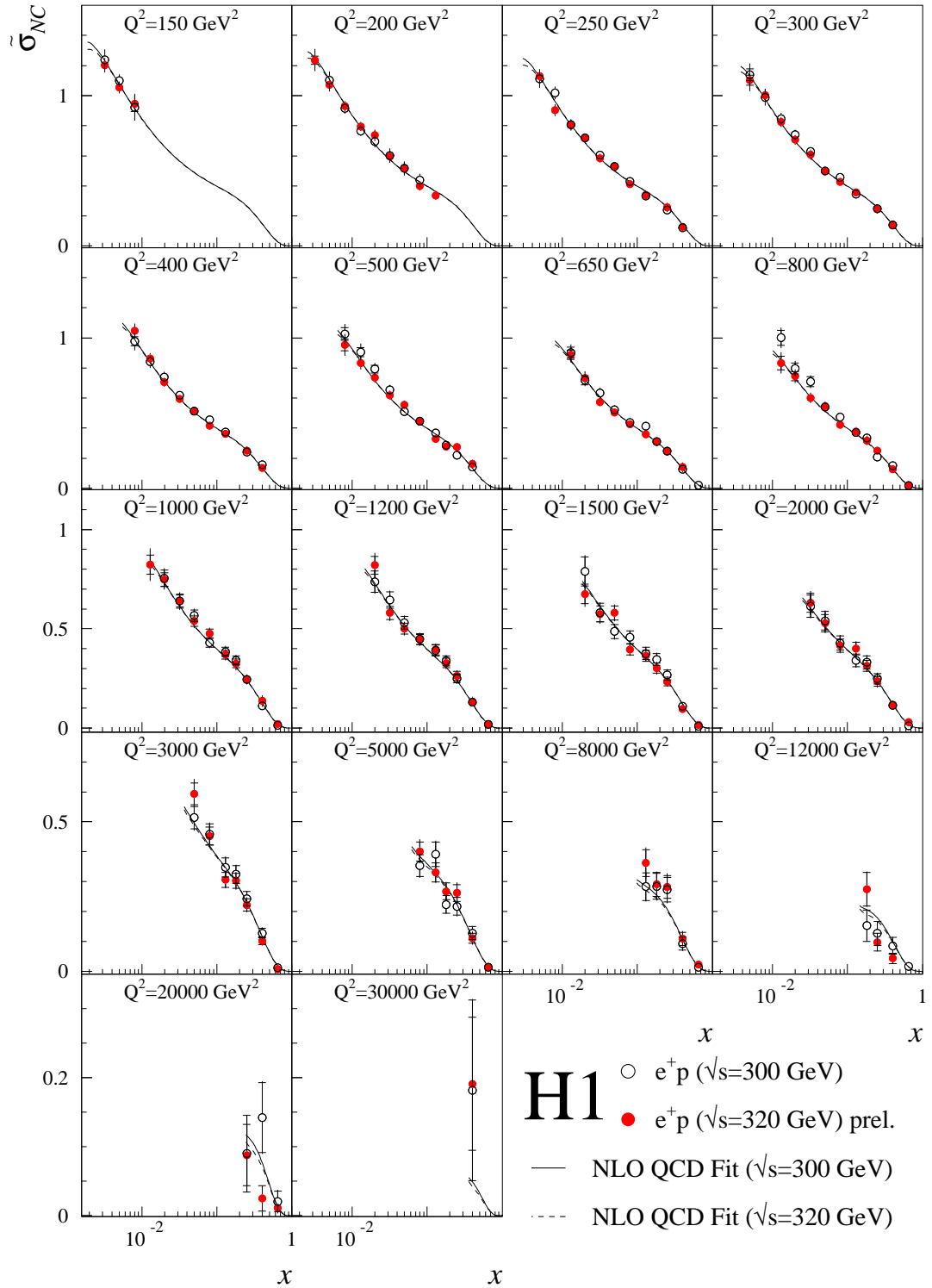


Figure 5.14: The  $e^+ p$  NC reduced cross section  $\tilde{\sigma}_{NC}$  is compared to the NLO QCD Fit [94]. Shown are the measurements from 1994-1999 data [94] and from 1999-2000 data [202] and the NLO QCD Fit predictions for different center-of-mass energies. The inner error bars represent the statistical error, and the outer error bars show the total error.

cross sections rise strongly as  $x$  decreases as seen in the low  $Q^2$  data, which can be interpreted as the increasing contributions from the gluon and sea quarks at low  $x$ . The measurements are well described by the standard DIS expectation from a NLO QCD Fit [94] to the  $e^+p$  1994-1997 data<sup>13</sup> as well as H1 structure function data at low  $Q^2$  [131] and fixed-target data by NMC [133] and BCDMS [17]. The difference in the center-of-mass energies is also indicated but remains small.

The similar comparison for the CC reduced cross sections is shown in Fig.5.15. The  $e^+p$  1994-1997 double differential CC cross sections cover the kinematic region for  $Q^2$  between 300 and 15 000 GeV<sup>2</sup> and for  $x$  between 0.013 and 0.4 [94]. The uncertainties on the measurements are dominated by the statistical errors. The largest systematic errors come from the uncertainty on the energy scale of the hadronic final state at high  $Q^2$  and from the uncertainty on the trigger efficiency at low  $Q^2$  and high  $x$ . A similar measurement has been published by the ZEUS experiment [203]. The new  $e^+p$  data [202], covering a similar range, are in good agreement with the published data and both measurements agree also well with the Standard Model (SM) expectations based on the same NLO QCD Fit mentioned above.

Given the good agreement between the two data sets and in order to facilitate the comparison of the  $e^+p$  data with the  $e^-p$  data in the later sections, we have combined the  $e^+p$  data at different center-of-mass energies to the higher energy in the following way<sup>14</sup>

$$\sigma_i = \frac{\sigma_{i,300}^{\text{meas}} \mathcal{L}_{300} + \sigma_{i,320}^{\text{meas}} \mathcal{L}_{320}}{\mathcal{L}_{300} (\sigma_{i,300}^{\text{th}} / \sigma_{i,320}^{\text{th}}) + \mathcal{L}_{320}} \quad (5.13)$$

where  $\sigma_{i,\sqrt{s}}^{\text{meas}}$  and  $\sigma_{i,\sqrt{s}}^{\text{th}}$  are respectively the measured and expected cross section. The statistical error is determined correspondingly and the systematic error is assumed to be fully correlated between the two measurements and taken from the new measurement.

---

<sup>13</sup>The agreement is equally good when the input data used in the fit was limited to  $Q^2 \leq 150$  GeV<sup>2</sup> [94]. The fit is any case independent of the new  $e^+p$  and  $e^-p$  data taken since 1998.

<sup>14</sup>The alternative way would be to make the correction to the measured cross section at 300 GeV from the 1994-1997  $e^+p$  data and to combine the corrected cross section with the one at 320 GeV from the 1999-2000  $e^+p$  data with the standard combination method using error weights. Indeed, the combined results obtained from both methods agree in the low  $Q^2$  region where the data are precise. However, the combined results can be substantially different in the region of higher  $Q^2$  and high  $x$  where the statistical error of the data is large ( $> 30\%$ ). The method using the luminosity weights is believed to be less sensitive to the statistical fluctuation.

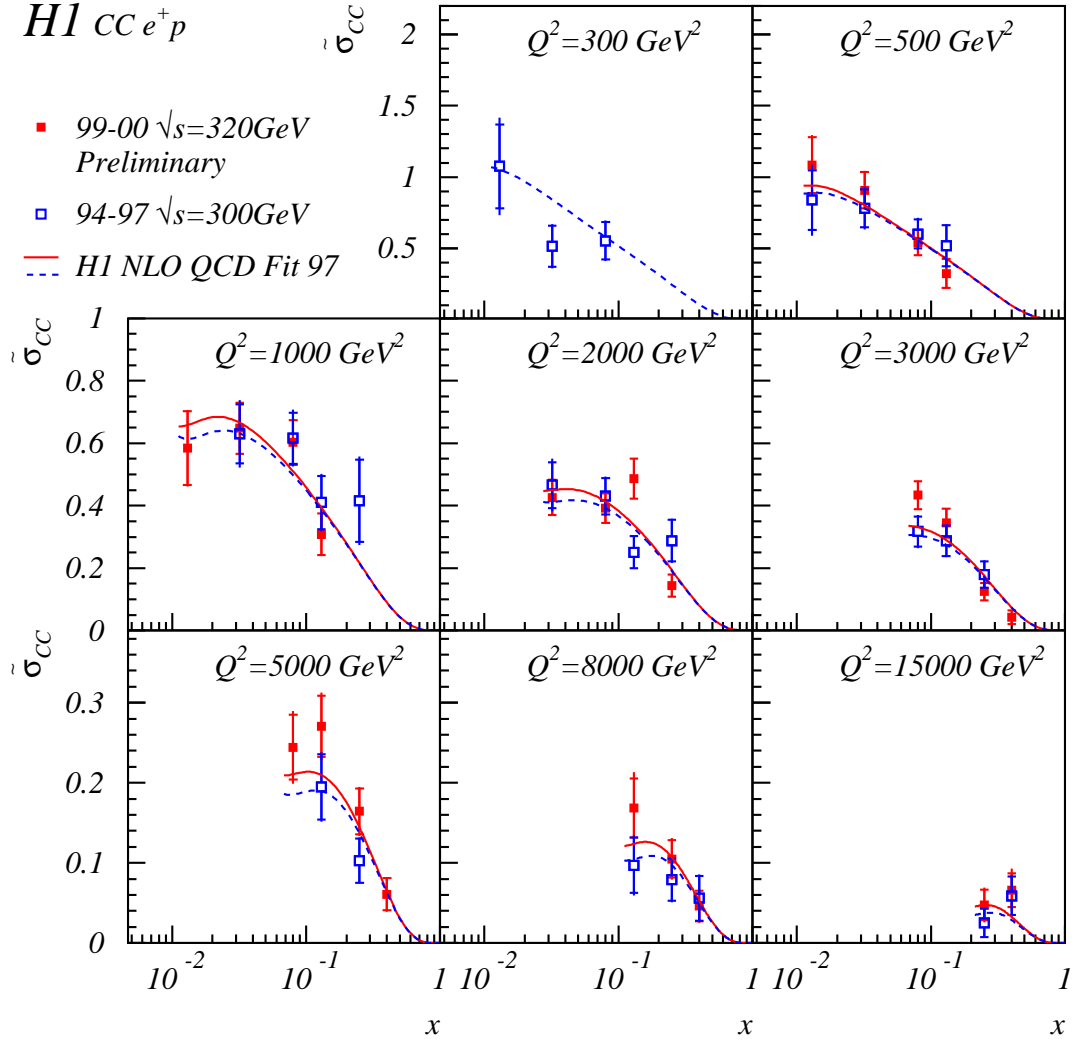


Figure 5.15: The  $CC e^+p$  reduced cross section  $\tilde{\sigma}_{CC}$  is compared to the NLO QCD Fit [94]. Shown are the measurements from 1994-1999 data [94] and from 1999-2000 data [202] and the NLO QCD Fit predictions respectively for  $\sqrt{s} = 320$  GeV (full curves) and 300 GeV (dashed curves). The inner error bars represent the statistical error, and the outer error bars show the total error.

### 5.2.3 Measurement and comparison of NC and CC reduced cross sections in $e^+p$ and $e^-p$ collisions

The combined  $e^+p$  NC reduced cross sections are compared with the results from the  $e^-p$  1998-1999 data [204] in Fig.5.16. For  $Q^2 \lesssim 1200 \text{ GeV}^2$ , where the cross section is dominated by the contribution from one-photon exchange, the data are essentially independent of the lepton-beam charges. With the increasing  $Q^2$  the  $e^-p$  cross section becomes larger than the  $e^+p$  cross section. The data thus give the clear evidence for the presence of the structure function  $xF_3$  (Eq.(5.9)). The standard DIS expectations from the NLO QCD Fit [94], which was partly constrained by the 1994-1997  $e^+p$  cross section data, are compared with the measured cross sections. The fit is found to give a good description of the  $x, Q^2$  behavior of the data, though in some of the phase space it has a slight tendency to be lower than the  $e^-p$  cross sections.

The combined  $e^+p$  CC reduced cross sections are compared with the results of the  $e^-p$  1998-1999 data [204] in Fig.5.17. Contrary to the NC data, the CC  $e^-p$  data are everywhere different from the  $e^+p$  data. This is the particular feature of the CC interaction mentioned already in Sec.3.1.2. At low  $Q^2$ , the difference is less pronounced because the sea quark contribution is relatively important, whereas at high  $Q^2$  and high  $x$ , the difference can mostly be attributed to the underlying quark flavor difference between  $xu$  and  $(1-y)^2xd$  as indicated respectively with the dashed and dash-pointed lines in Fig.5.17. Therefore the  $e^-p$  CC cross section at high  $Q^2$  and high  $x$  can be used to constrain the  $u$  valence quark while the  $e^+p$  CC cross section provides the constraint for the  $d$  valence quark (see Sec.5.3). The expectations from the same NLO QCD Fit are found to give a good description of the measured CC cross sections.

### 5.2.4 Measurement of the structure function $x\tilde{F}_3$ at high $Q^2$

Using the measured  $e^+p$  and  $e^-p$  double differential NC cross sections, both ZEUS [206] and H1 [204] have measured the structure function<sup>15</sup>  $x\tilde{F}_3(x, Q^2)$  at the high  $Q^2$  region. The measurement was obtained using Eq.(5.9) by subtracting the  $e^+p$  cross section from the  $e^-p$  cross section. Since the data are taken at slight different center-of-mass energies, a small correction<sup>16</sup> from the longitudinal

---

<sup>15</sup>It should be pointed out that the structure function  $x\tilde{F}_3(x, Q^2)$  measured at HERA arises from the contributions of the  $\gamma Z^0$  interference and  $Z^0$  exchange with the dominant contribution from the former (Eq.3.25), in which the weak neutral current couplings enter. Therefore it is different from the corresponding structure function  $xF_3 = x(u_v + d_v)$ , the sum of the  $u$  and  $d$  valence quarks (Eq.(3.54)), measured by neutrino-fixed-target experiments.

<sup>16</sup>The correction, estimated with  $\tilde{F}_L$  from the NLO QCD Fit [94], is about 10% at the lowest  $x$  and negligible elsewhere.

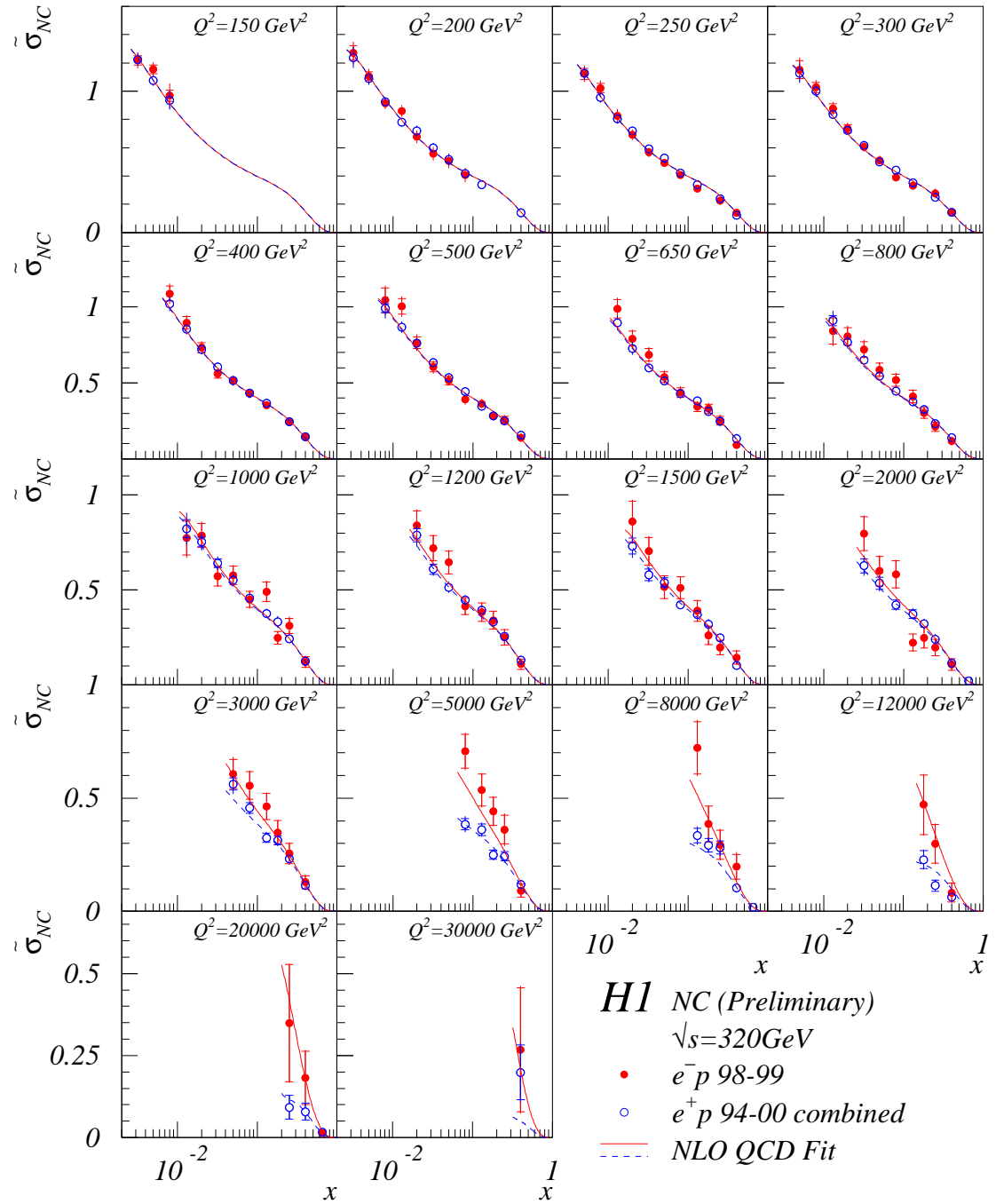


Figure 5.16: The combined  $e^+p$  NC reduced cross section  $\tilde{\sigma}_{NC}$  from 1994-2000 is compared to the  $e^-p$  cross section from 1998-1999 and the corresponding expectations from the NLO QCD Fit. The inner error bars represent the statistical error, and the outer error bars show the total error.

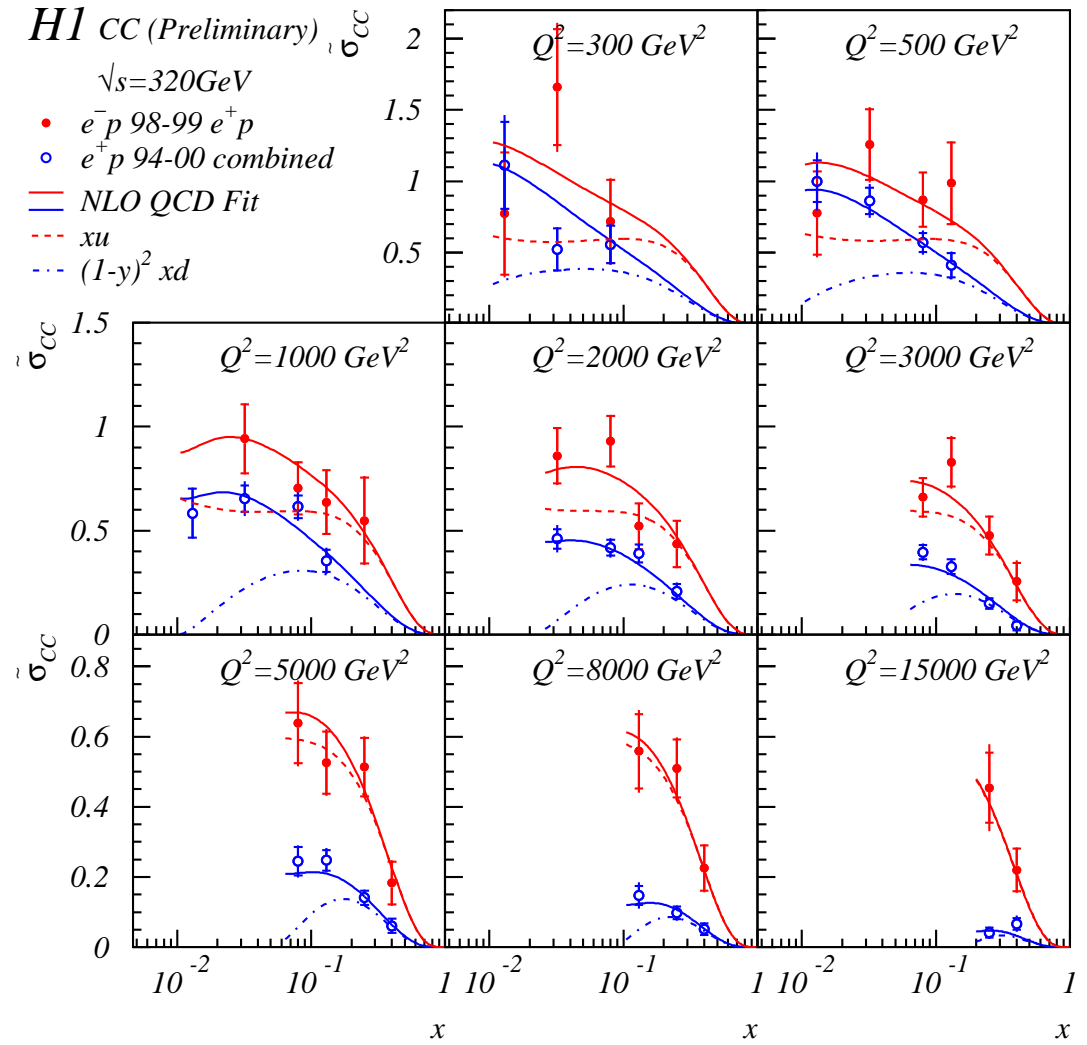


Figure 5.17: The combined  $e^+p$  CC reduced cross section  $\tilde{\sigma}_{CC}$  from 1994-2000 is compared with the  $e^-p$  cross section from 1998-1999 and the corresponding expectations from the NLO QCD Fit. The inner error bars represent the statistical error, and the outer error bars show the total error.

structure function is needed:

$$x\tilde{F}_3 = \left( \frac{Y_{-,320}}{Y_{+,320}} + \frac{Y_{-,300}}{Y_{+,300}} \right)^{-1} \left[ (\tilde{\sigma}^- - \tilde{\sigma}^+) + \tilde{F}_L \left( \frac{y_{320}^2}{Y_{+,320}} - \frac{y_{300}^2}{Y_{+,300}} \right) \right] \quad (5.14)$$

where the subscripts 300 and 320 denote the center-of-mass energies. The H1 results are shown in Fig.5.18 as a function of  $x$  at three values of  $Q^2$  at  $1500\text{ GeV}^2$ ,  $5000\text{ GeV}^2$ , and  $12\,000\text{ GeV}^2$ . The data are in good agreement with the expectation based on the H1 NLO QCD Fit [94] with a peak at  $x \simeq 0.1$  reflecting the valence quark structure of the constituent quarks. The ZEUS results are shown in Fig.5.19 as a function of  $Q^2$  for two values of  $x$  at  $0.56$  and  $0.1$ . The expectation of the SM, evaluated with both the CTEQ4 [208] and the MRST [58] parton distributions, gives a good description of the data.

### 5.2.5 Helicity structure of the CC cross sections

The measured double differential CC cross sections can be used to test the helicity dependence of the electron-quark interaction in the region of approximate Bjorken scaling,  $x \sim 0.1$ . In Fig.5.20, the reduced cross sections<sup>17</sup> from the combined  $e^+p$  1994-2000 data and the  $e^-p$  1998-1999 data are shown as a function of  $(1-y)^2$ . This kinematic variable is directly related to the scattering angle  $\theta^*$  in the electron-quark center-of-mass system through  $\cos^2(\theta^*/2) = 1-y$ . The  $e^+p$  and  $e^-p$  data show a different behavior. This is consistent with the expectations from the NLO QCD Fit [94]. Indeed, from Eqs.(5.11) and (5.12), one expects a small isotropic distribution from positron-antiquark scattering  $(\bar{u}, \bar{c})$  and a strong angular dependence on  $(1-y)^2$  from positron-quark scattering  $(d, s)$ , while for the  $e^-p$  interaction, the isotropic distribution is larger  $(u, c)$  and the angular dependence is weaker  $(\bar{d}, \bar{s})$ . In addition, both the isotropic distribution in the  $e^+p$  cross sections and the angular dependence in the  $e^-p$  cross sections increase as  $x$  decreases, this is consistent with an increasing sea quark contribution at lower  $x$ .

### 5.2.6 Measurement and comparison of the $Q^2$ dependence of NC and CC cross sections in $e^+p$ and $e^-p$ collisions

The single differential cross sections  $d\sigma_{\text{NC(CC)}}/dQ^2$  have also been measured by H1 [94, 202, 204] and by ZEUS [205, 203, 206, 207]. The combined  $e^+p$  NC and CC data are compared with the  $e^-p$  data respectively in Figs.5.21 and 5.22. The

---

<sup>17</sup>In Refs.[94, 204], the so-called structure function term  $\phi_{\text{CC}}$  was introduced, which is related to the reduced CC cross section by a weak correction factor  $\tilde{\sigma} = \phi(1 + \delta_{\text{weak}})$ . However, since this correction is small with respect to the uncertainty of the measurements, we choose not to distinguish them here.

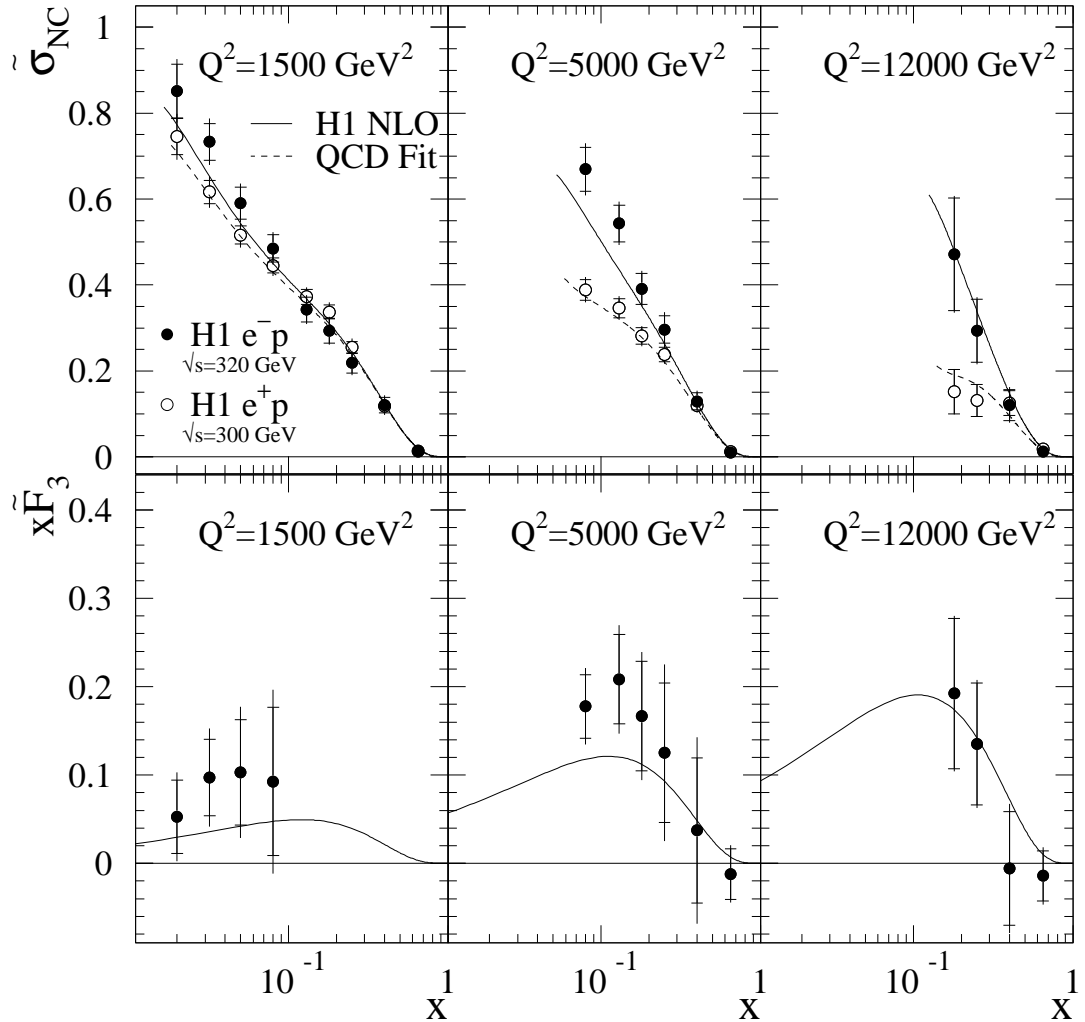


Figure 5.18: A measurement of the structure function  $x\tilde{F}_3$  by H1 [204] as a function of  $x$  for three values of  $Q^2$  at  $1500 \text{ GeV}^2$ ,  $5000 \text{ GeV}^2$ , and  $12000 \text{ GeV}^2$  based on the  $e^+p$  1994-1997 and  $e^-p$  1998-1999 NC data. The inner error bars represent the statistical error, and the outer error bars show the total error. The SM expectations for the reduced cross sections and  $x\tilde{F}_3$  from the H1 NLO QCD Fit [94] are also shown.

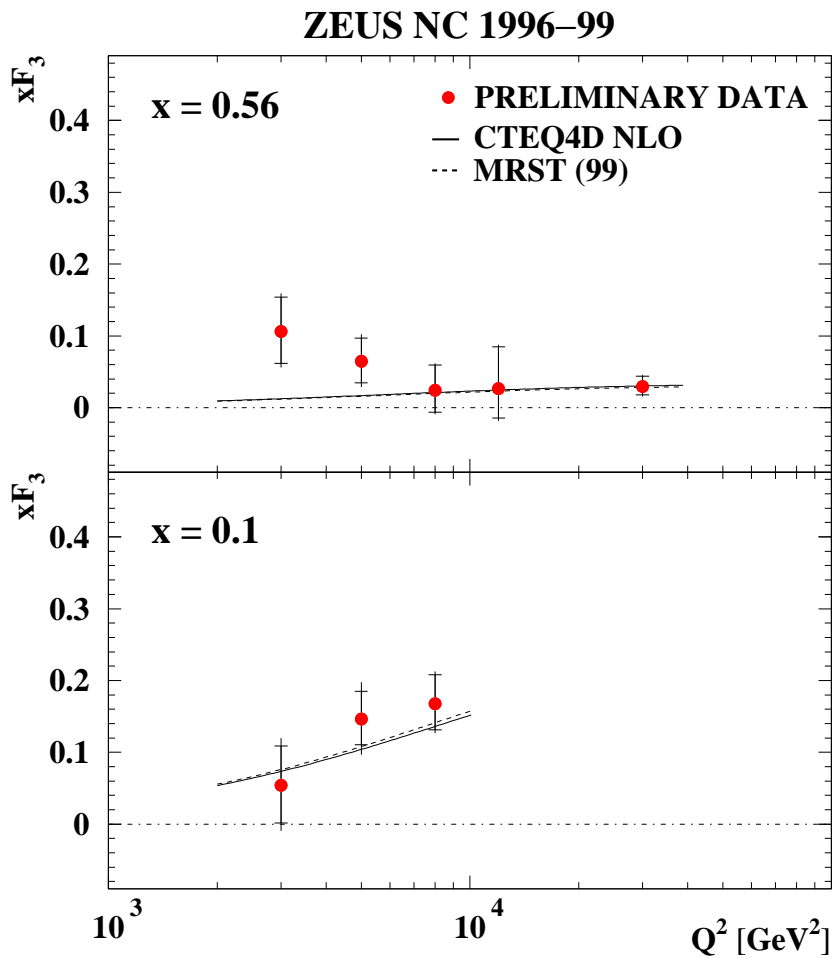


Figure 5.19: A measurement of the structure function  $x\tilde{F}_3$  by ZEUS [206] as a function of  $Q^2$  for two values of  $x$  at 0.56 and 0.1 based on the  $e^+p$  1994–1997 and  $e^-p$  1998–1999 NC data. The inner error bars represent the statistical error, and the outer error bars show the total error. The SM expectations from CTEQ4 [208] and MRST [58] are also shown.

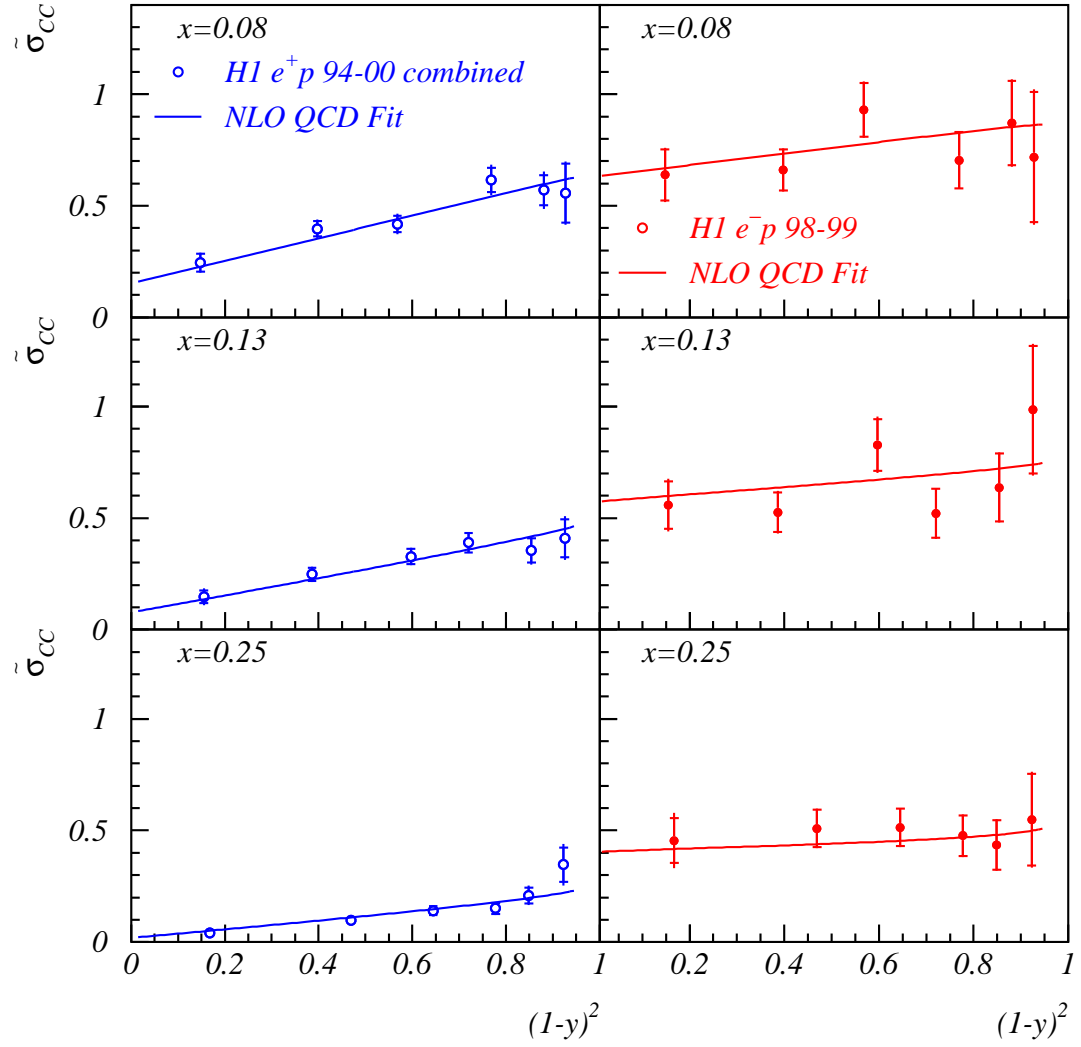


Figure 5.20: The  $CC$  reduced cross sections  $\tilde{\sigma}_{CC}$  from the combined  $e^+p$  1994-2000 data (left) and from the  $e^-p$  1998-1999 data (right) shown as a function of  $(1-y)^2$  for three  $x$  values 0.08, 0.13 and 0.25. The inner (outer) error bars represent the statistical (total) errors. The curves are expectations from the NLO QCD Fit [94].

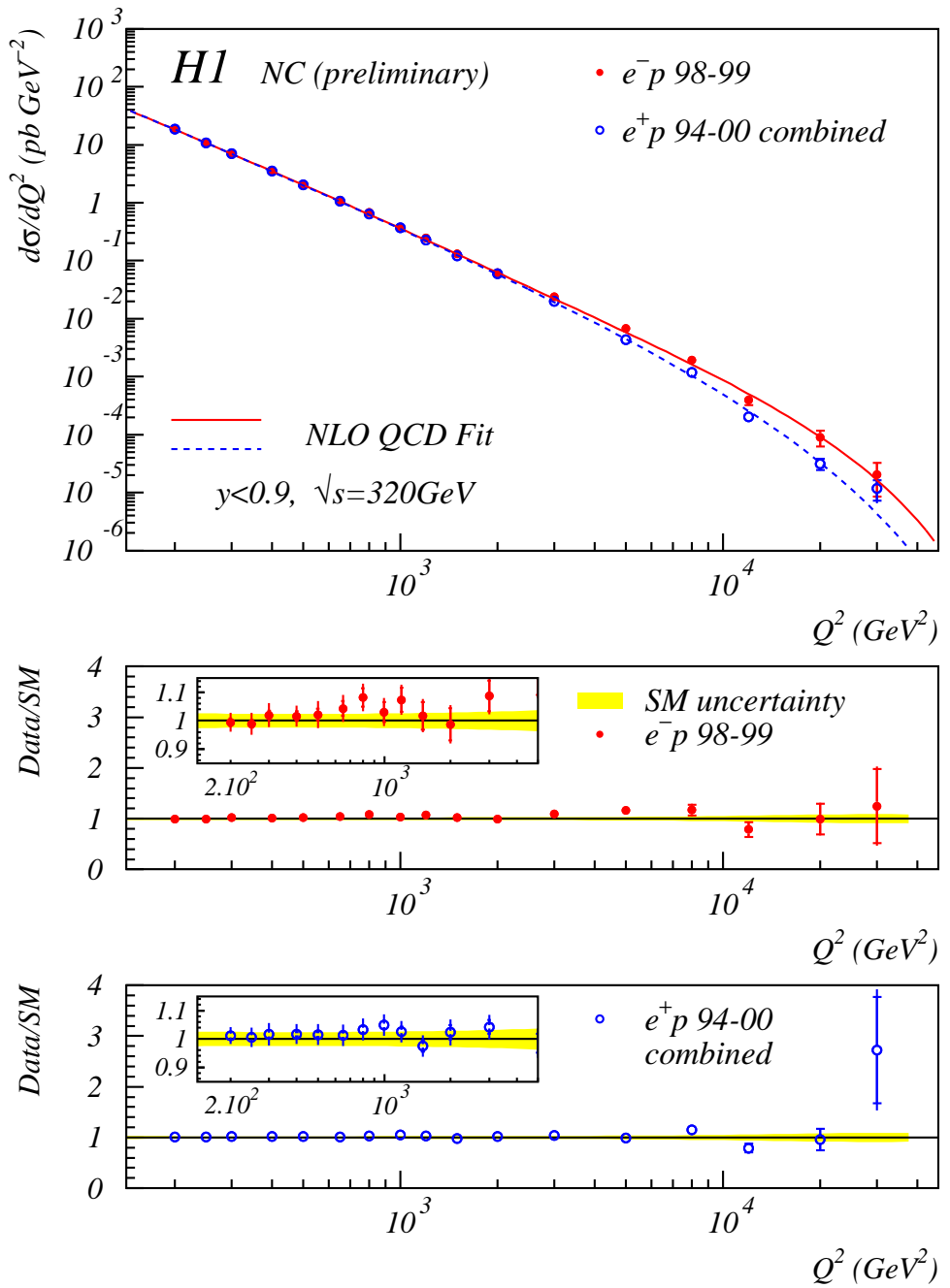


Figure 5.21: The combined  $e^+ p$  NC cross sections  $d\sigma/dQ^2$  from 1994-2000 are compared with the  $e^- p$  cross sections from 1998-1999 and the corresponding expectations from the NLO QCD Fit. The inner error bars represent the statistical error, and the outer error bars show the total error. The shaded error bands represent the uncertainties on the SM expectations of the  $e^- p$  and  $e^+ p$  cross sections.

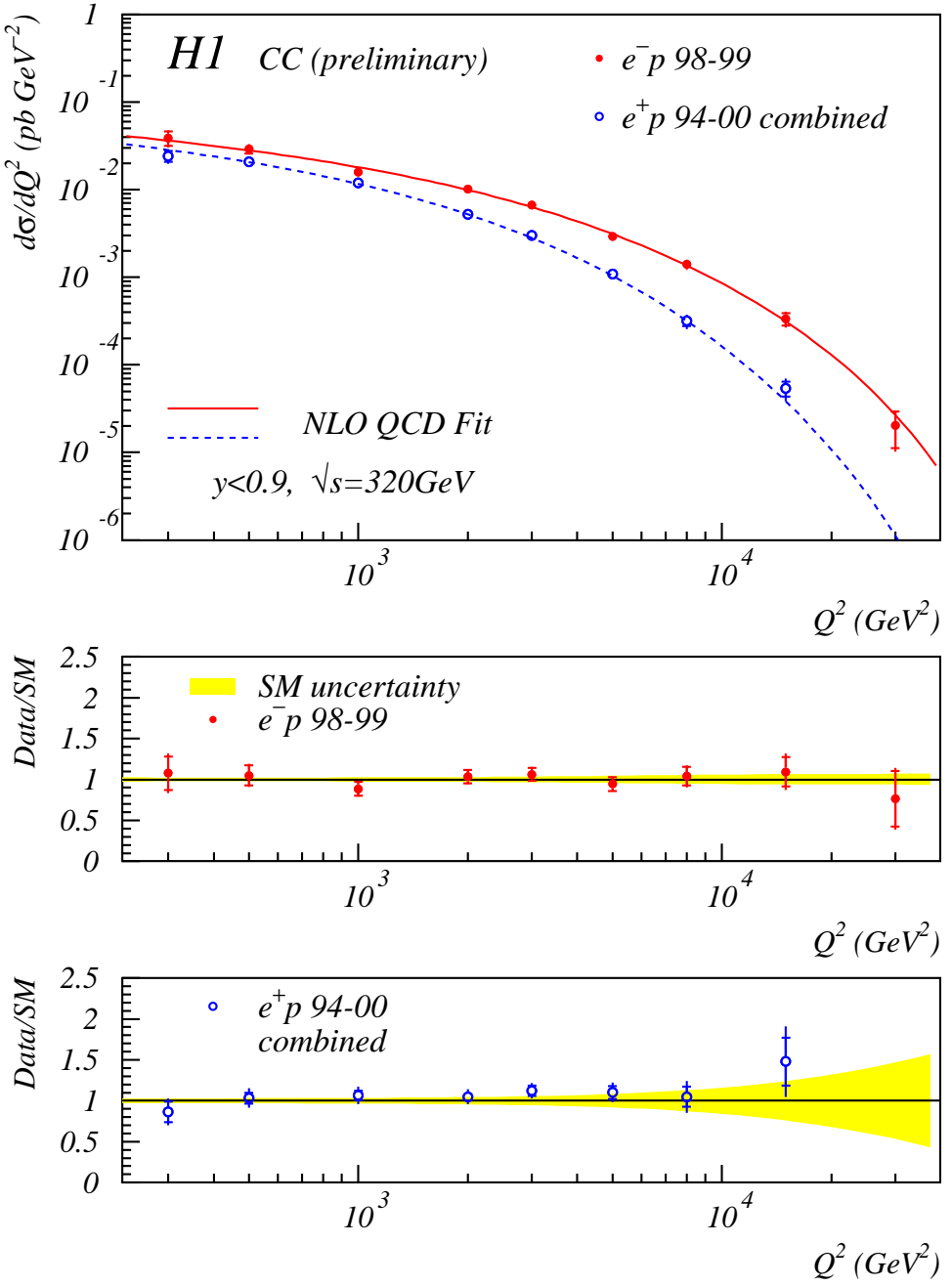


Figure 5.22: The combined  $e^+ p$  CC cross sections  $d\sigma/dQ^2$  from 1994-2000 are compared with the  $e^- p$  cross section from 1998-1999 and the corresponding expectations from the NLO QCD Fit. The inner error bars represent the statistical error, and the outer error bars show the total error. The shaded error bands represent the uncertainties on the SM expectations of the  $e^- p$  and  $e^+ p$  cross sections.

measurement of the NC cross sections spans more than two orders of magnitude in  $Q^2$ . The cross sections fall with  $Q^2$  by about six orders of magnitude. The  $e^-p$  NC data have a statistical precision varying between 1.3% and 58% from low to high  $Q^2$  and are dominated by the systematic uncertainty for  $Q^2 \lesssim 1000 \text{ GeV}^2$ . The combined  $e^+p$  NC data have a better statistical precision between 0.5% to 38%, which dominates over the conservatively estimated systematic uncertainty only at  $Q^2 > 8000 \text{ GeV}^2$ . The ratio of the measurements with the SM expectations, represented in the middle and lower figures respectively for the  $e^-p$  and the combined  $e^+p$  data, show that the data have no significant deviation from the SM DIS expectations, albeit may have some structure at the very high  $Q^2$  region in particular for the combined  $e^+p$  data. The SM uncertainty, which varies  $\sim 3\%$  to  $\sim 8\%$  from the low to high  $Q^2$  values shown, represents the uncertainty of the expectation due to the assumptions made in the fit, as well as the uncertainties of the experimental data entering the fit [94].

The  $e^-p$  CC data have a statistical precision between 7.5% and 19.2% with the best precision at  $Q^2 \simeq 3000 \text{ GeV}^2$ . The combined high statistics  $e^+p$  CC data have about the same precision at high  $Q^2$  and marginally better precision at other  $Q^2$  values due to the smaller  $e^+p$  CC cross sections. The cross section uncertainties are mostly dominated by the statistical errors. The CC cross sections covering about the similar  $Q^2$  range as the NC data shown in Fig.5.21 only vary over about three orders of magnitude. The difference is due to the dominant contribution at low  $Q^2$  from the photon exchange in the NC process. At high  $Q^2$ , the NC cross sections are comparable with the CC cross sections, as shown in Fig.5.23, confirming electroweak unification of bosons exchanged in the  $t$ -channel. The SM uncertainty is larger for the  $e^+p$  data, as at high  $Q^2$  the cross section is dominated by the  $d$  valence quark which is less well constrained than the  $u$  valence quark.

### 5.2.7 Measurement and comparison of the $x$ dependence of NC and CC cross sections in $e^+p$ and $e^-p$ collisions

The single differential cross sections  $d\sigma_{\text{NC(CC)}}/dx$  have also been measured by H1 [94, 204] and by ZEUS [205]. In Figs.5.24 the  $e^-p$  NC cross sections from 1998-1999 are compared with the  $e^+p$  data from 1994-1997. In order to see the difference due to the change in the lepton-beam charge, a small correction is applied to the  $e^+p$  data to account for the different center-of-mass energies. The H1 measurement for  $Q^2 > 1000 \text{ GeV}^2$  ( $Q^2 > 10000 \text{ GeV}^2$ ) extends in  $x$  from 0.02 to 0.65 (from 0.13 to 0.65). The cross sections rise towards low  $x$ , a behavior seen already from the double differential cross sections (Figs.5.14 and 5.16). The decrease of the cross section at low  $x$  edges are due to the kinematic cut  $y < 0.9$ . The SM expectations for  $e^-p$  and  $e^+p$  collisions are compared with the data. While only a small difference between the  $e^-p$  and  $e^+p$  data is seen for  $Q^2 > 1000 \text{ GeV}^2$ , it is much more pronounced for  $Q^2 > 10000 \text{ GeV}^2$  in accordance

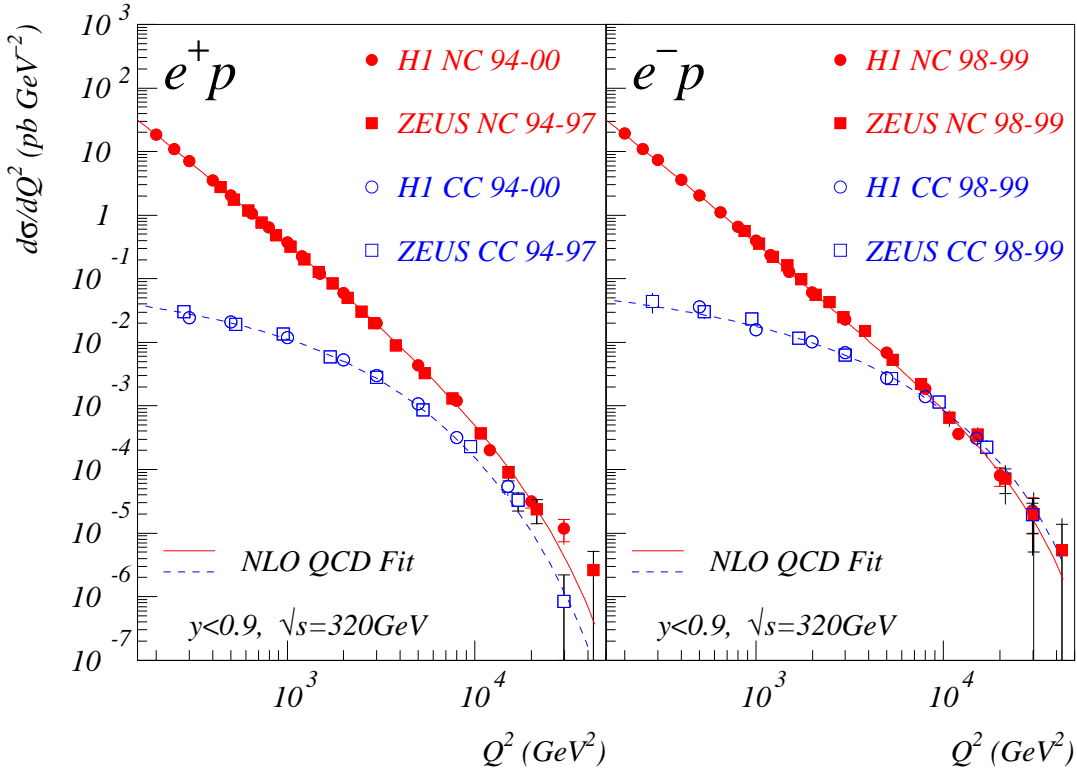


Figure 5.23: The NC and CC cross sections measured by H1 and ZEUS for  $e^+p$  (left) and  $e^-p$  (right) collisions in comparison with the corresponding SM expectations from the NLO QCD Fit [94]. The inner error bars represent the statistical error, and the outer error bars show the total error.

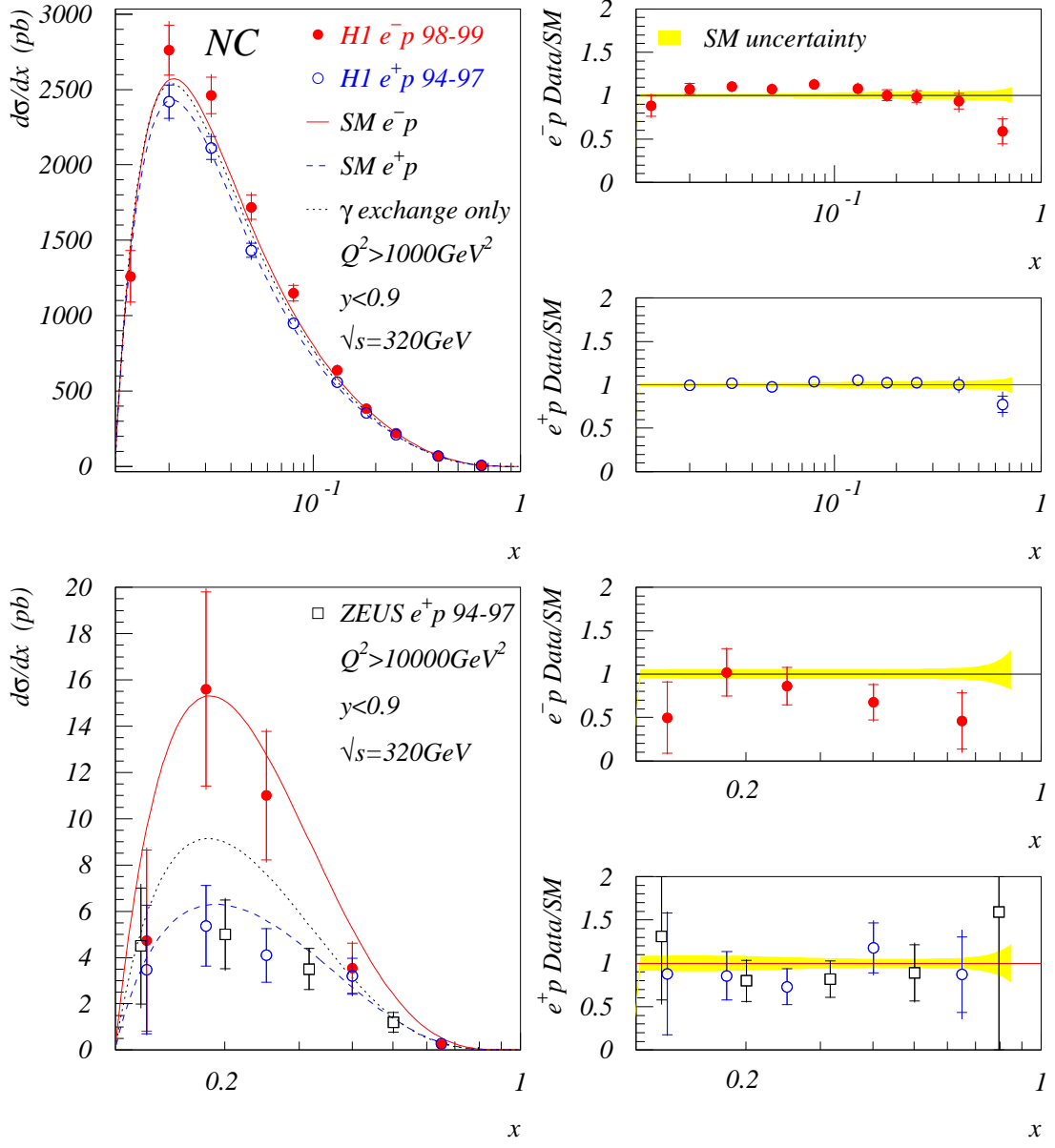


Figure 5.24: The  $e^- p$  NC cross sections  $d\sigma/dx$  from 1998-1999 in comparison with the  $e^+ p$  data from 1994-1997 and the corresponding expectations from the NLO QCD Fit [94]. The dotted lines represent the expectations from the pure photon exchange only. The inner error bars represent the statistical error, and the outer error bars show the total error. The shaded error bands represent the uncertainties on the SM expectations of the  $e^- p$  and  $e^+ p$  cross sections.

with the constructive and destructive interference from the contribution of  $x\tilde{F}_3$  (see Fig.3.1 and Sec.5.2.4). The measured cross sections clearly disagree with the expectation for pure photon exchange only, which is independent of the lepton-beam charges, as indicated with the dotted curves in Fig.5.24. The data are in good agreement with the SM expectations with a tendency to be lower<sup>18</sup> than the expectation for the  $e^-p$  data at  $Q^2 > 10000 \text{ GeV}^2$ , as well as at  $x = 0.65$  for all data in the full  $Q^2$  range. The implication will be discussed in Sec.5.3. Also shown are the SM uncertainties, which for  $Q^2 > 1000 \text{ GeV}^2$  varies between  $\sim 2.5\%$  at  $x = 0.02$  to  $\sim 7\%$  at  $x = 0.65$  and degrades slightly for  $Q^2 > 10000 \text{ GeV}^2$ .

The new  $e^-p$  CC cross sections measured by H1 using data taken in 1998-1999 [204] is compared in Fig.5.25 with the  $e^+p$  H1 data from 1994-1997 [94]. As

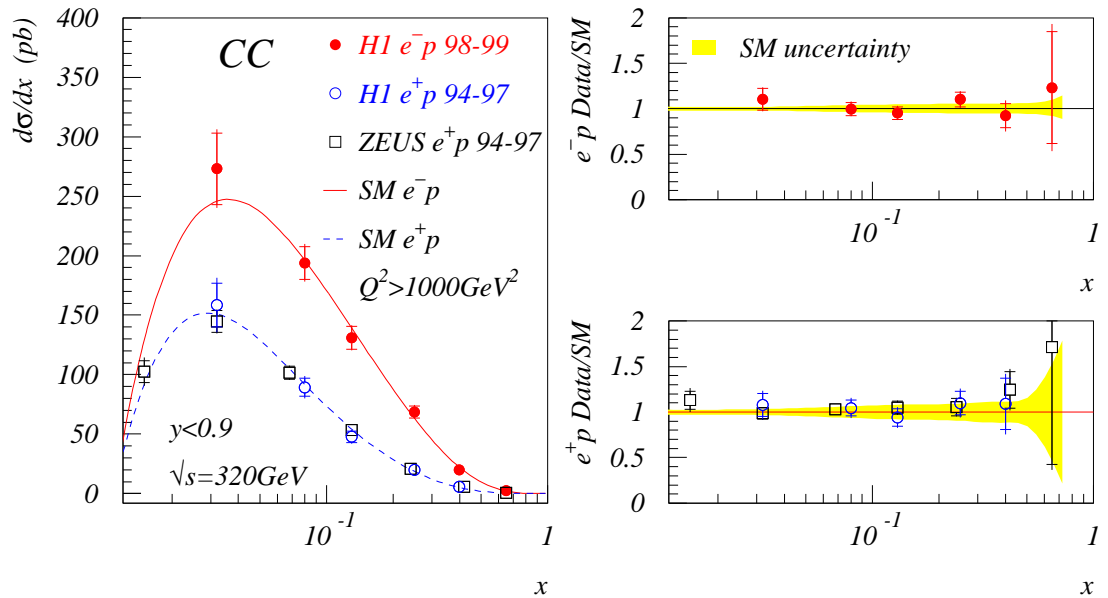


Figure 5.25: The  $e^-p$  CC cross sections  $d\sigma/dx$  from 1998-1999 in comparison with the  $e^+p$  data from 1994-1997 and the corresponding expectations from the NLO QCD Fit. The inner error bars represent the statistical error, and the outer error bars show the total error. The shaded error bands represent the uncertainties on the SM expectations of the  $e^-p$  and  $e^+p$  cross sections.

for NC, a small correction is applied to account for the different proton beam energies. The  $e^+p$  cross sections from ZEUS [203] is also shown<sup>19</sup>. The larger  $e^-p$  cross sections compared to the  $e^+p$  cross sections reflect again the different quark

<sup>18</sup>The agreement between the  $e^+p$  data and the expectation from the NLO QCD Fit is better since the data were included in the fit. The new  $e^-p$  data, which indicate some difference with the fit, should bring additional constraints on the various parton distribution functions.

<sup>19</sup>Since the original cross sections are measured for  $Q^2 > 200 \text{ GeV}^2$ , a (large) correction is needed, which amounts to 0.299, 0.594, 0.728, 0.783, 0.812, 0.823, and 0.817 respectively for  $x = 0.015, 0.032, 0.068, 0.13, 0.24, 0.42$ , and 0.65.

flavors probed by the  $W^\pm$  bosons in the  $e^\pm p$  scatterings and the helicity structure of the CC interaction (see Eqs.(5.11) and (5.12)). Within the experimental errors, the data agree well with the SM expectations represented by the NLO QCD Fit [94]. The uncertainties of the SM expectations are shown by the shaded error bands. As mentioned already in Sec.5.2.6, the uncertainty, which becomes increasingly large towards high  $x$ , is significantly larger for the  $e^+ p$  expectation than for  $e^- p$ .

### 5.3 Valence quark distribution at high $Q^2$ and high $x$

As it was demonstrated in Fig.5.17 (Sec.5.2.3), the CC cross sections at high  $Q^2$  and high  $x$  are dominated by the up and down valence quarks ( $xu_v$ ,  $xd_v$ ) contributions. These data can therefore be used to constrain these valence quark densities at high  $Q^2$  and high  $x$ . The NC cross sections, though they do not possess the same quark flavor discriminant power as the CC cross sections, provide an additional constraint on  $xu_v$  since its contribution to the NC cross section dominates over that of  $xd_v$  due to the larger quark charge.

There has been a renewed interest on the behavior of the ratio  $d/u$  at high  $x$  in recent years [209, 210]. The ratio  $d/u$  is relatively well constrained at  $x < 0.3$  by DIS structure function data as well as the  $W$  asymmetry measurement. At higher  $x$  ( $0.3 < x < 0.7$ ), the constraint becomes weaker since it is only available from DIS structure function data alone. These data are uncertain because of

- **Experimental systematic uncertainties:** The fixed-target data are often dominated by various systematic errors. It is not at all trivial how these errors are treated properly in a QCD analysis.
- **Higher-twist contribution:** The fixed-target data are located at relatively low  $Q^2$  and high  $x$ . The higher-twist contribution is expected to be important as it behaves as  $1/[(1-x)Q^2]$  with respect to the leading-twist contribution.
- **Large nuclear corrections:** As far as the  $x$  valence quark is concerned, it is constrained mainly by the deuteron data, of which the nuclear binding correction can be large. This explains why the uncertainty of the SM expectation on the  $e^+ p$  CC cross section (dominated by the  $d$  valence quark at high  $x$ ) was larger than that on the  $e^- p$  CC and  $e^\pm p$  NC cross sections (dominated by the  $u$  valence quark).

At even higher  $x$  ( $x > 0.7$ ) there is no reliable data available and the model predictions for  $u/d$  vary widely from 0 to about 0.2. In most of the conventional

QCD analyses performed up to now, the  $d/u$  ratio was assumed to approach zero as  $x$  goes to one. It has been argued recently that a large value around 0.2 is able to give a better description of existing data at high  $x$  [209].

When these parton densities are evolved to high  $Q^2$ , one has to take into account additional uncertainties:

- The uncertainty on the strong coupling constant  $\alpha_s$  and higher order perturbative corrections.
- The so called “feed-down” uncertainty [211]. The parton density, in the convolution on the right-hand side of the DGLAP equations (3.42) and (3.43), is sampled at  $x' \geq x$  (Eq.3.37). The evolution is thus susceptible to the feed-down of an anomalously large contribution at  $x \simeq 1$ . Such a contribution could escape detection by the fixed-target measurements while still influencing the evolution to the high  $Q^2$  region.

The HERA data at high  $Q^2$  as constraints on the valence quarks have thus the advantage that most of the these potential problems are absent. In the following two independent methods will be discussed to provide a determination of the valence quark distributions at high  $Q^2$ .

### 5.3.1 Local extraction of valence quark densities

The fact that the contribution of the valence quark densities dominates in the  $e^\pm p$  NC and CC cross sections at high  $x$  makes it possible to extract  $xu_v$  and  $xd_v$  locally and directly from the measured cross sections. The first extraction was performed by H1 for two values of  $x$  at 0.25 and 0.4 using the  $e^+p$  NC and CC cross sections from the 1994-1997 data:

$$xq_v(x, Q^2) = \sigma_{\text{meas}}(x, Q^2) \left( \frac{xq_v(x, Q^2)}{\sigma(x, Q^2)} \right)_{\text{th}} \quad (5.15)$$

where  $\sigma_{\text{meas}}(x, Q^2)$  is the measured NC or CC double differential cross sections, and the second factor on the right-hand-side of the equation is the theoretical expectation from the previous H1 fit [94]. Only those points where the  $xq_v$  contribution is greater than 70% of the total cross section are selected. The extracted parton densities are thus rather independent of the theoretical input as the uncertainty on the dominant valence quark contribution and that of the corresponding cross section largely cancel in the ratio.

With the new  $e^-p$  1998-1999 and  $e^+p$  1999-2000 data, similar extractions can be made and are extended to  $x = 0.65$  for  $xu_v$ . In practice, the  $d$  valence quark densities are determined from the combined  $e^+p$  CC cross sections discussed in Sec.5.2.2 (Eq.(5.13)). The  $u$  valence quark densities are determined respectively

from the combined  $e^+p$  NC,  $e^-p$  NC, and  $e^-p$  CC cross sections. The three independent determinations of  $xu_v$  are then combined. The resulting  $xu_v$  and  $xd_v$  represent an improved statistical precision of typically 50% and up to 100% at high  $Q^2$  with respect to the first extraction. The results are shown as the data points in Fig.5.26.

### 5.3.2 Valence quark densities from a new NLO QCD Fit

The valence quark distributions have also been determined from a new NLO QCD Fit<sup>20</sup> using all cross sections measured by H1 at high  $Q^2$ . The fit was performed with the NLO DGLAP evolution equations using the  $\overline{\text{MS}}$  renormalization and factorization scheme and treating the heavy flavors as massless quarks. Five quark and gluon components are parameterized in an MRS-like form at  $Q_0^2 = 15 \text{ GeV}^2$ :

$$xu_v = A_u x^{B_u} (1-x)^{C_u} (1+a_u \sqrt{x}) \quad (5.16)$$

$$xd_v = A_d x^{B_d} (1-x)^{C_d} (1+a_d \sqrt{x}) \quad (5.17)$$

$$xg = A_g x^{B_g} (1-x)^{C_g} \quad (5.18)$$

$$x(\bar{u} + \bar{c}) = A_1 x^{B_1} (1-x)^{C_1} (1+a_1 x) \quad (5.19)$$

$$x(\bar{d} + \bar{s} + \bar{b}) = A_2 x^{B_2} (1-x)^{C_2} (1+a_2 x) \quad (5.20)$$

The number of chosen parameters for each component are dictated by the input data sets and their precision. In order to have a reliable constraint on the gluon and sea quarks, the new low  $Q^2$  H1 data [135] (Sec.4.5) are also included. The minimum  $Q^2$  cut on the data is  $Q_{\min}^2 = 20 \text{ GeV}^2$ . The parameters  $A_u$  and  $A_d$  are constrained by the valence quark counting rules

$$\int_0^1 u_v dx = 2 \quad \text{and} \quad \int_0^1 d_v dx = 1. \quad (5.21)$$

The momentum sum rule allows the determination of one further normalization parameter, taken to be  $A_g$ . The rest of the parameters are constrained by the fit which uses the MINUIT program [62] to minimize the  $\chi^2$  defined as [135]

$$\chi^2 = \sum_{j=1}^{N_{\text{dataset}}} \left[ \sum_{i=1}^{N_j^{\text{data}}} \frac{\{f_{i,j}^{\text{data}} - f_{i,j}^{\text{fit}} [1 - \nu_j \delta \mathcal{L} / \mathcal{L} - \sum_k \delta_{i,k} (s_{j,k})]\}^2}{\sigma_{i,\text{stat}}^2 + \sigma_{i,\text{uncor}}^2} + \nu_j^2 + \sum_k s_{j,k}^2 \right] \quad (5.22)$$

---

<sup>20</sup>The fit differs from the one in [94] in that the new NC and CC cross sections measured from the 1998-1999  $e^-p$  and 1999-2000  $e^+p$  data at high  $Q^2$  shown in the previous sections are included as well as the new low  $Q^2$  precision data from 1996-1997 mentioned in Sec.4.5, and at the same time no fixed target data are used. The fit also differs from the one in [135] in that the latter uses only the  $e^+p$  data at  $\sqrt{s} = 300 \text{ GeV}$  and for  $Q^2 < 3000 \text{ GeV}^2$  so that the heavy flavors could be treated massively. The emphasis also differs, which for this fit is more on the valence quarks at high  $Q^2$  and high  $x$  while in [135] it is more on the gluon density at low  $x$  and on the extraction of  $\alpha_s$ .

where the sums run over the data  $i$ , various data sets  $j$  and sources  $k$  of correlated systematic uncertainties. The quantity  $\nu_j$  stands for the number of standard deviations for the relative normalization uncertainty of the data set  $j$ , and  $\delta_{i,k}(s_{j,k})$  the relative shift of the data  $i$  induced by a change by  $s_{i,k}$  standard deviations of the correlated systematic source  $k$ .

The results of the fit are presented in Table 5.2 in which the  $\chi^2$  is given for each data sets, together with their optimal normalization factors. The total  $\chi^2$

Table 5.2: *Results of the new NLO QCD Fit showing the used data sets and their contribution to the  $\chi^2$  and the optimal normalization factors.*

Data set	$e^+p$ NC	$e^+p$ CC	$e^-p$ NC	$e^-p$ CC	Low $Q^2$	Total
data points	134	29	115	26	65	369
$\chi^2$	81.9	19.9	95.6	36.4	55.3	289.1
normalization	1.001	1.006	1.010	1.005	0.9777	

per degree of freedom (dof) is  $289.1/(369-16)=0.82$ . The normalization factors are also well within the quoted luminosity uncertainty. The parameters of the fit are given in Table 5.3.

Table 5.3: *Fitted parameters of the quark and gluon distributions at  $Q_0^2 = 15 \text{ GeV}^2$ . The parameters  $A_u$ ,  $A_d$  and  $A_g$  are constrained by the sum rules.*

$xq$	$A_q$	$B_q$	$C_q$	$a_q$
$xu_v$	1.71	0.463	4.93	12.25
$xd_v$	4.90	0.872	5.89	-0.015
$xg$	3.39	-0.162	11.67	
$x(\bar{u} + \bar{c})$	0.140	-0.268	8.31	3.54
$x(\bar{d} + \bar{s} + \bar{b})$	0.140	-0.268	13.54	22.7

The resulting valence quark distributions  $xu_v$  and  $xd_v$  are shown in Fig.5.26 labeled “NLO QCD Fit: H1 only” in comparison with the results obtained from the local extraction method (Sec.5.3.1), and other parameterizations MRST [58], CTEQ5 [69], and the previous H1 NLO QCD Fit [94].

To conclude, the following points are ready to be listed:

- For the first time, the valence quark distributions at high  $x$  are constrained by the H1 experiment alone with an experimental precision (shaded error bands in Fig.5.26) varying between 6% at  $x = 0.25$  and  $x = 0.4$  and  $\sim 10\%$  at  $x = 0.65$  for  $xu_v$  and  $\sim 20\%$  for  $xd_v$ . The quoted uncertainties correspond

## H1 Preliminary

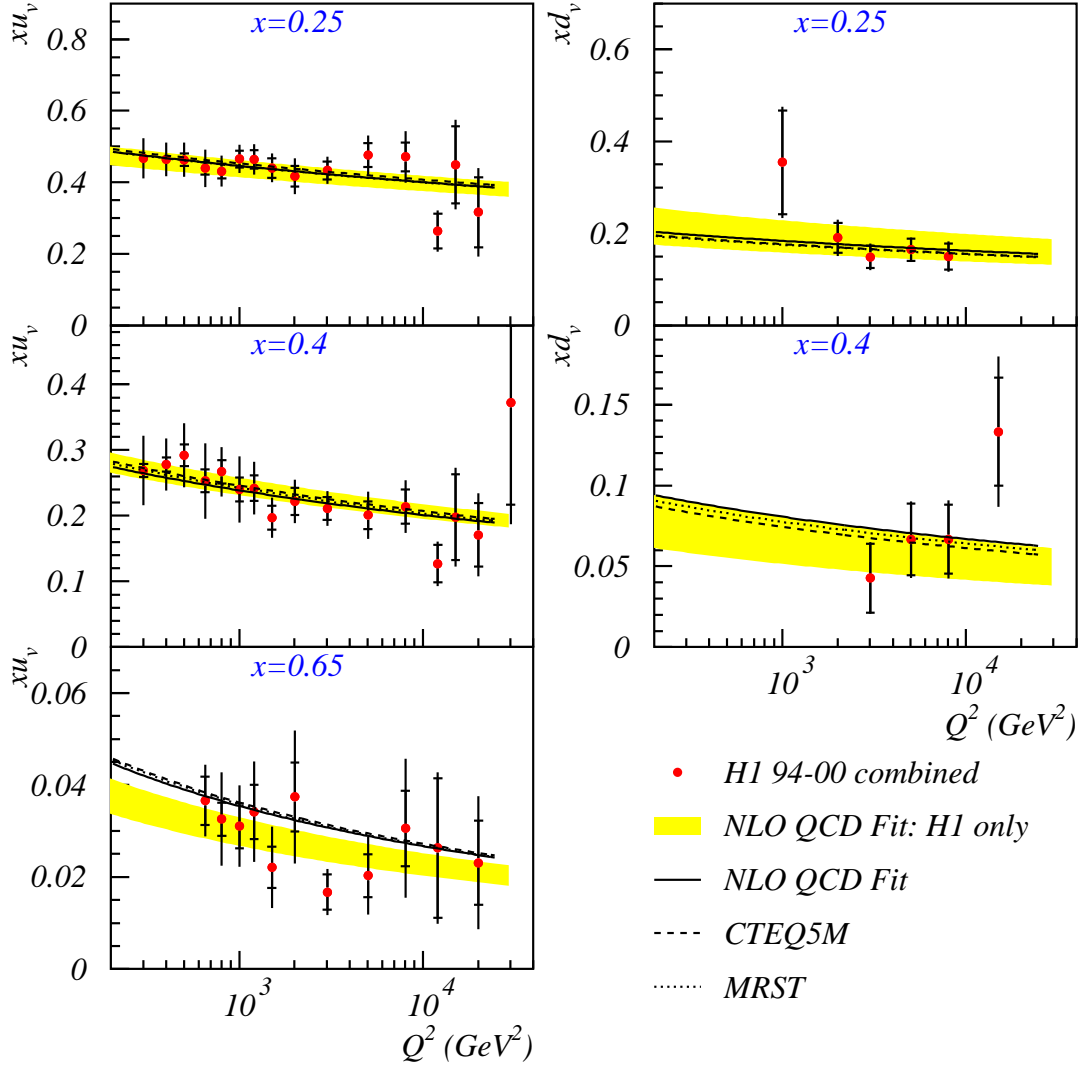


Figure 5.26: The valence quarks distributions  $xu_v$  and  $xd_v$  determined both with the new NLO QCD Fit (shaded error bands, labeled as “NLO QCD Fit: H1 only”, see text for the difference with the “NLO QCD Fit” of [94]) using all H1 data at high  $Q^2$  as well as the new low  $Q^2$  data [135] and with the local extraction method (data points with the inner and full error bars showing respectively the statistical and total errors) in comparison with other parameterizations which use fixed-target data at low  $Q^2$ .

to the experimental errors only. However, it has been studied with a few additional fits that other uncertainties are negligible:

1. The  $Q_{\min}^2$  cut has been varied from  $20 \text{ GeV}^2$  up to  $200 \text{ GeV}^2$ . As expected, the valence quarks at high  $x$  are constrained by the high  $Q^2$  data only.
2. The massless treatment of the heavy flavors has been replaced with the massive one. The results are stable.
3. The uncertainty of  $\alpha_s$  has been varied by  $\pm 0.0017$ , corresponding to the experimental precision of the latest H1 determination [135]. The resulting change on  $xu_v$  and  $xd_v$  is again small.

- The valence quark distributions determined with the new NLO QCD Fit are in good agreement with the other parameterizations at all values of  $x$  shown except for  $xu_v$  at  $x = 0.65$ , where the new valence density is about  $\sim 17\%$  lower than the other parameterizations with little dependence on  $Q^2$  in the covered range. These other parameterizations all used BCDMS data [17] to constrain  $xu_v$  at high  $x$ . However the discrepancy remains small, within about two standard deviations. It does point to a larger ratio of  $d/u$ , a preferable value as discussed by Yang and Bodek [209]. The only difference is that the larger ratio is achieved by a smaller  $xu_v$  here instead of a larger  $xd_v$ . It is therefore very important that the issue is clarified with the future HERA high-precision data at high  $Q^2$ .
- Finally, the results of the fit agree well with those obtained with the local extraction method.

## 5.4 Electroweak tests at HERA

So far in this report, we have concentrated on the tests and improvements on the current knowledge of the strong sector of the SM by implicitly assuming the validity of the electroweak sector. The electroweak parameters are fixed to the world average values provided mainly by  $e^+e^-$  high precision experiments.

In principle, the electroweak sector can also be tested at HERA. A first such test was performed by H1 with its first 14 CC candidates obtained from  $0.35\text{ pb}^{-1}$  of data taken in 1993 [188]. For the first time, the CC cross section was observed to be damped at high energy due to the propagator mass of the exchanged  $W$  boson in the space-like regime (Fig.5.27).

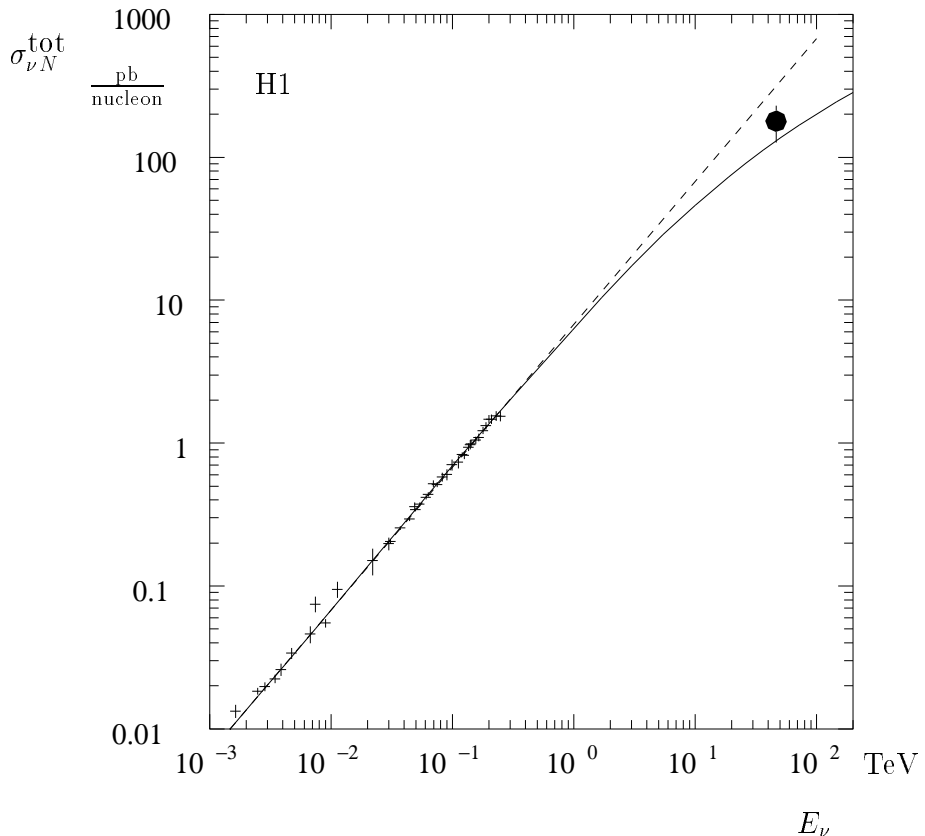


Figure 5.27: The energy dependence of the  $\nu N$  cross section. The crosses represent the low energy neutrino data [212] while the full circle refers to the CC result of the 1993 H1 data [188], which for the purpose of comparison, has been converted to a  $\nu N$  cross section. The experiment at HERA corresponds to an equivalent fixed-target energy of about 50 TeV. The full line represents the predicted cross section including the  $W$  propagator. The dashed line is the linear extrapolation from low energies.

This first test was made on the total CC cross section. Additional tests are now possible with differential CC cross sections. In fact, the double differential CC cross section can generally be expressed in terms of a propagator mass  $M_{\text{prop}}$  of the exchanged particle:

$$\frac{d^2\sigma_{\text{CC}}}{dxdQ^2} = \frac{G_F^2}{2\pi x} \left( \frac{M_{\text{prop}}^2}{M_{\text{prop}}^2 + Q^2} \right)^2 \tilde{\sigma}_{\text{CC}} \quad (5.23)$$

where  $\tilde{\sigma}_{\text{CC}}$  is the reduced CC cross section defined in Eq.(5.10). The normalization of the CC cross section is fixed by the Fermi coupling constant  $G_F$  while its  $Q^2$  dependence by  $M_{\text{prop}}$ .

Using the  $e^+p$  data taken from 1994 to 1997, which represent an increased integrated luminosity by two orders of magnitude with respect to the first CC data from 1993, both H1 and ZEUS have made a fit of the propagator mass  $M_{\text{prop}}$  to their cross section data [94, 203]. The propagator mass obtained is respectively

$$80.9 \pm 3.3(\text{stat}) \pm 1.7(\text{syst}) \pm 3.7(\text{pdf}) \text{ GeV} \quad \text{H1} \quad (5.24)$$

$$81.4^{+2.7}_{-2.6}(\text{stat}) \pm 2.0(\text{syst})^{+3.3}_{-3.0}(\text{pdf}) \text{ GeV} \quad \text{ZEUS} \quad (5.25)$$

where the last error is due to the uncertainty of the parton density distributions (pdf) dominated by the  $d$  valence quark. From this aspect and the fact that the  $e^-p$  CC cross section at high  $Q^2$  is an order of magnitude larger than the  $e^+p$  cross section, a better precision is expected from the  $e^-p$  data. Indeed, with an integrated luminosity of  $16.4 \text{ pb}^{-1}$  for the 1998-1999 H1  $e^-p$  data, which is less than half of that from the  $e^+p$  data, a similar fit yields [204]

$$79.9 \pm 2.2(\text{stat}) \pm 0.9(\text{syst}) \pm 2.1(\text{pdf}) \text{ GeV}. \quad (5.26)$$

The dominant experimental systematic error is from the hadronic energy scale uncertainty, which was estimated to be  $\pm 2\%$  for both the  $e^+p$  and  $e^-p$  analyses (Sec.5.1.4). However, the resulting uncertainty on the CC cross sections is smaller in  $e^-p$  collisions than in  $e^+p$  collisions due to the different  $Q^2$  dependence (Fig.5.22). In all these measurements, the pdf error is large than the experimental systematic uncertainty demonstrating the importance and the necessity to improve our knowledge on the parton distribution functions.

These measurements are in good agreement with the combined results  $M_W = 80.427 \pm 0.046 \text{ GeV}$  and  $M_W = 80.448 \pm 0.062 \text{ GeV}$  respectively from LEP II and  $p\bar{p}$  colliders [214]. To achieve such a precision at HERA would be difficult but is not impossible at the future high luminosity run [215]. Nevertheless the fact that the  $W$  mass measured at HERA in the space-like regime agrees so well with those when it appears as a real boson with subsequent decays or as a virtual boson in the space-like regime indicates that there is little space left for other exotic contributions to the measured CC cross sections at HERA.

Other tests e.g. on the weak neutral current couplings of quarks  $v_u$ ,  $a_u$ ,  $v_d$ , and  $a_d$  are possible but again have to wait for the future high luminosity runs with polarized beams [216].

## 5.5 Searches for new physics beyond the Standard Model

From an early  $e^+p$  data sample of 1994-1996 corresponding to an integrated luminosity of  $14.2 \text{ pb}^{-1}$  and  $20.1 \text{ pb}^{-1}$  respectively for H1 and ZEUS, both experiments have reported [11, 12] an excess of events at high  $Q^2 (> 15000 \text{ GeV}^2)$  and at large masses  $M = \sqrt{s}$ , the center-of-mass energies of the electron-parton collision, with respect to the SM DIS expectation for the NC process. H1 has also observed a less significant excess in the CC channel. In 1997, the HERA machine was particularly successful and both experiments have collected more  $e^+p$  data than they had before. Since then, new data from both  $e^-p$  and  $e^+p$  collisions have been collected respectively in 1998-1999 and 1999-2000 at a higher center-of-mass energy  $\sqrt{s} \simeq 320 \text{ GeV}$ . These data have been used extensively to search for new physics phenomena beyond the SM, of which three examples are briefly described in the following subsections.

### 5.5.1 Search for leptoquarks at HERA

The  $ep$  collider offers the unique possibility to search for  $s$ -channel production of new particles which couple to lepton-parton pairs. Leptoquarks are one such example. Leptoquarks are color triplet bosons which appear naturally in various unifying theories beyond the SM such as Grand Unified Theories [217] and Superstring inspired  $E_6$  models [218], and in some Compositeness [219] and Technicolor [220] models.

Leptoquarks are produced at HERA in the  $s$ -channel (Fig.5.28(a)). They appear also as exchanged bosons in the  $u$ -channel (Fig.5.28(b)). Leptoquark

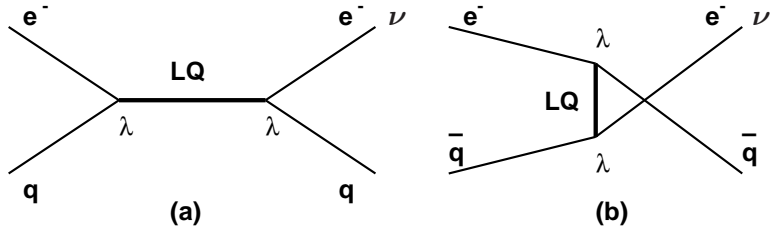


Figure 5.28: Diagrams (a)  $s$ -channel resonant production and (b)  $u$ -channel exchange of a leptoquark ( $LQ$ ) with fermion number  $F = 2$ . Diagrams involving a  $F = 0$  leptoquark are obtained from (a) and (b) by either changing the lepton-beam charge or exchanging  $q$  and  $\bar{q}$ .

states are classified according to the fermion number  $F = L + 3B$ , where  $L$  is the lepton number and  $B$  is the baryon number of the state. Thus for  $e^-p$

collisions, the fermion numbers are  $F = 2$  ( $F = 0$ ) for electron fusing with a quark (antiquark) from the proton whereas for  $e^+p$  collisions they are  $F = 0$  ( $F = -2$ ) for positron fusing with a quark (antiquark) from the proton. The  $F = 2$  leptoquarks would be produced with a larger cross section in  $e^-p$  collisions while the  $F = 0$  states are best searched for in  $e^+p$  collision data. The unknown Yukawa coupling of the leptoquark to an  $eq$  pair is denoted by  $\lambda$  in Fig.5.28. Leptoquarks coupling only to first generation fermions give  $e+q$  or  $\nu+q'$  final states leading to individual events indistinguishable respectively from standard NC and CC DIS events, which become backgrounds for the searches considered here. Statistically, however, one expects for scalar leptoquarks produced in  $s$ -channel a resonant peak in the mass distribution and an isotropical  $d\sigma/dy$  distribution where  $y = (1 + \cos \theta^*)/2$  with  $\theta^*$  being the decay polar angle of the lepton relative to the incident proton in the leptoquark center-of-mass frame. Events resulting from the production and decay of vector leptoquarks would be distributed according to  $d\sigma/dy \propto (1 - y)^2$ . These  $y$  spectra from scalar or vector leptoquark production are markedly different from the distribution ( $d\sigma/dy \propto y^{-2}$ ) expected at fixed  $x$  for the dominant  $t$ -channel photon exchange in NC DIS events. This is illustrated in Fig.5.29(a) for NC DIS events selected from  $e^+p$  1994-1997 data and in Fig.5.29(b) for a production of a scalar  $F = 0$  leptoquark of mass at 200 GeV, where the kinematic variables  $y_e$  and  $M_e = \sqrt{sx_e}$  were defined using the electron method (Sec.2.6.1).

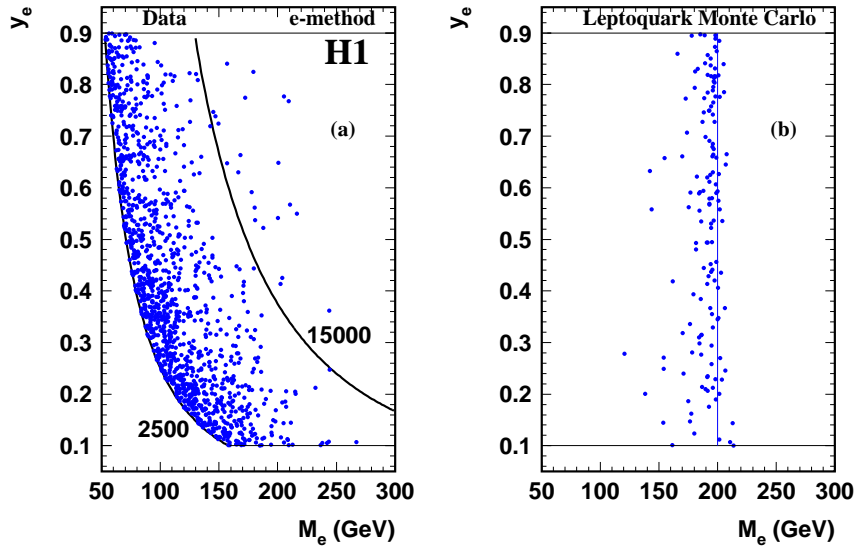


Figure 5.29: Kinematics in the  $y_e - M_e$  plane of (a) the selected NC DIS candidates from the  $e^+p$  1994-1997 H1 data (two isocurves at  $Q^2 = 2500 \text{ GeV}^2$  and  $15000 \text{ GeV}^2$  are plotted as full lines); (b) a scalar  $F = 0$  leptoquark of mass at 200 GeV decaying into  $e + q$  for a coupling  $\lambda = 0.05$  generated with the LEGO event generator [221].

For this reason, a mass dependent  $y$  cut is applied to optimize the signal significance and background contribution. The resulting mass distributions are

shown in Fig.5.30 for all  $e^\pm p$  data taken by H1 since 1994. The excess around 200 GeV in the  $e^+ p$  1994-1997 data is not confirmed by the new  $e^- p$  1998-1999 and  $e^+ p$  1999-2000 data.

Since no significant evidence for a leptoquark signal has been observed, constraints on the Yukawa coupling of leptoquarks were derived [222, 223, 224]. Two examples are shown in Fig.5.31 for a scalar leptoquark with  $F = 0$  ( $\tilde{S}_{1/2,L}$ ) from the  $e^+ p$  1994-1997 data and a scalar leptoquark with  $F = 2$  ( $S_{0,L}$ ) from the  $e^- p$  1998-1999 data in comparison with the indirect limits from H1 [226, 227] (Sec.5.5.3) and LEP [228], as well as limits from the Tevatron experiments [229]. At LEP [228, 230, 231], sensitivity to a high-mass leptoquark arises from effects of virtual leptoquark exchange on the hadronic cross section. In both examples shown, the H1 limits extend beyond the present reach of other colliders. Moreover the constraints obtained from the  $e^- p$  data on  $F = 2$  leptoquarks are more stringent than those from the previous higher statistics  $e^+ p$  data on  $F = 0$  states, due to the enhanced energy in the center of mass of the  $ep$  collision. Similar limits on  $F = 0$  leptoquarks have also been obtained by ZEUS using the  $e^+ p$  1994-1997 data [232].

### 5.5.2 Search for supersymmetry at HERA

Supersymmetry (SUSY) is one of the most likely ingredients for a theory beyond the SM. In particular the Minimal Supersymmetric extension of the Standard Model (MSSM) describes as well as the SM all experimental data, and in addition it offers among its appealing consequences solutions for the cancellation of quadratic divergences occurring in the scalar Higgs sector of the SM and models beyond the SM.

SUSY relates fermions to bosons and predicts for each SM particle a partner with spin differing by half a unit. For example selectrons  $\tilde{e}_L, \tilde{e}_R$  are scalar partners of electrons  $e_L, e_R$ , and similarly squarks  $(\tilde{u}_L, \tilde{d}_L), (\tilde{u}_R, \tilde{d}_R)$  are the partners of up and down quarks. Two Higgs doublets with vacuum expectation values  $v_2, v_1$  are necessary to generate masses for up-type quarks ( $v_2$ ) and for down-type quarks and charged leptons ( $v_1$ ). The partners of the gauge bosons  $W^\pm, Z^0, \gamma$  and the two Higgs doublets are called gauginos and higgsinos. They can mix and form two charged mass eigenstates  $\chi_{1,2}^\pm$  (charginos) and four neutral mass eigenstates  $\chi_{1,2,3,4}^0$  (neutralinos).

Since supersymmetric particles are not observed at the masses of their SM partners, SUSY must be broken. In the MSSM, this breaking is achieved by adding extra mass parameters  $M_2$  and  $M_1$  for the  $SU(2)$  and  $U(1)$  gauginos. Thus the masses of charginos and neutralinos depend on  $M_1, M_2, \tan\beta \equiv v_2/v_1$  and the higgsino mass parameter  $\mu$ .

$R$ -parity ( $R_p$ ), defined as  $R_p \equiv (-1)^{3B+L+2S}$ , is a multiplicative quantum

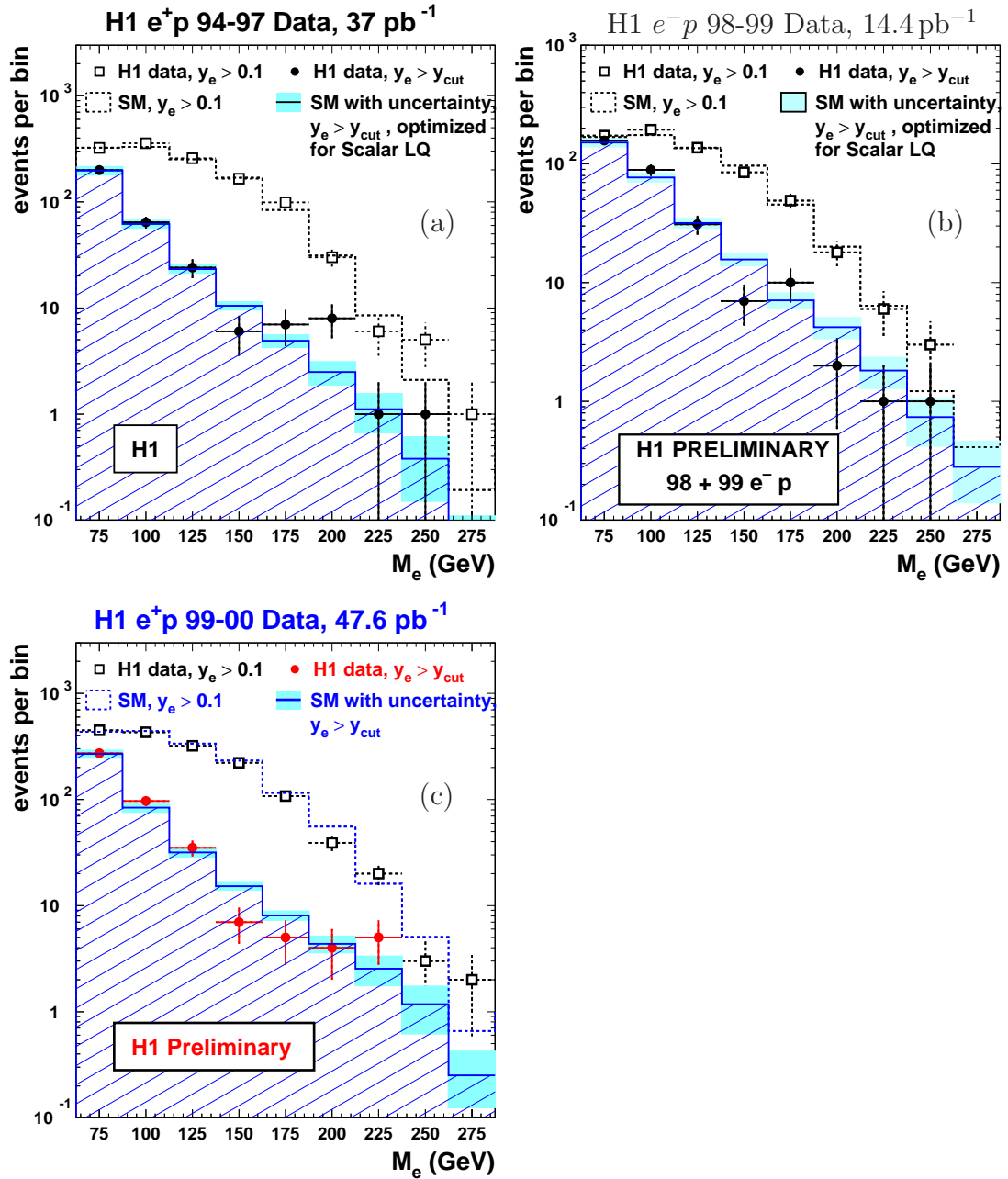


Figure 5.30: Mass spectra for NC DIS-like final states selected from the  $e^+p$  1994-1997 data (b),  $e^-p$  1998-1999 data (b), and  $e^+p$  1999-2000 data (c). The data (symbols) are compared with DIS expectation (histograms) before and after a mass dependent  $y$  cut designed to maximize the significance of an eventual scalar leptoquark signal. The greyed boxes indicate the  $\pm 1\sigma$  uncertainty of the statistical and systematic errors of the NC DIS expectation.

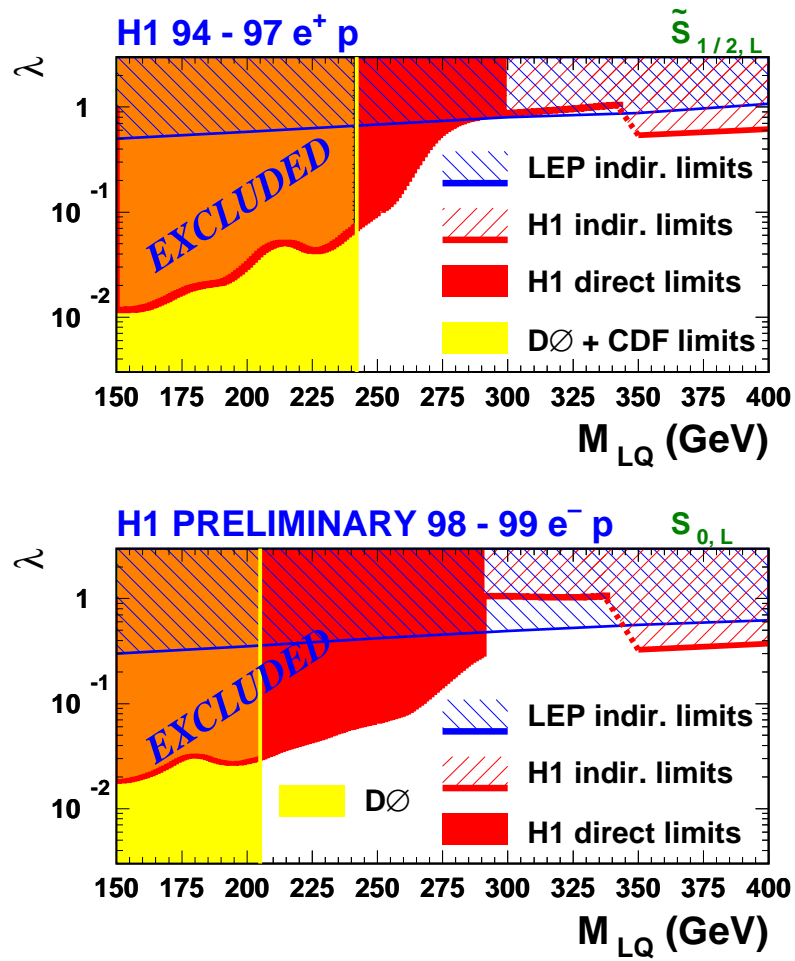


Figure 5.31: *Exclusion limits at 95% confidence level on the Yukawa coupling  $\lambda$  as a function of the leptoquark mass for (top) a scalar leptoquark with  $F = 0$  and (bottom) a scalar leptoquark with  $F = 2$  described by the Buchmüller-Rückl-Wyler model [225]. Greyed and hatched domains are excluded. The H1 indirect limits are derived in the analysis of contact interactions described in Sec.5.5.3.*

number which distinguishes particles ( $R_p = +1$ ) from SUSY particles ( $R_p = -1$ ). Here  $B$ ,  $L$ , and  $S$  denote respectively baryon number, lepton number, and spin of a particle. In SUSY models with  $R$ -parity conservation, supersymmetric particles can only be produced in pairs and the lightest supersymmetric particle (LSP), which is generally assumed to be  $\chi_1^0$ , is stable. At HERA the dominant  $R_p$ -conservation process is the production of a selectron and a squark via a  $t$ -channel exchange of a neutralino  $ep \rightarrow \tilde{e}\tilde{q}X$  (Fig. 5.32). The  $\tilde{e}$  and  $\tilde{q}$  can then decay into any lighter gaugino and their SM partners. The decay involving  $\chi_1^0$  gives an experimentally clean signature of missing transverse energy plus an electron and a hadronic system. Such a search has been performed by H1 [233] using  $6.38 \text{ pb}^{-1}$  of  $e^+p$  data from 1994-1995, and by ZEUS [234] using  $46.6 \text{ pb}^{-1}$  of  $e^+p$  data from 1994-1997.

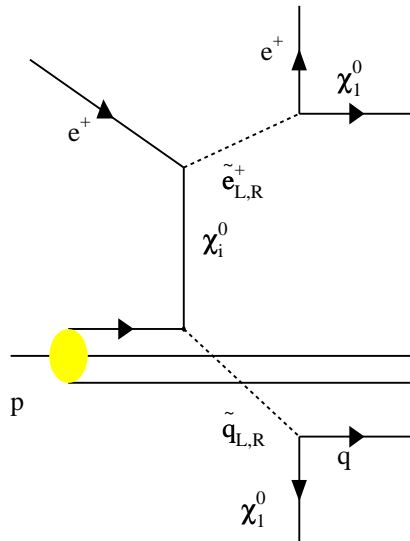


Figure 5.32: Selectron-squark production via neutralino exchange and the subsequent decays into the lightest supersymmetric particle  $\chi_1^0$ .

The most general SUSY theory which preserves gauge invariance of the SM allows, however, for  $R_p$  violating ( $\mathcal{R}_p$ ) Yukawa couplings  $\lambda, \lambda', \lambda''$  between one scalar squark or slepton and two SM fermions:

$$W_{\mathcal{R}_p} = \lambda_{ijk} L_i L_j \bar{E}_k + \lambda'_{ijk} L_i Q_j \bar{D}_k + \lambda''_{ijk} \bar{U}_i \bar{D}_j \bar{D}_k. \quad (5.27)$$

where  $i, j, k = 1, 2, 3$  are generation indices,  $L_i (Q_i)$  are the lepton (quark)  $SU(2)_L$  doublet superfields and  $\bar{E}_i (\bar{D}_j, \bar{U}_j)$  are the electron (down and up quark)  $SU(2)_L$  singlet superfields. Of particular interest for HERA are the  $\mathcal{R}_p$  terms  $\lambda' L_i Q_j \bar{D}_k$  as HERA provides both leptonic and baryonic quantum numbers in the initial state. The resonant squarks at HERA are thus singly produced (in contrast to the  $R_p$ -SUSY) in the  $s$ -channel (Fig. 5.33) with masses up to the kinematic limit

of  $\sqrt{s} \simeq 300 - 320$  GeV. From the theoretical understanding of unification, there is no clear preference between  $R_p$ -conservation and  $\mathcal{R}_p$ , it is thus mandatory that the latter possibility is also sought experimentally [235].

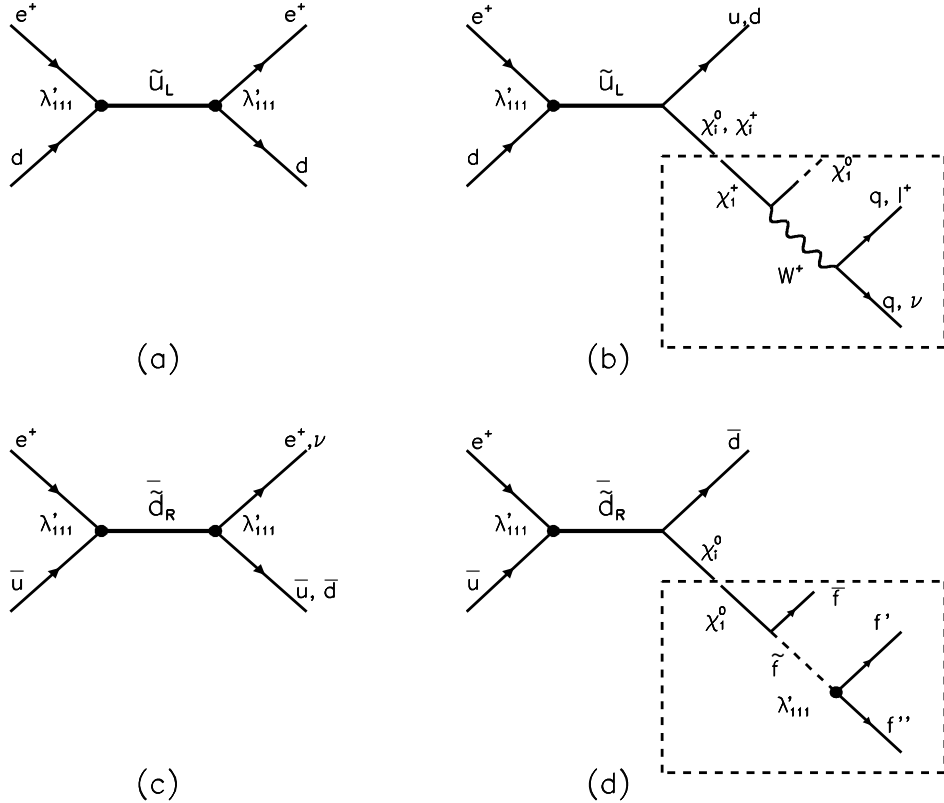


Figure 5.33: Lowest order  $s$ -channel diagrams for first generation squark production at HERA followed by (a), (c)  $\mathcal{R}_p$  decays and (b), (d) gauge decays. In (b) and (d), the emerging neutralino or chargino might subsequently undergo  $\mathcal{R}_p$  decays of which examples are shown in the dashed boxes for (b) the  $\chi_1^+$  and (d) the  $\chi_1^0$ .

Compared to the squarks in  $R_p$ -SUSY, the squarks in  $\mathcal{R}_p$ -SUSY can have additional decay modes decaying via Yukawa coupling into SM fermions as illustrated with two examples in Fig.5.33(b),(d). Moreover, the LSP (again assumed to be  $\chi_1^0$ ), which is no longer stable, decays via  $\lambda'_{1jk}$  into a quark, an antiquark and a lepton.

In cases where both production and decay occur through a  $\lambda'_{1jk}$ , the squarks in  $\mathcal{R}_p$ -SUSY behave as scalar leptoquarks (Sec.5.5.1) and the constraints obtained on leptoquarks are also applicable for squarks. There is however an interesting difference, namely the exclusion phase space covered by HERA data can be relatively larger for squarks than for leptoquarks. This is because the mass con-

straints of 242 GeV (205 GeV) from Tevatron [229] correspond to a branching ratio  $\beta_{eq}$  of the new particle into  $e + q$  of 1(0.5), which can be naturally small in  $\mathcal{R}_p$ -SUSY framework given the competition with gauge decay modes of the squarks.

With  $e^+p$  collisions, HERA is best sensitive to couplings  $\lambda'_{1j1}$  among the nine possible couplings  $\lambda'_{1jk}$ , where mainly  $\tilde{u}_L^j$  squarks are produced via processes involving a valence  $d$  quark. On the contrary, the  $e^-p$  data will allow to better probe couplings  $\lambda'_{11k}$  and  $\tilde{d}_R^k$  squarks.

Depending on whether the produced squarks undergo a  $\mathcal{R}_p$  decay or a gauge decay, there are many different final state event topologies, e.g. (a) a lepton plus a jet, (b) a neutrino plus a jet, (c) a right sign lepton plus multijets, and (d) a wrong sign lepton plus multijets. Topologies (a) and (b) are indistinguishable from NC and CC DIS events respectively as for leptoquarks. Topology (b) has only a low sensitivity with the  $e^+$  beam since the produced squarks  $\tilde{d}_R^{k*}$  couples to a sea quark  $\bar{u}$  from the proton (Fig. 5.33(c)), the density of which is small at high  $x$ . The main SM background for topology (c) is also from NC DIS where QCD radiation leads to multijets. Topology (d) has such a striking final state that it is essentially background free.

Under the assumption that only one of the Yukawa couplings  $\lambda'_{1j1}$  dominates<sup>21</sup>, mass dependent upper limits on these couplings are derived by combining all topologies. Combining all contributing channels with different topologies improves the sensitivity considerably, up to a factor of  $\sim 5$  at lowest masses, compared to what would be achieved using only the contribution from topology (a). The results [236, 237] are shown in Fig.5.34. The H1 limits are compared in Fig.5.34(a) to the most stringent indirect limits. The production of a  $\tilde{u}$  squark via a  $\lambda'_{111}$  coupling is very severely constrained by the non-observation of neutrinoless double beta decay [238] as shown by the dotted curve. The most severe indirect limit on the coupling  $\lambda'_{121}$ , which could allow for the production of squarks  $\tilde{c}$ , comes from Atomic Parity Violation [235, 239] and is indicated by the dashed curve in Fig.5.34(a). For squark masses below  $\sim 240$  GeV HERA limits significantly improve this indirect constraint on  $\lambda'_{121}$  by a factor of up to  $\sim 3$ . In Ref.[236], further limits are derived both in a constrained version of the MSSM by assuming a universal mass parameter  $m_0$  for all sfermions at very high scale and in the framework of the Minimal Supergravity Model, a more constrained SUSY model. The limits in the latter model extend beyond the domain covered by other collider experiments [240] especially at large  $\tan\beta$ .

---

<sup>21</sup>This is not unreasonable as in the SM the top quark Yukawa coupling is almost a factor of 40 larger than the bottom Yukawa coupling.

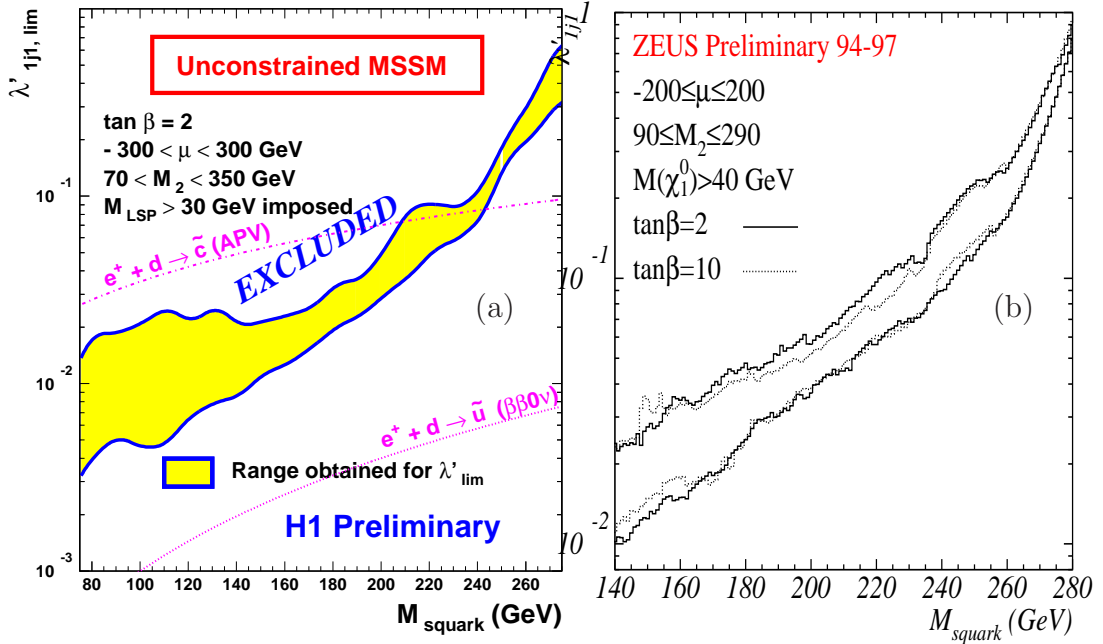


Figure 5.34: (a) Exclusion upper limits at 95% confidence level by H1 [236] on the coupling  $\lambda'_{1j1}$  as a function of the squark mass for  $\tan \beta = 2$ , in the ‘phenomenological’ MSSM. For each squark mass, a scan on the MSSM parameters  $M_2$  and  $\mu$  has been performed and the largest (lowest) value for the coupling limit is shown by the upper (lower) curve. (b) The similar limits from ZEUS [237] for  $\tan \beta = 2$  as well as for  $\tan \beta = 10$  (dotted lines).

### 5.5.3 Search for contact interactions

A broad range of hypothesized non-SM processes at mass scales beyond the HERA center-of-mass energy,  $\sqrt{s} = 300 - 320$  GeV, can be approximated in their low-energy limit by effective four-fermion  $eeqq$  contact interactions, analogous to the effective four-fermion interaction describing the weak force at low energies [241]. Here three sources are briefly discussed, conventional contact interactions arising from a substructure of the fermions involved, the exchange of a new heavy particle (e.g. leptoquark), low scale quantum gravity effects which may be observable at HERA via the exchange of gravitons coupling to SM particles and propagating into extra spatial dimensions.

New currents or heavy bosons may produce indirect effects through the exchange of a virtual particle interfering the  $\gamma$  and  $Z^0$  fields of the SM. In the present of  $eeqq$  contact interactions which couple to a specific quark flavor ( $q$ ),

the SM Lagrangian  $\mathcal{L}_{\text{SM}}$  received the following additional terms [242, 243]:

$$\mathcal{L} = \mathcal{L}_{\text{SM}} + \sum_{a,b=L,R} [\eta_s^q (\bar{e}_a e_b) (\bar{q}_a q_b) + \eta_{ab}^q (\bar{e}_a \gamma_\mu e_b) (\bar{q}_a \gamma^\mu q_b) + \eta_T^q (\bar{e}_a \sigma_{\mu\nu} e_b) (\bar{q}_a \sigma^{\mu\nu} q_b)] \quad (5.28)$$

where the sum runs over the left-handed ( $L$ ) and right-handed ( $R$ ) fermion helicities. The three terms correspond to respectively the scalar, vector, and tensor interactions. Only the vector term is considered at HERA since strong limits beyond the HERA sensitivity have already been placed on the other terms [243, 244, 245]. The effective coupling coefficients  $\eta_{ab}^q$  is defined as

$$\eta_{ab}^q = \epsilon \left( \frac{g}{\Lambda_{ab}^q} \right)^2 \quad (5.29)$$

where  $\epsilon = \pm 1, 0$  with  $\pm 1$  representing constructive and destructive interference with the SM currents,  $g$  is the overall coupling strength, and  $\Lambda_{ab}^q$  is the effective mass scale. In the study of possible fermion compositeness or substructure,  $g$  is conventionally chosen to be  $\sqrt{4\pi}$ , whereas for study of the virtual leptoquark, these parameters are related to the leptoquark mass  $M_{\text{LQ}}$  and the coupling  $\lambda$ :

$$\frac{g}{\Lambda} = \frac{\lambda}{M_{\text{LQ}}} \quad (5.30)$$

Based on the NC cross sections described in Sec.5.2.6, the lower bounds on the scale parameters  $\Lambda^\pm$  obtained by H1 [226] using the  $e^+p$  1994-1997 data range between 1.3 TeV and 5.5 TeV at 95% confidence level for various chiral structures. The limits from ZEUS [247] are similar and range from 1.7 TeV to 5 TeV. The most restrictive range from both experiments is for the  $VV$  model, where all contact terms enter with the same sign. Combining with the new  $e^-p$  1998-1999 and  $e^+p$  1999-2000 data, the H1 limits have been substantially extended and amount to 1.6 – 9.2 TeV [227]. The HERA results of direct searches for ( $eq$ ) compositeness are thus competitive with those of other experiments at LEP [248, 249] and Tevatron [250].

The same data have been used by H1 to derive lower limits on the ratio  $M_{\text{LQ}}/\lambda$  for the exchange of virtual leptoquarks for range between the center-of-mass energy  $\sqrt{s}$  and up to 1.7 TeV [227]. These measurements extend thus the direct leptoquark searches at HERA to high masses  $M_{\text{LQ}} > \sqrt{s}$ . Two examples have been shown for  $\tilde{S}_{1/2,L}$  and  $S_{0,L}$  in Fig.5.31. The most stringent limits, however, are those for vector leptoquarks with coupling to up quarks.

It has been recently suggested that gravitational effects may become strong at subatomic distances and thus measurable in collider experiments [251]. In such a scenario, which may be realized in string theory, gravity is characterized by a scale  $M_s \sim \mathcal{O}(\text{TeV})$  in  $4 + n$  dimensions. The extra spatial dimensions  $n$  are

restricted to a volume associated with the size  $R$  and the scale in  $4+n$  and the ordinary 4 dimensions are related by

$$M_P^2 \sim R^n M_S^{2+n}, \quad (5.31)$$

where  $M_P \sim 10^{19} \text{ GeV}$  is the Planck mass. An exciting consequence would be a modification of Newton's law at distance  $r < R$ , where the gravitational force would rise rapidly as  $F \propto 1/r^{2+n}$  and become strong at the scale  $M_S$ . Experimentally, gravity is essentially not tested in the sub-millimeter range [252] and scenarios with  $n > 2$  extra dimensions at large distances  $R \lesssim 100 \mu\text{m}$  are conceivable.

In models with large extra dimensions the spin 2 graviton propagates into the extra spatial dimensions and appears in the 4-dimensional world as a spectrum of massive Kaluza-Klein excitations with masses  $m^{(j)} = j/R$ , including the zero-mass state. The graviton fields  $G_{\mu\nu}^{(j)}$  couple to the SM particles via the energy-momentum tensor  $T^{\mu\nu}$

$$\mathcal{L}_G = -\frac{\sqrt{8\pi}}{M_P} G_{\mu\nu}^{(j)} T^{\mu\nu}. \quad (5.32)$$

Summation over the whole tower of Kaluza-Klein states  $j$  with masses up to the scale  $M_S$  compensates the huge  $1/M_P$  suppression and results in an effective contact interaction coupling [253]

$$\eta_G = \frac{\lambda}{M_S^4} \quad (5.33)$$

where  $\lambda$  is the coupling strength of order unity.

Lower limits from H1 on the scale parameter  $M_S$  are derived again from fits to the NC cross sections (Sec.5.2.6). For the  $e^-p$  data stronger bounds are obtained for positive coupling than for negative coupling. The opposite behavior is observed in  $e^+p$  scattering. Both lepton-beam charges thus complement each other and a combined analysis [227] of all  $e^\pm p$  data yields limits on  $M_S$  of 0.63 TeV for positive coupling  $\lambda = 1$  and 0.93 TeV for negative coupling  $\lambda = -1$  as illustrated in Fig.5.35. Similar investigations of virtual graviton exchange in  $e^+e^-$  annihilation provide comparable limits [248, 254].

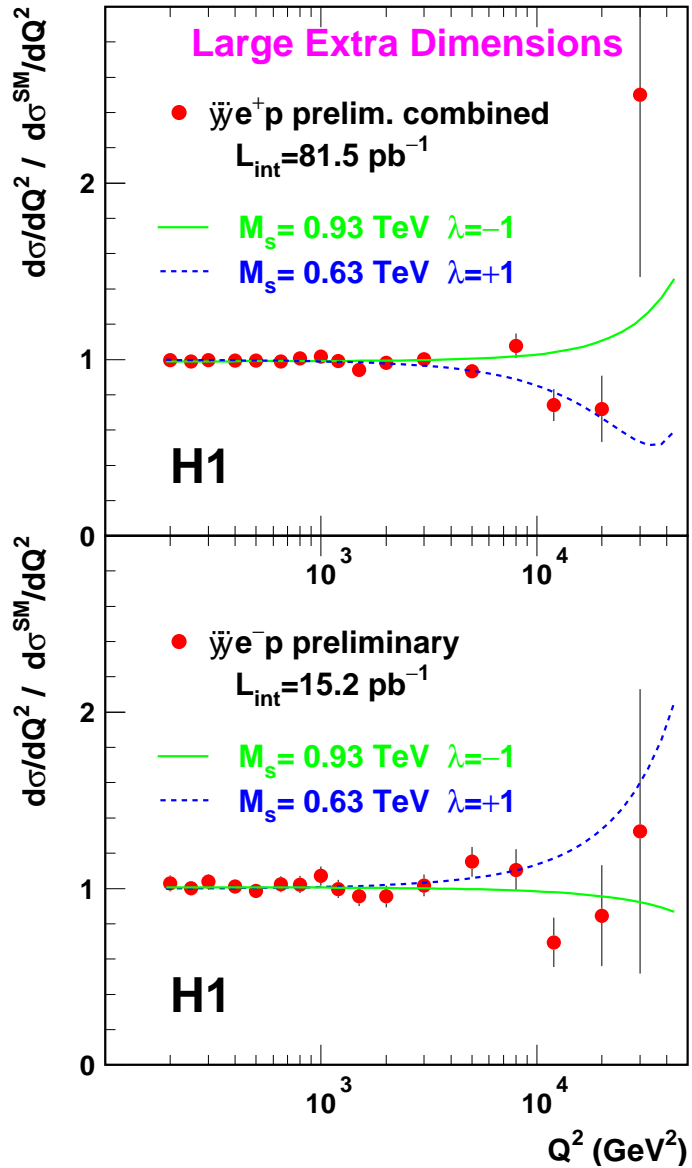


Figure 5.35: NC cross sections  $d\sigma/dQ^2$  normalized to the SM expectation for the combined  $e^+p$  and the  $e^-p$  scattering data. The curves show the effects of graviton exchange in large extra dimensions given by a common fit to the scale  $M_S$  (95% confidence level lower limits) with coupling  $\lambda = 1$  and  $\lambda = -1$ . The errors represent statistics and uncorrelated experimental systematics.

# Chapter 6

## Summary and outlook

The  $ep$  collider HERA has opened up a completely new kinematic domain unexplored in the previous fixed-target experiments. The results of the first measurement of the proton structure function at small  $x$  down to  $0.5 \times 10^{-4}$  came as a surprise for many: the measured  $x$  dependence of the structure function for a fixed momentum transfer  $Q^2$  revealed a strong rise towards low  $x$  reflecting an increasing number of slow partons being probed within the proton. This first measurement was based on about  $25 \text{ nb}^{-1}$  of data taken in 1992. One year later, the data have been increased by more than a factor of 10. The data have allowed the structure function measurement to be extended to values of  $Q^2$  beyond those measured at fixed-target experiments. By making use of the hard initial radiative events, it was possible to extend the kinematic region to lower  $Q^2$  and high  $x$ . With more data and the improved apparatus, the precision measurements are realized at HERA reaching a statistical precision below 1% and a systematic error of typically 3%.

The structure function measurement of 1993 has allowed a first determination of gluon density at low  $x$  based on the NLO DGLAP evolution equations. A strong-rise behavior toward low  $x$  is also found and is believed to be responsible for the observed behavior of the structure function. The subsequently improved measurements of the structure function have resulted in an ever-increasing knowledge of the gluon distribution at low  $x$ . Today the gluon density is better known at low  $x$  than at other ranges, a situation completely different to several years ago, before the HERA start. The latest precision measurement at low  $Q^2$  and  $x$  by H1 has not only provided a best determination of the gluon but also together with the BCDMS data one of the most precise measurements of the strong coupling constant  $\alpha_s$ .

The increased integrated luminosity has also allowed to explore the very high  $Q^2$  region up to  $\sim 30\,000 \text{ GeV}^2$ . With the earlier data from 1994 to 1996, an excess of events at high  $Q^2$  and high  $x$  was reported by H1 and ZEUS. With

new data available taken for different lepton-beam charges and higher center-of-mass energy, no excess was confirmed. The NC and CC cross sections have been measured both double differentially and single differentially in  $x$  and  $Q^2$ . The comparison of the  $e^\pm p$  NC cross sections has revealed the presence of the  $\gamma Z^0$  interference contribution at high  $Q^2$  and has allowed a first measurement of the structure function  $x\tilde{F}_3(x, Q^2)$  at high  $Q^2$ . The comparison of the  $e^\pm p$  CC cross sections has shown a huge difference in the cross sections reflecting the different quark flavors probed by the  $W^\pm$  bosons in the  $e^\pm$  scatterings. The comparable NC and CC cross sections at high  $Q^2$  has confirmed electroweak unification in the space-like regime.

The measurement of the NC cross sections covers a  $Q^2$  range of about four orders of magnitude, over which the cross sections fall with  $Q^2$  by more than eight orders of magnitude, a behavior well described by the Standard Model expectation based mainly on low  $Q^2$  data providing thereby a nontrivial test of the validation the QCD evolution. The Standard Model expectations also describe all other measurements with two possible exceptions:

- The NC cross sections at  $Q^2 > 20\,000 \text{ GeV}^2$  and  $x$  around 0.4 are higher than the expectation in both  $e^+p$  data samples taken at different center-of-mass energies. The excess remains however statistically not very significant.
- The NC cross sections at  $x = 0.65$ , the largest  $x$  value measured, are for  $e^+p$  and  $e^-p$  at essentially all  $Q^2$  lower than the expectation which is mainly based on the BCDMS data.

A NLO QCD fit using all high  $Q^2$  data shows the data at  $x = 0.65$  are about 17% lower than the expectation and there remains a discrepancy of about two standard deviations. The fit has demonstrated that the quark distributions at high  $x$  and high  $Q^2$  are constrained by the HERA data alone with an experimental precision of  $\sim 6\%$  at  $x = 0.25$  and  $x = 0.4$  and  $\sim 10\%$  at  $x = 0.65$  for the  $u$  valence quark and about 20% for the  $d$  valence quark. The results are in good agreement with that obtained by the local extraction method. These determinations are free from any nuclear correction in contrast to the current knowledge on the  $d$  valence quark which was mainly obtained from fixed-nuclear-target data at low  $Q^2$ .

The high  $Q^2$  data have also been used to test the electroweak sector of the Standard Model. The derived propagator mass of the  $W$  boson in the space-like regime agrees well with other direct or indirect measurements of a real or virtual boson in the time-like regime. The determination at HERA is however already limited by the uncertainty of the parton density distributions demonstrating the importance and necessity to improve our knowledge on these parton distributions for future precision measurements.

On the same data, various searches have been performed for seeking both resonance production of leptoquarks and squarks in  $R$ -parity violating supersym-

metric models, and contact interactions of a substructure of the involved fermions, exchange of a new virtual heavy particle, as well as low scale quantum gravity effects. No significant deviations from the Standard Model expectations were found and various limits have been derived. These limits either extend beyond or are comparable with those provided by indirect measurements or by direct searches at other colliders.

At high  $Q^2$ , the precision of essentially all current measurements are still limited by the statistical error. In order to improve the precision, to reach even higher  $Q^2$  and to fully explore the discovery potential of HERA, it is important to have as much data as possible and in a relatively short period of time with stable running conditions to minimize additional systematic uncertainties. This can only be achieved with a luminosity upgrade. The upgrade has started since the beginning of September 2000 and the new physics run of the HERA phase two is foreseen in September 2001. With this upgrade program for both the machine and the detectors together with the polarized beams, HERA, being one of few high energy machines running in the next years, will have an exciting and bright future.

# Acknowledgements

This is a report prepared for the ‘habilitation’ defense on Dec. 1, 2000 in front of the jury members: V. Brisson, M. Davier (chairman), J. Gayler, F. Le Diberder, and W. J. Stirling.

I wish to thank all my colleagues from the H1 and ZEUS experiments on whose research this report is based in particular U. Bassler, G. Bernardi, J. C. Bizot, V. Brisson, P. Bruel, J. Cao, A. Courau, C. Diaconu, L. Favart, M. Fleischer, A. Glazov, B. Heinemann, M. Hütte, M. Jacquet, M. Jaffre, S. Kermiche, M. Klein, M. W. Krasny, Ch. Leverenz, S. Levonian, P. Marage, A. Mehta, T. Merz, A. Panitch, C. Pascaud, E. Perez, J. P. Phillips, G. Radel, E. Rizvi, V. Shekelyan, Y. Sirois, C. Vallée and F. Zomer for their collaborations during various stages in the past eight years. I thank V. Brisson also for her constant encouragement during these years.

I am grateful for V. Brisson, J. Gayler, F. Le Diberder and C. Pascaud for their helpful comments on an earlier version of the report.

# Bibliography

- [1] R. Hofstadter, L. I. Schiff, “Nucleon Structure”, *Proc. of the Int. Conf. at Stanford*, Stanford University Press, 1964.
- [2] W. K. H. Panofsky, *Proc. 14th Conf. on High Energy Phys.* ed. J. Prentki and J. Steinberger, Vienna, Aug. 1968.
- [3] E. D. Bloom *et al.*, *Phys. Rev. Lett.* **23** (1969) 930; M. Breidenbach *et al.*, *Phys. Rev. Lett.* **23** (1969) 935.
- [4] W. Albrecht *et al.*, *Nucl. Phys.* **B13** (1969) 1.
- [5] D. J. Fox *et al.*, *Phys. Rev. Lett.* **33** (1974) 1504; Y. Watanabe *et al.*, *Phys. Rev. Lett.* **35** (1975) 898; E. M. Riordan *et al.*, SLAC PUB 1634, August 1975 (unpublished).
- [6] H. L. Anderson *et al.*, *Phys. Rev. Lett.* **38** (1977) 1450; B. A. Gordon *et al.*, *Phys. Rev. Lett.* **41** (1978) 615.
- [7] S. R. Mishra and F. Sciulli, *Annu. Rev. Nucl. Part. Sci.* **39** (1989) 259.
- [8] F. J. Hasert *et al.*, *Phys. Lett.* **B46** (1973) 138.
- [9] A. Benvenuti *et al.*, *Phys. Rev. Lett.* **32** (1974) 800; B. C. Barish *et al.*, *Proc. 17th Int. Conf. on High Energy Physics*, London (July 1974), p.111; *Phys. Rev. Lett.* **34** (1975) 538.
- [10] C. Y. Prescott *et al.*, *Phys. Lett.* **B84**, (1979) 524.
- [11] H1 Collab., C. Adloff *et al.*, *Z. Phys.* **C74** (1997) 191.
- [12] ZEUS Collab., J. Breitweg *et al.*, *Z. Phys.* **C74** (1997) 207.
- [13] See e.g. G. Altarelli *et al.*, *Nucl. Phys.* **B506** (1997) 3.
- [14] R. E. Tayler, *Proc. of the 4th Int. Symp. on Electron and Photon Interaction*, Liverpool (1969) p251.
- [15] SLAC-MIT Collab., G. Miller *et al.*, *Phys. Rev.* **D5** (1972) 528.

- [16] W. Albrecht *et al.*, Contributed paper to *Proc. of the 4th Int. Symp. on Electron and Photon Interaction*, Liverpool (1969) and DESY report 69/46 (1969) unpublished.
- [17] BCDMS Collab., A. .C. Benvenuti *et al.*, *Phys. Lett.* **B223** (1989) 485; *Phys. Lett.* **B236** (1989) 592.
- [18] P. C. Bosetti *et al.*, *Nucl. Phys.* **B142** (1978) 1.
- [19] CDHS Collab., H. Abramowicz *et al.*, *Z. Phys.* **C15** (1982) 19.
- [20] CCFR Collab., Seligman *et al.*, *Phys. Rev. Lett.* **79** (1997) 1213.
- [21] First reference in [17].
- [22] NMC Collab., M. Arneodo *et al.*, *Nucl. Phys.* **B483** (1997) 3.
- [23] E665 Collab., M. R. Adams *et al.*, *Phys. Rev. Lett.* **75** (1995) 1466.
- [24] D. H. Perkins, *Proc. of the 1975 Int. Symp. of Lepton and Photon Interactions*, p571.
- [25] V. Brisson, *Proc. of the Rencontres de Moriond*, Flaine (1976), Vol.2, p253.
- [26] J. Gayler, *Workshop on deep inelastic scattering and QCD*, Paris (1995), p5.
- [27] C. Rubbia, *Proc. 17th Int. Conf. High Energy Phys.* London (1974), ed. J. R. Smith p. IV-117.
- [28] A. M. Cooper-Sarkar, R. C. E. Devenish, A. De Roeck, *Int. J. Mod. Phys.* **A13** (1998) 3385.
- [29] H1 Collab., I. Abt *et al.*, *Nucl. Instr. Meth.* **A386** (1997) 310 and 348.
- [30] ZEUS Collab., M. Derrick *et al.* *Phys. Lett.* **B293** (1992) 465; “The ZEUS Detector: Status Report 1993”, DESY 1993.
- [31] HERMES Collab., Web Page: <http://www-hermes.desy.de/>.
- [32] HERA-B Collab., Web Page: <http://www-hera-b.desy.de/>.
- [33] W. Bartel *et al.*, *Proc. of the 1996 HERA Workshop*, Vol. 2, eds. G. Ingelman, A. De Roeck, R. Klanner, DESY (1996) 1095.
- [34] J. Gayler, “Improvement of Resolution in Non-Compensating Calorimeter by Energy Weighting”, H1 internal note, *H1-05/85-019*, 1985.
- [35] H1 Calorimeter Group, B. Andrieu *et al.*, *Nucl. Instr. and Meth.* **A336** (1993) 499.

- [36] R. Brun *et al.*, “GEANT3 User’s Guide”, CERN-DD/EE-84-1 (1987).
- [37] S. Bentvelsen, J. Engelen and P. Kooijman, *Proc. of the 1991 HERA Workshop*, Vol. 1, eds. W. Buchmüller and G. Ingelman, DESY (1992) 25; K. C. Hoeger, *ibid.* 43; and references therein.
- [38] U. Bassler and G. Bernardi, *Nucl. Instr. Meth.* **A361** (1995) 197.
- [39] L. W. Whitlow *et al.*, *Phys. Lett.* **B282** (1992) 475.
- [40] R. K. Ellis, W. J. Stirling, and B. R. Webber, *QCD and Collider Physics*, Cambridge 1996.
- [41] R. P. Feynman, *Phys. Rev. Lett.* **23** (1969) 1415; “Photon Hadron Interaction”, W. A. Benjamin, New York (1972).
- [42] J. D. Bjorken, *Phys. Rev.* **179** (1969) 1547.
- [43] C. G. Callan and D. Gross, *Phys. Rev. Lett.* **22** (1969) 156.
- [44] W. A. Bardeen *et al.*, *Phys. Rev.* **D18** (1978) 3998.
- [45] G. Altarelli, R. K. Ellis and G. Martinelli, *Nucl. Phys.* **B157** (1979) 461.
- [46] E. B. Zijlstra and W. van Neerven, *Nucl. Phys.* **B383** (1992) 525.
- [47] A. M. Cooper-Sarkar *et al.*, *Z. Phys.* **C39** (1988) 281.
- [48] L. N. Lipatov, *Sov. J. Nucl. Phys.* **20** (1975) 95; V. N. Gribov and L. N. Lipatov, *Sov. J. Nucl. Phys.* **15** (1972) 438; G. Altarelli and G. Parisi, *Nucl. Phys.* **B126** (1977) 298; Yu. L. Dokshitzer *Sov. Phys. JETP* **46** (1977) 641.
- [49] G. Altarelli and G. Parisi, in Ref.[48].
- [50] See e.g. W. L. van Neerven and A. Vogt, hep-ph/0007362; hep-ph/0006154.
- [51] E. A. Kuraev, L. N. Lipatov, and V. S. Fadin, *Sov. Phys. JETP* **45** (1977) 199; Y. Y. Balitsky and L. N. Lipatov, *Sov. J. Nucl. Phys.* **28** (1978) 822.
- [52] V. S. Fadin, and L. N. Lipatov, *Phys. Lett.* **B429** (1988) 127, hep-ph/9802290; M. Ciafaloni and G. Camici, *Phys. Lett.* **430** (1998) 349, hep-ph/9803389; references therein.
- [53] G. P. Salam, hep-ph/0005304.
- [54] R. S. Thorne, *Phys. Lett.* **B474** (2000) 372, hep-ph/9912284.

- [55] M. Ciafaloni, *Nucl. Phys.* **B296** (1988) 49;  
 S. Catani, F. Fiorani and G. Marchesini, *Phys. Lett.* **B234** (1990) 339;  
*Nucl. Phys.* **B336** (1990) 18.
- [56] A. Milsztajn and M. Virchaux, *Phys. Lett.* **B274** (1992) 221.
- [57] H. Plothow-Besch, PDFLIB User's Manual, Version 8.04, April 2000.
- [58] A. D. Martin *et al.*, *Eur. Phys. J.* **C4** (1998) 463, hep-ph/9803455.
- [59] CTEQ Collab., see <http://www.phys.psu.edu/~cteq>.
- [60] M. Albrow *et al.*, Contribution to Snowmass 96 Proceedings, hep-ph/9706470.
- [61] Review of Particle Properties, D. E. Groom *et al.*, *Eur. Phys. J.* **C15** (2000) 1
- [62] F. James, *CERN Program Library*, **D506**.
- [63] M. A. Parker *et al.*, *Nucl. Phys.* **B232** (1984) 1.
- [64] D. Allasia *et al.*, *Nucl. Phys.* **B239** (1984) 301; *Phys. Lett.* **B135** (1984) 231; *Z. Phys.* **C28** (1985) 321.
- [65] R. D. Field and R. P. Feynman, *Phys. Rev.* **D15** (1977) 2590.
- [66] G. R. Farrar and D. R. Jackson, *Phys. Rev. Lett.* **35** (1975) 1416.
- [67] NMC Collab., P. Amaudruz *et al.*, *Phys. Lett.* **B295** (1992) 159, and Erratum to CERN-PPE/92-124, CERN, April 1993.
- [68] K. Gottfried, *Phys. Rev. Lett.* **18** (1967) 1154.
- [69] CTEQ Collab., H. L. Lai *et al.*, *Phys. Rev. D* **55** (1997) 1280, hep-ph/9701256, hep-ph/9903282.
- [70] NA51 Collab., A. Baldit *et al.*, *Phys. Lett.* **B332** (1994) 244.
- [71] E886 Collab., E. A. Hawker *et al.*, *Phys. Rev. Lett.* **80** (1998), 3717, hep-ex/9803011.
- [72] CCFR Collab., A. O. Bazarko *et al.*, *Z. Phys.* **C65** (1995) 189.
- [73] H1 Collab., C. Adloff *et al.*, *Z. Phys.* **C72** (1996) 593.
- [74] ZEUS Collab., J. Breitweg *et al.*, *Phys. Lett.* **B407** (1997) 402.
- [75] M. Glück, E. Reya, and A. Vogt, *Z. Phys.* **C53** (1992) 127; *Phys. Lett.* **B306** (1993) 391.

- [76] M. Glück, E. Reya, and A. Vogt, *Z. Phys.* **C67** (1995) 433.
- [77] M. Glück, E. Reya and A. Vogt, *Eur. Phys. J.* **C5** (1998) 461.
- [78] E. Gotsman *et al.*, “Has HERA reached a new QCD regime?”, hep-ph/0010198.
- [79] P. D. B. Collins, “Introduction to Regge Theory and High Energy Physics”, Cambridge University Press (1977).
- [80] A. Donnachie and P. V. Landshoff, *Z. Phys.* **C61** (1994) 139.
- [81] A. Donnachie and P. V. Landshoff, *Phys. Lett.* **B437** (1998) 408; *Phys. Lett.* **B470** (1999) 243.
- [82] W. Hollik, *Proc. of the 1987 HERA Workshop*, Vol. 2, ed. R. D. Peccei, DESY (1987) 579.
- [83] H. Spiesberger, *Proc. of the 1987 HERA Workshop*, Vol. 2, ed. R. D. Peccei, DESY (1987) 605.
- [84] H. Spiesberger, *Proc. of the 1991 HERA Workshop*, Vol. 2, eds. W. Buchmüller and G. Ingelman, DESY (1992) 798.
- [85] A. D. Martin, W. J. Stirling, R. G. Roberts, *Phys. Lett.* **B306** (1993) 145; *ibid.* **B309** (1993) 492.
- [86] CTEQ Collab., J. Botts *et al.*, *Phys. Lett.* **B304** (1993) 159.
- [87] H1 Collab., I. Abt *et al.*, *Nucl. Phys.* **B407** (1993) 515.
- [88] ZEUS Collab., M. Derrick *et al.*, *Phys. Lett.* **B316** (1993) 412.
- [89] A. Donnachie and P. V. Landshoff, *Phys. Lett.* **B296** (1992) 227.
- [90] A. D. Martin, W. J. Stirling and R. G. Roberts, *RAL-93-077* (1993).
- [91] Z. Zhang, V. Brisson, and M. Jaffre, “A measurement of  $F_2(x, Q^2)$  with the 1993 data at high  $Q^2$  region”, H1 internal note, *H1-09/94-379*, 1994.
- [92] Y. Ban, PhD thesis, Université de Paris-Sud, *LAL 96-43*, 1996.
- [93] E. Chabert *et al.*, “QBGFMAR, An update PHAN package for cosmic and halo muon topological rejection in high  $P_T$  physics analysis”, H1 internal note, *H1-11/98-556* 1998;  
I. Negri *et al.*, “A minimal comprehensive set of muon background topological finders for high  $P_T$  physics analysis”, H1 internal note, *H1-10/96-498*, 1996.

- [94] H1 Collab., C. Adloff *et al.*, *Eur. Phys. J.* **C13** (2000) 609.
- [95] G. A. Schuler and H. Spiesberger, *Proc. of the 1991 HERA Workshop*, Vol. 3, eds. W. Buchmüller and G. Ingelman, DESY (1992) 1419.
- [96] A. Kwiatkowski, H. Spiesberger, and H. Möhring, *Z. Phys.* **C50** (1991) 165; *Compu. Phys. Commun.* **69** (1992) 155; *Proc. of the 1991 HERA Workshop*, Vol. 3, eds. W. Buchmüller and G. Ingelman, DESY (1992) 1294.
- [97] G. Ingelman, *Proc. of the 1991 HERA Workshop*, Vol. 3, eds. W. Buchmüller and G. Ingelman, DESY (1992) 1366.
- [98] B. Andersson, G. Gustafson and L. Lönnblad, *Nucl. Phys.* **B339** (1990) 393.
- [99] L. Lönnblad, *Comp. Phys. Commun.* **71** (1992) 15; *Z. Phys.* **C65** (1995) 285.
- [100] H1 Collab., I. Abt *et al.*, *Z. Phys.* **C63** (1994) 377.
- [101] ZEUS Collab., M. Derrick *et al.*, *Z. Phys.* **C59** (1993) 231.
- [102] T. Sjöstrand and M. Bengtsson, *Comp. Phys. Commun.* **43** (1987) 367; T. Sjöstrand, Lund Univ. preprint LU-TP-95-20 (August 1995) 321pp; CERN preprint TH-7112-93 (February 1994) 305pp.
- [103] B. Andersson, G. Gustafson, G. Ingelman and T. Sjöstrand, *Phys. Rep.* **97** (1983) 31.
- [104] N. H. Brook, A. De Roeck, and A. T. Doyle, *Proc. of the 1991 HERA Workshop*, Vol. 3, eds. W. Buchmüller and G. Ingelman, DESY (1992) 1453.
- [105] H. U. Bengtsson and T. Sjöstrand, *Comp. Phys. Commun.* **46** (1987) 43.
- [106] H1 Collab., T. Ahmed *et al.*, *Phys. Lett.* **B299** (1993) 374.
- [107] H1 Collab., T. Ahmed *et al.*, *Nucl. Phys.* **B439** (1995) 471.
- [108] H1 Calorimeter Group, B. Andrieu *et al.*, *Nucl. Instr. and Meth.* **A350** (1994) 57.
- [109] H1 Calorimeter Group, B. Andrieu *et al.*, *Nucl. Instr. and Meth.* **A336** (1993) 499.
- [110] V. Blobel, *Proc. 1984 CERN School of Computing*, Aiguablava, Spain, *CERN 85-09* (1985), 88; G. D'Agostini, *Nucl. Instrum. Methods* **A362** (1995) 487; G. Zech, DESY preprint, DESY 95-113, 1995.

- [111] R. Buchholz, PhD thesis, Universität Hamburg, 1996;  
A. Quadt, PhD thesis, Oxford University, 1997.
- [112] See e.g. Ch. Leverenz, PhD thesis, Universität Hamburg, 1995.
- [113] H1 Collab., S. Aid *et al.*, *Phys. Lett.* **B354** (1995) 494.
- [114] ZEUS Collab., M. Derrick *et al.*, *Z. Phys.* **C65** (1995) 379.
- [115] H1 Collab., T. Ahmed *et al.*, *Z. Phys.* **C66** (1995) 529;  
M. Fleischer, PhD thesis, Universität Hamburg, 1994;  
U. Obrock, PhD thesis, Universität Dortmund, 1994;  
L. Favart, PhD thesis, Université Libre de Bruxelles, 1995.
- [116] H. Bethe and W. Heitler, *Proc. Roy. Soc.* **A146** (1934) 83.
- [117] S. Levonian, private communication, and  
N. Gogitidze and S. Levonian, H1 internal note, *H1-02/96-471*, 1996.
- [118] R. Engel, Proceedings of the XXIXth Rencontre the Moriond, ed, J. Tran  
Thanh Van, (édition Frontières, 1994) 231.
- [119] A. Panitch, PhD thesis, Université Libre de Bruxelles, 1996.
- [120] H1 BEMC Group, “Calibration and Reconstruction of the BEMC”, H1  
internal report, *H1-08/92-234*, 1992.
- [121] S. Kermiche, PhD thesis, Université de Paris-Sud, *LAL 94-14*, 1994.
- [122] M. W. Krasny *et al.*, *Z. Phys.* **C53** (1992) 687.
- [123] B. González Piñeiro, PhD thesis, Université de Paris-Sud, 1996.
- [124] L. Favart, M. Fleischer, M. Hütte, and Z. Zhang, “The Structure Function  
 $F_2(x, Q^2)$  at Low  $Q^2$  from Radiative Events with H1 at HERA”, DESY  
Internal Report, *DESY FH1K-96-01*, May 1996.
- [125] M. Hütte, PhD thesis, Universität Dortmund, 1996.
- [126] A. Panitch and P. Marage, H1 internal note, *H1-05/93-297*, 1993.
- [127] S. Jadach and W. Płazek, *Proceedings of the Workshop on Physics at*  
*HERA*, Vol. 3, (1991) p.1330;  
W. Płazek, PhD thesis, *Acta Physica Polonica* **B24** (1993) 1229.
- [128] D. R. Yennie, S. C. Frautschi, and H. Suura, *Ann. Phys. (NY)* **13** (1961)  
379.

- [129] A. Arbuzov *et al.*, ‘HECTOR 1.00 A Program for the calculation of QED, QCD and electroweak corrections to  $ep$  and  $lN$  deep inelastic neutral and charged current scattering”, DESY 95-185.
- [130] A. Glazov, Private communication.
- [131] H1 Collab., S. Aid *et al.*, *Nucl. Phys.* **B470** (1996) 3.
- [132] ZEUS Collab., M. Derrick *et al.*, *Z. Phys.* **C69** (1996) 607.
- [133] NMC Collab., M. Arneodo *et al.*, *Phys. Lett.* **B364** (1995) 107.
- [134] H1 Collab., Paper no. 535 contributed to the *Int. Conf. on High Energy Physics*, Vancouver, July 1998.
- [135] H1 Collab., C. Adloff *et al.*, submitted to *Eur. Phys. J.* **C**.
- [136] BCDMS Collab., A. C. Benvenuti *et al.*, *Phys. Lett.* **B223** (1989) 490.
- [137] NMC Collab., M. Arneodo *et al.*, *Phys. Lett.* **B309** (1993) 222.
- [138] H1 Collab., I. Abt *et al.*, *Phys. Lett.* **B321** (1994) 161.
- [139] See e.g. G. Wolf, *DESY 94-022* (1994).
- [140] K. Prytz, *Phys. Lett.* **B311** (1993) 286.
- [141] ZEUS Collab., M. Derrick *et al.*, *Phys. Lett.* **B345** (1995) 576.
- [142] CTEQ Collab., MSUHEP-41024, See also Rev.[59].
- [143] ZEUS Collab., J. Breitweg *et al.*, *Eur. Phys. J.* **C7** (1999) 609.
- [144] See e.g. C. Pascaud and F. Zomer, LAL preprint, *LAL/95-05*, 1995.
- [145] WA70 Collab., M. Bonesini *et al.*, *Z. Phys.* **C38** (1988) 371.
- [146] E706 Collab., L. Apanasevich *et al.*, *Phys. Rev. Lett.* **81** (1998) 2642.
- [147] F. Bedeschi, talk at 1999 Hadron Collider Physics Conference, Bombay, January, 1999.
- [148] D0 Collab., B. Abbott *et al.*, *Phys. Rev. Lett.* **82** (1999) 2451.
- [149] H1 Collab., C. Adloff *et al.*, *Nucl. Phys.* **B545** (1999) 21.
- [150] See e.g. M. G. Ryskin *et al.*, *Z. Phys.* **C76** (1997) 231, hep-ph/9511228.
- [151] L. N. Hand, *Phys. Rev.* **129** (1963) 1834.
- [152] L. W. Whitlow *et al.*, *Phys. Lett.* **B250** (1990) 193.

- [153] E140X Collab., L. H. Tao *et al.*, *Z. Phys.* **C70** (1996) 387.
- [154] CCFR Collab., U. K. Yang *et al.*, *J. Phys.* **G22** (1996) 775.
- [155] H1 Collab., C. Adloff *et al.*, *Phys. Lett.* **B393** (1997) 452.
- [156] A. M. Cooper-Sarkar *et al.*, in Proc. of the HERA Workshop, Hamburg 1987, ed. R. D. Peccei, Vol.1, p. 231; A. M. Cooper-Sarkar *et al.*, in Proc. of the HERA Workshop, Hamburg 1991, eds. W. Buchmüller and G. Ingelman, Vol.1, p. 155.
- [157] M. W. Krasny *et al.*, *Z. Phys.* **C53** (1992) 687;  
W. Płaczek, PhD thesis, *Acta Physica Polonica* **B24** (1993) 1229.
- [158] L. Favart, M. Gruwé, P. Marage, and Z. Zhang, *Z. Phys.* **C72** (1996) 425, hep-ph/9606465.
- [159] S. Bethke, *J. Phys.* **G26** (2000) R27, hep-ex/0004021.
- [160] M. Davier, *33rd Rencontres de Moriond: Electroweak Interactions and Unified Theories*, Les Arcs, France (14-21 Mar. 1998).
- [161] W. J. Stirling, hep-ph/9709429.
- [162] D. Gross and C. H. Llewellyn Smith, *Nucl. Phys.* **B470** (1969) 337.
- [163] J. Chyla and A. L. Kataev, *Phys. Lett.* **B297** (1992) 385.
- [164] V. M. Braun and A. V. Kolesnichenko, *Nucl. Phys.* **B283** (1987) 723.
- [165] M. Dasgupta and B. Webber, *Phys. Lett.* **B382** (1993) 273.
- [166] CCFR Collab., J. H. Kim *et al.*, *Phys. Rev. Lett.* **81** (1998) 3595.
- [167] Last reference in [64];  
K. Varvell *et al.*, *Z. Phys.* **C36** (1997) 1;  
V. V. Ammosov *et al.*, *Z. Phys.* **C30** (1986) 175;  
P. C. Bosetti *et al.*, *Nucl. Phys.* **B142** (1978) 1.
- [168] CCFR Collab., P. Z. Quintas *et al.*, *Phys. Rev. Lett.* **71** (1993) 1307.
- [169] R. D. Ball and S. Forte, hep-ph/9607289.
- [170] S. Catani and F. Hautmann, *Nucl. Phys.* **B427** (1994) 475.
- [171] J. Santiago and F. J. Yndurain, *Nucl. Phys.* **B563** (1999) 45, hep-ph/9904344.
- [172] ZEUS Collab., M. Derrick *et al.*, *Z. Phys.* **C72** (1996) 399.

- [173] E665 Collab., M. R. Adams *et al.*, *Phys. Rev.* **D54** (1996) 3006.
- [174] A. Vogt, *Nucl. Phys. Proc. Suppl.* **79** (1999) 102, hep-ph/9906337.
- [175] J. Blümlein *et al.*, *Proc. of the 1996 HERA Workshop*, Vol. 1, eds. G. Ingelman, A. De Roeck, R. Klanner, DESY (1996) 52.
- [176] H1 Collab., T. Ahmed *et al.*, *Phys. Lett.* **B346** (1995) 415.
- [177] ZEUS Collab., M. Derrick *et al.*, *Phys. Lett.* **B363** (1995) 201.
- [178] E. Mirkes and D. Zeppenfeld, *Phys. Lett.* **B380** (1997) 205; S. Catani and M. Seymour, *Nucl. Phys.* **B485** (1997) 291, Erratum, **B510** (1997) 503.
- [179] H1 Collab., C. Adloff *et al.*, *Eur. Phys. J.* **C5** (1998) 625; *Eur. Phys. J.* **C6** (1999) 575, hep-ex/9807019.
- [180] H1 Collab., C. Adloff *et al.*, submitted to *Eur. Phys. J.*, DESY-00-145 (2000).
- [181] S. D. Ellis and D. E. Soper, *Phys. Rev.* **D48** (1993) 3160; S. Catani, Yu. L. Dokshitzer, M. H. Seymour and B. R. Webber, *Nucl. Phys.* **B406** (1993) 187.
- [182] ZEUS Collab., Contributed paper 891 to the 30th Inter. Conf. on HEP, Osaka, Japan, July 2000.
- [183] ALEPH Collab., R. Barate *et al.*, *Eur. Phys. J.* **C4** (1998) 409.
- [184] P. Bruel, PhD thesis, Université de Paris-Sud, 1998.
- [185] B. Heinemann, PhD thesis, Université Hamburg, 1999.
- [186] B. Reisert, PhD thesis, in preparation.
- [187] T. Sjöstrand, *Comput. Phys. Commu.* **82** (1994) 74.
- [188] H1 Collab., T. Ahmed *et al.*, *Phys. Lett.* **B324** (1994) 241.
- [189] H1 Collab., S. Aid *et al.*, *Z. Phys.* **C67** (1995) 565.
- [190] H1 Collab., S. Aid *et al.*, *Phys. Lett.* **B379** (1996) 319.
- [191] A. Pieuchot, J. Marks, and C. Vallée, H1 internal note, *H1-01/95-423*, 1995.
- [192] G. Martin, PhD thesis, Universität Hamburg, 1997.
- [193] A. Mehta, Private communication.
- [194] U. Bassler and G. Bernardi, *Z. Phys.* **C76** (1997) 223.

- [195] M. Jacquet, Z. Zhang, V. Brisson, S. Kermiche, and C. Vallée, “Absolute hadronic jet calibration of the H1 liquid argon calorimeter”, H1 internal note, *H1-04/99-571*, 1999.
- [196] J. Kurzhöfer, “The QJCONE jet algorithm and its implementation in H1PHAN, H1 internal note, *H1-08/94-375*, 1994.
- [197] V. Shekelyan, “Simulation and Reconstruction in H1 Liquid Argon Calorimeter”, H1-04/93-288 (1993).
- [198] This is one of routines developed by A. Mehta *et al* originally for diffractive analyses and later applied to the high  $Q^2$  analyses of the  $e^+p$  data of 1994–1997. See also reference [94].
- [199] J. Cao and Z. Zhang, “Towards an unbiased measurement of kinematic variables at low  $y$  region”, H1 internal note, *H1-12/99-580*, 1999.
- [200] A. Babaev *et al.*, “Proposal to upgrade the LAr calorimeter and trigger electronics”, H1 internal note, *H1-01/96-470*, 1996.
- [201] M. Borowski and M. Fleischer, “The performance of the liquid argon calorimeter electronic”, H1 internal note, *H1-12/98-559*, 1998.
- [202] H1 Collab., Contributed paper 975 to the 30th Inter. Conf. on HEP, Osaka, Japan, July 2000.
- [203] ZEUS Collab., J. Breitweg *et al.*, *Eur. Phys. J.* **C12** (2000) 411.
- [204] H1 Collab., C. Adloff *et al.*, submitted to *Eur. Phys. J.*
- [205] ZEUS Collab., J. Breitweg *et al.*, *Eur. Phys. J.* **C11** (1999) 427.
- [206] ZEUS Collab., Contributed paper 549 to Inter. Eur. Conf. on HEP 1999, Tampere, Finnland;  
Contributed paper 1049 to the 30th Inter. Conf. on HEP, Osaka, Japan, July 2000.
- [207] ZEUS Collab., Contributed paper 558 to Inter. Eur. Conf. on HEP 1999, Tampere, Finnland;  
Contributed paper 1050 to the 30th Inter. Conf. on HEP, Osaka, Japan, July 2000.
- [208] CTEQ Collab., H. L. Lai *et al.*, *Phys. Rev.* **D55** (1997) 1280, hep-ph/970125.
- [209] U. K. Yang and A. Bodek, *Phys. Rev. Lett.* **82** (1999) 2467, hep-ph/9809480.
- [210] S. Kuhlmann *et al.*, *Phys. Lett.* **B476** (2000) 291, hep-ph/9912283.

- [211] W. J. Stirling *J. Phys.* **G25** (1999) 1273, hep-ph/9902212.
- [212] D. Haidt and H. Pietschmann: Landolt-Börnstein New Series I/10, Springer (1988), p.213.
- [213] See e.g. A. M. Cooper-Sarkar *et al.*, *J. Phys.* **G25** (1999) 1387, hep-ph/9902277.
- [214] A. Gurtu, Planary talk “Precision Tests of the EW Gauge Theory”, *Int. Conf. on High Energy Physics*, Osaka, 2000.
- [215] V. Brisson *et al.*, *Proc. of the 1991 HERA Workshop*, Vol. 2, eds. W. Buchmüller and G. Ingelman, DESY (1992) 947.
- [216] R. J. Cashmore *et al.*, *Proc. of the 1996 HERA Workshop*, Vol. 1, eds. G. Ingelman, A. De Roeck, R. Klanner, DESY (1996) 163.
- [217] J. C. Pati and A. Salam, *Phys. Rev.* **D10** (1974) 275;  
P. Langacker, *Phys. Rep.* **72** (1981) 185;  
H. Georgi and S. L. Glashow, *Phys. Rev. Lett.* **32** (1974) 438.
- [218] A. Dobado, M. J. Herrero and C. Muñoz, *Phys. Lett.* **B191** (1987) 449;  
J. F. Gunion and E. Ma, *Phys. Lett.* **B195** (1987) 257;  
R. W. Robinett, *Phys. Rev.* **D37** (1988) 1321;  
J. A. Grifols and S. Peris, *Phys. Lett.* **B201** (1988) 287.
- [219] B. Schrempp and F. Schrempp, *Phys. Lett.* **B153** (1985) 101, and references therein;  
J. Wudka, *Phys. Lett.* **B167** (1986) 337.
- [220] S. Dimopoulos and L. Susskind, *Nucl. Phys.* **B155** (1979) 237;  
S. Dimopoulos, *Nucl. Phys.* **B168** (1980) 69;  
E. Farhi and L. Susskind, *Phys. Rev.* **D20** (1979) 3404; *Phys. Rep.* **74** (1981) 277.
- [221] LEGO 0.02 and SUSSEX 1.5, K. Rosenbauer, dissertation RWTH Aachen (in German), PITHA 95/16, July 1995.
- [222] H1 Collab., C. Adloff *et al.*, *Eur. Phys. J.* **C11** (1999) 447, hep-ex/9907002;  
*Erratum*, *Eur. Phys. J.* **C14** (2000) 553.
- [223] H1 Collab., Contributed paper 954 to the 30th Inter. Conf. on HEP, Osaka, Japan, July 2000.
- [224] H1 Collab., Contributed paper 953 to the 30th Inter. Conf. on HEP, Osaka, Japan, July 2000.

- [225] W. Buchmüller, R. Rückl and D. Wyler, *Phys. Lett.* **B191** (1987) 442; *Erratum*, *Phys. Lett.* **B448** (1999) 320.
- [226] H1 Collab., C. Adloff *et al.*, *Phys. Lett.* **B479** (2000) 358.
- [227] H1 Collab., Contributed paper 951 to the 30th Inter. Conf. on HEP, Osaka, Japan, July 2000.
- [228] OPAL Collab., K. Ackerstaff *et al.*, *Eur. Phys. J.* **C6** (1999) 1.
- [229] CDF and D0 Collab., “Combined Limits on First Generation Leptoquarks from the CDF and D0 Experiments”, hep-ex/9810015, Oct. 1998.
- [230] L3 Collab., M. Acciarri *et al.*, *Phys. Lett.* **B433** (1998) 163.
- [231] ALEPH Collab., R. Barate *et al.*, *Eur. Phys. J.* **C12** (2000) 183.
- [232] ZEUS Collab., J. Breitweg *et al.*, to appear in *Eur. Phys. J.* **C**; Contributed papers 1043 and 1044 to the 30th Inter. Conf. on HEP, Osaka, Japan, July 2000.
- [233] H1 Collab., S. Aid *et al.*, *Phys. Lett.* **B380** (1996) 461.
- [234] ZEUS Collab., J. Breitweg *et al.*, *Phys. Lett.* **B434** (1998) 214.
- [235] H. Dreiner, “Perspectives on Supersymmetry”, ed. G. L. Kane, World Scientific, hep-ph/9707435.
- [236] H1 Collab., Contributed paper 957 to the 30th Inter. Conf. on HEP, Osaka, Japan, July 2000.
- [237] ZEUS Collab., Contributed paper 1042 to the 30th Inter. Conf. on HEP, Osaka, Japan, July 2000.
- [238] R. Mohapatra, *Phys. Rev.* **D34** (1986) 3457; J. D. Vergados, *Phys. Lett.* **B184** (1987) 55; M. Hirsch, H. V. Klapdor-Kleingrothaus, and S. G. Kovalenko, *Phys. Lett.* **B352** (1995) 1; *Phys. Rev. Lett.* **75** (1995) 17; *Phys. Rev.* **D53** (1996) 1239.
- [239] P. Langacker, *Phys. Lett.* **B256** (1991) 277.
- [240] D0 Collab., B. Abbott *et al.*, *Phys. Rev. Lett.* **83** (1999) 4476.
- [241] E. Fermi, *Z. Phys.* **88** (1934) 161; *Nuovo Cimento* **11** (1934) 1.
- [242] E. J. Eichten, K. D. Lane and M. E. Peskin, *Phys. Rev. Lett.* **50** (1983) 811; R. Rücke, *Phys. Lett.* **B129** (1983) 363; *Nucl. Phys.* **B234** (1984) 91.

- [243] P. Haberl, F. Schrempp and H.-U. Martyn, *Proc. of the 1991 HERA Workshop*, Vol. 2, eds. W. Buchmüller and G. Ingelman, DESY (1992) 1133.
- [244] G. Altarelli *et al.*, *Nucl. Phys.* **B506** (1997) 3.
- [245] V. Barger *et al.*, *Phys. Rev.* **D57** (1998) 391.
- [246] H1 Collab., Contributed papers 951 ad 952 to the 30th Inter. Conf. on HEP, Osaka, Japan, July 2000.
- [247] ZEUS Collab., J. Breitweg *et al.*, *Eur. Phys. J.* **C14** (2000) 239.
- [248] OPAL Collab., G. Abbiendi *et al.*, *Eur. Phys. J.* **C13** (2000) 533.
- [249] ALEPH Collab., R. Barate *et al.*, *Eur. Phys. J.* **C12** (2000) 183; DELPHI Collab., P. Abreu *et al.*, *Eur. Phys. J.* **C11** (1999) 383; L3 Collab., CERN-EP/2000-061, hep-ex/0005028.
- [250] CDF Collab., F. Abe *et al.*, *Phys. Rev. Lett.* **79** (1997) 2192; D0 Collab., B. Abbott *et al.*, *Phys. Rev. Lett.* **82** (1999) 4769.
- [251] N. Arkani-Hamed, S. Dimopolous and G. Dvali, *Phys. Lett.* **B429** (1998) 263; *Phys. Rev.* **D59** (1999) 086004.
- [252] J. C. Long, H. W. Chen, and J. C. Price, *Nucl. Phys.* **B539** (1999) 23.
- [253] G. F. Giudice, R. Rattazzi and J. D. Wells, *Nucl. Phys.* **B544** (1999) 3, hep-ph/9811291.
- [254] L3 Collab., M. Acciarri *et al.*, *Phys. Lett.* **B470** (1999) 281.